Università degli Studi di Cagliari

Ph.D. DEGREE

Electronic Engineering and Computer Science

Cycle XXXIV

RF Modeling, Design, Characterization and Biomedical Applications of Magnetic Scaffolds

Scientific Disciplinary Sector(s)

ING-INF/02

Ph.D. Student: Matteo Bruno Lodi

Supervisors Prof. Giuseppe Mazzarella
Dr. Alessandro Fanti

Final exam. Academic Year 2020/2021
Thesis defence: April 2022 Session

UNIVERSITA' DEGLI STUDI DI CAGLIARI

Department of Electrical and Electronic Engineering

PhD in Electronic Engineering and Computer Science

RF Modeling, Design, Characterization and Biomedical Applications of Magnetic Scaffolds

Supervisors:

Prof. Giuseppe Mazzarella

Dr. Alessandro Fanti

Candidate: Matteo Bruno Lodi

Cicle XXXIV

Questa tesi può essere utilizzata, nei limiti stabiliti dalla normativa vigente sul Diritto d'Autore (Legge 22 aprile 1941 n. 633 e succ. modificazioni e articoli da 2575 a 2583 del Codice civile) ed esclusivamente per scopi didattici e di ricerca; è vietato qualsiasi utilizzo per fini commerciali. In ogni caso tutti gli utilizzi devono riportare la corretta citazione delle fonti. La traduzione, l'adattamento totale e parziale, sono riservati per tutti i Paesi. I documenti depositati sono sottoposti alla legislazione italiana in vigore nel rispetto del Diritto di Autore, da qualunque luogo essi siano fruiti.

Statement of Authorship

I declare that this thesis entitled "RF Modeling, Design, Characterization and Biomedical Applications of Magnetic Scaffolds" and the work presented in it are my own.
I hereby confirm that:

- this work was done while in candidature for this PhD degree;
- when I consulted the work published by others, this is always clearly attributed;
- when I quoted the work of others, the source is always given;
- I have acknowledged all main sources of help;
- with the exception of the above references, this thesis is entirely my own work;
- appropriate ethics guidelines were followed to conduct this research;
- for work done jointly with others, my contribution is clearly specified.

Abstract

Multifunctional, stimuli-responsive theranostic biomaterials are gaining attention from the scientific community for their use as versatile, complete platforms in contemporary biomedicine. By combining magnetic nanoparticles and bioceramic, polymeric or composite biomaterials, a magnetic implants or scaffold (MagS), which can be remotely controlled by static or dynamic magnetic fields, can be manufactured. To date, a plethora of MagS have been developed, characterized and tested for tissue engineering, drug delivery and for the hyperthermia treatment of tumors. In particular, bone tumors could be treated with MagS by performing radiofrequency local and interstitial hyperthermia. Furthermore, MagS allow to repair the healed tissue also ensuring drug delivery of magnetic carriers of growth factors. Despite the promising potential, quantitative, engineered and application-driven rules or models for designing MagS have not been provided yet. In this work, we focused on the theoretical and numerical modeling of the hyperthermia treatment of bone cancers by using magnetic scaffolds. We proposed a Cole-Cole model for describing the magnetic susceptibility spectra and investigate the heat dissipation of MagS. A nonlinear, multiphysics electromagneto-thermal model was developed and used to investigate the treatment planning of bone tumors with MagS. The proposed numerical framework allows to properly setup the extrinsic treatment parameters to perform an effective treatment in different physiopathological conditions. Furthermore, the in silico findings highlighted that manufacturing nonlinearities and geometric aspects can be relevant to the hyperthermic potential of MagS. Therefore, we designed and characterized polymeric scaffolds loaded with magnetic nanocrystals by a drop-casting procedure to control the pattern. By combining static magnetic measurements, thermogravimetric analysis and THz tomography, advanced simulations were carried out to assess how the loading patterns of MagS can influence the outcome of the hyperthermia treatment. The evaluation of the specific absorption rate (SAR) of MagS is a crucial aspect. By using a commercial ferromagnetic polymer, we 3D-printed MagS with biomimetic architecture and performed calorimetric measurements in air, de-ionized water and agar environment, to develop a reliable and robust protocol to estimate the SAR. The possibility of using MagS as core element of a magnetic drug delivery system was investigated by developing a novel nonlinear, multiphysics model for account the targeting of nanocarriers of growth factor with static magnetic fields, how to trigger the release of the biomolecule with radiofrequency heating and accelerate the bone tissue healing. Finally, the feasibility of using microwave to non-invasively monitor hyperthermia treatment was investigated with a simplified monodimensional model. This thesis work can foster the development of innovative theranostic modalities using MagS.

Biography

Matteo Bruno Lodi received the Bachelor's degree in Biomedical Engineering from the University of Cagliari, Cagliari, in 2016, and the Master's degree in Biomedical Engineering from Politecnico di Torino, Turin, Italy, in 2018.

His research activity deals with the modelling of bioelectromagnetic phenomena, especially hyperthermia treatment; the study, manufacturing, and synthesis of magnetic biomaterials for tissue engineering applications; and the use of microwave for biotechnology and environmental applications. He has co-authored several papers in top-tier international journals, such as *IEEE Journal of Electromagnetics, RF and Microwaves in Medicine and Biology*, *IEEE Journal on Multiscale and Multiphysics Computational Techniques*, *IEEE Transactions on Biomedical Engineering*, *IEEE Open Journal of Antennas and Propagations*, *Nature Communications*, and many others. He has given talks and demonstrations at several international conferences, while co-charing the session entitled *"Advances in Medical Applications of Electromagnetic Fields"* at *ICECom 2019*, and being part of the organizing committee of the 11^{th} *IEEE International Conference on Nanomaterials: Applications & Properties*. He is a member of the WG2: *"Better thermal-based EM therapeutics"* of the COST Action 17115 "MyWave".

He was awarded as Young Scientists at the General Assembly and Scientific Symposium of URSI in 2020 and 2021. In 2021 he was a co-author of the "2021 IEEE IST Best Student Paper Award" at *IEEE International Conference on Imaging Systems & Techniques*. He received a grant from the European Microwave Association (EuMA) for the attendance of the ESoA course entitled *"Diagnostic and Therapeutic Applications of Electromagnetics"*, and a grant from the COST Action CA17115 for the attendance of the *IX International School of Bioelectromagnetism Alessandro Chiabrera"*, where, in 2019, he received the Best Poster Award.

He has been appointed as Representative for the Young Professionals of IEEE Region 8 Nanotechnology Council. He is a member of the Editorial Board of the *IEEE Future Directions Technology Policy and Ethics newsletter*. He has been also acting as a reviewer for many high-quality journals (`https://publons.com/researcher/1586212/matteo-bruno-lodi/`).

Dissemination

This Ph.D. work resulted in 19 papers, published in international journals and conference proceedings, or currently under preparation. I would like to sincerely thank all of my co-authors for their valuable contributions by adopting the scientific "We" throughout this Ph.D. thesis work.

It is worth to clearly stress my contributions. The research presented in this Ph.D. thesis was envisioned and the majority of the work was performed by myself. In particular, the design approached and research directions were autonomously developed. I performed the literature review, the development of theoretical and numerical models, as well as their implementation in scripts and software, and the data analysis. Moreover, I drafted the papers for submission, while managing the peer-review pipeline, and, hence, performed the review. In this framework, I closely collaborated with the co-authors during all the pre- and post-editorial steps. The co-authors contributed to the preparation of the submitted works, while providing useful feedback, technical support on the approaches and critically discussing the developed techniques.
Three papers have received an award, and are highlighted in red.

For what concerns works (ii) and (xviii), I and Dr. Antonis Markidis equally contributed, with a strong help of Mr. Nicola Carboni for paper (ii). For work (iii), I must acknowledge that Mr. Andrea Vargiu for his contributions to the numerical simulations. In works (iv), I and Dr. Nicola Curreli put comparable efforts. The group from the Institute for Electromagnetic Sensing of the Environment -National Research Council of Italy (IREA-CNR) performed the THz characterization for paper (iv). On the other hand, in work numbered as (iv) I was in charge of developing the numerical framework and in performing the simulations. As regards works numbered as (v), (vii), my contribution was limited. For work (vi), I collaborate with Dr. Muntoni and Mr. Alessandro Ruggeri.

The detailed references to the papers are provided below.
Peer-reviewed Book Chapters

I. Matteo Bruno Lodi, Alessandro Fanti, "Biomedical Applications of Biomaterials Functionalized with Magnetic Nanoparticles", in *Smart Nanosystems for Biomedicine, Optoelectronics and Catalysis*, Intech Open, 2019. DOI: 10.5772/intechopen.89199.

Peer-reviewed Publications in Journals

II. Matteo Bruno Lodi, Antonis Makridis, Nicola Maria Carboni, Konstantina Kazeli, Alessandro

Fanti, Theodoros Samaras, Makis Angelakeris, Giuseppe Mazzarella, "Design and Characterization of Magnetic Scaffolds for Bone Tumor Hyperthermia", *IEEE Access*, vol. 10, pp. 19768-19779, 2021. DOI: 10.1109/ACCESS.2022.3151470

III. Matteo Bruno Lodi, Alessandro Fanti, Andrea Vargiu, Maurizio Bozzi, Giuseppe Mazzarella, "Mathematical Modeling Of Magnetic Scaffolds For Targeted Drug Delivery And Bone Repair", *IEEE Journal on Multiscale and Multihysics Computational Techniques*, vol. 6, pp. 201-213, 2021. DOI: 10.1109/JMMCT.2021.3134786

IV. Matteo Bruno Lodi, Nicola Curreli, Sonia Zappia, Luca Pilia, Maria Francesca Casula, Sergio Fiorito, Ilaria Catapano, Francesco Desogus, Teresa Pellegrino, Ilka Kriegel, Lorenzo Crocco, Giuseppe Mazzarella, Alessandro Fanti, "Influence of Magnetic Scaffold Loading Patterns on their Hyperthermic Potential against Bone Tumors", *IEEE Transaction on Biomedical Engineerign*, Early Access. 2021. DOI: 10.1109/TBME.2021.3134208

V. Michele Ghini, Nicola Curreli, Matteo Bruno Lodi, Nicolò Petrini, Mengjiao Wang, Mirko Prato, Alessandro Fanti, Liberato Manna, Ilka Kriegel, "Control of electronic band profiles through depletion layer engineering in core-shell nanocrystals", *Nature Communications*, vol. 13, no. 1, pp- 1-9, 2022. DOI: 10.1038/s41467-022-28140-y

VI. Chiara Dachena, Alessandro Fedeli, Alessandro Fanti, Matteo Bruno Lodi, Giorgio Fumera, Andrea Randazzo, Matteo Pastorino, "Microwave Imaging of the Neck by Means of Artificial Neural Networks for Tumor Detection", *IEEE Open Journal of Antennas and Propagation*, vol. 2, pp. 1044-1056, 2021. DOI: 10.1109/OJAP.2021.3121177

VII. Matteo Bruno Lodi, Giacomo Muntoni, Alessandro Ruggeri, Alessandro Fanti, Giorgio Montisci, Giuseppe Mazzarella, "Towards the Robust and Effective Design of Hyperthermic Devices: Improvement of a Patch Antenna for the Case Study of Abdominal Rhabdomyosarcoma with 3D Perfusion", *IEEE Journal of Electromagnetics, RF and Microwaves in Medicine and Biology*, vol. 5, no. 3, p. 197–205, 2021, 9169813. DOI: 10.1109/JERM.2020.3016890

VIII. Chiara Dachena, Alessandro Fedeli, Alessandro Fanti, Matteo Bruno Lodi, Matteo Pastorino, Andrea Randazzo, "Microwave Imaging for the Diagnosis of Cervical Diseases: A Feasibility Analysis", *IEEE Journal of Electromagnetics, RF and Microwaves in Medicine and Biology*, vol. 5, no. 3, pp. 277–285, 2021, 9281342. DOI: 10.1109/JERM.2020.3042711

IX. Matteo Bruno Lodi, Alessandro Fanti, Giacomo Muntoni, Giuseppe Mazzaerlla, "A Multiphysic Model for the Hyperthermia Treatment of Residual Osteosarcoma Cells in Upper Limbs Using Magnetic Scaffolds", *IEEE Journal on Multiscale and Multiphysics Computational Techniques*, vol. 4, 2019. DOI: 10.1109/JMMCT.2019.2959585

X. Alessandro Fanti, Matteo Bruno Lodi, Giuliano Vacca, Giuseppe Mazzarella, "Numerical Investigation of Bone Tumor Hyperthermia Treatment Using Magnetic Scaffolds", *IEEE Journal of Electromagnetics, RF and Microwaves in Medicine and Biology*,vol. 2, no. 4, pp. 294-301, 2018. DOI: 10.1109/JERM.2018.2866345

Peer-reviewed Publications in International Conference Proceedings

xi. Matteo Bruno Lodi, "Theoretical Considerations for the Design of Magnetic Scaffolds for Bone Tumor Hyperthermia", in *2021 XXXIVth General Assembly and Scientific Symposium of the International Union of Radio Science*, 2021. DOI: 10.23919/URSIGASS51995.2021.9560650.

xii. Matteo Bruno Lodi, Alessandro Fanti, "Multiphysics Modeling of Magnetic Scaffolds for Biomedical Applications", in *2021 IEEE 11th International Conference Nanomaterials: Applications & Properties (NAP)*, 2021. DOI: 10.1109/NAP51885.2021.9568562.

xiii. Matteo Bruno Lodi, "Challenging the Modeling of Magnetic Hyperthermia of Secondary Bone Tumors Using Magnetic Prosthetic Implants", in *2020 XXXIIIrd General Assembly and Scientific Symposium of the International Union of Radio Science*, 2020. DOI: 10.23919/URSIGASS49373.2020.9232176.

xiv. Simona Di Meo, Julian Bonello, Matteo Bruno Lodi, Iman Farhat, Lourdes Farrugia, Alessandro Fanti, Marco Pasian, Francesco Desogus, Charles V. Sammut, "On the dielectric/thermal characterization and calibration of solutions and materials for biomedical applications", in *2020 14th European Conference on Antennas and Propagation (EuCAP)*, 2020. DOI: 10.23919/EuCAP48036.2020.9135971.

xv. Matteo Bruno Lodi, Giuliano Vacca, Giacomo Muntoni, Alessandro Fanti, Giuseppe Mazzarella, "Non-linear Multiphysic Numerical Study of Bone Tumor Hyperthermia Using Magnetic Biomaterials", in *2019 IEEE MTT-S International Conference on Numerical Electromagnetic and Multiphysics Modeling and Optimization, NEMO 2019*, 2019. DOI: 10.1109/NEMO.2019.8853664.

xvi. Giacomo Muntoni, Alessandro Fanti, Matteo Bruno Lodi, Giorgio Montisci, "Optimum Design of Superficial Microwave Hyperthermia Treatment", in *2019 IEEE MTT-S International Conference on Numerical Electromagnetic and Multiphysics Modeling and Optimization (NEMO)*, 2019. DOI: 10.1109/NEMO.2019.8853791.

xvii. Matteo Bruno Lodi, Giuliano Vacca, Alessandro Fanti, Lorenzo Luini, Giuseppe Vecchi, Giuseppe Mazzarella, "Numerical Comparison of Magnetic Biomaterials for Hyperthermia Applications: The Osteosarcoma Case", in *13th European Conference on Antennas and Propagation, EuCAP 2019*, 2019.

Ongoing

xviii. Matteo Bruno Lodi, Antonis Makridis, Konstantina Kazeli, Alessandro Fanti, Theodoros Samaras, Makis Angelakeris, Giuseppe Mazzarella, "A Universal Protocol for Evaluating the Specific Absorption Rate of Magnetic Scaffolds", Under Preparation.

Nomenclature

Abbreviations

AC	Alternate Current
BDF	Backward Differentiation Formula
BM	Bone Marrow
DAS	Delay and Sum
DC	Direct Current
DD	Drug Delivery
DSC	Differential Scanning Calorimetry
ECM	Extra-Cellular Matrix
Fe-HA-PCL	Poly-Caprolactone (PCL) loaded with iron-doped hydroxyapatite (Fe-HA)
FEM	Finite Element Method
FM	Ferromagnetic
GF	Growth Factor
HA	Hydroxyapatite
HT	Hyperthermia Treatment
IV	Intravenous Injection
MagS	Magnetic Scaffold/s
MDD	Magnetic Drug Delivery
MF	Magnetic Field
MFH	Magnetic Fluid Hyperthermia
MHA	intrinsic Magnetic Hydroxyapatite
MNC	Magnetic NanoCrystals

ML	Machine Learning
MNPs	Magnetic Nano-Particles
MO	Metal Oxide
MPI	Magnetic Particle Imaging
MRI	Magnetic Resonance Imaging
MSC	Mesenchymal Stem Cell
MUMPS	MUltifrontal Massively Parallel Sparse direct Solver
NIR	Near-InfraRed
OB	Osteoblast
PAA	Poly-(Acrylic Acid)
PARDISO	PARallel DIrect SOlver
PBHE	Pennes' Bio-Heat Equation
PCL	Poly-Caprolactone
PE	Poly-Ethylene
PLA	Poly-Lactic Acid
PP	Poly-Propylene
PVA	Poly-Vynil Alcool
RBF	Radial Basis Function
RF	Radio-Frequency
ScR	Scaffold Release
SPM	Super-Paramagnetic
STL	Stereolithography
TE	Tissue Engineering
TGA	ThermoGravimetric Analysis
TGF	Transforming Growth Factor
TOF	Time Of Flight
TPMS	Triply Periodic Minimal Surfaces
VEGF	Vascular Endothelium Growth Factor

Table of contents

List of figures

List of tables

Chapter 1

Introduction

1.1 State of the Art

Modern biomedicine is seeking smart, stimuli-responsive biomaterials capable of performing contemporary therapies and diagnostics [1–3]. The devices for repairing a damaged tissue or restoring a loss functionality were initially passive, less harmful as possible biomaterials, but nowadays research efforts in the functional materials science focus on the development of multifunctional biomaterial platforms as ultimate goal. To this aim, a plethora of different platforms has been proposed, such as light-responsive tissue substitutes for photothermal therapy [4] or thermo-responsive hydrogels for drug release [5]. However, magnetic scaffolds (MagS) have gained interest as a versatile, complete system for several biomedical applications (Fig. 1.1) [6].

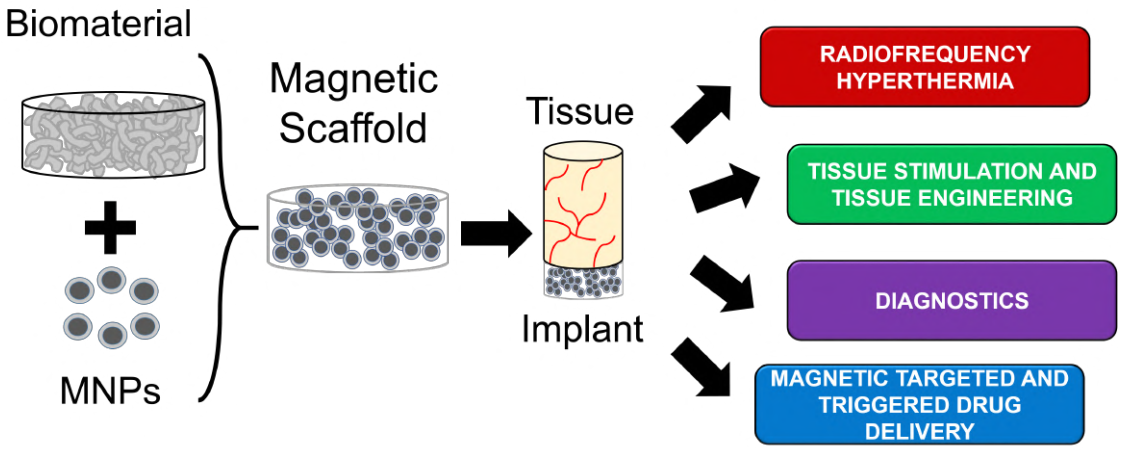

Figure 1.1. Magnetic scaffolds (MagS) are multifunctional devices made of biomaterial and magnetic particles which can be used for magnetic targeted drug delivery, diagnostics, tissue engineering and radiofrequency hyperthermia applications.

Magneto-responsive devices called MagS are traditional biomaterials (e.g., polymers, bioceramics or bioglasses) combined with magnetic nanoparticles (MNPs) [4, 7–17], as shown in Fig. 1.1.

MNPs are, by definition, nanostructures with a characteristic dimension <100 nm [17]. At the nanoscale, the physical properties of a nanomaterial are very different from its bulk counterpart [18], leading to unique and interesting features. MNPs can be prepared by co-precipitation, thermal decomposition, hydrothermal synthesis, microemulsion or microwave-assisted synthesis [19]. MNPs can be of pure metals, metal alloys, but, mostly, metal oxides (MO) are used [17–20]. Among MO, iron oxides (e.g., magnetite - Fe_3O4, maghemite - Fe2O3) are often employed for biomedical applications because of their biocompatibility and stability in physiological conditions [17–20]. The magnetic properties are another key factor [21–23]. However, magnetic features depends on the type of MNPs, on size and shape, and on the synthesis method [17–23]. MNPs are ferromagnetic (FM) when the unpaired electron spins in particles align in a spontaneous way and a magnetization, in absence of an externally applied magnetic field (MF), arise [17, 24]. On the other hand, if in the MNPs crystal the magnetic moments are antiparallel, in a zero MF, below the so-called Néel temperature, ferrimagnetism can be observed [24]. However, at the nanoscale finite-size effects and surface effects can lead to another type of magnetic response, called superparamagnetism (SPM) [18, 21–23]. As the size of the MNPs reduces, the state of lowest energy approaches a uniform magnetization, because of the balance between magnetostatic energy and the domain wall formation [17–24]. When the critical size (d_{cr} $\simeq$25 nm) is reached, the domain wall formation becomes energetically unfavorable, thus leading to a magnetostatic energy which force the so-called single-domain state. The critical size depends upon the saturation magnetization of the MNPs (M_s), its dimension (r_m), the strength of the crystal anisotropy energy (K_a) and the exchange forces [24]. In this scenario, assuming single-domain MNPs to be isolated, when the particle volume is reduced, the thermal energy (k_BT, where k_B is the Boltzmann's constant and T is the system temperature) is higher than the energy barrier of the crystal (K_aV_m, where V_m is the particle volume), allowing the MNPs magnetization to be easily reversed [21]. The transition to the SPM state occurs for temperatures above the so-called blocking temperature (T_B), while depending on the measurements time in experiments [21]. As a result, SPM nanoparticles presents no remanence, zero coercivity, no hysteresis and reversible magnetic properties [18]. All of the aforementioned magnetic responses of MNPs can be effectively exploit to produce a multifunctional device for biomedical applications [4, 7–17].

In this framework, MagS are smart materials which can be triggered by an external electromagnetic (EM) stimuli (which can be either static or dynamics), presenting a high potential for innovative treatments, enhanced drug delivery or alternative diagnostic approaches [4, 7–17]. The incorporation of MNPs into complex biomaterial systems lead to multifunctional devices that can be spatio-temporally controlled by an external magnetic field. Hence, MagS can be used for several biomedical applications, from diagnostic to the treatment of tumors, and are actively being developed and tested for cancer theranostics (Fig. 1.1).

The literature about magneto-responsive scaffolds is wide and several reviews have been published [4, 7–17]. These works mainly cover the fundamentals of manufacturing and characterization, with strong focus on the applications, mostly covering bioceramics [8, 13, 16] and hydrogels [9], addressing tissue engineering [10, 14] and hyperthermia [4, 8, 13, 15]. Despite these works underline that 3D MagS requires further study and optimization [17], the material science perspective is always the dominating point of view. Therefore, the general notions are not supported by an engineering focus, especially from the electromagnetic, radiofrequency (RF) and microwave (MW) engineering perspective, to quantitatively structure and drive the design, characterization and modeling of MagS. In this chapter we will

- define how MagS can be manufactured,
- present the biomedical applications of MagS,
- highlight lacks and flaws about characterization and modeling aspects,

thus reviewing and analyzing the state of the art of MagS from a new perspective.

As shown in Fig. 1.2.a, the number of publication about magnetic scaffolds grows steadily from the first work of Kokubo and colleagues on magnetic bioglasses in 1990 [13, 25], reaching almost a hundred of works to date.

MagS can be manufactured by using chemical methods or physical routes [4, 7–17]. Among the chemical methods, magnetic precursors in ionic form (e.g., Fe^{2+}, Fe^{3+}) are used to carry out sol-gel synthesis [25–27], doping [28, 29], hydrothermal process [30], co-precipitation [31] or in-situ crystallization [32]. Chemical methods are mostly fit for obtaining magnetic bioceramics or glass ceramics [8, 13, 15], such as the iron-doped ferromagnetic hadrystonite [33], or the P_2O_5-Fe_2O_3-CaO-SiO_2 ferromagnetic glass ceramic from [26], magnetic bredigite [34] (Fig. 1.2.b). Bioceramic- or bioglasses-based MagS represents about a third of the analyzed works. On the other hand, physical methods, such as blending [9], casting [35,36], freeze-drying [37–39], electrospinning [40–42], impregnation or dip-coating [43–45] are more appropriate to load gelatin, hydrogels and polymers with MNPs. Examples are the poly-ethylene glycole and gelatin methacrylate scaffold for patterning cell culture by means of static magnetic fields [46], or the solvent casting MagS made of silk-elastine protein with $CoFe_2O_4$ MNPs [35], or poly-lactic acid membranes with aligned nanofiber loaded with Fe_3O_4 [47]. Polymer matrix are the preferred platform and half of the work focus on this biomaterial. However, in about a tenth of the works, different materials and manufacturing approaches can be combined to obtain a composite, with more than two phases, such as magnetic bone cements [48], or as 3D-printed Fe_3O-4-loaded mesoporous bioglasses and poly-(caprolactone) (PCL) scaffold [49], the carbonate-apatite-chitosan- alginate scaffold with calcium aluminum ferrite ($CaAl_4Fe_8O_19$) MNPs [37]. Few works addresses metallic, ferromagnetic steel implants [50–52].

From this discussion, we can highlight the spread and fuzzy nature of MagS, in terms of manufacturing methods, biomaterials, but also MNPs. From the available reviews [4, 7–17] and from our analysis, there is not a rule for selecting these elements, thus the design is driven by

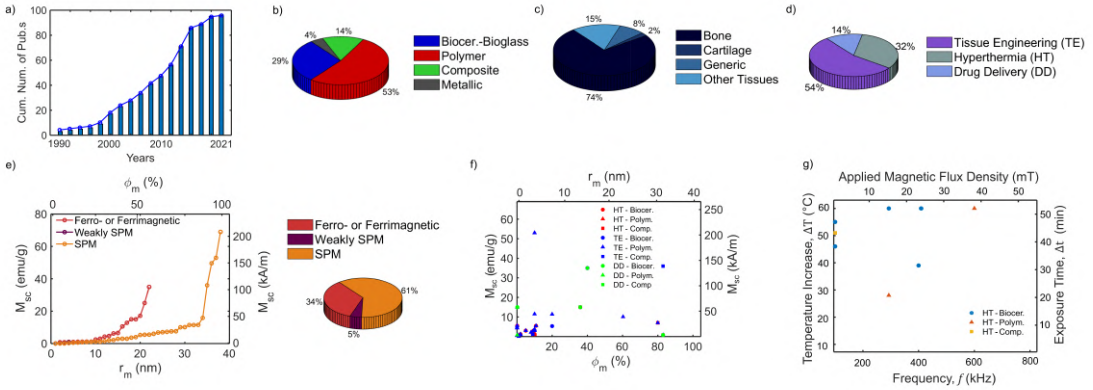

Figure 1.2. a) Cumulative number of publications about magneto-responsive biomaterials for biomedical applications from 1990 to 2021. b) Classification of multi-functional magnetic scaffolds (MagS) according to the biomaterial matrix. c) Clustering of the analyzed MagS by biomedical applications: Tissue Engineering (TE), Hyperthermia treatment (HT) and Drug Delivery (DD). d) Overview of the targeted biological tissues. e) b) Variation of the scaffolds saturation magnetization, M_{sc} in emu·g^{-1} and kAm^{-1}, as a function of the radius (r_m, in nm) and the volume fraction (ϕ_m, in %) of the magnetic nanoparticles (MNPs) embedded in the scaffold. c) Statistics of magnetism types: Ferro- and ferrimagnetic, Weakly Superparamagnetic, Superparamagnetic (SPM) .

the given biomedical application and a trial-and-error empirical process. However, bare, uncoated MO MNPs are widely adopted, whilst circa two-fifths of the works under analysis made use of coated nanoparticles. By taking a look at Fig. 1.2.e, the resulting saturation magnetization of the available MagS (M_{sc}) as a function of the MNPs size (r_m) and the loading fraction of MNPs in the biomaterial (ϕ_m), we can noticed that the average saturation magnetization is 8.381 emu/g ± 6.64 emu/g (29.335 kA/m ± 23.16 kA/m). In this framework, about a third are FM scaffolds, with nanoparticles up to 20 nm, a M_{sc} up to 40 emu/g and a maximum achievable loading fraction of ∼40%. Few works (∼4.12%), when analyzing the static magnetic response of MagS, reported a weakly-superparamagnetic, ambiguous behavior, restricted to similar scaffold saturation magnetization and loading fractions. Half of MagS are SPM and present the wider range of M_{sc} and ϕ_m (1.2.e). SPM MagS are preferred because of their reversible magnetic properties [4, 7–17].

After having analyzed the type of MagS, their manufacturing methods and magnetic response, it is fundamental to analyze the biomedical applications and hence underline the potential and value of this innovative platform for biomedicine.

As sketched by Fig. 1.3, MagS can act as a mechano-transducer device, directly at the cell level [38, 53–57], actuating pN forces [38], or increasing the expression of integrins, through the activation of their pathway [54], and modifies the local Ca^{2+} fluxes thus influencing adhesion, proliferation and differentiation of cells [55]. This is why MagS can be used for magnetic guidance of tissue repair by using static, low frequency (1-100 Hz) or pulsed EM fields [58]. The 45.36% of MagS is mainly designed and tested for tissue engineering (TE), as summarized by Fig. 1.2.c. Most

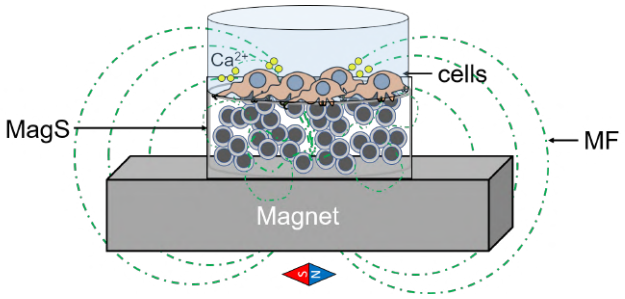

Figure 1.3. Sketch of magnetic scaffold (MagS) as mechano-transducer of an external magnetic field (MF) stimulus, local perturbation of Ca^{2+} fluxes and as activator of the integrin pathway.

(∼three-quartes) of polymeric and bio-ceramic MagS developed for TE are meant to be used as bone substitutes [38, 43, 45, 54, 55, 59], whilst cartilage [60] and other tissues are poorly considered as target, being the topic of few works. For instance, the regeneration of sciatic nerve tissue was tackled in [61]. A magnetic fibrin and agarose substitute of the oral mucosa have been proposed [53]. From an experimental point of view, the value and potential of MagS for TE can be assessed by in vitro tests [36, 62, 63], as done by most of the works. Instead, the biocompatibility can be assessed by animal or human in vivo tests [64–66]. Very few work performed in vivo tests. However, from an engineering and modeling perspective, only simplified, frequency and strength independent, monodimensional models were proposed [67]. Furthermore, by analyzing the results shown in Fig. 1.2.f, we can infer it is not possible to easily correlate MagS properties (M_s, ϕ_m) with the TE application.

As shown in Fig. 1.2, another application of MagS is drug delivery (DD). About a tenth of the analyzed works investigated this potential application. MagS can be used in several ways as platform for DD. Traditional biomaterials for DD are loaded with drugs (e.g., doxorubicin, cisplatin) or biomolecules, which are released when the bioceramic or polymer is degraded by the cells [68]. MagS can accelerate the release process or spatio-temporally control it. Indeed, static or low-frequency MF can be used mechanically trigger the release from hydrogel networks, such as experimentally demonstrated by [9, 69]. On the other hand, by applying a RF (100-800 kHz) MF, the MNPs embedded in the MagS can dissipate a huge amount of heat which can deteriorate a sacrificial layer to free the drug or biomolecule [70], as shown in Fig. 1.4. This concept of DD system was investigated in [33, 49].

However, the appealing approach for overcoming burst release, poor spatial control and the impossibility of re-loading with MagS was proposed in [43]. This strategy aims to combine MagS and innovative MNPs carriers of drugs or growth factors (GFs). Indeed, for some tissues, especially the peculiar bone, the DD is required to repair large defects [71], but a graft or implant is needed to mechanically support the injured area [1–3]. Therefore, as summarized by Fig. 1.4, if a MagS is implanted, a static magnetic field can be used to drive MNPs carrying drugs or GFs, target them at the injury site (i.e., at the scaffold location) and then trigger the drug release by RF-heating [43, 72].

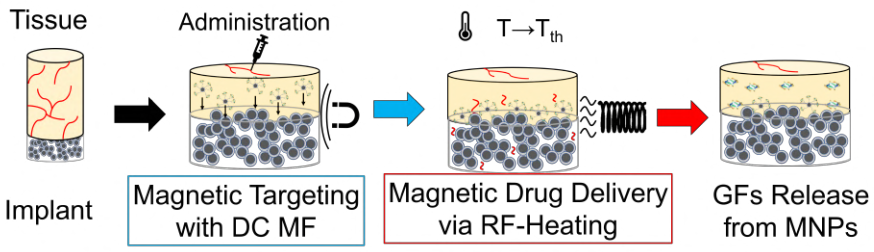

Figure 1.4. Magnetic scaffolds (MagS) can be used as core element for magnetically controlled and activated innovative drug delivery systems. Static (DC) magnetic fields (MF) can be used for the targeting. Radiofrequency (RF) MF can be used to trigger the release of drugs, such as growth factors (GFs)

Considering the findings reported in Fig. 1.2.f, is not trivial to identify a rule for designing MagS for DD with a fit M_s or ϕ_m value. Despite this innovative and fully magnetic drug delivery (MDD) strategy was proposed and preliminary tested in simplified experimental setups, there is a complete lack of understanding of which MagS, MNPs and extrinsic field parameters would be needed to carry out the process shown in Fig. 1.4.

Given that MagS would be implanted for TE or DD purposes, it is worth underlining that these multifunctional platforms can also be used in combination with currently available diagnostic modalities to monitor tissue re-growth and biomaterial degradation [73], as given in Fig. 1.1. MagS were tested for in vivo magnetic resonance imaging (MRI) to monitor bone healing, vascular ingrowth and assess the implant integration by quantifying the changes in the transverse relaxation times T_2 [74, 75], and their safe and compatible use was assessed [76]. However, despite being non-invasive, MRI is an expensive diagnostic modality [74–76]. In this regard, MNPs were already considered as contrast agents to enhance the performance of microwave imaging (MWI) of breast tumors [77–82]. However, to date, MagS were not considered yet as core element of a MWI system for remotely monitoring tissue healing or the MDD process. Furthermore, the possibility of using magnetic particle imaging (MPI) [83] to retrieve spatial and dynamic information about implanted MagS has never been investigated. Therefore, there is room for investigating the feasibility of innovative diagnostic modalities which exploit MagS.

The last, but not least, application of MagS is their possible use as agents for performing thermal treatment against cancers [4,7–17], as shown in Fig. 1.1. Hyperthermia treatment (HT) is a thermal therapy used in oncology, and its aim is to rise the temperature of a target tissue in the range 41-45°C to initiate a cascade events to kill cancer cells, while enhancing the effectiveness of radio- and chemotherapy [84–87]. The first magnetic bioglasses from [25] was conceived to be implanted after surgery, then treat residual bone tumor cells by delivering heat through the application of an external RF MF. The most relevant aspect of using MagS for performing HT is that, if the residual cancer cells are killed and the local recurrence is controlled, the scaffold can be used to promote tissue repair and restore the functionality (see Fig. 1.3). In this framework, MagS are the more biocompatible version of thermoseeds used in colo-rectal cancers [50], or alternative to

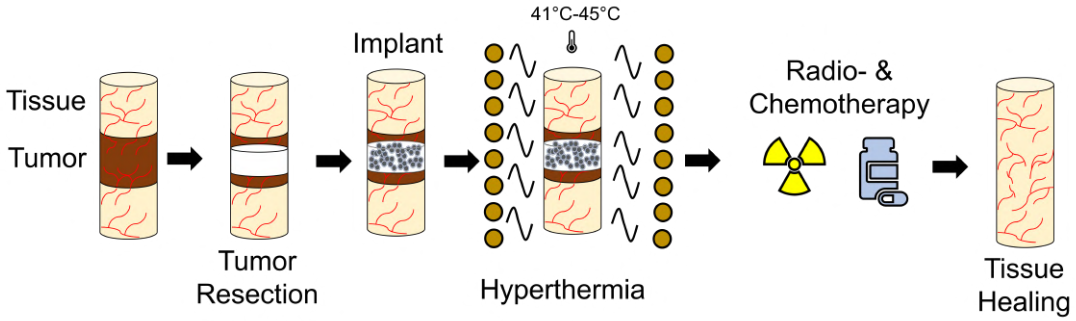

Figure 1.5. Sketch of the rationale for using magnetic scaffolds as biocompatible, implanted thermoseeds for controlling local recurrence rate of bone cancers through hyperthermia treatment.

FM surgical implant inserted in a tumor bed for the delivery local HT in the sub-MHz frequency (90 kHz) [52]. About a third of the literature works about MagS claim to have manufactured and characterized a device for HT [25, 27, 33, 49, 66]. However, by observing the findings from Fig. 1.2.g, a large variability in temperature a spread distribution of the temperature increases as a function of the working frequency f and the strength of the applied field can be noticed. To these findings it must be added that the thermometric methods, the apparatus and sample environment used to assess the hyperthermic potential of MagS present significant differences and underestimated uncertainty. The adoption of standardized metric is poorly applied [88]. Given that HT as a clinical procedure as its own quality and assurance guidelines [88], as well as technical requirements, there is need to revise the modeling of HT of tumors with MagS to provide an organized, robust and reliable framework for performing an effective design of the magneto-responsive device and to plan a high-quality treatment.

With the analysis of the state of the art about MagS we have identified three fundamental biomedical applications for these multifunctional theranostic platforms for biomedicine. In particular, i) hyperthermia, ii) magnetic drug delivery and iii) the noninvasive diagnostics or monitoring. Furthermore, we have highlighted the lack of an engineering point of view. Therefore, in this thesis work we will deal with the modeling, design, characterization of these biomedical applications of MagS.

1.2 Aims

With the analysis of the state of the art, we have highlighted that the literature about MagS offers a huge amount of fuzzy, not aggregated data, while lacking of engineering models, from and EM, RF and MW perspective, which can support the design and use of these multifunctional biomaterials. To fully exploit the great potential of MagS for the aforementioned biomedical applications (Fig. 1.1), it is mandatory to immediately tackle the issue of lacks of models. Therefore, this thesis work aims at:

- facing the problem of modeling the hyperthermia treatment of tumors with MagS, in order to provide a framework to relate the material properties, as well as its non-linearities, with the therapeutic outcome, while dealing with the accurate estimation of the hyperthermic potential.
- address the challenge of developing a theoretical or numerical framework for describing the role and potential of MagS in performing the magnetic drug delivery for tissue repair.
- investigate the feasibility of using MagS as a contrast agents to exploit microwave imaging as innovative diagnostic modality to monitor the hyperthermia treatment or the implant degradation and tissue repair.

1.3 Structure and Contents

This thesis work is organized as follows.

The biological, clinical, modeling and technical aspects of the hyperthermia treatment are introduced in Chap. 2. The concepts for using MagS in cancer therapy are discussed, and a new multiphysics, nonlinear numerical framework for simulating the HT with MagS is proposed.

After having understood the most relevant parameters for hyperthermia, in Chap. 3, we designed, characterized and modeled different type of MagS. In detail, in Sect. 3.1, we studied if and how the loading pattern of MNPs in the biomaterial could influence the outcome of the hyperthermia treatment. To this aim, a drop-casting manufacturing process was developed, and several physical and morphological characterization techniques have been adopted to derive useful data for performing a thorough in silico study aimed at determining if loading inhomogeneity can affect the effectiveness of the thermal therapy.
In Sect. 3.2, we designed biomimetic architecture for 3D-printing MagS with a commercial magnetic filament. Since the methodologies for estimating the hyperthermic potential of MagS are different, presenting largely variable pieces of equipment, thermometry methods and modeling, we investigated three different experimental setups for identifying a reliable and robust protocol aimed at standardizing the quantification of the hyperthermic ability of MagS.

The possible use of MagS as core element of innovative drug delivery systems aimed at accelerating tissue repair is discussed in Chap. 4. A multiphysics model is developed to build a numerical platform to study how relate the material properties with the magnetic targeting of nanocarriers of active biomolecules, as well as with the triggering of the release by radiofrequency heating, while assessing the effects on the biological process of tissue healing.

In Chap. 5, for the first time, a preliminary analysis is carried out to assess if microwaves can be used as a tool for monitoring the hyperthermia treatment with MagS or to evaluate their in vivo degradation. A simplified monodimensional propagation model is used to perform the frequency selection and retrieve suitable properties of the matching medium to ensure an effective microwave signal transmission.

Finally, in Chap. 6, conclusions are provided, the contributions and main findings of this thesis work are summarized, while the future research directions are discussed.

Chapter 2

RF Hyperthermia with Magnetic Scaffolds

2.1 Hyperthermia Treatment: Fundamentals and Technological Aspects

Heat can be an effective therapy against cancers [85–87, 89]. Hyperthermia treatment has the clinical goal of rising the temperature of a target tissue in the range 41–45°C, thus causing the boost of the immune system response, the increase of cytotoxicity through pH modification, the production of free radicals, also inducing the direct damage of DNA and hamper its repair and replication at the cellular level, while provoking vasodilation and perfusion enhancement, hence increasing the permeability to chemotherapeutic drugs and enhancing the radiation effectiveness [85–87, 89], as shown in Fig. 2.1.a.

In order to achieve an effective HT, high quality heating equipment, accurate thermal dosimetry and quality assurance are mandatory [89]. Thermal therapies can be classified into local, locoregional or whole body heating (WBH) [89]. Local heating approaches are interstitial hyperthermia [88], nanoparticle heating, intraluminal heating and superficial heating (Fig. 2.1.b). On the other hand, locoregional heating administration modalities include phased array systems, capacitive technique and perfusion devices [89].

The heat in the biological tissues can be administered with different type of energies, such as ultrasounds (US) [90]. However, US can be problematic for body regions with heterogeneous tissues, cavities or bony interfaces, since strong refraction and reflection cause an excessive overheating [89]. In this thesis, we will focus on EM energy. EM heating strategies use a time-varying field to cause heat dissipation by ionic conduction currents in the extracellular fluid if the working frequency is in the kHz range, or, instead, initiate dielectric heating by molecular dipole rotation and polarization of water molecules inside cells (if $f > 1$ MHz) [89], as shown in Fig. 2.1.c. We can further categorized

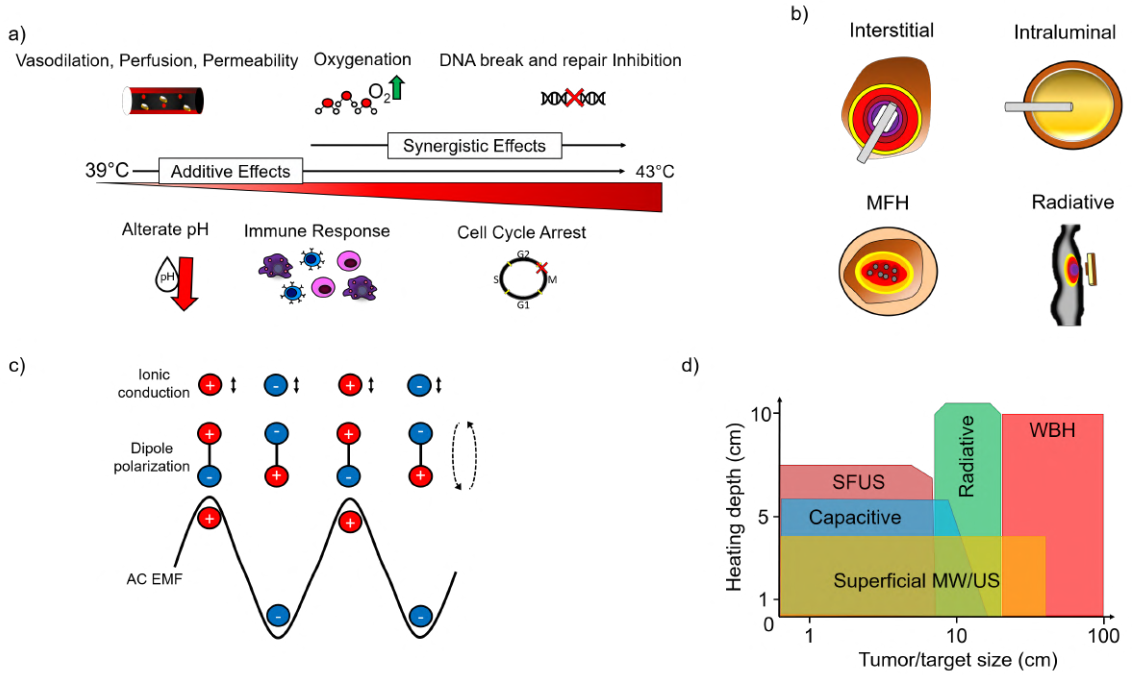

Figure 2.1. a) Summary of biological effects of hyperthermia. b) Pictorial representation of different hyperthermia techniques and heat administration modalities. c) Heating mechanism for Electromagnetic-based hyperthermia: capacitive, radiofrequency, microwave, IR heating). d) Heating depth from the skin (cm) vs. tumor/target size (cm) for some hyperthermic techniques.

EM HT modalities according to f and the penetration depth. Capacitive heating (Fig. 2.1.b)) can be realized with metal electrodes and an RF generator working at 8, 13.56 or 27.12 MHz. Typically, a so-called water bolus bag is used to transfer the energy into the body and to apply skin cooling, and control both surface and deep tissue temperature [89, 91]. As shown in Fig. 2.1.d, capacitive heating can treat superficial and deep-seated tumors, but excessive temperatures, or hot spots, can occur at interfaces between tissues due to the orientation of main electric field components or to inhomogeneous distribution of the power due to a local variation of the EM properties [84]. For small-to-large tumors (1-10 cm), radiative hyperthermia can be used. MW in the industrial, scientific and medical bands of 433 MHz, 915 MHz and 2450 MHz are used [70, 84, 89]. As shown in Fig. 2.1.b, a single antenna, an array or a phased array of antennas can be used to radiate EM energy, and water bolus is still used as matching medium and cooling system. Radiative HT can result in inhomogeneous power absorption and temperature distribution, leading to hot spots at tissue interfaces. As shown in Fig. 2.1.d, the heating depth of radiative hyperthermia can be limited. In the case of deep-seated tumors, interstitial RF or MW needle-like applicators can be employed (Fig. 2.1.b). Also infrared (IR) heating (f >300 GHz) is used, since O–H bonds in water strongly absorb this type of energy [4, 89]. Even if applied with optical fiber guided laser, IR heating as a limited penetration depth of ∼1 cm.

To date, several devices and apparatus have been proposed and developed for the proposed heating strategies, as reviewed by [70, 84, 89]. The HT technology depends upon the heating techniques, is related to the required heating depth, must take into account if focusing is needed, but also on the clinical scenario. Deep-seated tumors are difficult to be treated, without drawbacks and side-effects, by using the aforementioned limitations [85, 86, 89] and for this kind of tumors MagS can be a potential effective solution.

2.2 Issues and Limitations of Radiative Hyperthermia of Deep-Seated Tumors

Several reports present results that shows how microwave radiative hyperthermia can effectively treat tumors located to a depth of ∼3-4 cm [85, 86], but the significant heating of surrounding non-target healthy tissues cannot be avoided [52]. To achieve higher penetration depths (Fig. 2.1.d), complex optimization strategies aimed at power steering and EM energy focusing by phases and amplitude selection for phased array feedings must be developed and used [89, 92].

Anyway, since the control of constructive and destructive interference is not total, local hot spots and heating inhomogeneities may still occur. In this framework, the localized and selective heating of tumors can be realized by placing heat sources (thermoseeds) inside or nearby the tumor (Fig. 2.1.b) [50, 52]. FM interstitial implants, heated with kHz-MHz MF, in the shape of needles, rods or spheres can be used [89]. As shown in Fig. 2.1.d, deep-seated tumors can be treated, resulting in a heating localized within 3–4 mm from the thermo-seed [88]. Interstitial HT can be used in synergy with brachytherapy [89]. Another advantage is that interstitial HT with thermoseeds can be performed remotely, by exposing the patient and implant to the MF (Fig. 1.5). Indeed, recently, magnetic nanocomposite polymeric stents for treating intraluminal tumors have been proposed [93]. With suitable alloys, the tuning of Curie temperature above the therapeutic threshold can be achieved and a self-regulating thermoseed can be developed [17]. The interstitial HT of deep-seated tumors with thermoseeds presents more benefits than MW HT, but it could be preferred to magnetic fluid hyperthermia (MFH) [18, 20, 21, 23]. Indeed, MFH has the limitations of inhomogeneous distribution of MNPs in tissues, which calls to a dynamic adaptive adjustment of the MF amplitude, thus presenting a complex treatment planning [17, 89].

To further support the need and value of MagS as potential tools for performing interstitial HT of bone tumors, we will briefly present the level of complexity and the possible outcome for MW HT by commenting a recent work [94]. The MW treatment of an abdominal sarcoma, shown in Fig. 2.2.a, is considered as case-study. The sarcoma is assumed to have a inhomogeneous perfusion [94]. We consider a simplified layered phantom, which consists of fat, muscle and internal organs. The circular patch antenna shown in Fig. 2.2.b is re-designed to achieve a robust and effective performance. Therefore, the geometrical parameters of the antennas are varied, and tested varying the thickness of fat (t_{fat}) and muscle (t_{mus}) layers. An example of simulated return loss is

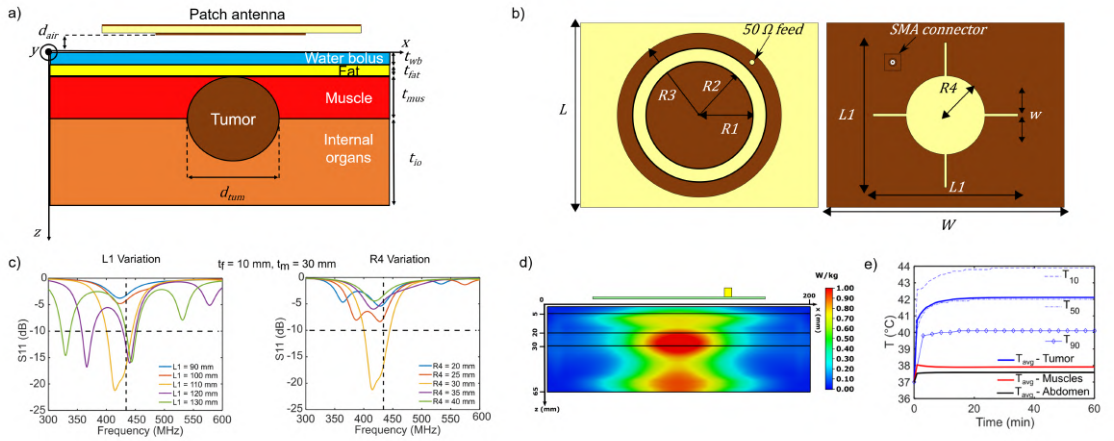

Figure 2.2. a) Surface phantom model for an abdominal rhabdomyosarcoma. The biological tissues radiated by the patch antenna during the hyperthermic treatment are fat, muscle, tumor mass, and an effective medium representing the abdominal internal organs. b) Geometry of the top and bottom layer of the circular patch antenna. c) Simulated return loss (S11) of the antenna varying $L1$ and $R4$. d) SAR evaluated at 434 MHz for the re-worked robust version of the patch. e) Average temperature distribution (T_{avg}) within the biological tissues and T10, T50 and T90 for an applied time-varying power and 3D continuum perfusion model. The average phantom dimensions are used: $t_{fat} = 15\,\text{mm}$, $t_{mus} = 10\,\text{mm}$, $t_{io} = 35\,\text{mm}$.

given in 2.2.c. By investigating the specific absorption rate (SAR) distribution in the phantom, reported in Fig. 2.2.d, it is possible to notice a relevant power absorption behind the spherical tumor. Even though the proposed design is improved with respect to its original configuration [94], the possibility of hot spots cannot be avoided and tumors set to a maximum depth of $\sim$3 cm can be treated effectively, but using a controlled time-varying power, as shown by the results from Fig. 2.2.e.

Sarcomas are a possible example of deep-seated tumors. However, other classes of neoplasms could severely benefit from the use of MagS as HT agents. Primary and secondary bone cancers are a class of pathologies which can strongly benefit from HT [87, 95, 96]. Osteosarcomas (OS) are highly malignant, aggressive and blastic tumors, which affects mainly young subjects (15-25 years old), and have high-recurrence (40%) and metastatic (20%) rates, while being radio-resistant bone tumors [95, 97]. An OS lesion (up to $\sim$5 cm) can originate in different body location, such as the distal femur, the proximal tibia and the proximal humerus [97, 98]. In particular, the osteosarcoma of the methaphysis of the upper end of the humerus constitutes a 10% of all primary tumors [99]. In any of the aforementioned body areas the tumor can settle intra-medullary or intracortically, or peripherally [100]. The neoplastic cells produce a noticeable amount of osteoid or bone with a high rate, in a centrifugal way around a relevant vascular network [98, 99]. The cell growth can determine a pressure which can damage and fracture surrounding healthy bone tissue, causing impairment and pain to the patient [96–100]. Other bone tumors are cartilage-forming (Chondrosarcomas), bone-marrow (Ewing sarcoma), and soft-tissue ones (Fibrosarcoma - FS). FS

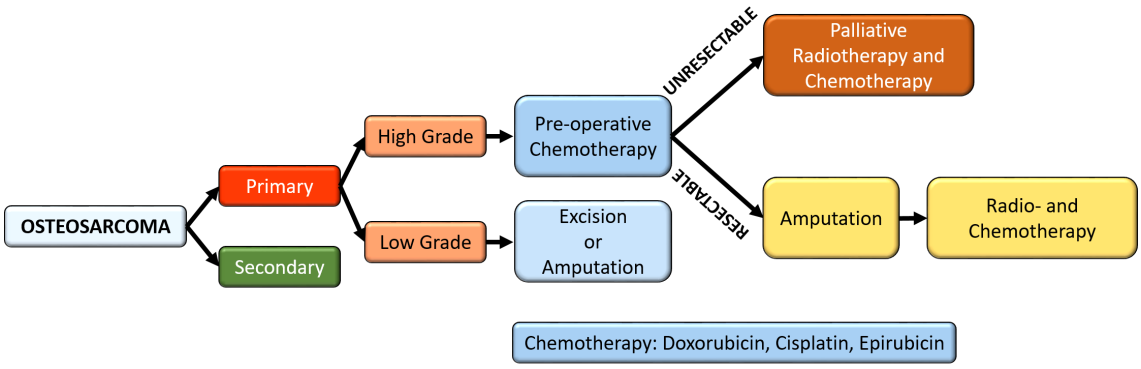

Figure 2.3. Clincal management of osteosarcoma tumors.

is a malignant neoplasm arranged in a fascicular architecture of interlaced trabecular bundles, with scarce vascularization. It tends to extend to soft tissues [100]. A 10-year survival rate equal to 28% for this kind of neoplasm has been reported [101].

Surgical resection of bone tumors, especially OS, is the gold-standard approach A [96], and, actually, an unavoidable clinical decision, as shown in Fig. 2.3. However, the surgery consists in amputation or limb-sparing tumor resection, resulting in disabling outcomes [87, 96]. Alternative strategies are studied, e.g., cryotherapy or embolization, but they are still at the experimental stage [95]. The clinical outcomes of HT as an adjuvant biophysical therapies are gaining the interest of scientific community [102], and some phase I and II trials for locoregional hyperthermia of bone tumors are ongoing [89]. MW HT as standalone therapy showed insufficient clinical outcomes [103–106], while combined to other therapies, can lower the recurrence rate of more than 20%, but results in a postoperative 30% fracture rate, ascribed to bone weakening [103,104]. Besides the specific limitations of surgery and MW-HT, both approaches require a graft or a biomaterial, i.e., a scaffold, for post-operative management. By combining the strict anti-cancer therapeutics and the postoperative orthopedic requirements, the technological advancements in HT delivery lead to the innovative idea of manufacturing MagS to be used as implanted thermoseeds to perform local, interstitial HT of bone cancers by applying an external RF field (Fig. 1.5).

To push the forefront towards new clinical landscapes, a more definitive takeoff of this nan-otherapy against tumors is required. To this aim, it is fundamental that MagS must satisfy the minimum quality assurance requirements of the interstitial HT [88]. In other words, a given MagS should be capable of increasing the system temperature to the therapeutic level of 41-45°C and deposit at least 0.5 W/g in the target volume in response to a RF MF against deep-seated tumors. However, a suitable platform for evaluating theoretically or numerically how MagS behaves during the HT of bone tumors is missing.

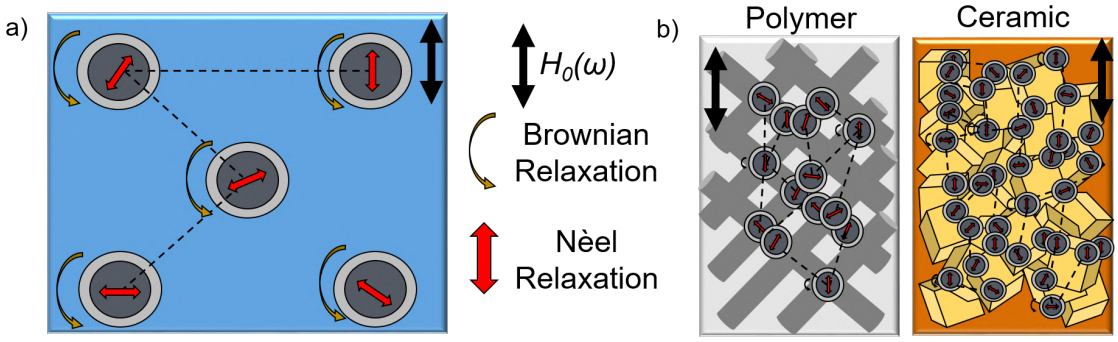

Figure 2.4. a) Schematic picture of the level of interaction of magnetic nanoparticles in a fluid. b) Schematic representation of nanoparticles in a magnetic scaffold (MagS) of polymer and ceramic matrices.

2.3 A Non-Linear Multiphysics Model for Hyperthermia Treatment with Magnetic Scaffolds

The starting point to derive a model capable of seizing the essential features of the HT of bone tumors with MagS must start with the understanding of how the MNPs exposed to the RF MF dissipate power.

Theoretical works dealing with the simplified EM modeling and with the solution of bio-heat equations [50, 107–109] have been proposed. Other works that refined the coupling between the EM and thermal models, computing the currents and field distributions, can be found in [110–113]. However, these models neglected the presence of vessels with dimensions higher than 2 mm, thus biasing and altering the EM and thermal field patterns, as well as the predicted therapeutic outcome [84, 114]. Therefore, patient specific models for the hyperthermia ablation of bone tumors located in the distal portion of the femur were derived from computerized tomography [115]. However, the computational burden of such an accurate geometry can be a relevant limitation when dealing with treatment planning or optimization [84, 116]. It should be pointed out that none of the cited model dealt with the multiphysics nature of the hyperthermia treatment and applied it to the modeling of bone tumor treatments using magnetic scaffolds, as done in [117, 118].

In this chapter we aim at identifying is to develop a multiphysics numerical model for investigating the use of magnetic scaffolds as thermoseeds for the hyperthermia treatment of residual bone cancer cells.

2.3.1 Complex Magnetic Susceptibility

The power per volume unit (Wm^{-3}) dissipated by an ensemble of superparamagnetic nanoparticles, under the action of a sinusoidal, time-varying external magnetic field, is given by [119]

$$P_m = \pi \mu_0 f |\mathbf{H}|^2 \chi'' \tag{2.1}$$

where μ_0 is the vacuum permeability in $\mathrm{H{\cdot}m^{-1}}$, f is the working frequency (in Hz), $\mathbf{H}$ is the magnetic field vector (in $\mathrm{Am^{-1}}$) and χ'' is the imaginary part of the complex magnetic susceptibility, defined as

$$\chi(f) = \chi' - j\chi''. \tag{2.2}$$

A more in-depth analysis of the complex magnetic susceptibility of magnetic scaffolds is required. In the case of magnetic fluid hyperthermia (MFH), for mono-disperse MNPs, homogeneously distributed in a medium with finite viscosity η (Pa·s), as shown in Fig. 2.4, the particles can be assumed to be poorly interacting, thus their susceptibility spectra follows a Debye model [119]

$$\chi(f) = \frac{\chi_0}{1 + 2\pi f \tau} \tag{2.3}$$

where χ_0 is the static susceptibility and $\omega = 2\pi f$ is the angular frequency, whilst τ is an effective relaxation time [119], defined as

$$\frac{1}{\tau} = \frac{1}{\tau_B} + \frac{1}{\tau_N}. \tag{2.4}$$

This effective time is given by the contemporary occurrence of particle and dipolar relaxation, ascribed to two different mechanisms [120]. As first, the Brownian motion of the nanoparticles in the viscous medium occurs, whose characteristic time (τ_B) is [119]

$$\tau_B = \frac{2\eta V_h}{k_B T} \tag{2.5}$$

where V_h is the hydrodynamic radius of the MNPs (in $\mathrm{m^{-3}}$), k_B is the Boltzmann's constant ($\mathrm{J{\cdot}K^{-1}}$) and T is the system temperature, in K. On the other hand, the dipolar relaxation, which accounts for the internal remagnetization process, follows the Néel mechanism, whose characteristic time (τ_N) is defined as

$$\tau_N = \tau_0 e^{\frac{K_a V_m}{k_B T}} \tag{2.6}$$

where τ_0 is the pre-exponential factor (which ranges from 1 ns to 1 ps), K_a is the anisotropy energy in $\mathrm{Jm^{-3}}$, V_m is the particle volume in $\mathrm{m^3}$.

It is worth noting that Eq. (2.3) is valid under the assumption of weak field, so that the Zeeman energy of the particle interactions ($\mu_0 \mu_m \mathbf{H}$) with the heating field is linear and much less than $k_B T$ [121]. However, for the case of magnetic scaffolds and nanocomposite magnetic thermoseeds (Fig. 2.4), the level of particle interaction and the relaxation mechanism differ significantly from the scenario of the MFH. As discussed in the Introduction, chemical doping of bioceramic with magnetic ions (e.g., Fe^{2+}, Fe^{3+}) produces local substitution of Ca^{2+} in hydroxyapatite, bredigite

and hardystonite lattices [28, 33, 122], resulting in the in situ formation of a magnetic phase. On the other hand, in the case of polymeric matrices, as the medium viscosity η increases, the frequency response of the magnetic susceptibility modifies and the resonance vanishes, while the heat dissipation is enhanced, as underlined by [123]. Furthermore, physical routes for embedding MNPs in hydrogels can cause the cross-link of the gel chains with the polymeric coating, blocking and hindering Brownian motion, as reported for a Poly-(Acrylic Acid) (PAA) hydrogel with magnetite nanoparticles [124]. Also 3D-printed filaments loaded with MNPs showed a non-Debye behavior [93]. Magnetic printed Poly-Propylene (PP) stents with magnetite nanoparticles, for hyperthermia treatment of bile duct tumors, present a drastically different complex susceptibility than their free counterpart in suspension [93]. In this framework, the physical environment in biomaterials is similar to tissues (Fig. 2.4) [121], hence the Néel relaxation is the most relevant mechanism, since

$$\lim_{\eta \to \infty} \frac{1}{\tau_B} \to 0, \tag{2.7}$$

resulting in

$$\frac{1}{\tau} \simeq \frac{1}{\tau_N}. \tag{2.8}$$

From a physical point of view, the internal remagnetization process is dominant in highly viscous systems, since the energy of the magnetic interaction overcomes the thermal energy, causing aggregation [121]. The long-range interactions between particles can be relevant [125], as can be estimated by the index Υ [125, 126]

$$\Upsilon = \frac{\mu_0 \mu_2^2}{2\pi k_B T r_m^3} \tag{2.9}$$

where r_m^3 is the lower bond of the volume packaging and steric hindrance in the system.

Given the theoretical basis [121] and the evidences found in the literature [93, 123, 124, 127–129], we propose that the frequency response of the complex magnetic susceptibility of MagS can be framed in a theoretical model which assumes that the relaxation dynamic of MNPs clusters modifies and lead to the appearance of a distribution of anisotropy energies [125], thus resulting to a continuum of relaxation times. In mathematical term, a Cole-Cole model can be used [130, 131]

$$\chi(f) = \frac{\chi_0}{1 + (2\pi f \tau_N)^{1-\gamma}} \tag{2.10}$$

where γ is the so called broadening parameter, and describes the relaxation times distribution [130–132]. If $\gamma \to 0$, Eq. (2.10) resolve in a Debye equation. On the other hand, when $\gamma \to 1$ the relaxation time distribution broadens [130].

To compute Eq. (2.1), it is necessary to evaluate the initial susceptibility χ_0, which is defined as [119, 133]

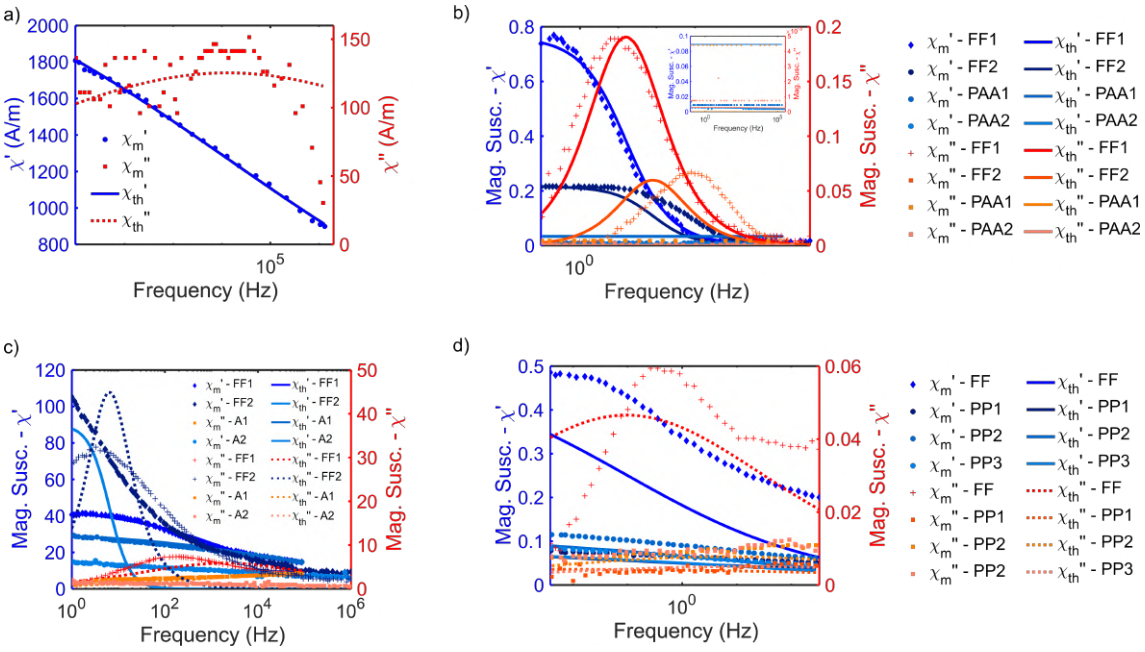

Figure 2.5. a) Complex magnetic susceptibility data for Resovist magnetic nanoparticles (10 nm) immobilized in epoxy resin. b) Complex magnetic susceptibility of 2 wt.% magnetite nanoparticles (sample 1, 11 nm) and cobalt ferrite (sample 2, 11 nm) in aqueous solution (ferrofluid, FF) and immobilized in Poly-(Acrylic Acid) (PAA) hydrogels. c) Complex magnetic susceptibility of magnetite FF before and after the immobilization in agar gel. d) Complex magnetic susceptibility of magnetite nanoparticles, synthesized via co-precipitation in FF, then immobilized inside acrylamide hydrogels and freeze-dried in Poly-Propylene (PP) filaments. The fitting curves are reported.

$$\chi_0 = \frac{\phi_m M_s}{\mathbf{H}} \left[\coth\left(\frac{\mu_m \mathbf{B}}{k_B T}\right) - \frac{k_B T}{\mu_m \mathbf{B}} \right] \tag{2.11}$$

In Tab. 2.1 examples of literature works which have dealt with the AC magnetic response of MNPs embedded in a biomaterial matrix are provided. We have digitized the data by using the online tool *WebPlotDigitizer* [134]. The data are taken from [93, 123, 124, 127, 128] and reported in Fig. 2.5. We investigated if the magnetic response of the MNPs in the biomaterial can be fitted and interpreted by using Eq. (2.10).

In this thesis, we expanded our previous approach [131] and tested the Cole-Cole model with a large experimental setup. In detail, we used a Genetic Algorithm (GA) routine to minimize the following objective function to retrieve the vector parameters $\mathbf{x}$ [131]

$$f_{obj}(\mathbf{x}) = \sum_{q=1}^{N_f} \left| \chi_m(f) - \chi_{th}(f,\mathbf{x}) \right|^2 \tag{2.12}$$

where N_f is the number of frequency point, χ_m and χ_{th} are the measured and theoretically estimated complex magnetic susceptibility values. The initial population was set to 35000 individuals, the

Table 2.1. Results for the Analysis of Complex Magnetic Susceptibility

Sample	χ_0	τ (s)	γ	**Cole-Cole Error** (δ_χ, %)	**Debye Error** (δ_χ,
Resovist MNPs in Epoxy	$2.54{\cdot}10^3$ (A/m)	$1.21{\cdot}10^{-5}$	0.874	0.124	-8.25
Fe_3O_4 FF	0.765	0.01	0.411	11.0	30.98
Fe_3O_4 in PAA	0.089	$1.47{\cdot}10^{-11}$	0.9	10.23	-30.70
$CoFe_2O_4$ FF	0.2174	0.002	0.411	5.34	16.14
$CoFe_2O_4$ in PAA	0.016	0.108	0.826	5.98	-17.96
Fe_3O_4 FF	44.779	$8.14{\cdot}10^{-5}$	0.674	2.06	17.64
Fe_3O_4 in A	30.710	$4{\cdot}10^{-6}$	0.75	-1.96	49.56
Fe_3O_4 FF	90.011	0.025	0	7.17	35.67
Fe_3O_4 in A	25.7469	0.01	0.89	2.0	-12.49
Fe_3O_4 FF	0.503	1.672	0.766	22.4	45.72
3% Fe_3O_4 in PP	0.131	61.188	0.916	12.15	44.55
5% Fe_3O_4 in PP	0.126	$1{\cdot}10^{-3}$	0.901	-0.81	24.508
7% Fe_3O_4 in PP	0.083	0.012	0.845	8.79	18.44

maximum number of iterations was set to 150 [131]. The relative percentage error (δ_χ) has been chosen as figure of merit for evaluating the fitting quality, so that

$$\delta_\chi = \frac{1}{N_f} \sum_{q=1}^{N_f} \frac{\chi_m(f) - \chi_{th}(f)}{\chi_m(f)} \tag{2.13}$$

The error was evaluated for the Debye and Cole-Cole models for comparison. A negative δ_χ implies that the theoretical susceptibility underestimate the measured value, whilst, on the other hand, a positive δ_χ reflects an overestimated theoretical value.

The results from the fitting are shown in Fig. 2.5, and the coefficients are reported in Tab. 2.1. By comparing the relative percentage error (δ_χ) for the Debye and Cole-Cole models, we can highlight that the non-resonant law can better describe the magnetic susceptibility spectra of MNPs in biomaterials (Tab. 2.1). By comparing the fitting parameters retrieved for the MNPs in ferrofluid with that of immobilized MNPs, it can be noticed that χ_0 lowers, up to an order of magnitude. Furthermore, an increase in the value of the broadening parameter can be highlighted. The case of MNPs in the PAA hydrogel [124] is a very peculiar one. Indeed, differently from what reported for the magnetite particles included in a PP filament [93], from Fig.s 2.5.b, it is possible to observe that the rapid Néel relaxation of large particles is almost quenched after the incorporation, because the particles are immobilized inside the polymer network. This is an extreme and limiting case. However, for the data shown in Fig. 2.5.c and 2.5.d, the susceptibility spectra of [123] and [93] presented enhanced dissipation and losses, appealing for hyperthermia. Given these findings, in the following of this thesis work we will consider the Cole-Cole model as the theoretical framework for describing the frequency response of MagS.

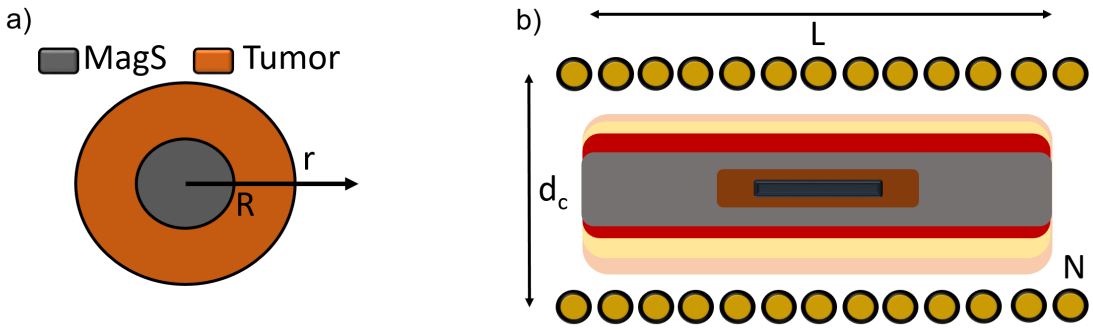

Figure 2.6. a) Illustration of the heating coil and the treatment setup. b) Simplified geometry of the problem. A magnetic scaffold (MagS) of radius $R = 5\,\text{mm}$ is assumed to be implanted in a semi-infinite tumor medium.

2.3.2 Theory

From an analytical and modeling point of view, the interstitial HT with MagS could be understood and studied by relying on the theory of ferromagnetic implant heating from Stauffer et al. [50], or re-adapting the solutions to bio-heat equation for magnetic fluid hyperthermia [109], such as those derived in steady [107] or transient form [108]. In this section, we aim at deriving a steady-state solution to the bio-heat transfer problem governing the HT of bone tumors with MagS, in a simplified geometry, to highlight the most relevant parameters and properties of magnetic scaffolds for planning the thermal therapy.

We consider the case of a cylindrical magnetic scaffold, with radius R, implanted after the surgical excision of a bone tumor. The implant is considered surrounded by the target residual tumor cells, which is assumed to be a semi-infinite medium, as shown in 2.6.a.

An alternate current (AC) magnetic field ($\mathbf{H}$) working at a given frequency f, is supposed to be applied to the system, thus being the cause of heat dissipation by the MNPs in the biomaterial. The exposure system can be a solenoid, a pancake coil, with N turns, length L and excited by a sinusoidal current I, in which a human limb is inserted (Fig. 2.6.b) To account for the electromagnetic field source in the problem, we can approximate our derivation by assuming the coil long enough, and by considering that if the coil diameter d_c is much larger than the scaffold diameter $2R$ (i.e., $d_c \ll 2R$), then a uniform, homogeneous and constant ($\mathbf{H} = H$) magnetic field in the geometry of Fig. 2.6 is present

$$H \simeq= N\frac{I}{L}. \tag{2.14}$$

Furthermore, from an EM perspective, the MagS is typically a dielectric insulating objects, so that $\sigma \ll j\omega\epsilon_0\epsilon_r$, being σ the electrical conductivity (in Sm^{-1}), $\omega = 2\pi f$, whilst ϵ_0 and ϵ_r are the dielectric permittivity of vacuum and the relative permittivity of the medium. Hence, standard solution for conducting cylinder exposed to a plane wave could not be used in this case [50].

Under these assumption, the power dissipated by MagS can be quantified by Eq. (2.1), relying on the Cole-Cole law (Eq. (2.10)), since the linear response theory and the Debye model do not apply when MNPs are constricted in a highly viscous or solid matrix, since the inter-particles interactions lead to a vanishing of the resonant response [131]. From Eq. (2.1)-(2.11), is possible to highlight that the design parameters of magnetic scaffolds are ϕ_m, M_s, V_m and K_a. In fact, the amount of nanoparticles loaded in the biomaterial is an unknown function of the manufacturing process, but it is a tunable quantity [8–10, 13, 15]. The dipole moment of the MNPs and the crystal energy can be adjusted during particle synthesis, by controlling the dispersion of particle sizes and the coating of the MNPs [19, 135, 136]. In order to sought a closed-form expression, we manipulate Eq. (2.10) to explicit the imaginary part as follow [137]

$$\chi'' = \frac{1}{2}\frac{\cos\left(\frac{\gamma\pi}{2}\right)}{\cosh\left[(1-\gamma)\ln\left(2\pi f\tau_N\right)\right] + \sin\left(\frac{\gamma\pi}{2}\right)}. \tag{2.15}$$

The treatment outcome can be evaluated by solving the Pennes' Bio-Heat Equation (PBHE)

$$\rho C_p \frac{\partial T}{\partial t} = k\nabla^2 T - \rho_b C_{p,b}\omega_b(T - T_b) + P_m \tag{2.16}$$

where ρ is the tissue density (in kg·m^{-3}), C_p is the specific heat capacity (J·K^{-1}kg^{-1}), k is the thermal conductivity of the tumor. The blood perfusion ($\rho_b C_{p,b}\omega_b(T - T_b)$) is included in the model [50, 107–109]. The blood thermal properties are indicated with the subscript "b". The blood arterial temperature is T_b, equal to 37°C.

To solve Eq. (2.16) some assumption must be made. We assume the EM and thermal properties to be constant and independent from space and temperature. Given that we aim at evaluating the quality of HT with MagS, the characteristic time scale of the therapy is on the order of 30-60 min, thus allowing to sought a steady state solution, so that $\frac{\partial T}{\partial t} \to 0$. Re-arranging Eq. (2.16), transforming the problem in spherical coordinates, neglecting the heat contact resistance at the interface between the two media, we can derive the temperature increase (ΔT) for $r > R$, by imposing that for $r \gg R$, $T = T_b$, as [50, 107, 137]

$$\Delta T = \frac{1}{3}\frac{P_m}{k}\frac{R^3}{r}\frac{e^{-\sqrt{\frac{\rho_b C_{p,b}\omega_b}{k}}(r-R)}}{1 + R\sqrt{\frac{\rho_b C_{p,b}\omega_b}{k}}}. \tag{2.17}$$

A complete expression can be obtained. However, before, we have to substitute Eq. (2.15) into Eq. 2.1, to get

$$P_m = \frac{1}{2}\pi\mu_0 f H^2 \chi_0 \frac{\cos\left(\frac{\gamma\pi}{2}\right)}{\cosh\left[(1-\gamma)\ln\left(2\pi f\tau_N\right)\right] + \sin\left(\frac{\gamma\pi}{2}\right)}. \tag{2.18}$$

Inserting the definition of χ_0 from Eq. (2.11), we derive the following expression

$$P_m = \frac{1}{2}\pi\mu_0 f H \phi_m M_s \left[\coth\left(\frac{\mu_m\mu_0 H}{k_B T}\right) - \frac{k_B T}{\mu_m\mu_0 H}\right]\left[\frac{\cos\left(\frac{\gamma\pi}{2}\right)}{\cosh\left[(1-\gamma)\ln\left(2\pi f\tau_N\right)\right] + \sin\left(\frac{\gamma\pi}{2}\right)}\right]. \quad (2.19)$$

By inserting Eq. (2.19) into Eq. (2.17).

$$\Delta T = \frac{\pi\mu_0 f H \cdot \phi_m M_s \cdot R^3}{6kr}\left[\coth\left(\frac{\mu_m\mu_0 H}{k_B T}\right) - \frac{k_B T}{\mu_m\mu_0 H}\right]\left[\frac{\cos\left(\frac{\gamma\pi}{2}\right)}{\cosh\left[(1-\gamma)\ln\left(2\pi f\tau_N\right)\right] + \sin\left(\frac{\gamma\pi}{2}\right)}\right]\frac{e^{-\sqrt{\frac{\rho_b C_{p,b}\omega_b}{k}}(r-R)}}{1 + R\sqrt{\frac{\rho_b C_{p,b}\omega_b}{k}}} \quad (2.20)$$

The proposed model could be used to setup suitable optimization procedures aimed at finding the size and M_s of nanoparticles to achieve a given temperature increase, in a way similar to what done for MFH in [77].

2.3.3 Multiphysics Model

A major limitation of the theoretical model and of Eq. (2.20) is that they do not take into account the physical evidence that the heat dissipated by Néel relaxation or hysteresis losses by the MNPs in the MagS depend on the system temperature, and, hence, during the treatment, as the scaffolds and tissues heat, the power dissipation and the magnetization dynamic of MagS modify [117, 118, 138]. Variations of few % to several % may occur for the temperature range typical of HT [118]. An accurate treatment planning must account for these significant variations. Furthermore, the pattern of power dissipation, due to the exposure to the RF magnetic field, in the MagS and biological tissues is oversimplified, partially neglecting the solution of the coupled electromagnetic problem [84]. For the simplified geometry shown in Fig. 2.6.b the absence of non-target healthy tissue and vascular details can strongly affect the computation of the deposited power and estimated temperature [84]. Therefore, it is mandatory to refine both the geometrical and physical description of the HT of bone tumors with MagS.

Geometry

In Fig. 2.7, we present the minimum geometry for investigating the HT of bone tumors with MagS. These are meaningful representations of the biological problem which would not results in excessive computational burden [115]. We will discuss two cases which extend and improve the analysis domain shown in Fig. 2.6.b. We begin to develop our model by assuming a very narrow volume of tissue around the implant. A spherical MagS having radius $r_{sc} = 5\,\text{mm}$ [139]. Near the scaffold, there is a region where new bone forms to heal the surgical fracture [140]. Healing process starts with hematoma and local ischemia (first 7 days), and ends with an inflammatory phase (up to 14 days) [140]. For this reason, a small fracture with radius varying in the range 0.1-0.5 mm [139,140] has been considered. The tumor region is modeled as a uniform tissue spherical

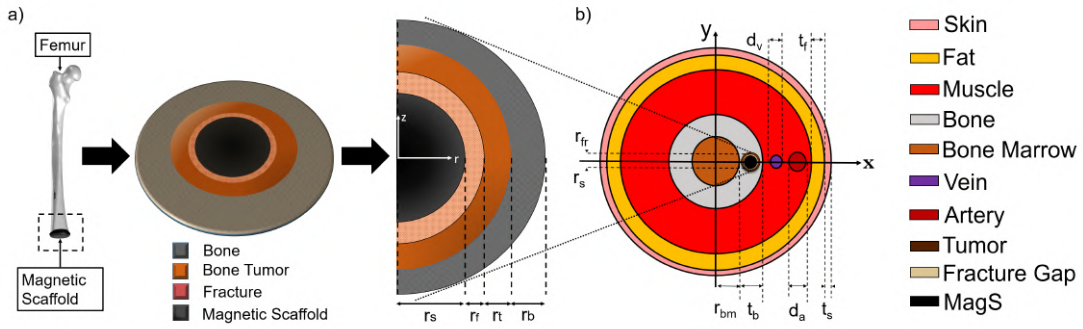

Figure 2.7. a) The case of a scaffold implanted after long bone tumor surgical treatment is analyzed. A transverse section of bone, residual cancer tissue, fracture gap and scaffolds are considered. b) Simplified 2D geometry for a human upper limb affected by a bone tumor, which is surgically reduced, and treated with an implanted MagS.

area of radius r_t. The bone tumor volume is assumed to be reduced after surgical intervention and assumed to vary from 0.1 mm to 0.5 mm.

Since bone tumor can affect the methaphysis of the proximal humerus [99], a 2D surface model of the proximal upper limb segment is considered and shown in Fig. 2.7.b. The arm is approximated to a circle of radius $r_{arm} = 5$ cm [141,142]. Moving from the outside to the inside, the arm present a layer of skin (t_s =1.5 mm), the fat layer ($t_f = 10$ mm), the muscles region (i.e. the triceps brachii, the brachialis, the biceps [142]) with a radius r_{mu} of 43 mm, the humerus bone ($r_b = 20$ mm [141,142]), and, finally the bone marrow ($r_{bm} = 5$ mm). The center of the xy-coordinate system is set at the center of the bone marrow circle. The bone tissue is divided in a cortical portion and a cancellous part, which are 1 mm and 19 mm thick, respectively. The 2D geometry shown in Fig. 2.7.b is symmetric with respect to the $x > 0$ half space. The brachial vein and brachial artery are modeled as circles with their center on the the x-axis ($y = 0$) [141,142]. The diameter of the brachial vein is $d_v = 3$ mm whereas the artery diameter is $d_a = 4$ mm [143]. The vein has its center in ($r_{mu} - d_a - d_v - 3$ mm, 0) and the artery at coordinates ($r_{mu} - d_a$, 0). These moderately-large vessels cannot be neglected since their contribution to the heat transfer phenomena during the HT is relevant [84,114]. In Fig. 2.7.b, a 10 mm bone tumor, of radius r_t, grown peripherally, halfway between the bone marrow and the cortical portion of bone, is considered. The tumor can be approximated to a circular shape relying on the findings from [97]. The tumor size can vary after the surgery [66]. The portion of the tumor, fracture gap and MagS is the same of Fig. 2.7.a [117]. It is assumed that after the resection of the tumor in a portion with thickness $t_t = r_t - (r_f + r_s)$=0.5 mm the tumor cells are still present.

EM Problem

In general, under the quasi-stationary assumption, the goal of a model for magnetic hyperthermia is to derive the spatial distribution of the magnetic vector, $\mathbf{H}$ (Am^{-1}), and of the electric field vector, $\mathbf{E}$ (Vm^{-1}), by solving the Maxwell's equation in the frequency domain [50, 111]:

$$\begin{aligned} \nabla \times \mathbf{H} &= j\omega\epsilon\mathbf{E} + \mathbf{J} \\ \nabla \times \mathbf{E} &= -j\omega\mu\mathbf{H} \end{aligned} \tag{2.21}$$

where $\mathbf{J}$ is the current density vector. The quantity ϵ, in Fm^{-1}, is the dielectric permittivity of the medium, whereas μ is the magnetic permeability of the material. With the fields $\mathbf{H}$ and $\mathbf{E}$ it is possible to quantify the power deposited in the tissues and to determine the spatio-temporal evolution of the temperature field in the systems of Fig. 2.7. The electromagnetic properties at body temperature and at the frequency of 300 kHz is reported in Tab. 2.2.

The computation of EM fields distribution is sometimes neglected by [107,108], and homogeneous MF are assumed [117,137]. This can lead to underestimate the power dissipated due to the conduction current in non-target tissues (e.g., in muscle or skin) [144]. The hypothesis of uniformity and homogeneity of the external magnetic field is a rather limiting assumption and it can be assumed as valid only locally and for a very small volume of tissue in proximity to the scaffold [117]. Therefore, Eq.s (2.21) must be solved assuming an external magnetic field ($\mathbf{H_0}$, with working frequency f generated by a single layer coil with radius a and length L, N turns, carrying a current I, which is approximately equivalent to a cylindrical surface current, i.e. [145]:

$$H_0(x,y) = -\frac{2NI}{L}\left(\frac{a}{L}\right)^2\left[1 - 6\left(\frac{\sqrt{x^2+y^2}}{L}\right)^2 - 3\left(\frac{a}{L}\right)^2\right]. \tag{2.22}$$

For the analysis of HT a coil available from the literature was selected [146, 147]. In particular, the coil has a diameter of 10.5 cm and is 28.5 cm length, with 50 turns [146]. The coil is supposed to surround the arm. The current I in the coil can be tuned to produce a magnetic field suitable to perform the treatment in an effective way, i.e., tens of A to obtain thousands of Am^{-1} [50, 103, 104, 146, 148]. In this scenario the induced electric field is about one order of magnitude lower than the strength of the magnetic field, i.e., around tens of Vm^{-1}, on average [144].

The presented analysis is restricted to the transverse section of the proximal humerus (i.e., the xy-plane, for $z = 0$) since the typical dimensions of magnetic scaffolds are much lower than the single layer coil and the arm lengths (i.e., ∼1 cm x 0.5 cm against ∼30 cm x 11 cm). Indeed, ±0.5 cm from the coil center the variations of the applied magnetic field along the longitudinal direction (or z-axis) is about 0.02% of the maximum field value [145]. It is possible to infer that the power deposited along the coil axis is almost constant, for the scaffold length. Hence, the problem of RF heating and the study of the HT can be performed focusing on the transverse section of human upper limbs.

Table 2.2. Electromagnetic properties of scaffold and tissues at 300 kHz and 37°C.

Material or Tissue	ϵ_r	σ (S·m^{-1})
MHA	12.5	$2.1{\cdot}10^{-3}$
Fracture gap - Inflamed	3580	0.545
Bone Tumor: OS	192	0.196
Bone Marrow	60.1	$4.16{\cdot}10^{-3}$
Cancellous Bone	350	0.085
Cortical Bone	191	0.0214
Muscle	5300	0.407
Fat	64.1	0.043
Skin	1090	$1.93{\cdot}10^{-3}$
Blood	4690	0.721

Non-linearities in the EM Problem

We introduce the concept that MagS would modify their intrinsic magnetic properties as the hyperthermia treatment is carried out. It is fundamental to formalize and explicit the dependence of the heat dissipation from the system temperature. Indeed, starting from the static susceptibility χ_0, for magnetic field with strength much lower than the thermal energy barrier, Eq. (2.11) can approximated to an inversely dependent law from temperature [117, 131], i.e.

$$\chi_0(T) \simeq \frac{\mu_0 \phi_m V_m M_s^2}{k_B T}. \tag{2.23}$$

Therefore, during the treatment the χ'' would reduce due to a hyperbolic reduction of χ_0. Furthermore, with respect to Eq. (2.10), the term τ_N, defined in Eq. (2.6), depends upon the ratio between the anisotropy energy of the magnetite crystal and the thermal energy. Hence, τ_N is a strong nonlinear function of the temperature. However, we must underline that, in Eq. (2.6) the term τ_0, the pre-exponential factor, is commonly supposed to vary from 1 ns to 0.1 ps [19, 24]. However, its value depend on the intrinsic properties of the magnetic nanoparticle embedded in the scaffold and also on T [19]

$$\tau_0(T) = \frac{\sqrt{\pi}}{4} \frac{M_s(0)}{K_a \gamma_e} \left[\frac{1}{\upsilon_f} + \upsilon_f \left(\frac{M_s(T)}{M_s(0)} \right)^2 \sqrt{\frac{K_a V_m}{k_B T}} \left(1 + \frac{k_B T}{K_a V_m} \right) \right] \tag{2.24}$$

where $M_s(0)$ is the magnetization extrapolated at -273 °C (i.e. 0 K) from the Zero Field Cooled (ZFC) and Field Cooled (FC) curves [18]. The term M_s(T) is the magnetization of the MNPs in the scaffold at the desired temperature and it can be approximated by a linearly decreasing function of T for the hyperthermia range of 37°C-45°C. The slope is an intrinsic property of the scaffold and must be derived from experimental measurements. The term γ_e is the electron gyromagnetic ratio in s^{-1}T^{-1}. Finally, the dimensionless constant υ_f can be written as [19, 24, 117]:

$$\upsilon_f = \upsilon\gamma_e M_s(0) \tag{2.25}$$

where υ is a dimensionless damping constant set equal to 0.45 [117].

With the Equations (2.1), considering Eqs. (2.6), (2.23) and (2.24), it is possible to model both the frequency and temperature dependence of the magnetic properties of scaffolds. In this way, the quantification of the power losses during the heat treatment as a function of temperature can be carried out. An example of the temperature dependence of the intrinsic magnetic parameters for the magnetic hydroxyapatite scaffold from [28] is shown in Fig. 2.8. Given these findings, $P_m(f,\mathbf{H}) = P_m(f,\mathbf{H},T)$.

To date, most of the work dealing with MagS have implicitly assumed that the MNPs in the biomaterials are uniformly dispersed [33, 49, 117, 118, 131, 149, 150]. However, from the microscopic and morphological characterizations of MagS it is possible to infer that, depending on the manufacturing technique, the MNPs can distribute in a inhomoegeneous way. This non-ideality, due to manufacturing process, can add further non-linearity and affect the HT outcomes. In this chapter, given the efforts for developing an effective platform for planning the treatment of bone tumors with MagS, we consider, for the first time, that the MNPs in the scaffolds are not homogeneously distributed. In detail, we assume that the MNPs profiled follows an inverse gaussian-like distribution, or, from a mathematical point of view

$$\phi_m(x,y) = e^{\frac{\sqrt{x^2+y^2}}{r_{sc}}} \tag{2.26}$$

where r_{sc} is the scaffold radius, as in Fig. 2.7.b. This modification of the model would imply that the power dissipated by the magnetic scaffold would depends on the spatial variables, since the EM field distribution (Eq. (2.21)) in the prosthesis and in its surrounding tissues depends on ϕ_m.

Finally, the last nonlinear feature is the fact that also EM properties of tissues slightly varies with temperature [84, 138]. Therefore, to accurately evaluate the EM pattern and the power losses due to the conduction currents in the system, the dielectric properties of the scaffolds matrix and tissues are reported in Tab. 2.2, for the working frequency of 300 kHz and at 37°C. These values are defined as ϵ_{T_b} and σ_{T_b}. The EM properties are mainly taken from [117, 151]. The dielectric properties of tissues are known to vary linearly with temperature in the hyperthermia range (from 37°C to 45°C), as reviewed by Rossman et al. [138]. Therefore the following is assumed for both the dielectric permittivity, ϵ, and the electric conductivity, σ

$$\begin{aligned} \frac{\epsilon(T)}{\epsilon_{T_0}} &= (1 + K_\epsilon \Delta T) \\ \frac{\sigma(T)}{\sigma_{T_0}} &= (1 + K_\sigma \Delta T) \end{aligned} \tag{2.27}$$

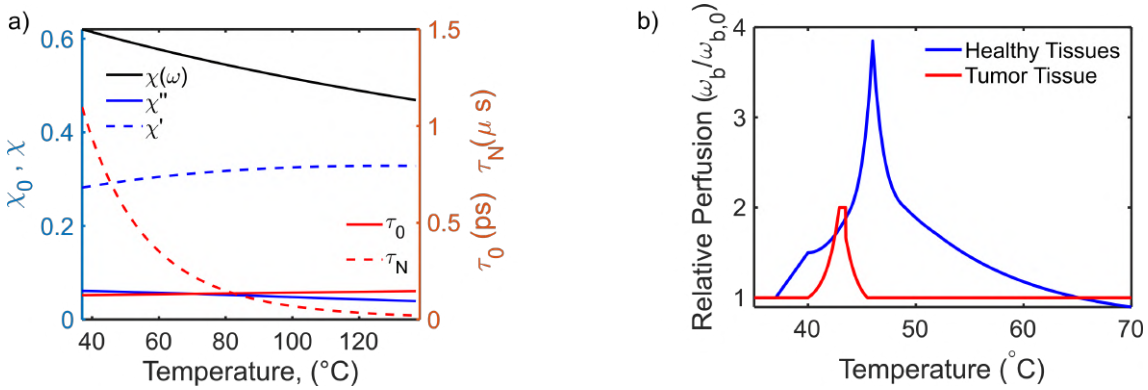

Figure 2.8. a) Static magnetic susceptibility (χ_0), real and imaginary part of magnetic susceptibility according to the Cole-Cole model, plotted as a function of system temperature. The external magnetic flux density field is set to 1 mT and $f = 293$ kHz. The temperature influence on the pre-exponential constant τ_0 and on the Néel relaxation time is drafted. b) Temperature dependence of healthy and tumor tissues blood perfusion.

where the values of coefficient K_ϵ and K_σ are assumed to be equal to $3\%{\cdot}^\circ\mathrm{C}^{-1}$ for the given biological tissue [117, 138]. With this expedient, the EM problem can account for the thermal drift of the power losses during the hyperthermia treatment, thus allowing for a more accurate monitoring of the thermal dose delivered to the tumor cells.

Bio-Heat Problem

Having discussed the EM, we must underline that, differently from [6, 137], the non-specific and undesirable dielectric losses (P_e) are evaluated, then summed to P_m to obtain the overall dissipated power, Q_{EM}, which is used as a source term in the parabolic PBHE [84, 92, 117, 152]

$$\rho C_p \frac{\partial T}{\partial t} = \nabla(k\nabla T) - \rho_b C_{p,b}\omega_b(T - T_b) + Q_{EM} + Q_{met} \tag{2.28}$$

Symbols and terms retain their usual meaning. The thermal properties at the initial temperature T_b employed in the simulations are summarized in Tab. 2.3.

The heat capacities and thermal conductivities are taken from [117, 138, 151]. In a way similar to the dielectric properties, the thermal conductivities and heat capacities of the healthy and pathologic tissues are supposed to vary linearly with the system temperature [138], so that

$$\begin{aligned} \frac{k(T)}{k_{T_b}} &= (1 + K_k \Delta T) \\ \frac{C_p(T)}{C_{p,T_b}} &= (1 + K_c \Delta T). \end{aligned} \tag{2.29}$$

The coefficients K_k and K_c, in $\%{\cdot}^\circ\mathrm{C}^{-1}$, are, respectively, $0.5\%{\cdot}^\circ\mathrm{C}^{-1}$ and $0.33\%{\cdot}^\circ\mathrm{C}^{-1}$, but for the

Table 2.3. Thermal properties of scaffold and tissues at 37°C.

Material or Tissue	ρ (kg·m^{-3})	k (Wm^{-1}K^{-1})	C_p (Jkg^{-1}K^{-1})	Q_{met} (Wm^{-3})	ω_b (s^{-1})
MHA	3100	1.33	700	-	-
Fracture gap: Inflamed	1114	0.558	2450	5262.5	$6.95{\cdot}10^{-3}$
OS Bone Tumor	1908	0.32	1313	57240	0.595
Bone Marrow	980	0.19	2065	450.8	$4.90{\cdot}10^{-4}$
Cancellous Bone	1178	0.31	2274	450.8	$4.90{\cdot}10^{-4}$
Cortical Bone	1908	0.32	1313	147	$1.63{\cdot}10^{-4}$
Muscle	1090	0.49	3421	911.9	$1.82{\cdot}10^{-3}$
Fat	911	0.21	2348	464.41	$1.52{\cdot}10^{-3}$
Skin	1109	0.37	3391	1617	$1.73{\cdot}10^{-3}$
Blood	1050	0.52	3617	-	-

blood is -0.1%·°C^{-1} due to the high water content.

Special attention must be paid to the tissue perfusion rate, ω_b, since this physical quantity is very relevant to the effectiveness of the hyperthermia treatment [84, 153]. There is a noticeable difference in the perfusion values across healthy tissues, but also between the tumor and the normal tissues [97, 114, 154]. Moreover, the perfusion rate is not a constant and its values strongly varies with temperature: if the temperature approaches 40-43°C it can increase in a non-linear way up to two- or fourfold the value at 37°C. Therefore, to reproduce this behavior of biological tissues in our model, the blood perfusion was implemented as a piecewise function of T according to the data of Fig. 2.8.b from [154]. For the healthy tissues the variation of blood perfusion, $\omega_b(T)$, with respect to the value ω_0 at 37°C (see Tab. 2.3), can be described by the following piecewise function

$$\frac{\omega_b(T)}{\omega_{b,0}} = \begin{cases} 1 & T \leq 37 \\ 1 + \dfrac{1}{6}(T-37) & 37 \leq T \leq 40 \\ 1.5 + \dfrac{1}{32}(T-40)^2 & 40 \leq T \leq 44 \\ 2 + 1.85\dfrac{e^{44-T}-1}{e^{21}} & 44 \leq T \leq 46 \\ 3.85 - 1.85\dfrac{e^{46-T}-1}{e^{-3}-1} & 46 \leq T \leq 49 \\ 2 - 0.3\dfrac{(1.15^{49-T}-1)}{1.15^{-3}-1} & 49 \leq T \leq 52 \\ 1.7 - 0.7\dfrac{1.1^{52-T}-1}{1.11^{12}-1} & 52 \leq T \leq 70 \end{cases} \tag{2.30}$$

For the tumor tissue the relative temperature variation is rather different and can be evaluated as

$$\frac{\omega_B(T)}{\omega_{b,0}} = \begin{cases} 1 & T \leq 40 \\ 1 + \dfrac{2.3^{T-40} - 1}{2.3^{2.9} - 1} & 40 \leq T \leq 43 \\ 2 & 43 \leq T \leq 43.5 \\ 2 - \dfrac{2.3^{43-T} - 1}{2.3^{-2.4} - 1} & 43.5 \leq T \leq 45.5 \\ 1 & 45.5 \leq T \leq 70 \end{cases} \tag{2.31}$$

This model was also used to test cylindrical MagS in simplified scenarios [155]. In Fig. 2.8.b the piecewise functions are represented for temperatures ranging from 37°C to 70°C. It must be noticed that the peaks are centered around about 45°C and to 43°C for the healthy and tumor tissues, respectively. This is due to their significantly diverse thermo-tolerance [154, 156]. Moreover, from Fig. 2.8.b, it can be noticed that the peak value for the healthy tissues is two times higher than the value of cancerous one. However, their perfusion at 37°C, i.e. ω_0, is order of magnitude different (see Tab. 2.3). These non-linear dependence can significantly weight in the quality of the HT simulation and it is therefore necessary to take them into due account in the in silico model [84].

Eq. (2.28) is solved considering the heat fluxes to be continuous at each tissue interface for the geometry in Fig. 2.7.b. At the skin-air interface the natural convection and the radiation to surrounding environment must be included in the model. Therefore, to solve Eq. (2.28), the following Neumann boundary condition must be solved for the heat flux [84, 152, 157]

$$-\mathbf{n} \cdot \nabla T = h(T - T_{air}) \tag{2.32}$$

where h is the effective heat transfer coefficient equal to 7.7 $\mathrm{Wm^{-2}K^{-1}}$ and T_{air} is 22°C [152].

As regards the vessels, the brachial artery and vein have a diameter higher than 2 mm, which implies that the heat balance in the muscle cannot be represented by the PBHE [114]. The presence of these vascular elements can completely alter the temperature profile, since they act as temperature sinks [158].Since a complete solution of the heat transfer equation in the vascular compartments requires the computation of the non-linear Navier-Stokes equation in a 3D geometry, in this work a simplified approach is preferred. Neglecting the mechanical changes due to the vasodilation in response to temperature variation, the heat transfer between blood, vascular blood and the muscle is modeled using an equivalent convective boundary condition [114, 158]

$$q_i = h_i(T - T_i). \tag{2.33}$$

The effective heat transfer coefficient for the vein or artery (h_i, with $i = a,v$, depending on artery or vein, respectively) is a function of the geometry of the vessel (diameter and length), the thermal properties of the blood (k_b, $C_{p,b}$) and also on the fluidodynamic properties, i.e., the fluid viscosity η, in Pa·s, and the density. To derive the heat transfer coefficients h_i for artery (a) and vein (v) it is useful the correlation between the Nusselt and Graetz dimensionless number found in [158]

$$Nu = \frac{h_i d_i}{k_b} = 4 + 0.155 e^{1.58 \cdot log(Gz)}. \tag{2.34}$$

Remembering that the Graetz number is defined as [159, 160]

$$Gz = \frac{d_i}{l_i} Re \cdot Pr \tag{2.35}$$

where the Reynolds and the Prandtl numbers are [159, 160]

$$\begin{aligned} Re &= \frac{\rho_b d_i \tilde{v}_i}{\eta} \\ Pr &= \frac{\eta C_{p,b}}{k_b}. \end{aligned} \tag{2.36}$$

In Eq. (2.36) the term $\tilde{v}_{a,v}$ is the average velocity in the brachial artery or the vein, respectively. Substituting Eq. (2.36) in Eq. (2.35) and then inverting Eq. (2.34), we get

$$h_i = \frac{k_b}{d_i} \left[4 + 0.155 e^{1.58 \cdot log\left(\frac{\rho \tilde{v}_i C_{p,b} d_i^2}{l_i k_b} \right)} \right]. \tag{2.37}$$

Considering that $d_a = 4\,\text{mm}$, $d_v = 3\,\text{mm}$, $l_a = l_v = 31\,\text{cm}$, employing the velocity values $\tilde{v}_a = 5\,\text{ms}^{-1}$ and $\tilde{v}_v = 2.5\,\text{ms}^{-1}$ [143, 158, 160], with the blood thermal properties given in Tab. 2.3, the effective heat transfer coefficients are $130\,\text{Wm}^{-2}\text{K}^{-1}$ and $180\,\text{Wm}^{-2}\text{K}^{-1}$ for the artery and vein, respectively.

The initial temperature was set $T_b = 37°\text{C}$ for all tissues and for the scaffold.

Thermal Dose and Therapy Assessment

Special care must be devoted to the quantification of the outcome of the hyperthermia treatment. It is known that for tumors, as for osteosarcoma cells, the critique thermal dose is 43°C for 60 min [161]. The heating of the tumor must be spatially and temporally controlled to ensure an effective exposure. The performance of the implanted magnetic scaffolds can be assessed with the proposed model thanks to the resolution of the coupled electromagneto-thermal model.

The multiphysics model presented therein also aims in establishing if the employment of a non-uniform external magnetic field and the presence of MagS, for the system in Fig. 2.7.b, can produce unwanted overheating of healthy tissues. Indeed, the skin and bone tissues must not be damaged during the treatment. Considering that bone cells initiate the necrosis process if a dose of 47°C for 1 min is delivered, and taking into due account that blisters, burns and toxicity may arise in skin if the temperature is maintained at 43-44°C for 30 min the hyperthermia treatment should be monitored also at these anatomical sites. Meanwhile, the thermal dose delivered to the tumor cells should be assessed.

The thermal dose to the target tumor region of OS can be derived by calculating the cumulative

equivalent minutes at 43°C [117, 153, 162]

$$CEM43 = \int_{t_0}^{t_{final}} R^{43-T(t)} dt \tag{2.38}$$

where R is the temperature dependence of the rate of cell death, i.e. $R = 0.5$ for $T > 43$°C, $R = 0.25$ for 39°C$\geq T \geq 43$°C and, finally, $R = 0$ for $T < 39$°C. The $CEM43$ is a number comprised between zero and infinite [117, 153, 162]. The higher the $CEM43$ in the tumor, the better the hyperthermia treatment. This index is used to assess if magnetic scaffolds can be employed to perform adjuvant hyperthermia therapy on residual bone tumor cells.

Simulation Details and Resolution Scheme

The EM problem is solved, in the frequency domain, for the 2D geometry of Fig. 2.7.c employing the *RF module* of the commercial FEM software COMSOL Multiphysics version 5.5a (COMSOL Inc., Burlinghton, MA)[1]. Firstly, a uniform and homogeneous distribution is considered as a background field. Then, Eq. (2.22) was implemented in the commercial software to investigate the influence of the exposure to a non-homogeneous field. The spatial distribution of the magnetic field is computed considering the magnetic scaffold with properties given in Tab. 2.2.
The EM physic is coupled to the Bio-Heat transfer through Eq. (2.28), which is solved in the time domain using the *Bio-Heat Transfer* module from COMSOL Multiphysics v5.5 (Comsol Inc., Burlinghton USA). The temperature is discretized with quadratic Lagrange elements. The computation is carried out considering the temperature variation of tissues thermal properties, reported in Tab. 2.3, and blood perfusion (i.e. Eq.s (2.29)-(2.31)). The EM and thermal field have very different time scales, i.e. few μs for the EM field versus several thousands of μs for the thermal field. This allow to consider the computation of electric and magnetic field as a stationary problem, assuming that the EM properties does not vary significantly for the given time step. Therefore, moving from the initial temperature distribution at time $t = 0$, the EM power losses can be evaluated and then used to solve the thermal balance. The electromagnetic problem is solved in the frequency domain using the *AC/DC* module. The magnetic vector potential was discretized by using quadratic finite elements. Given the new temperature distribution at time $t + \Delta t$, the Maxwell's equations and the deposited power can be computed again to re-evaluate the PBHE. These switching is repeated until the final time is reached. This resolution scheme was implemented using the COMSOL built-in *Frequency-Transient* solver. A direct MUMPS solver employing BDF scheme and Newton method is used for solving the coupled problem, with a maximum of 500 iterations, a Jacobian update once per time step and no stabilization and acceleration. The EM fields are only re-computed when and if the electromagnetic properties of the materials have changed significantly according to the temperature field, according to a criterion involving the relative tolerance of the time-dependent solver, i.e. 0.1%. The solver is allowed to automatically increase the time step for the PBHE if the EM properties of the scaffold and tissues materials are not varying in a significant way. Further

[1] `https://www.comsol.it/release/5.5`

details about the numerical resolution of coupled electromagneto-thermal problems can be found in [118, 163].

2.4 Findings and Recommendations

The proposed nonlinear multiphysics model was used to investigate the performances of MagS against bone tumors. Firstly, we investigated, for the geometry of Fig. 2.7.a, how the geometrical and physiological features of the bone fracture can affect the HT. In this case we assumed a homogeneous MF. Then, we investigated if different types of bonce cancers could be treated.

When external field is homogeneous (Fig. 2.11.a), the heating is uniform and homogeneous, radially spreading from the MagS, transferring by conduction. In this framework, the presence of the surgical fracture gap must be included and its influence assessed. The average temperature in the bone cavity is reported in Fig. 2.9.a. Fig. 2.9.a shows clearly that the external field required by the HT treatment must be evaluated taking into account the fracture, and its state. Otherwise, the required external field will be largely underestimated. In case of an ischemic fracture, the strength of external field should be increased with respect to the inflamed state to achieve the same desired temperature increase. Therefore, in situ hyperthermia treatment with magnetic scaffolds should be performed during the inflammatory phase.

FS is a poorly vascularized type of bone tumor [97] therefore, it holds that $\rho_b C_{p,b} \omega_b (T - T_b) \ll P_m$, as observed during numerical experiments. Hence, moderate MF strength allow to keep the temperature above 43°C for 60 min in tumor, as reported in Fig. 2.9.b). To prevent healthy bone to overcome the safety limit (47°C for 1 min or more [49]) the field envelope cannot be constant, and must be properly designed. The envelope of Fig. 2.9.b has been optimized to get an effective treatment. For PCL, a 17 mT field at 293 kHz is sufficient to completely disrupt the population of residual tumor cells of any dimension. On the other hand, MHA, which has stronger saturation magnetization [28], requires 10 mT. The OS is a very active and perfused tumor [100], therefore stronger fields are required to achieve the therapeutic performance. A constant magnetic flux density (see Fig. 2.9.c) applied for 85 min, can effectively treat OS with MHA scaffolds. The required external field must, however, be increased for larger tumor size. For MHA the magnetic field strengths ranges from 20 mT up to 50 mT at 293 kHz. For the FeHa/PCL scaffold, the frequency was augmented to 409 kHz, as in [49]. Without this frequency change, large OS could not be successfully treated, as shown in Figures 2.9.c. It should also be noted that Fe-Ha-PCL fails in treating OS with radius higher than 0.1 mm even using a field at 409 kHz, unless the field intensity is significantly larger than 50 mT [49]. This finding implies that different MNPs, with a higher volume ratio, should be embedded in the scaffold, or, instead, the extrinsic field parameter must be tuned.

Given these results, in the following we will focus on OS, as the most critical biological target. For the geometry of upper arm in Fig. 2.7.b, the proposed nonlinear model was tested and used to

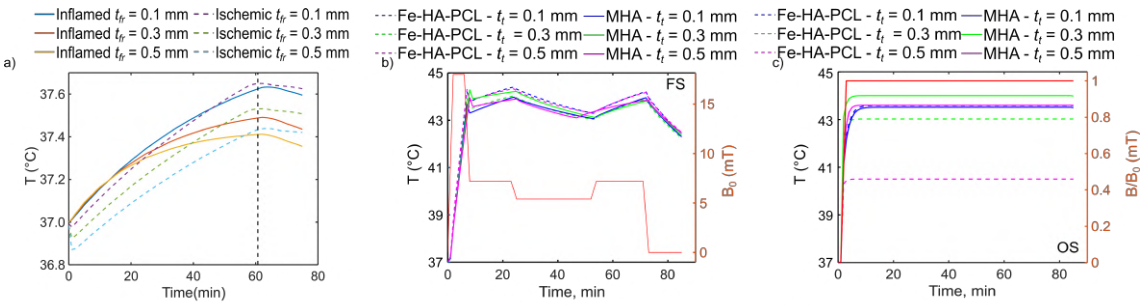

Figure 2.9. a) Average temperature in fracture volume vs. time and for both the inflamed and ischemic case. The dashed black line indicates the time point at which the external RF magnetic field is turned off. b) Average temperature increase in Fibrosarcoma (FS) region, considering an inflamed fracture ($B_0 = 17$ mT for Fe-Ha-PCL, whereas 20 mT for MHA. Exposure time is 85 min. The optimal applied field can be modeled as a descending ramp since FS is a low perfused tumor. c) Average temperature increase in Osteosarcoma region. MHA scaffolds are able to keep temperature above the therapeutic threshold.

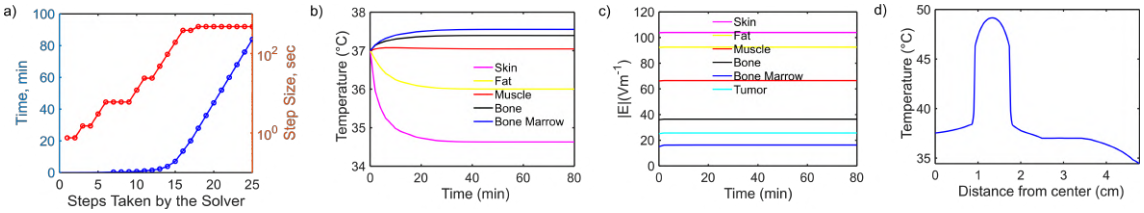

Figure 2.10. a) Variation of the step size during the solver iterations. b). Average values of the electric field norm in the non-target tissues during the treatment. c) Time evolution of the average temperature in the non-target tissues during the treatment. d) Spatial dependence (x-direction) of temperature at $t = 80$ min. The effect of the MagS is local. The non-target tissues are in safe condition at the end of the treatment.

investigate the spatio-temporal dynamics of EM fields and temperature patterns. In Fig. 2.10.a, the changes in the step size for solving the fully, bi-directionally coupled electro-magneto thermal model are shown. With our model, given the average tissue temperature profiles shown in Fig. 2.10.b, it is possible to evaluate that the norm of the electric field in the tissue varies in the first 5 min of the HT. The temperature of the non-target tissues during 80 min of HT was monitored in order to account if any potential damage or unwanted overheating could occur. The curves for the skin, fat, muscle, bone and bone marrow layers are reported in Fig. 2.10. It can be notice that the highest temperature values occur in bone and bone marrow, i.e. nearby the MagS, whilst in the other tissues the temperature levels are lower and approximately equal to T_b. Of course, observing the average value of the electric field norm in tissues over time, the levels are almost constant and decrease from the skin to the tumor, coherently to the distribution in the coil system. Furthermore, it is worth noting that the skin layer can exchange heat with air by natural convection and irradiation, and therefore, its temperature decreases, trying to equilibrate with the surroundings. Furthermore, the action of the brachial artery and vein is evident, from Fig. 2.10.c. Since the dielectric losses are much lower than the power deposited by the magnetic phase contained in the

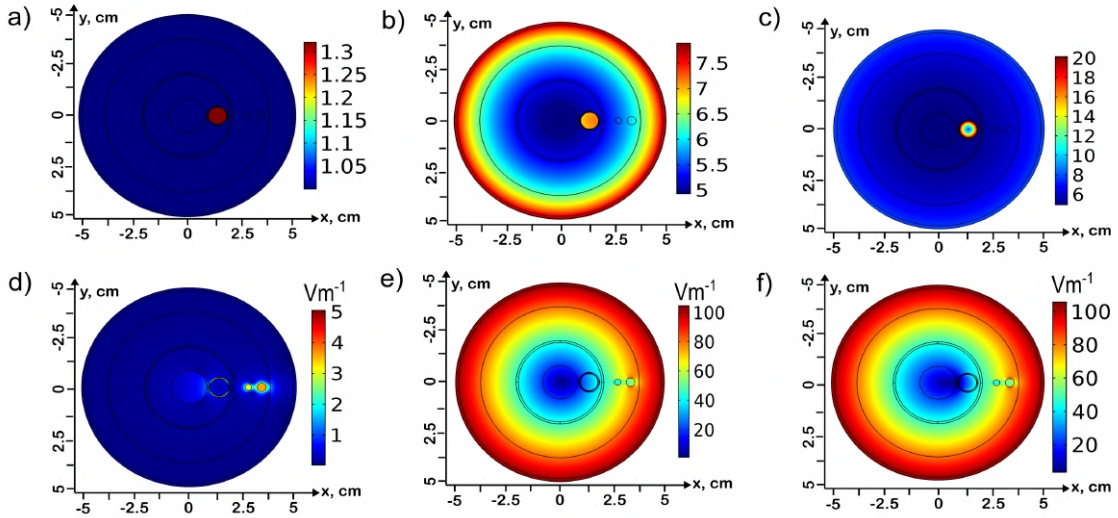

Figure 2.11. a) Normalized distribution of the norm of the magnetic field ($|\mathbf{H}(\mathbf{x},\mathbf{y})/\mathbf{H_0}|$) in the arm when a uniform external magnetic field is applied. b) Normalized distribution of the norm of the magnetic field ($|\mathbf{H}(\mathbf{x},\mathbf{y})/\mathbf{H_0}|$) in the arm when a nonuniform external magnetic field is applied. The magnetic density flux field produced by a coil with 50 turns, a length of 28.5 cm and a diameter of 10.5 cm. c) Normalized distribution of the norm of the magnetic field ($|\mathbf{H}(\mathbf{x},\mathbf{y})/\mathbf{H_0}|$) in the arm when a nonuniform external magnetic field is applied. d) 2D pattern of the norm of the electric field in the arm when a uniform external magnetic field is applied. e) 2D pattern of the norm of the electric field in the arm when a nonuniform external magnetic field is applied. The magnetic density flux field produced by a coil with 50 turns, a length of 28.5 cm and a diameter of 10.5 cm. f) 2D pattern of the norm of the electric field in the arm when a nonuniform external magnetic field is applied. The profile of the MNPs in the scaffold is assumed to follow the inverse Gaussian distribution.

prosthetic implant [164], the heating is very local, i.e. the temperature gradient is steep between the scaffold and the healthy bone tissue, as shown in Fig. 2.10.d. As a consequence, the temperature in the area containing the residual cells of the metastatic cancer reaches and overcome the therapeutic value of 42°C.

By taking a deeper look at the differences in the modeling approach, we considered how the field inhomogeneities and the possible non-uniform loading of MNPs in the MagS could affect the HT outcome. Assuming a uniform distribution of MNPs in the MagS, the differences in the electric and magnetic fields pattern was evaluated in the case of a uniform external magnetic field and compared with the field produced by a single layer coil (Fig. 2.11.a and 2.11.b). In the two cases, the field is comparable in magnitude. However, we can highlight that in Fig. 2.11, the field level is 1.25 times higher than the applied value, whilst, in Fig. 2.11.b, the normalized distribution indicate that in the magnetic scaffold (having $\chi_0 = 0.38$ at 37°C), and its surrounding, the field is about seven times higher than $\mathbf{H_0}$. This significant difference is of interest in the evaluation of the power losses due to the MNPs in the scaffold, since P_m is proportional to $|\mathbf{H}|^2$.

Moving from the Maxwell's equations and considering the results from Fig. 2.11.d and 2.11.e, it is possible to infer that in both cases local $\mathbf{E}$ field discontinuity are present, which can be associated

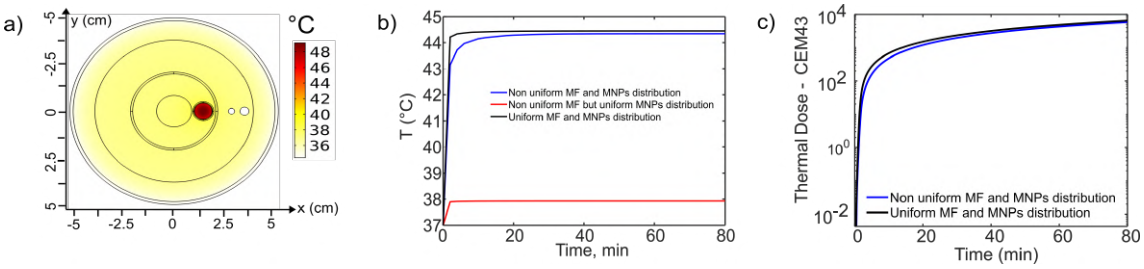

Figure 2.12. a) Temperature distribution in the arm at $t = 80$ min, with a nonuniform magnetic field (MF) of $12\,\mathrm{kAm}^{-1}$ and a scaffold doped with MNPs distributed non-uniformly. b) Average temperature in the OS tumor versus time. c) Semi-logarithmic plot of the cumulative thermal dose, $CEM43$, delivered to the residual OS cells during the treatment. The different exposure conditions and the various MNPs distribution possibilities are tested.

with relevant temperature increase during the HT [84, 89] This is confirmed by the results shown in Fig. 2.11.d and Fig. 2.11.e. In the case of the external uniform MF, the electric field is altered by the presence of biological materials with high dielectric permittivity and conductivity, i.e., the tumor, muscle and blood vessels. The contrast with the EM properties of surrounding tissues is relevant. This finding permits to infer that the assumption of a uniformity of the source can be misleading. Indeed, the dielectric heating in Fig. 2.11.d is restricted to the bone tumor, which is a very favorable condition. However, the use of a more realistic distribution for the field source leads to a noticeably different physical situation, as presented in Fig. 2.11.e. Each tissue experiences a relevant induced current, i.e. about from 20 to 10 times the value produced in the case of Fig. 2.11.d. The external layers are the ones exposed to higher electric field levels. This is why the temperature of skin and the muscle sites was monitored and unwanted overheating does not verify (Fig. 2.10.b).

After having clarified the differences in the assumption of the distribution and uniformity of the external magnetic field, the influence of the features of the magnetic scaffold on the fields distribution was investigated. In particular, we investigated the possible non-ideal manufacturing of the nanocomposite material and how this can influence the HT Herein, the external MF is supposed to be non-uniform. The volume fraction of MNPs is assumed to be equal to that of previous cases. Therefore, the only difference is the spatial distribution of MNPs. The hypothesis that the nanoparticles are more concentrated at the edges and boundaries of the scaffold rather than in the center lead to valuable differences with previous findings. In Fig. 2.11.c, the normalized magnetic field has strong spatial variation in the scaffold and its surroundings. The maximum value of the magnetic field is about three times higher than the strength of the case in Fig. 2.11.a and 2.11.b. This means that the power deposited by the MNPs is higher locally. This feature due to manufacturing processes such as ferrofluid impregnation or the 3D printing can be an advantage [27, 49, 127, 150]. In fact, the scaffold center should not be heated. The heat must be conducted to the OS region, which is very close to the biomaterial boundaries. Less significant differences arise in comparing Fig. 2.11.f with Fig. 2.11.e. The maximum, average, and minimum

values are similar. However, between the bone marrow and the scaffold the **E** field distribution is slightly altered.

Finally, the thermal outcome of the RF exposure was investigated. The different exposure cases and the two cases of MNPs distribution in the scaffold are compared. As regards the temporal evolution of the 2D temperature field, from a qualitative point of view, the differences are scarce, and are not shown therein. Further results can be found in [117, 118, 164]. Therefore, the final temperature distribution for the case of a non-ideal MagS exposed to a nonuniform RF magnetic field is shown in Fig. 2.12.a. It can be verified that the therapeutic temperature is reached at the tumor site, whilst the non-target tissues are in a relatively safe condition. It should be pointed out that the magnetic field strengths are about one order of magnitude lower than those employed which employed a uniform distribution for the applied RF magnetic field (i.e., $12\,\mathrm{kAm^{-1}}$ in the nonuniform case, versus, $72\,\mathrm{kAm^{-1}}$ for the uniform magnetic field configuration) [28, 49, 117]. From Fig. 2.12.a, it can be further verified that the skin, fat, muscle, bone, and bone marrow are not damaged and their temperature do not overcome a maximum value of 40°C. These findings are consistent with the in vivo results reported by Mastumine et al. [66]. Indeed, if the average temperature values on the 2D tissue regions are considered, the temperature does not exceed the value of 37.5°C in the bone marrow and tends to T_b in the other tissue layers (Fig. 2.10.b). This is due to the very local heating effect of the magnetic thermoseed. This outcome can be controlled by properly setting the amplitude and frequency of the external magnetic field.

To study the HT using magnetic scaffolds, the average value of the temperature in the OS region was derived. From a quantitative and qualitative point of view, the temperature evolution at the tumor site is similar to the findings from [148] and [51, 66]. To be effective, the tumor should be heated above 43°C for at least 60 min. From Fig. 2.12.b, it is possible to observe that, to reach the therapeutic temperatures for a uniformly loaded MagS exposed to a uniform external RF field, the strength of MF should be six times higher. In the case of exposure to a nonuniform magnetic field, the power per unit volume dissipated by the SPM scaffold of hydroxyapatite was evaluated. A value of $1.20{\cdot}10^8\,\mathrm{W{\cdot}m^{-3}}$ was derived ($12\,\mathrm{kAm^{-1}}$, 300 kHz). This value is 5.6 lower than the value of $6.7{\cdot}10^8\,\mathrm{W{\cdot}m^{-3}}$ experimentally derived for the ferromagnetic PCL-aluminum scaffold of Pelaez et al. ($30\,\mathrm{kAm^{-1}}$, 360 kHz) [51]. After the postprocessing of the temperature versus time data from Fig. 2.12.b, following the $CEM43$ [162], it is possible to analyze the outcome of the treatment, for the different exposure conditions and magnetic scaffold types, in a more accurate way. The $CEM43$ index is shown in Fig. 2.12.c. The $CEM43$ for the case of a nonuniform magnetic field applied to a MagS with a uniform MNPs distribution is zero for all time because the temperature is lower than 39°C, therefore, this curve is not reported. The cumulative thermal dose is very similar in the two configurations. However, for a uniform magnetic field applied to a magnetic prosthetic implant with nanoparticles homogeneously distributed, the thermal dose is 10% higher than the $CEM43$ calculated for the configuration of nonuniform magnetic field and MNPs non-homogeneously distributed (a $CEM43$ of 6531.2 against 5848). The order of magnitude of the $CEM43$ is comparable to the findings of other literature works [124, 152]. This difference is

related to the higher and overestimated magnetic field amplitude in the case of uniform source and MNPs distribution. The rise of the temperature is very different in the two cases, i.e., a steeper temperature increase in the uniform case occurs. Indeed, it is possible to infer that the external EM fields distribution has a lower effect on the average temperature of the OS tumor after 80 min HT, whilst the spatial distributions of MNPs can lead to a significantly different average temperature in the target tissue. From these findings, it is possible to affirm that the rather different approach in modeling the RF source can lead to overestimation of the field amplitude and may compromise the treatment planning or outcome. Moreover, the different MNPs distribution is found to have a strong influence on the way the heat is conducted to the tumor. For the same strength of the magnetic field, the maximum temperature in the tumor is 6°C lower for the scaffold with a uniform MNPs distribution. In this case, the treatment should be considered failed (since the thermal dose delivered to the OS cells is zero) and $\mathbf{H_0}$ should be higher than 12 $\mathrm{kAm^{-1}}$. This can be imputed to the different diffusion of heat in such a system, i.e., in other words, more time and energy are spent to heat the scaffold rather than heating the OS residual cells. Therefore, the proposed model has the advantage of including the manufacturing features of the hydroxyapatite magnetic scaffold and of allowing to study the influence on the HT.

In this chapter we have challenged the problem of modeling the HT of bone tumors using MagS exposed to a RF MF. After the complex magnetic susceptibility spectra of MagS has been modeled, starting from theoretical considerations, we proposed a multiphysics nonlinear model which allowed us to identify that

- the temperature dependence of EM and thermal properties cannot be neglected,
- the assumption on the external MF distribution can strongly affect the quality and value of the simulated HT,
- the MNPs distribution in MagS can affects the selection of the field parameters and the therapeutic outcome.

Chapter 3

Magnetic Scaffolds: Design, Manufacturing and Characterization

After having discussed the state of the art of magnetic scaffolds, and having underlined that a large variety of biomaterials, nanoparticles and manufacturing methods have been used, resulting in a several different types and examples of multifunctional magneto-responsive devices, in this chapter we are going to face the issues of designing, manufacturing and characterizing MagS. In particular, in Sect. 3.1 we will address the effects of MNPs loading patterns on hyperthermia [165], whilst in Sect. 3.2 we are dealing with the problem of characterizing the SAR of MagS, testing biomimetic 3D-printed devices [166, 167].

3.1 Drop-Casted Magnetic Scaffolds

3.1.1 Introduction

In Fig. 1.5, we presented that combining the strict anti-cancer therapeutics and the postoperative orthopedic requirements, the technological advancements in hyperthermia delivery lead to the innovative idea of manufacturing nanostructured magnetic biomaterials, called MagS, to be used as implanted thermoseeds to perform local, interstitial HT of bone cancers by applying an external RF field. Given that, in the literature, several MNPs with different response (ferri-, ferromagnetic and superparamagnetic) are used, combined with a plethora of biopolymers or bioceramics, relying on many different physical or chemical methods, to date, the investigation of the effects of manufacturing on the final hyperthermia outcome has never been performed. In this chapter, as sketched by Fig. 3.1, we propose a modified dip-coating technique for loading magnetic nanoparticles with

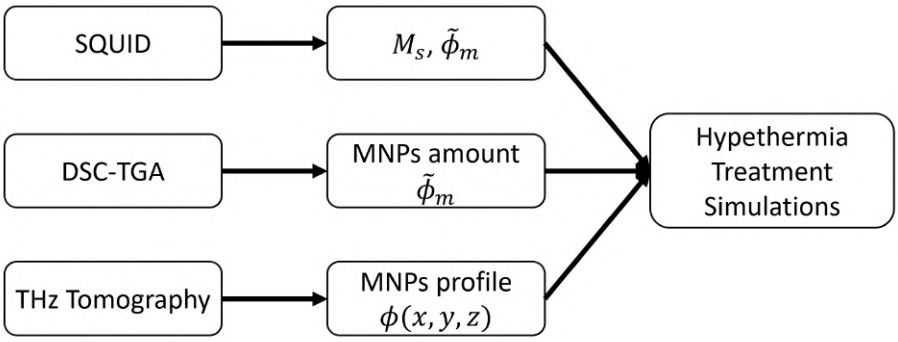

Figure 3.1. The physiochemical characterization of magnetic scaffolds aims to extract the magnetic properties of the sample through the analysis of the saturation magnetization M_{sc}, derive the amount of magnetic nanoparticles with DSC-TGA measurements $\widetilde{\phi}_m$, and retrieve the nanoparticles profile inside the biomaterial, $\phi(x,y,z)$. This information is used to simulate the hyperthermia treatment with the magnetic scaffolds and study the influence of nanoparticles' pattern on the quality of treatment.

controlled spatial pattern, and then characterized with different investigation techniques the MagS to perform numerical simulation of the hyperthermia treatment to study the influence on the treatment outcome.

3.1.2 Related Works

Magnetic hydrogels have been obtained by blending procedure to include MO (e.g., γ-Fe_2O_3, Fe_3O_4, $CoFe_2O_4$) MNPs within the scaffold [9], resulting in moderate saturation magnetization (M_{sc}) values for the scaffolds (ranging from 0.1 to 11 emu/g). MagS with more pronounced magnetic properties (M_{sc} = 1-20 emu/g) were obtained by sol-gel techniques, co-precipitation, hydrothermal process or other chemical routes to obtain intrinsically magnetic hydroxyapatite [28], β-tricalcium phosphate [8, 122], modified hardystonite ($Ca_2ZnSi_2O_7$) [33] or bredigite ($Ca_7Mg(SiO_4)_4$) scaffolds [34]. For bioceramic MagS, the amount of magnetic crystalline phase, the final microstructure, and the particle's interactions are key factors in determining the hyperthermia potential [8, 13]. The tuning and control of these parameters can be rather complex, and the process synthesis can be relatively expensive [13].

In this context, the use of polymeric matrix for MagS was investigated. Electrospinning of chitosan, poly(lactic acid) (PLA), polyvinyl alcohol (PVA), and silk fibroin was performed to obtain magnetic, quasi-3D nanofibrous structures, with a M_{sc} of about 2-8 emu/g, but limited hyperthermia and regenerative potential [60, 168]. A 3D printed magnetic nanocomposite scaffold made of poly-caprolactone (PCL) filament loaded with Fe_3O_4 MNPs demonstrated a heating rate of 1°C/min when exposed to a field intensity of 15 mT and at a frequency of 293 kHz [150]. More complex, biomimetic scaffold geometries can be magnetized following dip-coating or ferrofluid impregnation procedures [43, 44, 72, 168–170]. The easy technique consists in the physisorbtion of a

MNPs colloidal suspension in the biomaterial surface defects and inhomogeneities by capillarity. With these methods, a hybrid collagen-hydroxyapatite matrix can be loaded with 1-5 wt.% of MNPs and reach 15 emu/g if the procedure is repeated multiple times [43]. Similarly, silk fibroin scaffold can be magnetized successfully by ferrofluid, showing hyperthermic potential [72]. However, it is worth to highlight that the impregnation procedures do not guarantee a uniform dispersion of the MNPs in the scaffold matrix, as underlined by the static magnetic measurements of [44], which measured a 20% variation of the saturation magnetization in about 5 mm. Diphasic distribution of maghemite MNPs in polymers was studied [169], with poor reasoning on the design and implications.

Overall, state-of-the-art analysis [43, 44, 72, 168–170] highlight that the influence of how the loading pattern could affect the MagS performance was underestimated, or, as previously discussed, investigated only from a numerical point of view, without the support of experimental data [118]. As a matter of fact, the tunability and controllability of the production process have never been investigated in relation to the functional properties and final applications. Since MagS can be interpreted as a novel, more bio-compatible version of steel thermoseeds used for the treatment of deep-seated tumors [8, 13, 50, 66], they are constrained to the high-quality assurance criteria of interstitial hyperthermia [88]. It is therefore mandatory to investigate, from an engineering point of view, how and if different loading patterns could hamper the HT of bone tumors.

In this chapter we aim to investigate if and how the magnetization degree and loading pattern of magnetic scaffolds can influence the outcome of the HT of bone tumors. To this aim, the design and production of magnetic scaffolds was achieved by controlled deposition of ferrite magnetic nanocrystals (MNCs) on commercial PCL scaffolds featuring a 90°-shifted highly porous mesh. The manufactured magnetic scaffolds are characterized in terms of static magnetic response. The amount of magnetic phase and thermal stability are assessed through differential scanning calorimetry and thermogravimetric analysis. The morphological investigation is carried out by electron microscopy and the spatial distribution of the MNCs in the scaffold volume is retrieved by THz tomography. By combining the magnetic properties and the loading patterns, we performed numerical nonlinear and multiphysics simulations to investigate the influence of the spatial distribution of MNPs in the scaffold on the quality of the hyperthermia treatment of bone tumors.

3.1.3 Magnetic Scaffolds Preparation

3.1.3.1 Magnetic Nanoparticles Synthesis and Characterization

The preparation of iron oxide magnetic nanocrystals samples (MNC1 and MNC2) was performed through a modified partial oxidation route protocol [171]. Briefly, iron (II) sulfate ($FeSO_4 \cdot 7H_2O$) was let react under N_2 atmosphere at 90°C with potassium nitrate (KNO_3) and potassium hydroxide (KOH, all from Sigma Aldrich) in water. MNCs were isolated from the reaction mixture by magnetic separation, washed and re-dispersed in water.

Samples features were investigated by transmission electron microscopy and X-ray diffraction

(XRD). XRD patterns were recorded using Cu-Kα radiation on a Panalytical Empyrean diffractometer equipped with a graphite monochromator on the diffracted beam and an X'Celerator linear detector. The results are reported in [165] and in Fig. 3.6 in the following.

Transmission electron microscopy (TEM) images were recorded on a Hitachi H-7000 instrument running at 125 kV and on a Jeol JEM 1400 Plus operating at 120 kV. Samples for TEM observation were deposited on a C-coated copper grid. These analysis were carried at CeSAR (Centro Servizi Ricerca d'Ateneo)[1] core facility of the University of Cagliari.

3.1.3.2 Scaffolds Architecture and Drop-Casting Loading

In this study, the polymeric scaffolds produced by 3D Biotek (3D Biotek LLC, NJ, USA) were purchased from Sigma-Aldrich (Merck KGaA, Darmstadt, Ge). These standard PCL disks have a 5 mm diameter and are 1.6 mm in height. The set of 3D-Insert is constituted by a 90°-interlaced fiber architecture, with a fiber diameter of 300 μm, spaced by 300 μm, resulting in a nominal porosity of about 80%. A representative image of the bare, unloaded PCL scaffold is reported as M0 in Fig. 3.2.

In order to produce the MagS, the water-based dispersion of the MNCs was first sonicated and then a drop was deposited on the PCL scaffolds, as depicted in Fig. 3.2.a. NdFeB permanent magnet (Webcraft GmbH, DEU, S-20-20-N, diameter 10 mm, height 20 mm, 20 mm, 4.5 kg of attraction force, ∼1T at the surface) was located at the bottom of the PCL scaffold in order to promote the MNCs uptake. Finally, the scaffold was dried in a furnace at 40°C, under static air.

For the production of magnetic scaffolds M1 to M6, sample MNC1 was used, and ten magnet-guided depositions followed by drying was performed to achieve a different loading of nanoparticles. Polymer modification through the incorporation of MNCs is an easy manufacturing approach, which allow to obtain desired patterns, also homogeneous distributions. Scaffolds labeled as Strip, PCL FeOx 14-16 were prepared by deposition of sample MNC2. In this case, before the deposition process, a water-repellent tape with the desired pattern was applied to one side of the original PCL scaffold. The tape limits MNC deposition in the selected area, leading to non-homogeneous distribution of MNCs in the scaffolds, as shown in Fig. 3.2.b. Then, the tape was removed, and the scaffold was dried at 40°C. The resulting MagS samples are shown in Fig. 3.2.c.

3.1.4 Methods for Magnetic Scaffolds Characterization

3.1.4.1 Static Magnetic Measurements

Static magnetic characterizations were carried out using a super-conducting quantum interference device (SQUID) from Quantum Design (MPMS XL EverCool), available at the Italian Institute of Technology (IIT). Magnetic scaffolds have been loaded inside the instrumentation with a

[1] https://www.unica.it/unica/page/it/centro_servizi_di_ateneo_per_la_ricerca_cesar_it_1

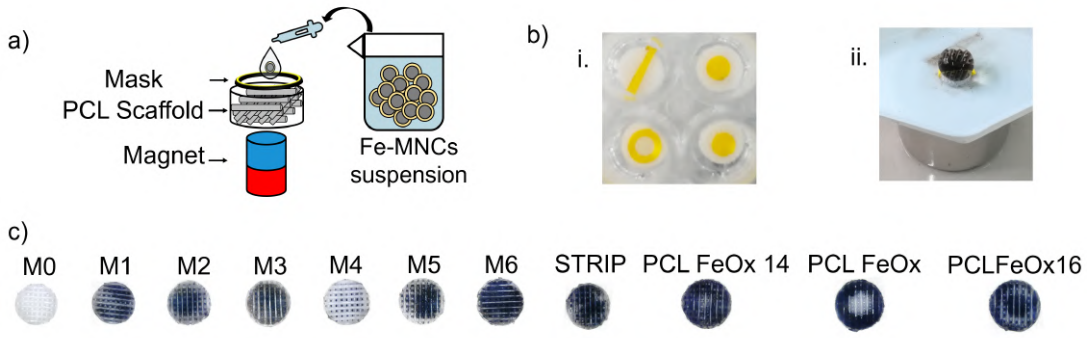

Figure 3.2. a) Magnetic scaffolds fabrication: magnetic nanocrystals (MNCs), dispersed in water, are dripped onto the PCL scaffolds and the deposition is carried out under the driving force of the external magnet. b) i. Examples of arrangements of waterproof adhesive tape as masks for patterning the MNCs in the biomaterial. ii. Example of the sample preparation during the drop-casting. c). Optical images of the PCL scaffolds loaded with magnetic nanocrystals as obtained by the proposed modified drop-casting process. The manufacturing method is controlled to result in a wide variety of magnetic nanoparticles distribution, and patterns in the biomaterial.

perpendicular orientation with respect to the applied magnetic field. All magnetization curves were acquired exploiting high sensitivity Reciprocating Sample Option (RSO), applying fields between -7 and 7 Tesla at a constant temperature of 310 K (37°C), in order to replicate the susceptibility of the particles at physiological temperatures.

The measured magnetization curves (**M**, in emu) were fitted to the following equation [131]

$$\mathbf{M}(\mathbf{B}) = \widetilde{\phi}_m M_s \left[\coth \frac{\mu_m \mathbf{B}}{k_B T} - \frac{k_B T}{\mu_m \mathbf{B}} \right] \tag{3.1}$$

where $\widetilde{\phi}_m$ is the average amount of MNCs loaded in the biomaterial matrix, M_s is the saturation magnetization of the single nanoparticle, μ_m is the nanoparticle longitudinal magnetic moment and $\mathbf{B}$ is the applied external, longitudinal magnetic flux density (in T), k_B is the Boltzmann's constant and T is the system temperature (in K). The fitting is performed using Matlab 2021a (The MathWorks Inc., MA, USA) considering as unknown the term $\widetilde{\phi}_m$.

The response of the manufactured magnetic scaffolds was also evaluated measuring the minimum distance of attraction in presence of a static magnetic field generated by the same permanent NdFeB magnet used during the drop-casting procedure, as done in [172].

3.1.4.2 Morphological Characterization and Microstructure Observation

The presence, clustering, and distribution of the MNPs in the polymeric matrix, as well as the scaffold internal morphology were verified with Scanning Electron Microscopy (SEM) imaging. The JEOL JSM-7500FA (JEOL, Jap) microscope from Electron Microscopy Facility at IIT (Genoa, IT) was employed to assess the spatial distribution of the MNCs in the produced magnetic scaffolds

samples. The SEM images were analyzed using the open-source software Image Processing and Analysis in Java (ImageJ, NIH Gov.). The distributions of the pore size, the radii of the magnetic nanoparticles and the presence of clusters in the scaffolds were assessed.

3.1.4.3 Differential Scanning Calorimetry and Thermogravimetric Analysis

The simultaneous Differential Scanning Calorimeter (DSC)-Thermogravimetric (TGA) analyzer SDT Q600 (TA, New Castle, DE) was used to determine the MNCs loading in a selected scaffold [168, 172, 173]. A 40 μl alumina pan was used as a sample holder. The initial temperature was 20°C. The protocol consists of a heating ramp with a slope of 20°C·min^{-1} up to the final temperature of 1000°C, under N2 sample purge flow at a flow rate of 100 mL/min.

The temperature values at different mass percentages (T10% T50% T90%) are considered. The first and second derivatives of the weight vs. temperature were investigated.

3.1.4.4 THz Tomography

Nowadays, several approaches are considered for characterizing the pore size, distribution and architecture of biomaterials [174, 175], as well as drug loading capabilities or functional properties [176, 177]. Among these, THz imaging is of interest because it allows for sample characterization without compromising its integrity. Furthermore, the free-space wavelength (λ) in the THz regime ranges from 0.3 mm to 30 μm, thus ensuring enough space resolution to investigate and retrieve peculiar biomaterial features, in a cheaper and faster way than using other approaches, such as, for instance, magnetic resonance imaging apparatus [176]. Herein, THz time of flight (TOF) imaging technique [178] has been exploited to estimate the spatial distribution of MNPs in the PCL scaffolds.

THz TOF imaging, also known as THz pulsed imaging (TPI), has the unique property of providing a 3D "map" of the object by exploiting data collected in reflection mode [178].

In brief, the object is probed by a pulse signal and the reflected waveform is collected as a time-dependent function in a certain observation time window. The reflected pulses and their temporal delay reveal the internal structure of the sample (if the object is nonmetallic). It is, indeed, worth pointing out that the TOF, i.e. the time t that the waveform employs to propagate from the emitter to an electromagnetic discontinuity and to go back to the receiver, is related to the distance d between THz probes and the detected discontinuities as

$$TOF = 2 \cdot \frac{d}{v}, \tag{3.2}$$

being v the electromagnetic wave propagation velocity into the object.

THz data have been collected by means of the Zomega THz FiCO system [179, 180] available at the Institute for Electromagnetic Sensing of the Environment - National Research Council of Italy (IREA-CNR). The system is equipped with ad hoc designed imaging module (see Fig. 3.3.a) and collects data in normal reflection mode in 40 GHz up to 3 THz frequency range. Fig. 3.3

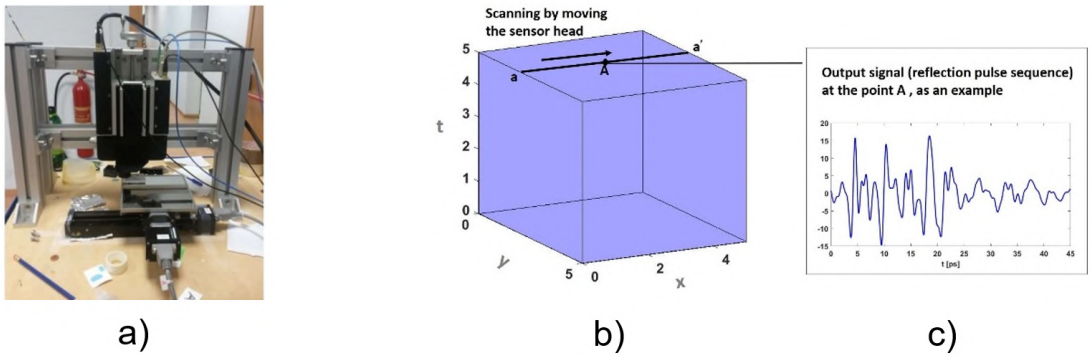

Figure 3.3. a) Imaging module of the Zomega FiCO System available at the IREA-CNR at Naples. . Data Measured by the FiCO system: a) Acquisition of THz data along a line a-a'. b) Single point measurement.

describes the measurement process of the FiCO system. The system provides 3D data (2D in space + 1D in time) collected using an automatic planar scan, moving along x and y directions (see Fig. 3.3.a), within a 100 ps observation time window. At each measurement point, the air–object interface as well as all the electromagnetic discontinuities inside the object generate reflections, which are recorded as a time-dependent waveform. Fig. 3.3.b shows an example of a single-point measurement.

THz data have been gathered on a 10 mm x 10 mm wide scan area, which is discretized by square pixels, 0.12 mm in side length, for all the samples analyzed (see Fig. 3.2.c). The samples have been placed on a support to have a unique spatial reference.

THz data have been processed by means of the procedure detailed in Appendix, which provides two main outputs:

- The Magnetization Index (I_m), which encodes the amount of MNPs present in the sample under test. The I_m is calculated from the 2D binarized magnetization map (Fig. 3.4.h in Appendix) as the ratio between the number of pixels containing MNPs (yellow pixels marked with 1 in Fig. 3.4.h) and the total number of pixels discretizing the scanning area and intercepting the sample.

- The 2D MNPs distribution map (Fig. 3.4.i) which shows the parts of the sample under test where MNPs are mostly concentrated and allows to appraise the potential of the manufactured magnetic scaffolds for the hyperthermia treatment of bone tumors. This map is obtained by multiplying pixel by pixel the binary magnetization map times (Fig. 3.4.h) and the map of the filtered THz signal amplitude (Fig. 3.4.b).

More details about the THz methodology can be found in [165].

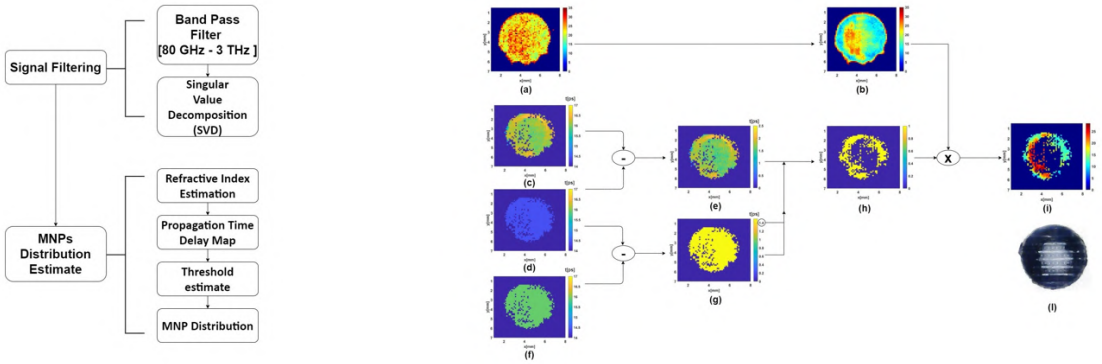

Figure 3.4. Multi Steps procedure used to extract 2D magnetic nanoparticles (MNPs) distribution map. Example of the developed THz data processing applied to the sample PCL15: a) raw THz data in false color. b) THz data after band pass and singular value decomposition filters. c) 2D map of the propagation time distribution (in picoseconds) in a magnetic scaffold (PCL-FeOx15). d) propagation time for the reference blank scaffold. e) time delay difference. f) sample loaded homogeneously with MNCs. g) threshold mask. h) 2D magnetization map.

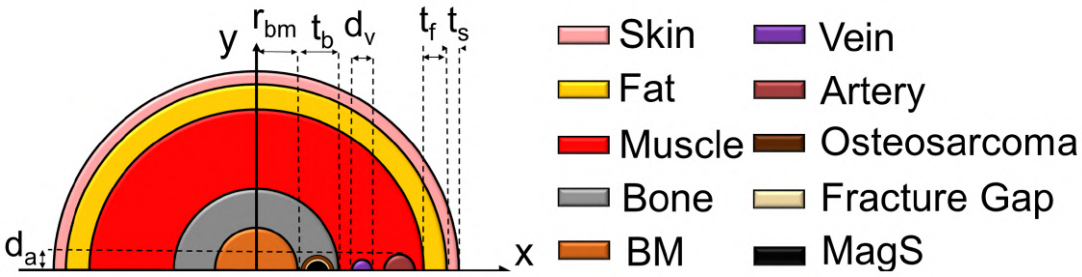

Figure 3.5. Simplified geometry of a human upper limb used for the evaluating the in silico influence of MNPs inhomogeneous loading in MagS on the hyperthermia treatment of bone tumors.

3.1.4.5 In Silico Tests of Hyperthermia Treatment with Magnetic Scaffolds

The aim of this chapter is to investigate if and how the loading patterns of magnetic scaffolds could affect the hyperthermia treatment of residual bone tumor cells, shown in Fig. 1.5. We characterized the physiochemical properties of MagS implemented through the drop-casting and derived essential information for performing extensive and accurate in silico experiments of the hyperthermia treatment of bone tumor.

In this framework, the multiphysics and numerical model described in Chap. 2.3 was used [118,165]. As depicted in Fig. 3.5, a MagS, with a radius of 5 mm, is assumed to be implanted after the surgical resection of an osteosarcoma tumor, which leaves a margin of residual cells 0.5 mm thick, grown between the marrow and the cortical region of a human upper limb. The system geometry, shown in Fig. 3.5, is a layered surface phantom consisting of a skin layer with thickness t_s of 1.5 mm, a fat and a muscle layer having thicknesses $t_f = 10$ mm and $t_m = 3$ mm, respectively. The bone

humerus, with radius $r_{bm} + t_b = 20\,\text{mm}$ and the bone marrow (BM), having radius $r_{bm} = 10\,\text{mm}$, are taken as the center of the coordinates system. The brachial artery and vein were considered in the geometry to account for the heat transfer. The system is assumed to be exposed to the magnetic field generated from a solenoid working at a given frequency f. The electromagnetic properties of the tissues are taken from [118]. The PBHE is solved assuming as initial distribution the steady-state temperature distribution resulting in the equilibrium of a 37°C for all tissues and an air temperature of 25°C. Heat exchange by convection is assumed at the skin-air interface, given a convective heat transfer coefficient of $7.7\,\text{Wm}^{-2}\text{K}^{-1}$. At the muscle-vessel boundaries an effective convection mechanism is assumed [118].

Previous literature works [72, 117, 118], considered the amount of MNPs in the biomaterial to be a constant, approximately equal to the volume-averaged contents, which can be derived from the static magnetic measurements or DSC-TGA analysis. However, this assumption leads to a misleading estimation of the hyperthermia treatment parameters.

The power dissipated by the MagS (Eq. (2.1)) depends linearly on the particle volume and quadratically from the saturation magnetization of the MNCs, but it also depends linearly on the volume fraction. It is worth noting that the wavelength (λ) of the RF field ($\sim$ few meters) applied for performing the interstitial HT is much higher than the size of the implant and the size of the scaffolds and MNPs (i.e., $l_{ch} \ll \lambda$, where l_{ch} is a characteristic length equal to sub-mm features). Given the sub-wavelength variation, the EM problem can be approximated to a quasi-static regime and, from the thermal point of view, a variability in the loading patter can lead to significant differences in terms of final tumor temperature and treatment quality. Therefore, for the case of MagS manufactured with the proposed dip-coating procedure, and shown in Fig. 3.2, the power dissipated by the MagS (Eq. (2.1)) requires a different definition. In particular, to evaluate the frequency response of the MagS according to the Cole-Cole model (Eq. (2.10)), the initial susceptibility (χ_0) must be considered to be space-dependent, given that the fraction of MNPs in the biomaterial is an unknown function of space, i.e.

$$\phi_m = \phi(x,y). \tag{3.3}$$

Therefore, other than the frequency and temperature dependence, given that $P_m = P_m(x,y)$, the HT of bone tumors becomes a more complex problem.

The loading pattern $\phi(x,y)$, which depends on the processing conditions, is obtained from THz tomography (see Fig. 3.4). We used the post-processed THz images to derive a closed-form equation for each of the ten scaffolds shown in Fig. 3.2.c. To this aim, the MNPs distributions were translated and fitted to a finite series of radial basis functions (RBF)

$$\phi(x,y) = \sum_{i=1}^{n=8} a_i e^{-b_i \left[\sqrt{(x-x_{0,i})^2+(y-y_{0,i})^2}\right]^2} \tag{3.4}$$

where a_i is the maximum amplitude of the basis function, b_i is the variance-related parameter and

Table 3.1. Coefficients of the RBFs for the MNPs distribution of the ten MagS.

	Min.	**Max.**
a_i	0	1
b_i	0.001	20
$x_{0,i}$	-7	7
$y_{0,i}$	-7	7

$x_{0,i}$ and $y_{0,i}$ are the centers of the i-th basis function, within the scaffold domain in the geometry from Fig. 3.5. The values of the coefficients for the eight RBF are found by minimizing, in a least square sense, the difference between Eq. 3.4 and THz post-processed data by using the *"lsqcurvefit"* function from Matlab 2021 (The MathWorks Inc., MA USA). The range for the coefficients of the RBFs are reported in Tab. 3.1.

3.1.5 Findings and Recommendations

3.1.5.1 Characterization

The XRD patterns are quite similar for the two MNCs samples and are consistent with the formation of nanocrystalline iron oxide with a spinel structure which can be ascribed to the formation of magnetite Fe_3O_4) and/or maghemite (γ-Fe_2O_3). The XRD peak broadening suggests that MNC1 features larger average crystalline domains as compared to MNC2. In particular, the average size of crystalline domains ($< d >$XRD) as assessed through the Scherrer equation [181] based on profile fitting by Panalytical Highscore software and corrected by instrumental broadening using a lab reference, turned out to be 58 nm and 32 nm for MNC1 and MNC2, respectively.

TEM analysis supports the nanocrystalline nature of the two samples, indicating the occurrence of nanocrystals with cubic and cubo-octahedral morphology (see Figure 3.6), together with some elongated nanocrystals which appear in MNC1, likely associated with goethite. The average size of the nanocrystals is consistent with XRD data; in addition, TEM indicates that MNC1 shows a broader size distribution as compared to MNC2.

The static magnetic response of the magnetic scaffolds manufactured with the proposed drop-casting technique was investigated. The saturation magnetization values for the used MNCs, at room temperature, are expected to be superparamagnetic and in the range from 70-80 Am^2kg^{-1}, based on investigation of similar samples [171]. The static magnetic response of the MagS manufactured by the drop-casting procedure is presented in Fig. 3.7.a. All the scaffolds present a superparamagnetic behavior, with negligible coercive forces. The MagS with the higher saturation magnetization are the sample M6 and PCL FeOx16 (see Fig. 3.2.c), as can be observed by Fig. 3.7.a (∼8.8 and 7 emu/g). This strong magnetic characteristic is due to the 12.1% of MNCs loaded in it. From Tab. 3.2, despite these two exceptions, it is possible to notice that samples loaded with similar MNCs populations present a coherent distribution of saturation magnetization and loading values (i.e., M1-M5 scaffolds, loaded with MNC1 particles, present very similar saturation magnetization and

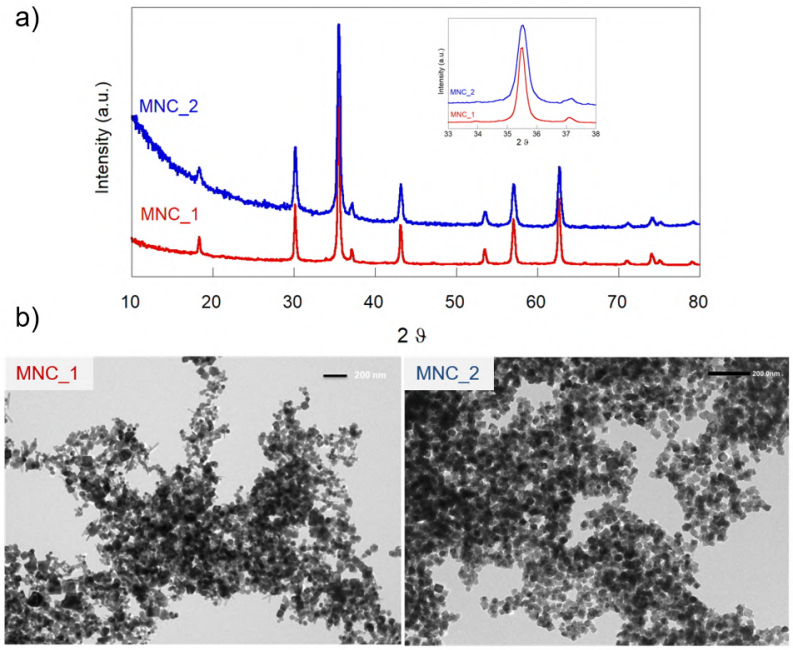

Figure 3.6. a) XRD patterns and b) corresponding representative TEM mages of the iron oxide MNCs samples (MNC1, MNC2) used to produce PCL-based magnetic scaffolds.

loading values). From the findings reported in Fig. 3.7.a and Tab. 3.2, it is possible to notice that the drop-casted method for manufacturing MagS results in average saturation magnetization of about 3.062±2.664 emu/g, for an average loading of about 2.42%. The static magnetic measurements are confirmed by the attraction distances shown in Fig. 3.7.b. Indeed, for the M6 and PCL FeOx16, the measured minimum attraction distance of 2.5-3.0 cm ± 0.2 cm.

The results of TGA characterization for the bare (M0) and MNCs-loaded scaffold (M5) are reported in Fig. 11. The TGA curve of the bare PCL scaffold (M0) shows a single relevant weight loss which takes place at around 400°C. The thermal behavior of the polymeric matrix is coherent to the analysis from [172, 173]. This main mechanism of weight loss is also observed in the MNCs-loaded (M5) scaffold. On the other hand, as no mass variations due to the PCL substrate are expected above this temperature, the weight at 600°C was used to assess the MNCs overall loading in the substrate ($\widetilde{\phi}_m$), which in the case of the M5 scaffold turned out to be ∼1.89 wt.%, for an approximate weight of 0.036 mg of magnetite.

The value of MNCs loaded in the scaffold found by DSC-TGA is very similar to the values obtained by the fitting procedure, resulting in a difference below 1% (Tab. 3.2).

The MNCs distributions for the ten MagS are reported in Fig. 3.8. From the processing of the high-THz signals and scans, the refractive index (n) and the magnetization index (I_m) were derived

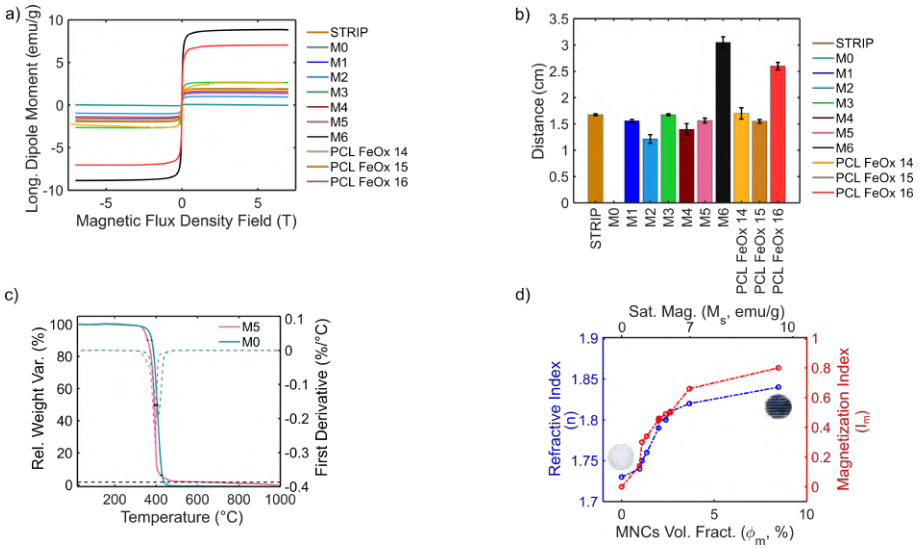

Figure 3.7. a) Scaffold magnetization as a function of an external static magnetic field for the ten scaffolds (M1-M6, PCL FeOX 14 - PCL FeOx 16) and the reference, unloaded PCL disk (M0). b) Minimum attraction distance (cm) from the NdFeB magnet. c) Example of the relative weight (W%), and its first derivative, versus temperature for the sample M5. The temperatures at 90%, 50% and 10% of the initial weight are highlighted. The residual magnetite mass is evaluated at 600°C. d) Refractive index (n) and magnetization index (I_m) as a function of the average loaded volume fraction of magnetic nanocrystals ($\widetilde{\phi}_m$) and of the saturation magnetization of the magnetic scaffolds (in emu/g). The unloaded PCL, reference scaffold M0 and the sample M6 are shown.

Table 3.2. Fitting and THz results.

Sample	M_{sc} (emu/g)	$\widetilde{\phi}_m$ (%)	R^2	d (mm)	n	I_m
M0	0.001	0	-	1.30	1.73	0
M1	1.467	1.99	0.98	1.28	1.80	0.46
M2	1.01	1.36	0.99	1.27	1.75	0.30
M3	2.67	3.66	0.98	1.76	1.75	0.50
M4	1.92	2.63	0.96	1.50	1.74	0.14
M5	1.40	1.90	0.99	1.36	1.81	0.46
M6	8.86	12.01	0.92	1.20	1.84	0.66
PCL FeOx 14	2.61	2.01	0.96	1.26	1.82	0.80
PCL FeOx 15	1.96	2.38	0.98	1.21	1.81	0.49
PCL FeOx 16	1.66	2.02	0.96	1.30	1.79	0.45

and reported in Tab. 3.2.

3.1.5.2 Simulations Results

The samples manufactured by the drop-casting procedure were characterized by SQUID magnetometry to obtain the scaffold saturation magnetization (M_{sc}), the maximum amount of MNPs in the sample ($\widetilde{\phi}_m$) and the loading pattern of the biomaterial ($\phi(x,y)$). As depicted in Fig. 3.1, these information were used to simulate the hyperthermia treatment of bone tumors using the different

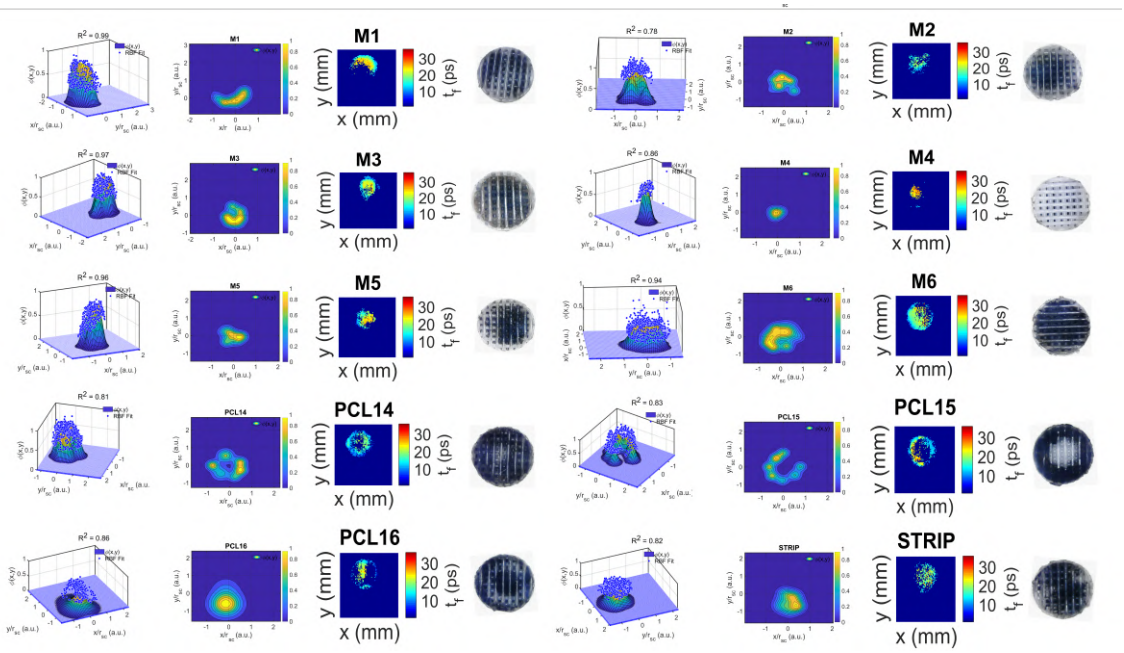

Figure 3.8. The 2D MNPs distribution maps for the magnetic scaffolds manufactured with drop-casting method and the fittings results, with residuals (R^2), are reported.

MagS samples. By using the profiles derived from THz scans, we performed extensive and accurate in silico experiments of the hyperthermia treatment of bone tumors.

Given the fitting parameters from Tab. 3.2, the magnetic power losses (P_m, Eq. (2.1)) for MagS have been estimated. In the simulations of the hyperthermia treatment of bone tumors we set the magnetic field to an amplitude of 30 mT and a working frequency of 300 kHz [28, 117, 118, 150]. MagS loaded with MNC2 exhibit a higher hyperthermia potential. Indeed, P_m is about one order of magnitude higher than those of MNC1-loaded scaffolds (due to the smaller size of the MNC2 nanoparticles (32 nm vs. 58 nm) [135], as shown in Fig. 3.9.

Multiphysics, non-linear simulations were used to investigate how the spatial distribution could also influence the power deposited power, and are shown in Fig. 14. The SAR distribution was assessed to evaluate if the deposited power could harm any non-target tissue (Fig. 3.10.a). For all MagS samples, the simulated SAR levels are elevated in the muscle and in the scaffold volume. By investigating the 2D temperature pattern, at $t = 80$ min, for the sample PCL FeOx 16 (Fig. 3.10.b), a hot region can be identified in the implanted thermoseed volume and in the tumor region, whilst in non-target tissues temperature a more in-depth analysis is required. Therefore, the maximum temperature in the skin, fat, muscle, bone and bone marrow tissues was considered and the average $\pm$ standard deviation, computed across all MagS samples, was reported in Fig. 3.10.c. From the analysis of the time evolution of the average temperature in the Osteosarcoma tumor region (Fig. 3.10.d), the scaffolds M3, M5 and M6, but also PCL FeOx14-16 can reach and

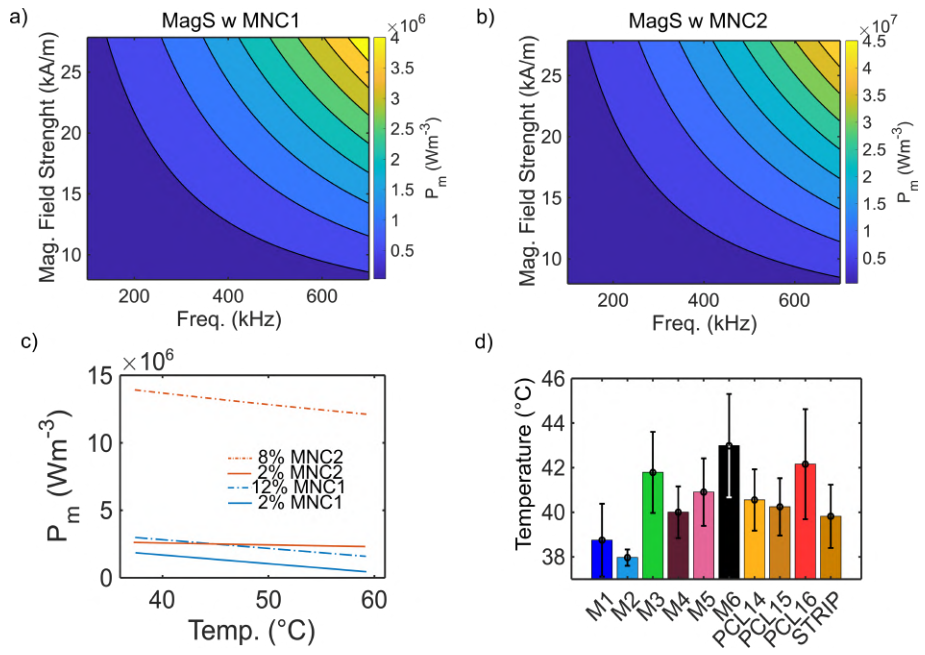

Figure 3.9. a) Power per volume unit (P_m, Wm^{-3}) dissipated by a drop-casted MagS with 8% of MNC1, for different magnetic field strength and working frequencies. b) Power per volume unit (P_m, Wm^{-3}) dissipated by a drop-casted MagS with 8% of MNC2 for different magnetic field strength and working. c) Power per volume unit (P_m, Wm^{-3}) dissipated by drop-casted scaffolds made with MNC1 and MNC2 for average and maximum values of the volume fraction, evaluated as a function of temperature, at $H = 30$ mT and $f = 300$ kHz.

withstand the therapeutic temperature range, whilst the features of M1, M2 do not enable effective treatment. Under the simulated treatment conditions, the samples M4 and STRIP are very close to the threshold value and a slight adjustment to the extrinsic field parameters would result in an enhanced dissipation. The very different therapeutic outcome could be understood by observing that temperature patterns, at the final time of 80 min, along the x- and y-directions varies for all the magnetic scaffolds differs, depending on the loading pattern, in terms of peak height symmetry and broadness, as shown in Fig. 3.10.e and Fig. 3.10.f.

3.1.5.3 Discussion

The results presented in Tab. I and Figs. 10-14 elucidate that the loading patterns of magnetic scaffolds can affect the potential therapeutic capability of these multifunctional devices against bone cancers, regardless the features of the MNCs.

A first explanation can be ascribed to the fact that the different spatial loading can impact the static magnetic properties of the sample, as shown in Fig. 10 and Tab. I. The drop-casting method developed for obtaining different loading pattern of magnetic scaffolds, can result in rather different distributions of the MNCs in the samples and, therefore, clusters can form, which may

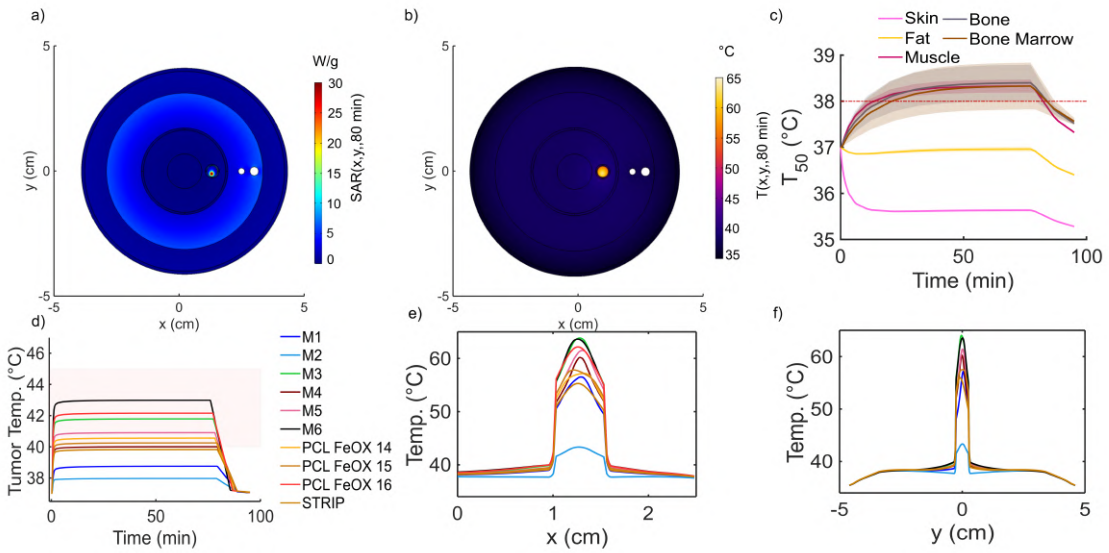

Figure 3.10. a) Simulated bi-dimensional distribution of the Specific Absorption Rate (SAR), in W/kg, at $t = 80$ min for the PCL FeOX 16 magnetic scaffold. b) Simulated 2D distribution of the temperature, in °C, at $t = 80$ min for the sample PCL FeOX 16. c) Maximum temperature, in °C, in the healthy tissues (skin, fat, muscle, bone and bone marrow) during the hyperthermia treatment. The temperature is presented as the average ± standard deviation computed for all samples. d) T50 vs. time for the drop-casted magnetic scaffolds. The shaded area represents the therapeutic range. e) Temperature profile along the x-coordinate ($y = 0$), at $t = 80$ min, for all the magnetic scaffolds. e) Temperature profile along the y-coordinate, passing through the scaffold, at $t = 80$ min, for all the magnetic scaffolds.

influence negatively the final magnetic properties after the loading procedure. In this framework, the possibility of non-linear magnetic effects due to the loading may arise [13, 43, 44, 168]. From the SEM images reported in Fig. 3.11 it can be noticed that the MNCs are mostly distributed on the surface of PCL fibers, but the iron presence can be tracked also within the low magnetization samples M2 and M4. As confirmed by Fig. 3.11, the magnetization procedure causes some regions where the MNCs are concentrated and presenting large (∼23 μm), irregular aggregates, which determines an increase in the particle-particle interaction level. The manufactured MagS presents appealing magnetic features, concerning the available literature counterparts. Indeed, the attraction distances shown in Fig. 3.7.b are comparable to those reported in [182] for cylindrical PGA scaffolds of 0.9-1.5 cm in diameter, with 2-8% loading of commercial 20 nm magnetite particles (having M_s ranging from 2.5 to 8 emu/g). The magnetization of our drop-casted MagS results in larger attraction distances, higher than the values of 0.4-0.8 cm reported in [172] for PCL scaffolds embedding 5% and 10% of 10 nm magnetite nanoparticles. These magnetic features make our drop-casted MagS appealing for bone tissue engineering, but especially for bone tumor hyperthermia.

Given the promising comparison with other magnetic scaffolds synthesized and characterized for bone tumor hyperthermia [8, 13, 28, 122, 150], we evaluated the hyperthermic potential of the drop-casted magnetic scaffolds in silico, for the geometry in Fig. 3.5. The extrinsic, treatment

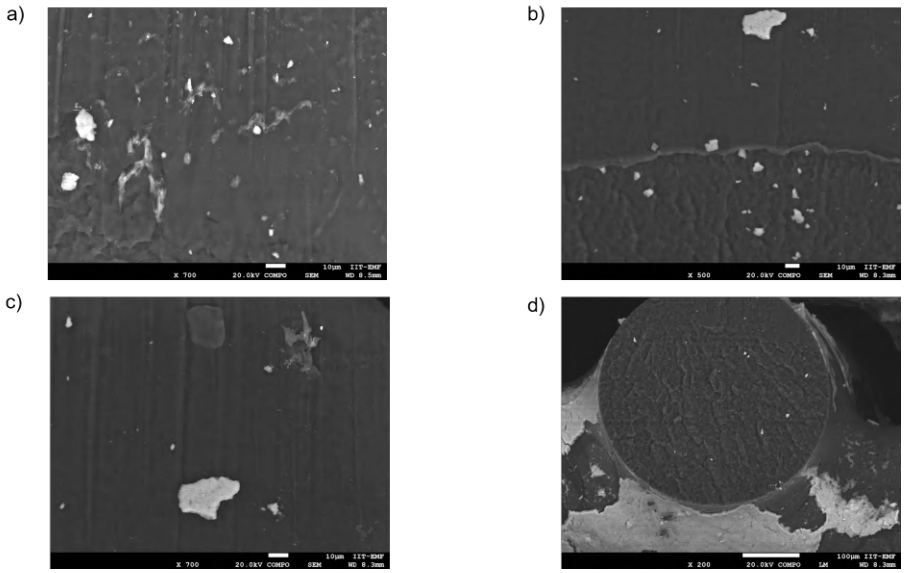

Figure 3.11. Inside view of the polymeric scaffold and of the magnetic nanocrystals. A fiber-like structure is observed with presence of MNCs clusters, mostly present on the surface of the fiber.

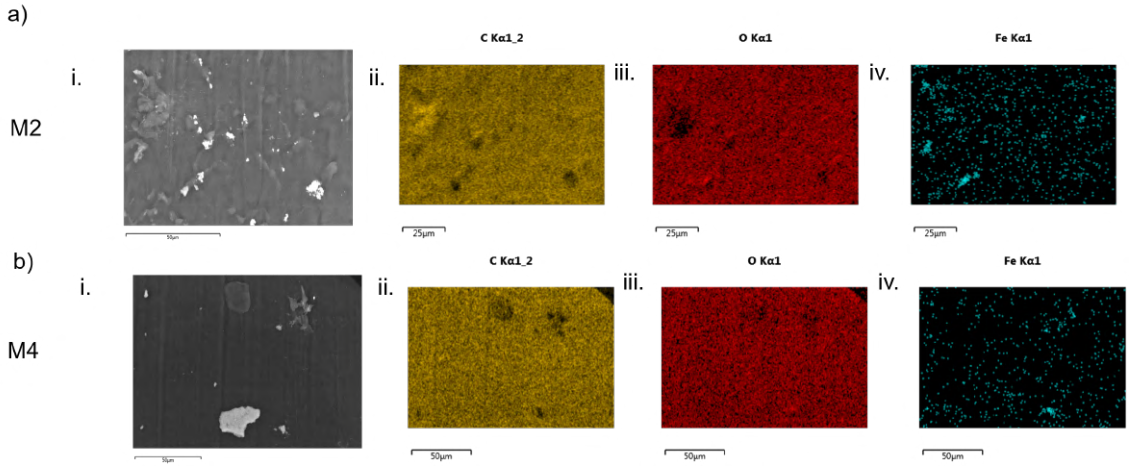

Figure 3.12. SEM images of the PCL polymeric scaffolds M2 (a) and M4 (b): i. Cross section of the biomaterial fiber. Bi-dimensional maps of the ii. carbon (C), iii. oxygen (O) and iv. iron (Fe) signal from the EDS analysis.

parameters of 30 mT and 300 kHz are a reasonable trade-off between heat administration, healthy tissue safety [85, 149], while being in accordance with other literature studies [118, 122, 150]. The fact the MNCs in the scaffold are not homogeneously distributed, as shown in Fig. 3.8, can affect the final heating performances against the residual Osteosarcoma cells, as shown in the 2D SAR and temperature patterns in Fig. 3.10.a and 3.10.b. The average and peak (∼12 and 30 W/g, respectively) SAR values in the MagS are comparable to that reported in the literature [13, 122].

As additional figures of merit, we consider the spatial variation of the temperature along the x- and y-axis and the T50, defined as the iso-temperature that cover at least 50% of the tumor volume, and allows to predict standard hyperthermia treatment quality [84,88,92,183]. From Fig. 3.10.d, it is possible to notice that M1, M2 and STRIP samples would not be capable of reaching the therapeutic range, despite their saturation magnetization and average loading fraction (Tab. 3.2) were promising and comparable to the other samples. However, by considering the MNCs distributions retrieved from THz scans (Fig. 3.8), part of the scaffold volume is not occupied by the MNCs, as supported by the computed magnetization index. By investigating the spatial distribution of the temperature inside the MagS, shown in Fig. 3.10.e and 3.10.f, we can support this assumption by underlining that the temperature gradients for these samples are too narrow and, in an anisotropic fashion, the heat diffusion to the surrounding target residual cancerous cells is not homogeneous. Therefore, during the HT with M1, M2 and STRIP sample, the healthy tissues does not experience overheating (Fig. 3.10.c). Furthermore, by observing Fig. 3.10.d, it is possible to infer that the set of MagS drop-casted with MNC1 particles in a relatively more homogeneous way (Fig. 3.8), i.e., M3, M5 and M6 are promising candidates for performing the hyperthermia treatment of bone tumors. Indeed, after 80 min of treatment, these thermoseeds could reach T50 values of 42±11.8°C, 40.9±1.5°C and 43±1.75°C, respectively. This is a noticeable result, since a reduced hyperthermia potential was expected. However, taking into account the spatial influence of the MNCs distribution, shown in Fig. 3.10.e and 3.10.f, the broader spatial arrangement can ensure a significant therapeutic hyperthermia treatment. On the other hand, the samples PCL FeOx 15 and 16, which presented an annular distribution of magnetic particles with high power losses, are also a valuable solution for administering the heat to the residual Osteosarcoma cells. Indeed, together with the huge void volume in the biomaterial and the observed low magnetization index (Tab. 3.2) the differences in MNCs with different features and the temperature gradients which are kept steep lowering the distance from the target should be taken into account (Fig. 3.10.e, Fig. 3.10.f). It must be noticed that bone and bone marrow can experience a maximum temperature increase of about 37.5±1.3°C, for about 30 min, on average. Bone and bone marrow are in safe conditions, since these tissue damages if exposed to higher thermal doses, i.e. 47°C for 1 min [184,185]. Furthermore, the heat stimulus delivered to healthy bone cells in the range of Fig. 3.10.c is known to be a positive stimulus for accelerating osteogenesis [186,187]. Therefore, from our numerical simulations, the HT with MagS could be effective in enhancing the effectiveness of radio- and/or chemotherapy while initiating new bone formation, thus opening new clinical scenarios for using magnetic scaffolds in orthopedic oncology.

In conclusion, in this chapter, we dealt with the investigation of the effects of the MNPs loading patterns on the HT potential of MagS against bone tumors. In particular, we developed a drop-casting method that allowed us to provide a set of different spatial arrangements of MNPs in a PCL matrix. Then, static magnetic, thermogravimetric and THz tomography characterization was carried out, combining the information in a unique multiphysics, non-linear model to investigate, in silico, the influence of the loading pattern on the quality of the hyperthermia treatment. From

our analysis, we found that together with the intrinsic properties of the magnetic particles, their spatial arrangement in the biomaterial could be sought to perform an effective treatment. It should be pointed out, however, that the heating of the target volume can present a large deviation of the temperature distribution, i.e. an average standard deviation of $\pm 1.5 \circ$C around the therapeutic threshold values (Fig. 3.9.d).

Overall, our investigation can provide valuable feedback and state that the manufacturing of homogeneously loaded magnetic scaffolds is advisable, although, the strategy of loading the outer edges of the scaffold can perform effectively. From our numerical study, to plan hyperthermia treatment with magnetic scaffolds, the loading and spatial distribution of MNCs must be controlled and reconstructed [120, 188, 189]. In this work, we have demonstrated that this crucial information can be extracted using THz tomography. However, despite the numerical investigation, the variability of deposited power and resulting temperature patterns, due to the inhomogeneous distribution of nano-heaters inside the biomaterial, demands for an experimental extensive, rigorous and specific investigation of the magnetic scaffolds SAR, aimed at providing a standardized framework for quantifying the therapeutic potential of these innovative devices [190]. The proposed approaches and our findings could be relevant to material scientists, bioengineers and clinicians who aim to manufacture, characterize, and use magnetic scaffolds as multi-functional tools against, but not limited to, bone tumors.

3.2 TPMS Scaffolds

3.2.1 Introduction

Magnetic tissue scaffolds are a promising powerful tool for performing interstitial tumor hyperthermia against the residual bone cancer cells, after surgical intervention. The design of the implant architecture is crucial for several biomedical requirements. The biomaterial matrix of MagS has been designed for satisfying the TE requirements of the tissue to repair [4, 7–17], however, to date, the influence of implant topology on the hyperthermia treatment outcome has never been assessed. In this section, the aim is to investigate how and if the scaffold architecture can affect the hyperthermic potential of the magnetic scaffolds. In this section, a simple methodology for designing biomimetic scaffolds using triply periodic minimal surfaces (TPMS) is presented. A set of geometries is 3D printed by fused deposition modeling, using a commercial poly-lactic acid filament filled with magnetite particles, never tested for biomedical applications. To the complex morphology and spatial arrangement of the MagS, as pointed out bu the results from our numerical experiments, the distribution of MNPs in the biomaterial can greatly vary. We already discussed this point in the Chap. 1 (Fig. 1.2.g) and showed that the temperature increase, exposure parameters (i.e., field strength and working frequency) and apparatus used for testing of MagS hyperthermic potential are not standardized, as it is the methodology and figure of merits for quantifying their fitness to the quality assurance guidelines [88]. In this regard, the problem of developing a reliable estimation of the heating potential of MagS should be tackled immediately. In particular, the lessons learned from the standardization and reproducibility issues in MFH could be applied to the realm of MagS [190, 191]. With a set of different experimental setup, supported with numerical simulations, in this section, thanks to the fruitful collaboration with the Aristotle University of Thessaloniki, we will face the problem of identifying a suitable protocol for reliably estimating the specific absorption rate (SAR) of MagS.

3.2.2 Related Works

MagS are currently under investigation as a complete tool for orthopedic oncology given their osteogenic features, the tissue engineering potential and the possibility to be used as local heaters for the HT of bone cancers. Despite the plethora of available MagS [4, 7–17], the research efforts were mainly oriented towards the investigation of the material synthesis issues [36], such as in the case of PVDF embedding $CoFe_2O_4$ scaffolds with woven interconnected structure developed using the solvent casting method [192], or toward the proof-of-concept of heating capability when exposed to a RF magnetic field, such as the case of the 90°-fiber mesh 3D printed poly-caprolactone (PCL) scaffold loaded with magnetic hydroxyapatite particles [150]. As a matter of fact, in the open literature, it is difficult to find a study about MagS which combine the orthopedic requirements while carrying out a through and extensive characterization of the hyperthermic potential, while accounting for the influence of the geometrical features.

In clinical practice, the implanted biomaterials is required to have a porous (70-90%) interconnected structure, with biomimetic properties, i.e., it should replicate the bone tissue architecture in order to favor implant integration as much as possible [5, 31]. Natural bone has complex and irregular pores with surface morphology and size distribution [193]. To mimic this features, the state-of-the-art scaffolds are designed and manufactured relying on mesh-fiber geometries, squared cells, or, with enhanced biomimetic features, using implicit surface, such as Triply Periodic Minimal Surfaces (TPMS) [193]. Indeed, the use of implicit surfaces bone scaffolds has the advantages of providing large and complex topological structures [193]. Furthermore, TPMS-based scaffolds demonstrated increase permeability to body fluids and nutrients ($10^{-8}\,m^2$ vs. an average of about $10^{-9}\,m^2$) [194]. The mechanical properties of TPMS architecture resulted in an effective elastic modulus higher than the standard counterparts (e.g., fiber mesh) [195], for lower porosity values, while ensuring a better stress distribution [196, 197]. All these features made the TPMS architecture very appealing for developing bone scaffolds [195–197].

In this framework, given the forecasted application of using TPMS MagS as devices for performing HT of bone tumors, it is mandatory to assess the influence of the geometry on the local heating administration.

Another relevant literature gap, is the spread, different and non standardized methodology for testing the heating potential of MagS. To push the forefront towards new clinical landscapes, a more definitive takeoff of this nanotherapy against tumors is required. Therefore, it is fundamental that MagS must satisfy the minimum quality assurance requirements of the interstitial hyperthermia treatment [88]. In other words, a given MagS should be capable of increasing the system temperature to the therapeutic level of 41-45°C and deposit at least 0.5 W/g in the implant volume in response to an AC RF MF against deep-seated tumors [25, 66, 89]. We are going to demonstrate that in the literature the methodology is largely variable, with a spread variety of experimental setup and conditions, in which different thermometric methods are used without accounting for uncertainty. For instance, the calorimetric characterization of samples of Poly-MetilMetAcrilate (PMMA) embedding Fe_3O_4 particles was carried out by recording with an infrared camera the temperature of the saline-sample system (with variable volume from 0.1 mL-0.2 mL), exposed to a magnetic field [198]. A variability of ±4.3°C from the maximum recorder temperature. In [198], issues in the repeatability due to sample placement inside the coil are evident. The misalignment of thermoseed implants to the external heating device is a relevant aspect in temperature and power losses estimation [190, 191, 199]. For the P_2O_5-Fe_2O_3-CaO-SiO_2 ferromagnetic glass ceramic system for bone tumor hyperthermia a 0.263 W/g value was estimated by using the linear slope method [200], at 100 kHz, under the action of a 0.5 mT magnetic field, produced by a custom coil apparatus [26]. The hyperthermia potential characterization was carried out on in a test tube, filled with deionized water, recording the temperature every 60 s for 3 min with a fiber thermometer. The 2-3 mm in diameter and 0.9 g samples of apatite wollastonite, heat-treated glass ceramic (29% CaO, 31% SiO2, 40% Fe_20_3, 3% BzO_3 and 3% P_20_5 (wt%)) synthesized by the group of Kokubo were implanted in rat tibial metaphysis and then characterized under the action of a 100 kHz, 30 mT external

magnetic field produced by a C-type toroidal core of an induction generator [25]. The heating ability of the glass-ceramic implants was assessed through fluoroptic thermometers, which recorder a maximum temperature at the center of the thermo-seed equal to 45°C in 50 min, resulting in an estimated SAR of 10 W/g. The temperature variability in the rat tibia was of about ±5°C in the extra-cortical regions, indicating a large variability due to the temperature probe positioning [25]. Calorimetric measurements with a magnetic induction furnace of sol-gel Calcium Zinc Iron Silicon Oxide (CZIS) samples were performed [201,202]. The measurements were carried out by placing 2 g of glass ceramic, with ferromagnetic $ZnFe_2O_4$ particles, in 20 ml deionized water in a quartz cuvette, positioned in the center of the coil. The maximum temperature rise, recorded with a thermocouple (having resolution of 0.1°C), starting from 24°C, was of minimum 29°C to a maximum of 39°C in 3 min under the action of a 50 mT magnetic field working at 100 kHz. The estimated SAR varies in the range 5-9 W per gram of sample [202]. The 3D-printed, superparamagnetic PCL scaffolds embedding MBG and magnetite nanoparticles where manufactured and characterized as tissue substitutes, drug delivery systems and hyperthermia agents [49]. The magnetic MBG-PCL, when exposed to a 409 kHz and 18 mT magnetic field (DM100 System - nB nanoScale Biomagnetics, Spain) demonstrated capable of increasing the temperature of 1 ml of water up to 60°C, starting from 20°C, for 8 min-15 min of exposure [49]. The temperature was recorded with an optical fiber, but the details about its placement and the influence on the measurement was not reported. It is worth stressing that the external field was not turned off to investigate the effective heating and the contribution of the background media was not considered. Under these experimental conditions, the derived SAR varied from 1.4 to 4.7 W/g. The effect of the variability of experimental setup, combined with the neglection of uncertainty sources, is evident by the reported 5-30 W/g SAR values, obtained for the weakly superparamagnetic tri-calcium phosphate (β-$Ca_3(PO_4)_2$) co-substituted with Fe^{3+}-Co^{2+}2 ions thermoseeds exposed to a 335 kHz and 13.5 mT magnetic field, in 1 mL of distilled water, for 40 min (ΔT of 12-22.5°C, starting from 26°C, measured with a copper thermocouple) [122]. More recently, the calorimetric response of injectable graphite-modified Fe_3O_4-calcium phosphate bone cement scaffolds (blocks of 9 mm x 4 mm) of Zhang et al. was tested under the action of a 340 kHz, 10 mT magnetic field, SAR values of 18.75-30.20 W/g were obtained from the temperature increase after 200 s, acquired by means of an infrared thermometer [203,204].

From this discussion, a dedicated, extensive and thorough experimental and numerical analysis aimed at elucidating how to perform the SAR estimation of MagS is required.

3.2.3 Scaffold Architecture

TPMS is a surface embedded on $\mathbb{R}^3$ which is minimal, i.e., present a medium curvature equal to zero, and it is periodic on the three directions x, y and z. Typically, TMPS can be modelled by using the Enneper-Weiestrass parametric representation [205–207]. Mathematically speaking, the surface is constructed by composing patches computed with integrals in the complex domain. Among the different approaches for generating the TPMS coordinates, the parameterization of

Table 3.3. Surface and associated function

Surface	**Function** (F)
P	$\cos(X)+\cos(Y)+\cos(Z)=k$
D	$\cos(X)\cos(Y)\cos(Z)-\sin(X)\sin(Y)\sin(Z)=C_0$
G	$\sin(X)\cos(Y)+\sin(Z)\cos(X)+\sin(Y)\cos(Z)=C_0$
I-WP	$2[\cos(X)\cos(Y)+\cos(Y)\cos(Z)+\cos(Z)\cos(X)]-[\cos(2X)+\cos(2Y)+\cos(2Z)]=C_0$
L	$0.5[\sin(2X)\cos(Y)\sin(Z)+\sin(2Y)\cos(Z)\sin(X)+\sin(2Z)\cos(X)\sin(Y)]$ $-0.5[\cos(2X)\cos(2Y)+\cos(2Y)\cos(2Z)+\cos(2Z)\cos(2X)]+0.15=C_0$

these kind of surfaces in the complex domain is not a straightforward and suitable approach for the computational representation [208]. Indeed, in the Euclidean space, the TMPS can be approximated by an implicit function, i.e. as a level surface (isosurface) of a function $F:\mathbb{R}^3\rightarrow\mathbb{R}$, which is a combination of sinus and cosine. The most famous and useful functions for generating TMPS for biomedical applications are reported in Tab. 3.3, where $X=w_x x$, $Y=w_y y$ and $Z=w_z z$, being w_x, w_y and w_z are the spatial periods and C_0 is a constant.

TPMS possess two important mathematical properties: minimality and periodicity. For a computationally efficient Computer Aided Design (CAD) it is of relevance to discuss them. A pivotal results is the minimality of TPMS. In order to verify this feature the mean curvature for surfaces in implicit form can be used [209]

$$K_M=\frac{\nabla(F)H(F)\nabla(F)^T-|\nabla(F)|Trace(H)}{|\nabla(F)|^3} \tag{3.5}$$

where $\nabla(F)$ is the gradient, $H(F)$ is the Hessian matrix and $Trace(H)$ is the trace of $H(F)$ of the arbitrary function F from Tab. 3.3. Minimality ensures very good mechanical properties and a stiffness suitable for orthopedic applications, while minimizing the amount material used for the scaffold manufacturing (e.g., in 3D printing or sintering). The other relevant mathematical property is periodicity. Indeed, since TMPS are level surfaces of harmonic functions, they inherit their periodicity in a given domain. The periodicity simplifies noticeably the computation and the repetition of a unit cell to develop a solid from TPMS, allowing to extend it indefinitely in space.

However, to date if and how minimality and periodicity can affect functional performances, such as heating and SAR has been poorly investigated.

Since the surgical resection of bone tumors leave a gap, which must be filled with the scaffold, it is necessary to provide the implant in a suitable shape, in order to simplify and adapt the scaffold to the surgically treated bone boundaries. In previous studies it was shown that it is possible to design a solid from TPMS within a shape of arbitrary boundaries starting from the deformation of a parallelepiped [193, 210]. From a mathematical point of view, this implies that a continuous function f_t from the defected bone boundaries to the parallelepiped exists. Supposing that the defect shape can be approximated to a cylinder, which is fit to long bones, the transformation law is $f_t:\mathbb{R}^3\rightarrow\mathbb{R}^3$ and can be expressed as

$$(x,y,z) \mapsto \begin{cases} (0,0,z) & x^2+y^2=0 \\ \left(\frac{x\max\{|x|,|y|\}}{\sqrt{x^2+y^2}}, \frac{y\max\{|x|,|y|\}}{\sqrt{x^2+y^2}}, z\right) & x^2+y^2\neq 0 \end{cases} \tag{3.6}$$

An example of the transformation using Eq. (3.6) is shown in Fig. 3.13. The transformation is necessary since usually the computational domain is $[x_0,x_1]\times[y_0,y_1]\times[z_0,z_1]$. Eq. (3.6) can be applied directly to a TPMS, as shown in Fig. 3.13. The output is a surface, not a solid. Therefore, it is necessary to create a volume. In other words, an unclosed implicit surface can be closed only if one or more intersecting surfaces can be found, which is the utmost issue for the structuring of a curved surface in three-dimensional space.

By using the software Matlab 2019b (The MathWorks Inc., Boston USA), the *"TPMS Scaffold"* application was developed for deriving TPMS scaffolds [211]. Given a TPMS surface with law F from Tab. 3.3, it is possible to generate a solid volume by creating two offset surfaces, an inner and an outer one, which must be linked and closed to form the final solid, porous biomimetic architecture for bone tumor treatment. The proposed graphic user interface (GUI) allows to choose among the TPMS from Tab. 3.3, compute the two offset surfaces by using the *"isosurface"* function and derive the final solid in *".stl"* format [212]. To respect the minimality and speed up the computation, instead of working on each mesh polygons, we select two constants $C_1 > C_2$ and a height $0 < h < 1$. The inner surface is $F(x,y,z) = C_2$, whilst $F(x,y,z) = C_1$ is the external one, as shown in Fig. 3.13.c. In order to derive the solid, the surface junction between them at the height h is the set of points which satisfies the inequality $C_2 < F(x,y,z) < C_1$. The set of surface boundary points is triangulated [193] and the convex hull is found for the inner and outer surface, then, the redundant, intersecting and non-manifolds triangles are removed and the closing surfaces are found, as shown in Fig. 3.13.c. Thus, the solid TPMS-based scaffold with a cylindrical bone-fit shape is obtained, as shown in Fig. 3.13.d.

3.2.4 Materials and Methods

3.2.4.1 Magnetic Iron PLA

The commercial magnetic-polymer composite filament Magnetic Iron PLA purchased from Proto-Pasta was used to print the magnetic thermoseeds samples. The filament consists of a nominal 40 wt.% of iron microparticles ($\sim$40 μm in size) loaded in a polylactic acid (PLA) polymer matrix (NatureWork's 4043D Ingeo Biopolymer) [213–215].

3.2.4.2 Fused Deposition Modeling

The sample geometry was checked using Rhinoceros v7 (McNeel, Canada) modeling software, then the IdeaMaker software was used to derive the stereolithography (STL) files and the g-code for printing them with the Raise3D Pro2 Plus 3-D printer. The extrusion temperature was set to 210°C for the 0.45 mm nozzle, with a 100% infill density and a 50 mm·s^{-1} printing speed. The

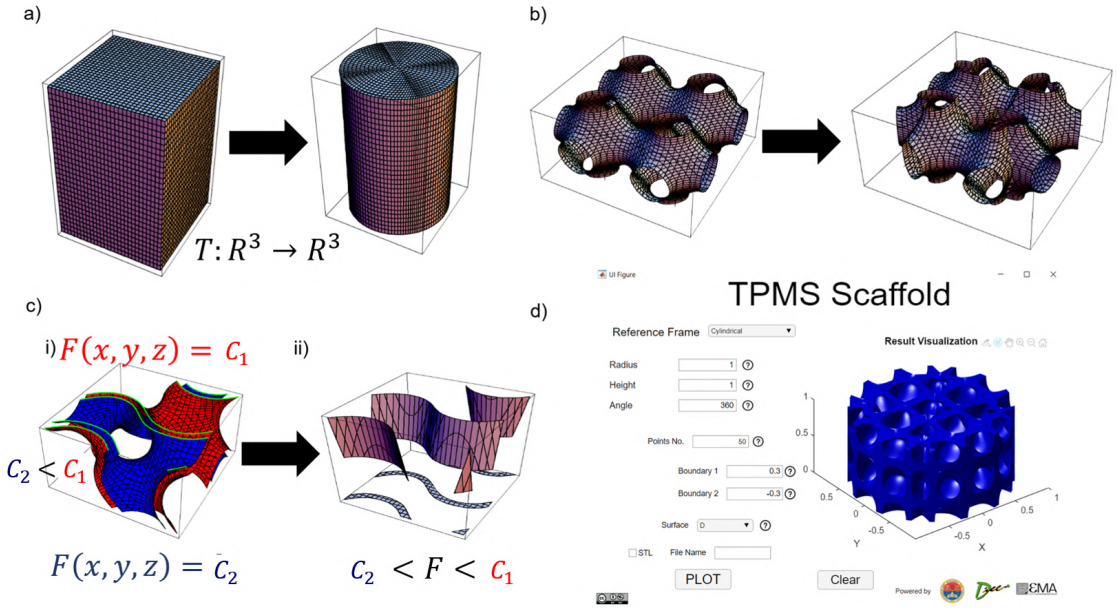

Figure 3.13. Description of the steps for deriving scaffolds based on solid triply periodic minimal surfaces (TPMS) architecture: a) Transformation of the parallelepiped frame into cylinder: the two objects have the same height while the parallelepiped base, a square with side l, is transformed into a circle with l/2 radius. b) Transformation applied to a P-surface in $[-1,1]^2 \times [0,1]$. c) i. The inner and the external G-Surface plotted in $[0,1]^2 \times [0,1/2]$. ii. Closure surfaces and borders of the sections (green curves). d) Example of the developed GUI: final solid scaffold based on a D-surfaces.

.

Table 3.4. Resume of TPMS MagS Properties

Sample	**Geometry**	**Avg. Pore Size** (μm)	**Ferromagnetic** (Y/N)	**Weight** (g)
S1	90°-SF^2	0.35	N	2
S1f	90°-SF	0.35	Y	3.7
S2, S3	G surf.	0.3	N	0.85
S2F, S3F	G surf.	0.3	Y	1.42
S4, S5	L surf.	0.32	N	2.18
S4F, S5F	L surf.	0.32	Y	3.2

bed temperature was set to 45°C. As a reference geometry, we printed a standard 90°-shifted mesh scaffold (S1, S1F). We printed two G-surface (S2, S3, S2F, S3F) and two L-surface (S4, S5, S4F, S5F) scaffolds, having size 1.8 cm × 1.8 cm × 2.5 cm, using non-magnetic and iron-filed PLA. A summary of their geometrical features is provided in Tab. 3.4. The samples are shown in Fig. 3.15.a.

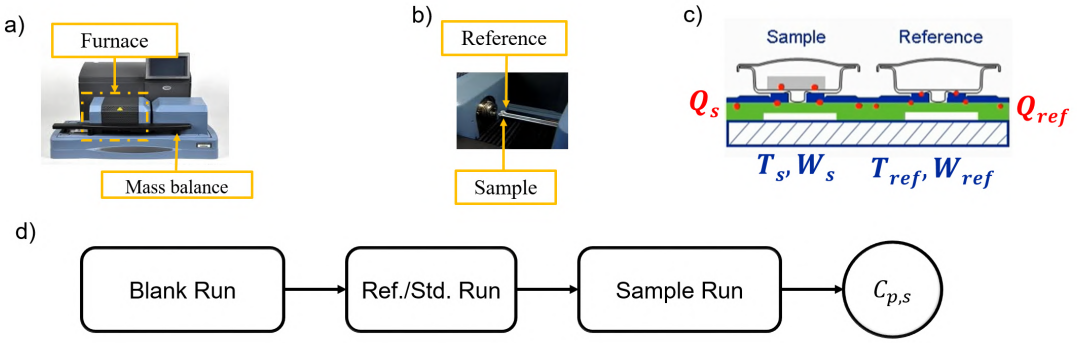

Figure 3.14. a) Experimental apparatus for the thermal measurements. b) Details of the reference and sample pans. c) Schematic description of the heat fluxed and signal recorder during measurements. d) Workflow for measuring the specific heat capacity according to the ASTME1269-11 standard.

3.2.4.3 Static Magnetic Measurements

Magnetic hysteresis loops of the magnetic filament were recorded at 300 K using an Oxford Instruments 1.2H/CF/HT Vibrating Sample Magnetometer (VSM), for magnetic field strengths ranging from -1 to 1 T. These measurements were performed at Aristotle University of Thessaloniki.

3.2.4.4 Thermogravimetric Analysis and Specific Heat Measurement

The simultaneous Differential Scanning Calorimeter (DSC)-Thermogravimetric (TGA) analyzer Q600M (TA, New Castle, DE) was used to quantify the thermal stability and the content of magnetic phase in the filament after thermal degradation [168, 172, 173, 213, 216]. A 40 μl alumina pan was used as a sample holder. The same type of alumina pan is employed as reference material during the differential measurement. The initial temperature was 20°C. The protocol consists of a heating ramp with a slope of 20°C·min^{-1} up to the final temperature of 1000°C. The temperature values at different mass percentage (T20%, T50%, T90%) are considered. The first derivative of the weight vs. temperature was investigated for the thermal degradation analysis. From the DSC-TGA analysis, the content of the magnetic phase dispersed in the polymeric matrix is analyzed and used as information to complement the estimation of dissipated power during the hyperthermia treatment.

In order to simulate and gain insights into the heat transfer phenomena occurring during the HT of bone tumors, performed using the commercial magnetic filament under analysis, we characterized the filament in terms of its specific heat (C_p). Indeed, the thermal conductivity of the Proto-Pasta filament was measured in [213] and a value of ∼0.47 W·m^{-1}K^{-1} was reported. In this framework, we adopted the measurement methods from the ASTME1269-11 standard [217], as done in [218]. A summary of the procedure is given in Fig. 3.14. In detail, we performed a blank run and recorded the mass (W_0, in g) and heat (Q_0, in W·g). Then a reference run with alumina standard

was performed, acquiring the W_{ref} and Q_{ref} signals. The specific heat of alumina ($C_{p,ref}$) is known [217]. This step is necessary for the baseline removal. Finally, a run with the magnetic sample, placed in good contact with the pan, was carried out by heating the sample from 15°C to 70°C. All measurements were performed using a heating rate of 10°C/min. The specific heat of the sample ($C_{p,s}$, in $J \cdot g^{-1}K^{-1}$) is found as [217,218]

$$C_{p,s} = C_{p,ref} \frac{Q_s - Q_0}{Q_{ref} - Q_0} \frac{W_{ref}}{W_s} \tag{3.7}$$

3.2.5 The Proposed Protocol for the Specific Absorption Rate Measurement

3.2.5.1 Experimental Setup

As discussed in the introduction, several works dealt with the experimental characterization of the hyperthermic potential of magnetic scaffolds for bone tissue engineering [150]. However, taking a look into the methodologies, conditions and setup used for the calorimetric measurements of these kind of solid samples embedding magnetic particles, it is possible to underline that the good practices, recommendations and standardization developed for MNPs characterization were neglected or scarcely adopted [190,191,219]. However, MagS, being implantable medical devices to be used as heat source in the interstitial hyperthermia treatment of bone tumors, must follow the recently released requirements for quality assurance in interstitial hyperthermia [88]. Therefore, more robust, accurate and in depth characterization is required.

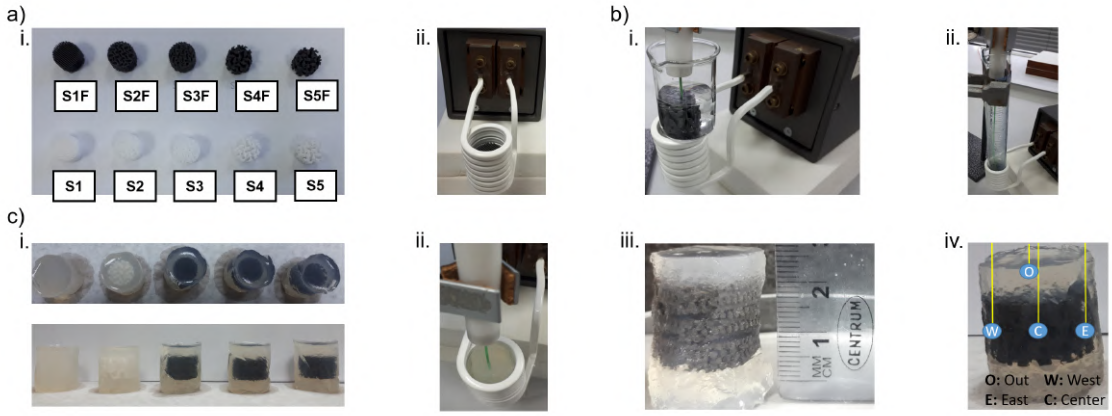

Figure 3.15. a) i. Optical image of the Fe-PLA Proto-Pasta magnetic scaffolds with TPMS architecture. ii. In-air or free space setup: experimental induction heating apparatus and sample placement. b) i. Sample placed in a becker filled with distilled water, outside the induction heating coil. ii. Sample placed in distilled water inside the induction heating coil. c) Top-view of the agar phantom-scaffold systems. ii. Side view of the agar phantom-scaffold systems. iii. Dimensions of the agar phantom. iv. Details of the measurements site inside the sample and in the agar phantom .

All samples from Fig. 3.15.a were placed in the middle of an 8-turn coil. Instead of applying a radiofrequency magnetic field and deriving the specific absorption rate (SAR) from the initial-slope method, we followed the strategy from [190, 220], in order to reduce the uncertainties due to measuring conditions and experimental setup. Therefore, the envelope of the external magnetic field is turned-off at a given time in order to allow the thermal recovery of the system, thus permitting to subtract the contribution of the environment [190, 220]. Coil cooling water temperature was kept stable at 18.9°C during whole experimental procedure. Three different experimental setup were considered. First, the 3D printed TPMS scaffold was exposed to the induction heating system in air. An infrared (IR) camera (FLIR i3, FLIR Systems, USA) was used to acquire images, from which the average sample temperature is derived.

Then, the magnetic scaffold was placed in distilled water, as shown in Fig. 3.15.b. Approximately 5 mL of distilled water was used as the solution medium. The field amplitude was increased to 30 mT and the working frequency was 400 kHz. Five symmetrical holes were opened to place the optical fiber for temperature recording (Fig. 3.15.b).

Finally, the printed magnetic scaffolds were placed in an agarose ($10\,\mathrm{mg{\cdot}ml^{-1}}$) phantom system, as shown in Fig. 3.15.c. The phantom agar is supposed to better mimic the biological environment [190]. Pure agar and the sample S4 were used as references.

3.2.5.2 Numerical Model

Given the extensive characterization of TPMS magnetic scaffolds, we developed a numerical framework for simulating the multiphysics phenomena related to the calorimetric measurements. In this framework, we aim to corroborate the experimental findings and refine the problem of modeling these functional biomaterials, thus paving the way for coping with the issue of planning the treatment with these innovative devices [88, 117, 118, 166, 167]. To this aim, a simplified geometry was assumed.

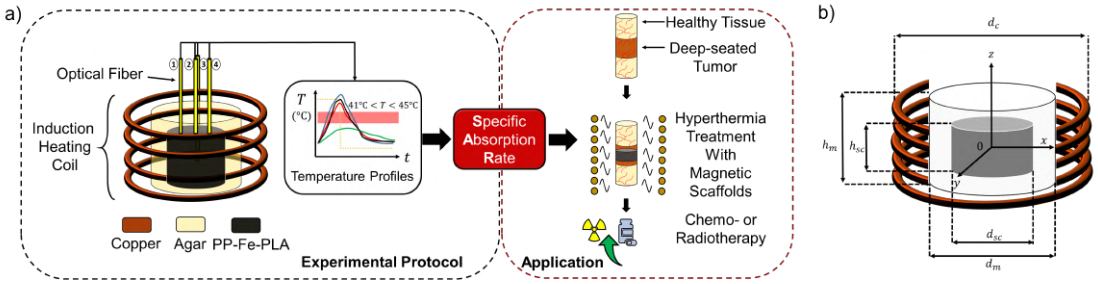

Figure 3.16. a) Sketch of the proposed experimental protocol for assessing the specific absorption rate (SAR) of biocompatible magnetic scaffolds to be used as implants for local, interstitial hyperthermia treatment of deep-seated cancers. b) System geometry for the numerical simulations of the different experimental setup for the calorimetric characterization of magnetic scaffolds. The heating system has conductors mad of copper, whilst the light grey cylinder represent the surrounding medium (i.e., air, water or agar) and the dark grey cylinder is the 3D-printed magnetic Fe-PLA scaffold.

Table 3.5. Material Properties

Material	ϵ_r	μ_r	σ ($\mathrm{Sm^{-1}}$)	k ($\mathrm{W{\cdot}m^{-2}K^{-1}}$)	C_p ($\mathrm{J{\cdot}kg^{-1}K^{-1}}$)	ρ ($\mathrm{kg{\cdot}m^{-3}}$)	**Ref.**
Air	1	1	0	-	-	-	[94]
Agar	70	1	0.2	0.48	4000	100	[221, 222]
Copper	-	1	$5{\cdot}10^{7}$	-	-	-	[94]
PLA	2.5	1	10^{-6}	0.29	1.800	900	[223]
Fe-PLA	3	8	10^{-5}	0.47	∼1.200	2745	[213–215]
Distilled Water	76	1	$5{\cdot}10^{-6}$	0.57	4.2	1050	[94]

The finite element method (FEM) commercial software Comsol Multiphysics v5.5 (Comsol Inc., Burlinghton, MA USA) was used to simulate the experimental setup for the specific absorption rate measurements, in the case of a homogeneous cylindrical scaffold made with the Proto-Pasta magnetic PLA (Fig. 3.16.a). The geometry for the simulations is shown in Fig. 3.16.b. A homogeneous cylindrical scaffold, made with the Fe-PLA, with magnetic permittivity μ_r and dielectric permittivity ϵ_r, was considered. The properties are reported in Tab. 3.5. The cylinder has diameter $d_{sc} = 2\,\mathrm{cm}$ and height $h_{sc} = 2\,\mathrm{cm}$. The induction heating coil is excited with a sinusoidal current (I_{exc}), working at a frequency f, which is turn on at $t = 0$ and turned-off at t_{off}. The Ampere's law, in the time-harmonic field formulation, govern the electromagneto-thermal problem, i.e.

$$\nabla \times \mathbf{H} = \mathbf{J} \tag{3.8}$$

$$\mathbf{E} = -j\omega\mathbf{A} \tag{3.9}$$

$$\mathbf{J} = \sigma\mathbf{E} + j\omega\mathbf{D} + \mathbf{J_e} \tag{3.10}$$

$$\nabla\mathbf{A} = \mathbf{B} \tag{3.11}$$

where $\mathbf{A}$ is the magnetic vector potential, $\mathbf{H}$ is the magnetic vector ($\mathrm{A{\cdot}m^{-1}}$), $\mathbf{E}$ is the electric field vector ($\mathrm{Vm^{-1}}$), whilst σ is the electrical conductivity (in $\mathrm{S{\cdot}m^{-1}}$), $\mathbf{J}$ is the current density ($\mathrm{A{\cdot}m^{-2}}$). The time-dependence from $e^{j\omega t}$ was omitted in Eq. (3.11). The term $\mathbf{D} = \epsilon_0\epsilon_r\mathbf{E}$ is the electric displacement field ($\mathrm{C{\cdot}m^{-2}}$). In Eq. (3.11), $\mathbf{J_e}$ is the external current density. The electromagnetic problem was solved making use of the *AC/DC module*, with the aid of the *Magnetic Field* interface, working in the frequency domain, under the assumption of a quasi-static process [220]. The solution of the Maxwell's' equation through the vector potential formulation allows to compute the magnetic field produced by the 8-turn copper coil (diameter $d_c = 2.54\,\mathrm{cm}$, height $h_c = 4.3\,\mathrm{cm}$, coil wire diameter $d_sc = 0.53\,\mathrm{cm}$) inside the sample and the background media, which can be air, or water or agar (see Fig. 3.16.b). The power dissipated by the ferromagnetic scaffolds (P_m) is evaluated as

$$P_m = fA_{hyst} \tag{3.12}$$

where A_{hyst} is the hysteresis loop area, derived from static magnetic measurements, and scaled by the specific density of the sample. Eq. (3.12) is proportional to the mass of the Fe-PLA sample. The term P_m is higher than the power dissipated due to the eddy currents in the ferromagnetic and in the agar material ($P_e = \frac{1}{2}\sigma|\mathbf{E}|^2$). However, the heating in the phantom cannot be neglected, being relevant to the measured temperature and the estimated SAR.

The total electromagnetic power ($P_{EM} = P_e + P_m$) dissipated by the ferromagnetic scaffold is used as source term for a generalized unsteady Fourier's equation [190], from which the spatial and temporal dynamics of the temperature field inside the sample are computed. In mathematical terms

$$\rho C_p \frac{\partial T}{\partial t} = \nabla \cdot (k \nabla T) - \mathbf{u} \cdot \nabla T + P_{EM} \tag{3.13}$$

where ρ is the material density ($\mathrm{kg{\cdot}m^{-3}}$), C_p is the specific heat capacity ($\mathrm{J{\cdot}kg^{-1}K^{-1}}$), whilst k is the thermal conductivity ($\mathrm{W{\cdot}m^{-2}K^{-1}}$). The physical properties of the samples are reported in Tab. 3.5. The *Heat Transfer in Solid* module was used to solve Eq. (3.13).

In the general heat transfer balance Eq. (3.13), $\mathbf{u}$ is the convective velocity field vector ($\mathrm{m{\cdot}s^{-1}}$). The form and nature of this term depends upon the experimental conditions. Therefore, a clarification is in order. To replicate in silico the thermographic measurements performed in air (Fig. 3.15.a), and in the case of the in-agar setup (Fig. 3.15.c), the external boundaries of the sample or agar can exchange heat by convection with the surrounding air ($T_a = 20°\mathrm{C}$), i.e.

$$-\mathbf{n} \cdot \nabla T = h_{air}(T - T_a), \tag{3.14}$$

being $\mathbf{n}$ the normal vector, exiting the surface. The heat transfer coefficient (h_{air}) is derived from the cooling phase of the experimental heating curves. As a result, the heat transfer problem for the free space and in-agar experimental setups (Fig. 3.15.a and 3.15.c) was modeled as an unsteady conduction problem, thus implying that

$$\mathbf{u} = 0 \quad \forall\, x, y, z \tag{3.15}$$

Instead, for MagS placed in distilled water, as shown in Fig. 3.15.b, the heat transfer problem was assumed to be non-linear by taking into account the convective motion due to the temperature gradients in the system ($\mathbf{u} \neq 0$). Therefore, the Navier-Stokes' equation was solved [224, 225]

$$\frac{\partial \mathbf{u}}{\partial t} + \rho(\mathbf{u} \cdot \nabla)\mathbf{u} = \nabla \cdot \left[-P\mathbf{I} + \eta(\nabla \mathbf{u} + (\nabla \mathbf{u})^T) - \frac{2}{3}\eta(\nabla \cdot \mathbf{u})\mathbf{I}\right] = 0 \tag{3.16}$$

$$\rho \frac{\partial \mathbf{u}}{\partial t} + \nabla \dot{(}\rho \mathbf{u}) = 0 \tag{3.17}$$

where η is the dynamic viscosity (equal to 1 cP for water) and $\mathbf{I}$ is the identity matrix. Eq.(3.17) is subject to the following open boundary condition at the water-air interface

$$-\mathbf{n}\cdot\mathbf{u}=0, \tag{3.18}$$

and a no-slip condition at the inner surfaces of the larger cylinder shown in Fig. 3.16.b, so that

$$\mathbf{u}=0. \tag{3.19}$$

The *Laminar Flow* interface was used to implement Eq. (3.17). Eq. (3.17) is solved coupled to the Eq. (3.13).

For the last setup (Fig. 3.15.c), the simulated temperature field is used to compute the SAR as [190]

$$SAR=\frac{w_a}{w_{sc}}C_p\frac{\Delta T}{\Delta t} \tag{3.20}$$

where w_a and w_sc are the weight of the agar and of the MagS, whilst the specific heat is that of the agarose phantom. The term $\frac{\Delta T}{\Delta t}$ is the initial slope of the heating curve.

3.2.6 Findings and Recommendations

From the magnetization versus magnetic flux density curve shown in Fig. 3.17.a, it is possible to notice that the magnetic filament presents a relatively small coercive force of ∼12.5 mT, with a small loop, similar to soft ferromagnets, and a saturation magnetization (M_s) of about 126 $\mathrm{Am^{-2}kg^{-1}}$. M_s indicates the amount of iron to PLA in filament, considering that bulk iron's M_s is 220 $\mathrm{Am^{-2}kg^{-1}}$. This finding is also in perfect agreement with the magnetic response data of the filament and of 3D printed items with 1-2 layers, a 100% infill density reported by [214]. The amount of magnetic phase and the distribution along the fiber were assessed by DSC-TGA and microscopy. Indeed, from Fig. 3.17.b, it is possible to notice a 50% primary loss at a temperature of about 303°C which corresponds to the thermal degradation of the PLA matrix [172,173], as confirmed by the analysis of the first derivative of the sample weight with respect to the temperature. The residual mass at 600°C is about 45.67% of the initial weight, which correspond to the amount of non-organic crystalline phase of the iron in the filament, observed also in SEM images (Fig. 3.17.d-3.17.f).

In Fig. 3.17.c the specific heat of the magnetic polymer is shown. In the temperature range typical of the HT of bone tumors with magnetic scaffolds [118], the composite material is capable of storing an energy per amount of mass and temperature of about 1.24 $\mathrm{Jg^{-1}K^{-1}}$, on average, which is approximately the value estimable assuming a linear, volumetric mixing between magnetite and PLA (∼4.8% difference). In this work the quadratic temperature dependence of the physical properties, given a variation of -0.6%·°$\mathrm{C^{-1}}$, is neglected in the simulations to solve a linear problem and hence lower the computational burden.

The temperature versus time curves acquired by IR thermography for the five magnetic scaffolds (and their nonmagnetic counterparts), in air, exposed to a 15 mT magnetic field, working at 400 kHz, are reported in Fig. 3.18.a. The bare PLA samples do not heat up, given the low conductivity

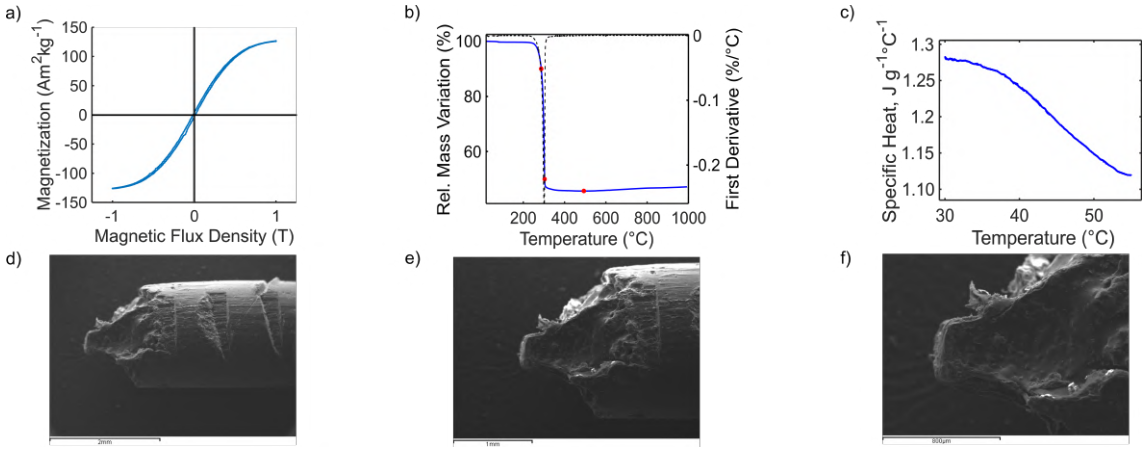

Figure 3.17. a) Magnetization ($Am^{-2}kg^{-1}$) of the Iron-PLA Proto-Pasta filament, before printing, as a function of the external applied magnetic flux density field (T). The residual magnetic flux density is about 12.5 mT and the saturation magnetization is $\sim$126 $Am^{-2}kg^{-1}$. b) Thermogravimetric analysis (TGA) of the Fe-PLA Proto-Pasta filament, in the range 20°C-1000°C. The normalized weight (%) and the first derivative over temperature are presented. c) Specific heat ($Jg^{-1}C^{-1}$) of Fe-PLA Proto-Pasta filament in the temperature range 30-60°C. d)-f) Scanning Electron Microscope (SEM) images of the Iron-PLA Proto-Pasta fibers at different magnifications.

(see Tab. 3.5), but tend to equilibrate their temperature with air. Furthermore, it is possible to notice that the maximum temperature is about 56.5±1.5°C and it is reached in about 55±5 s, for S3F, S4F and S5F samples. Between the standard 90-°-shifted mesh magnetic scaffold (S1F) and the TPMS architectures differences in the peak temperatures and in the cooling rate with the surrounding medium can be observed in Fig. 3.18.a. Furthermore, the simulated time evolution of the average temperatures for a homogeneous cylindrical magnetic scaffolds is very similar to that of scaffolds S1F, as shown in Fig. 3.18.a. The discrepancy between the numerical simulations and the temperature profiles of TPMS MagS is probably due to the geometric features and the sample porosity.

From the findings of Fig. 3.18.a, the Proto-Pasta ferromagnetic filament looks very promising for magnetic hyperthermia application. However, this experimental configuration is not very representative of the in vitro or in vivo-like thermal and electromagnetic environment experienced during the interstitial hyperthermia treatment (Fig. 3.16). Therefore, we placed the magnetic scaffolds samples inside 5 mL of distilled water, (Fig. 3.15.b) in a glass container, and recorder the temperature by placing an optical fiber at the top surface of the material opening the five holes shown in Fig. 3.15.b. With respect to the in-air setup, the field amplitude was increased to 30 mT in order to reach the same temperatures. The measured temperature profiles are reported in Fig. 3.18.b. The reference architecture S1F can heat up the water to 56±2°C. The simulated temperature profile for the non-linear heat transfer of the homogeneous ferromagnetic cylinder exposed to the RF magnetic field are very similar to that of S1F sample, as shown Fig. 3.18.b. From the modified law of cooling, and taking into account the response of the environment, we can

notice that the L-surface scaffold (S4F) can reach the maximum temperature of 59°C in ∼200 s, whilst the gyroid architecture (S2F) could raise the temperature to 45°C. The heating and cooling rate are faster for S2F and S1F, if compared to S1F and the simulated homogeneous case. The fact that the TPMS architecture experience a different heat transfer regime is also epitomized by the comparison of the temperature pattern of SF4 sample placed just outside the coil (see Fig. 3.15.b). Even though the convective motion of water is considered, the numerical simulations fails in reproducing the experimental results.

From Fig. 3.18.b, all ferromagnetic scaffold samples succeeded to surpass the hyperthermia temperature limit within 10 min or earlier. However, from this calorimetric measurements, we can infer that the heating efficiency varies due to material quantity. Indeed, by weighting the samples we could better explain the heating behavior, since S1F, S2F and S4F weight 3.7 g, 1.4 g and 3.2 g, respectively (Tab. 3.4). Furthermore, additional uncertainty about the temperature values may arise from the temperature probe placement. Therefore, it is worth noting that the SAR values can be estimated after standardizing the experiment. Hence, given these findings in this setup, we must underline the selection of the most promising architecture requires additional study.

To the aim of refining the experimental condition for assessing the hyperthermic potential of ferromagnetic TPMS scaffolds, we used agarose gel as a medium to mimic the electromagnetic and heat transfer environment of biological tissues. As shown in Fig. 3.15, for lowering the influence of the probe placement on the measured temperature, five different optical fibers positions were selected in order to provide more reliable temperature and SAR results. The measured temperatures in the five locations inside the sample and the agar phantoms, for each ferromagnetic scaffold, are reported in Fig. 3.19. A large variability of the peak temperature in the sample is noticed:

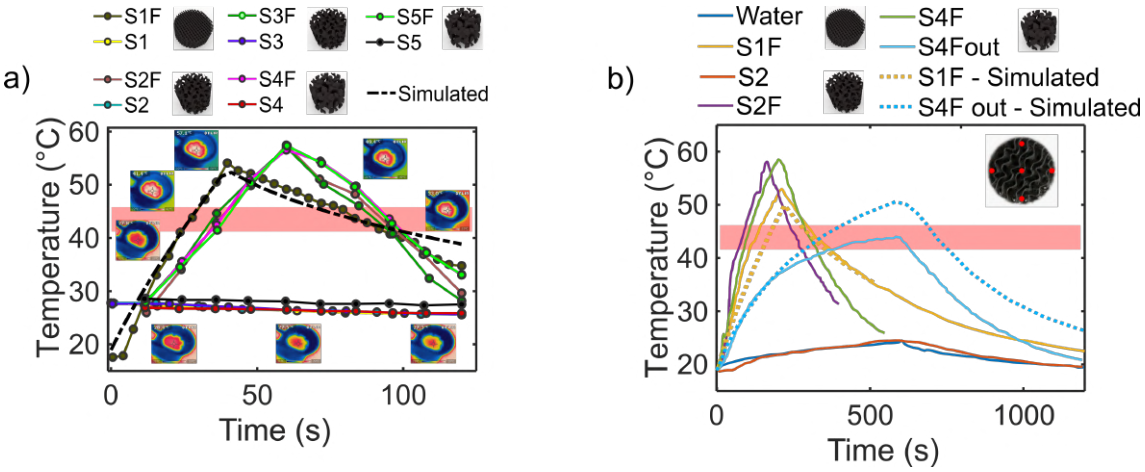

Figure 3.18. a) Temperature profiles, derived from the thermographic images, for PLA and Fe-PLA TPMS scaffolds placed in the coil in air, and compared to the simulation results. b) Temperature profiles of S1F, S2F and S4F scaffolds in distilled water, exposed to a 30 mT magnetic field, working at 380 kHz. Also the thermal response of the water environment is reported. The non-magnetic polymeric equivalent is always tested for comparison.

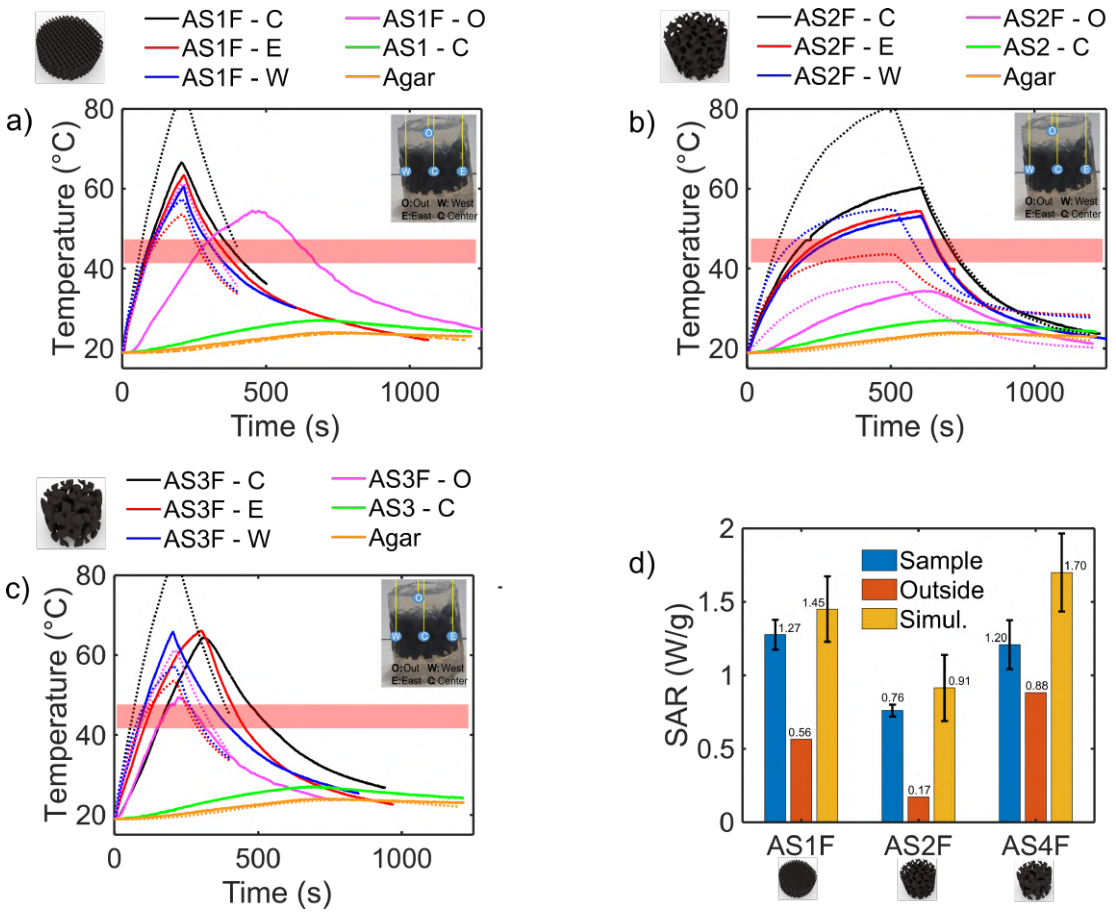

Figure 3.19. Temperature profiles in agar for a) S1F scaffold (90°-mesh), b) S2F scaffold (Gyroid) and c) S4F scaffold (L-surface), and comparison with the multiphysics simulations (dashed lines), for an external field of $B_0 = 30\,\text{mT}$ and $f = 365\,\text{kHz}$. d) Estimated specific absorption rate (SAR) values in the sample, compared to simulations, and in the phantom (Outside).

for the S1F, an average temperature of 61.5±3°C, for S2F 55±4°C and for S4F 64.6±7°C. The highest temperature were recorded in the center of the samples for S1F and S2F, but not for S4F, which presented a relevant homogeneity in terms of heating. The numerical simulations, on the other hand, overestimate the temperature in the sample center, while the simulated profiles for all the samples are fit with the measurements in W and E location points (Fig. 3.15.a-3.15.c). By carefully analyzing Fig. 3.15, it can be noticed that at about 5 mm away from the thermo-seed surface, the temperature decay, and the thermal gradient, can be relevant. Indeed, S1F showed a 5.5°C decrease, whilst S2F a ∼24°C reduction and S4F a ∼14.6°C lowering. In this framework, given the different temperature rises, during the evaluation of the hyperthermic potential of these ferromagnetic TPMS scaffolds, an averaging procedure must be taken into account in future studies.

With the recorder temperature profiles, according to Eq. (3.20), we evaluated the specific absorption rate per mass unit of agar. The results are reported in Fig. 3.15.d. It is possible to

noticed that the SAR of the scaffold estimated by averaging the five measurements inside the sample ranges from $0.8\,\mathrm{W{\cdot}g^{-1}}$ to $1.3\,\mathrm{W{\cdot}g^{-1}}$ (Fig. 3.15.d). These SAR values are enough for ensuring an effective hyperthermia treatment, according to [88]. On the other hand, when measuring outside the scaffold volume (point O in Fig. 3.15.c), the SAR levels ranges from 0.173.15.d to 0.883.15.d. The SAR estimated from the numerical simulation tends to overestimate the measured value, but, considering the large temperature variation in the sample volume, the in silico findings overlap with the measured values, resulting in a maximum difference of $\sim 0.5\,\mathrm{W{\cdot}g^{-1}}$ from the experimental levels. The SAR findings given in Fig. 3.15.d indicates that the different scaffold architecture can slightly affect the average hyperthermic potential. These results further demonstrate that the estimation of the SAR of MagS requires further numerical and more accurate experimental analysis.

In this chapter we dealt with the investigation of the influence of material characteristics, experimental parameters and estimation methodology on the specific absorption rate of magnetic scaffolds for the hyperthermia treatment of deep-seated tumors. In particular, we specified an experimental procedure to perform accurate measurement of heating efficiency of 3D printed magnetic scaffolds. To unravel this unexplored research field, the proposed experimental protocol prescribes that the hyperthermic potential of MagS should be evaluated in agar phantoms and averaging multiple sampling point.

Chapter 4

Drug Delivery and Tissue Engineering with Magnetic Scaffolds

4.1 Introduction

We have introduced previously that in the case of deep-seated bone tumors, surgical resection is almost unavoidable. Subsequently, a graft or implant is needed. However, to avoid the local recurrence, HT with MagS can be performed. If the HT with MagS is effectively planned and performed, then, the post-operative management and post-treatment must deal with the repair and regeneration of the healthy bone tissue (see Fig. 1.5). To this aim, the scaffold architecture is relevant, and TPMS-based strategy can be used [166, 193]. However, other than geometrical and mechanical aspects, additional features and design variables can be optimized to boost the tissue response.

Tissue engineering (TE) is the field of science whose aim is to develop tools and devices able to favor or selectively elicit the physiological process of tissue repair and regeneration [1, 2, 226]. For bone tissue, these devices are called scaffolds and are polymeric or ceramic objects to be implanted [1, 2, 226, 227]. Their first function is structural: they must withstand the injured tissue during its healing [1, 2, 226, 227]. However, scaffolds should be designed to establish conditions to favor the mesenchymal stem cells (MSCs) migration, adhesion, and differentiation [68, 226]. Given that bone tissue presents peculiar requirements, such as matching of mechanical properties, large nutrient supply, early vascularization, the way bone scaffolds are designed is drastically changing, and the passive, structural mechanics paradigms is integrated in a multifunctional, biomimetic contest [1, 2, 226, 227]. Many research efforts have been spent ot turn bone scaffolds into functional objects capable of minimizing tissue rejection and inflammatory response [227].

Faster integration and bone repair was studied by delivering specific physical stimuli transduced by the biomaterials [1, 2, 226, 227] by using scaffolds with nanostructured topography [228], or implanting devices capable of releasing ionic species (e.g., Ca^{2+}, Ag^{+}, Cu^{+}) or growth factors (GFs) [229]. Hence the scaffold itself may constitutes a local drug delivery system. However, traditional drug-loaded scaffolds are associated with i) burst release, ii) scarce spatial control and iii) impossibility of reloading. [68].

These limitations of drug-loaded scaffolds have led to the investigation of the bone scaffold functionalized with magnetic MNPs to obtain a remotely controlled functional device [43, 57, 230–232]. MagS, as nanocomposite magnetic material, present strong saturation magnetization (2.5-100 $\mathrm{kAm^{-1}}$), and, if implanted in the injured bone, can be exploited as an in situ magnet able to control and enhance the magnetic drug delivery (MDD) of growth factors to the defect site [43, 57, 231, 232]. However, despite the promising character of MagS as core element of an innovative, smart drug delivery system, only few preliminary proof-of-concept experiments have been performed, with scarce or none attention to the modeling. Previous works which dealt with the numerical study of MagS as a part of a MDD simply solved a linear magnetostatic problem and inferred the attraction probability of MNPs or magnetized cells estimating a threshold based on the analysis of magnetic field gradients [57, 72, 233]. The forces and concentration patterns, as well as cellular or tissue-related aspects have been underestimated or completely neglected. To fully exploit the potential of MagS as versatile, complete biomedical device, it is mandatory to provide a strong physical and engineering framework for their design and use.

However, the experimental and technological scenario for using MagS as MDD tools is far more complex. Indeed, most of the technologically available MDD systems can be triggered by thermal release [234–236]. Recently, Monsalve et al. manufactured a poly(ethylene glycol)-coated iron oxide nanoparticles with Transforming Growth Factor-β (TGF-β), which is released in its active form through an external RF MF (58 mT, 359 kHz) [235]. The heating favors the thermal degradation of the sulfo-SMCC complex and frees the bioactive molecule [235]. Similarly, the group of Meikle et al. used thermoresponsive poly(epsilon-lysine) dendrons to tether Vascular Endothelial Growth Factor (VEGF) to magnetite MNPs [236]. Under the action of a 30 mT magnetic field, working at 293 kHz, this latter MDD system was heated from 20°C to 45°C in deionized water, for 300 s. The 18% of loaded VEGF was released [236]. The choice of these GFs for the bio-conjugation is strategic for bone tissue engineering [227, 229]. VEGF and TGF-β are used since they can recruit MSCs osteoprogenitor cells, regulate inflammatory pathways, form new blood vessels [227, 229]. However, the timing, dose and distribution affects GFs activity. Therefore, the therapeutic window should be carefully chosen to obtain high level of bone formation. Despite these magnetic nano-systems for drug delivery have been manufactured and preliminary tested, there is lack of computational models capable of dealing with the system design, treatment planning and the investigation of biological effects.

In this chapter, we deal, for the first time, with the mathematical modeling of the combined use of magnetic scaffolds and MNPs carrying GFs to favor bone regeneration process [237]. We aim

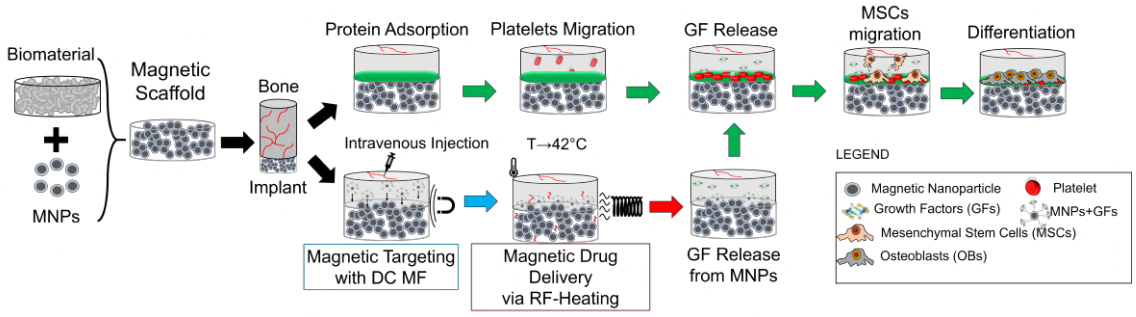

Figure 4.1. Magnetic scaffolds (MagS) are biomaterial functionalized with magnetic nanoparticles (MNPs). They can be implanted to enhance bone healing. During normal healing, the proteins adsorb on the biomaterial, recalling the platelets, which release growth factors (GFs). The mesenchymal stem cells (MSCs) are attracted by GFs, then migrate, adhere to the MagS, proliferate and differentiate in osteoblasts (OBs). During this process, MNPs carrying GFs can be injected intravenously and attracted to the scaffold surface using a static magnetic field (DC MF). Then a radiofrequency (RF) field is applied to heat the system up to 42°C and release the GFs, which has the effect of fastening and enhancing the bone repair process.

to model the administration and drug transport of the MDD system to the MagS in a way controlled by an external static magnetic field, as presented in Fig. 4.1. The magnetic drug carriers are intravenously injected and attracted to the MNPs-loaded implant by using a static magnetic field. The drug is released after heating the system to 42°C. The GF is then free to exert its specific biological action. The release of the GFs via RF-heating is investigated considering the multiphysics aspects involved in the process. Finally, the biological effect of the GFs is studied to evaluate if the proposed delivery strategy can favor the bone healing process and hence be of interest for regenerative medicine.

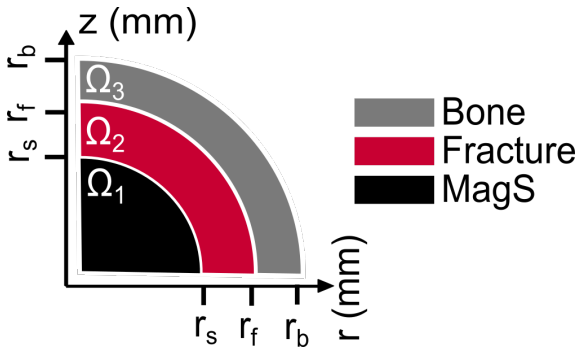

Figure 4.2. 2D axial-symmetric analysis domain representing an implanted scaffold, in gray black ($r_s = 5.5\,\text{mm}$), surrounded by a fracture gap, depicted in red, ($r_f = 2\,\text{mm}$) and the host bone, shown in yellow grey ($r_b = 10\,\text{mm}$).

4.2 The Proposed Mathematical Framework

The case of a scaffold implanted in a long bone after surgery is considered. A transverse section of bone ($r_b = 17.5\,\text{mm}$, domain Ω_3) with a 2 mm fracture gap (r_f, domain Ω_2) and scaffold ($r_s = 5.5\,\text{mm}$, domain Ω_1) is considered, as shown in Fig. 4.2. Assuming a spherical scaffold geometry or considering the cross-section of a cylindrical implant, the problem is reduced to a 2D axial-symmetric formulation [237].

4.2.1 The Non-Linear Magnetostatic Problem

In presence of a static, uniform and homogeneous magnetic field ($\mathbf{B_0}$), applied on the z-direction of the system presented in Fig. 4.2, the magnetic nanoparticles dispersed in the scaffold give rise to a uniform magnetization vector ($\mathbf{M}$) according to the following non-linear law [43, 72, 131]

$$\mathbf{M}(\mathbf{B},\phi,T) = M_s \phi \mathrm{L}\left(\frac{\mu_m \mathbf{B}}{k_B T}\right) \tag{4.1}$$

where k_B is the Boltzmann's constant, T is the system temperature, M_s is the saturation magnetization of the single nanoparticle in the MagS (in Am^{-1}). The resulting scaffold saturation magnetization is indicated as M_{sat}. The function $\mathrm{L}(x) = \coth(x) - \frac{1}{x}$ is the Langevin function [131]. The magnetic moment of the MNPs is μ_m (in JT^{-1}), whilst ϕ is the average volumetric fraction of MNPs in the biomaterial matrix. For each scaffold the MNPs are assumed to be monodisperse in size and to be homogeneously distributed in the prosthetic implant [117, 131].

Considering that MagS magnetic response is non-linear, the computation of the resulting spatial distribution of the magnetic field must be sought in a magnetostatic problem framework. To this aims, we use the scalar magnetic potential ψ_m to solve [126]

$$\begin{aligned} \nabla \times \mathbf{H} &= 0 \\ \mathbf{H} &= -\nabla \psi_m. \end{aligned} \tag{4.2}$$

We considered a ferrofluid impregnated hydroxyapatite-collagen scaffold (Impregnated HA) [43], an implant made of hydroxyapatite chemically doped with iron ions (MHA) [28] and a 3D printed poly-caprolactone (PCL) scaffold loaded with intrinsic magnetic hydroxyapatite (FeHA-PCL) [127, 150]. The features of the scaffolds considered in this work are reported in Tab. 4.1. Depending on MNPs characteristics and the manufacturing process, the saturation magnetization varies from low ($2.5\,\text{kAm}^{-1}$) to very high values ($100\,\text{kAm}^{-1}$) [9–16, 43, 238]. It is very crucial to investigate how the material parameters can influence the proposed magnetically targeted drug delivery strategy sketched in Fig. 4.1.

In presence of the static external magnetic fields, strong field gradients arise between the scaffold and the surrounding diamagnetic tissues (creating a force field in the domain Ω_2 and Ω_3). Therefore, the magnetic carriers in the system will experience an attractive force toward the scaffold. Previous

Table 4.1. Properties and characteristics of magnetic scaffolds.

	Unit	Impregnated HA	MHA	FeHa-PCL
M_s	$\mathrm{kAm^{-1}}$	414.45	310.8	336.7
r_m	nm	50	10	14
ϕ	%	12.5-25	1.6	9.18
M_{sat}	$\mathrm{kAm^{-1}}$	2.6-100.36	0.94	6.15

works assumed that magnetic field gradients higher than $1.3\,\mathrm{Tm^{-1}}$ can determine a magnetic force sufficient to attract MNPs to the scaffold [43, 57, 72, 233]. However, this is a limited view of the problem.

In this chapter, relying on a continuum-based approach, we refined the computational modeling of the magnetic attraction of MNPs to the scaffold by explicitly addressing the problem of the coupling between magnetostatic and mass transport phenomena. To this aim, the magnetic force ($\mathbf{F_m}$, in N) exerted on the MNPs can be computed as [133]

$$\mathbf{F_m} = \frac{(M_{s,m_2} V_{m_2})^2}{6 k_B T} \nabla |\mathbf{B}|^2 \tag{4.3}$$

where M_{s,m_2} is the saturation of the magnetic carrier to attract, whilst V_{m_2} is the volume of the MNPs core. The properties for the nanocarriers of GFs from [235] and [236] are reported in Tab. 4.2.

To effectively target the MNPs to the MagS (Fig. 4.1), it is necessary to maximize Eq. (4.3). In this framework, we can already infer that it is possible to act of on the magnetic field gradient to enhance $\mathbf{F_m}$. This can be done tuning the strength of the external magnetic field ($\mathbf{B_0}$) or on the MagS properties, such as MNPs loading, or the intrinsic magnetic properties of the carriers. Indeed, MDD can be fostered by designing and manufacture magnetic carriers of growth factor with high saturation magnetization. However, recalling biocompatibility issues and haemodynamic problems, the volume of the MNPs to attract should be controlled [133]. From a material science point of view, the contemporary satisfaction of these criteria is a non-trivial task.

Under the action of the magnetic force (Eq. (4.3)), the drug shuttles are set in motion with a velocity $\mathbf{v_m}$ (in $\mathrm{ms^{-1}}$), defined as [237]

$$\mathbf{v_m} = \frac{\mathbf{F_m}}{6 \eta r_{m-d}} \tag{4.4}$$

where r_{m-d} is the hydrodynamic radius of the MNPs plus the tethered GF molecule, and η is the viscosity of the extracellular matrix (ECM), in Pa·s. A value of 450 Pa·s was used to mimic the drag that the MNPs would experience in the fibrin matrix [239].

The Comsol *AC/DC module* is used for solving the non-linear magnetostatic problem. The magnetic potential is discretized with quadratic elements. A steady, direct MUltifrontal Massively Parallel Sparse direct Solver (MUMPS) solver, with Newton method, is used. The maximum

Table 4.2. Features of the magnetic drug carriers.

	VEGF+MNPs [236]	TGF-β+MNPs [235]	Units
M_{s,m_2}	60	80	emu·g^{-1}
V_{m_2}	1413.70	4188.88	nm^3
r_{m-d}	16.685	53.0	nm
D_m	0.1	0.315	mm^{2}d^{-1}
k_{rel}	0.82	12	h^{-1}
$C^0_{m,inj}$	40	6.73	mg·ml^{-1}
C^0_{GF}	0.194	40	μg·ml^{-1}
$\mathbf{B_0}$	30	58	mT
f	293	350	kHz
SAR	13.911	186.0	W·g^{-1}

number of iteration was set to 250, the initial damping was equal to 1 and the minimum damping factor to 10^{-4}.

4.2.2 Tissue-scale Modeling of Mass Transport and Attraction of Magnetic Nanoparticles

Given the knowledge of the magnetic field, force and the velocity, we face the problem of describing the attraction of the magnetic carriers to the MagS, i.e., the coupling to the mass transport at the tissue-scale. The goal is to derive a framework which can predict the spatial distribution of the MNPs to attract.

For the process shown in Fig. 4.1, the population of MNPs is subject to the magnetic force due to the scaffold presence and is drifted to the implant, against the action of a random dispersal flux [240]. To investigate the pattern of C_m in the injured area, a diffusion-advection equation holds [131, 160, 240]

$$\frac{\partial C_m}{\partial t} = D_m \nabla^2 C_m - \mathbf{v_m} \cdot \nabla C_m - k_c C_m \tag{4.5}$$

where D_m is the diffusion coefficient of the nano-scale drug delivery system (in m^{2}s^{-1}). The influence of the scaffold on the MNPs administration in the bone cavity (domain Ω_2 in Fig. 4.2) is accounted by the term $\mathbf{v_m}$ (Eq. (4.4)). The degradation term $k_c C_m$ accounts for the capture, inactivation and elimination of the MNPs from the endoplasmatic reticulum [241]. In this chapter, given the size of the MNPs from Tab. 4.2, k_c was set to $4.85{\cdot}10^{-7}$ d^{-1} [241].

To solve Eq. (4.5), for simulate the magnetic drug delivery process from Fig. 4.1, it is necessary to constrain the concentration to a fixed value at the interface between bone and fracture (between domain Ω_2 and Ω_3 in Fig. 4.2). We assume here, differently from [72, 131], that the magnetic carriers are intravenously injected [240]. The concentration of MNPs at the host bone boundary (Ω_3

Table 4.3. Parameters for describing the intravenous injection of MNPs

Param.	Value	Unit
$D_{m,b}$	25	mm^2d^{-1}
s	0.018	mm^{-1}
v_c	0.1	$cm{\cdot}s^{-1}$
l_c	25	μm
r_c	0.1	μm
η_b	3	cP
t_m	0.5	μm

in Fig. 4.2) is assumed to depend on particles characteristics and from the local microvasculature tissue properties, so that [160, 240]

$$C_m^0|_{bone} = C_{m,i}^0 \frac{L_p s(1-\theta)(P_e - P_i)}{e^{Pe_{mv}-1}} \tag{4.6}$$

where $C_{m,i}^0$ is the concentration of the injects MNPs in $mg{\cdot}ml^{-1}$. In Eq. (4.6), L_p is the hydraulic conductivity of the vascular network in bone tissue, i.e. [160]

$$L_p = \frac{\psi r_c^2}{8\eta_b t_m \sqrt{\psi}} \tag{4.7}$$

where ψ is the porosity of the capillaries, whilst r_c is the average radius of the capillaries, in μm, *eta* is the blood viscosity, and t_m is the thickness of capillaries membranes (in μm). The symbol s is the surface area of the
capillaries per volumetric unit of tissue, as reported in Tab. 4.3.

In Eq. (4.6), θ indicates the sieving coefficient, which depend on the ratio between the size of the carrier and the capillary pores ($\nu = r_{m_2}/r_c$)

$$\theta = (1-\nu)^2[2-(1-\nu)^2]\left[1 - \frac{2}{3}\nu^2 - 0.136\nu^3\right] \tag{4.8}$$

The sieving coefficient is almost total (∼99%) for both the MNPs [235, 236].

The terms P_e and P_i are the Sterling's and interstitial pressure, with average values of 25 mmHg and -3 mmHg, respectively [160]. Finally, Pe_{mv} is the Peclet number of the micro-vascular system [160], defined as

$$Pe_{mv} = \frac{v_c l_c}{D_{m,b}} \tag{4.9}$$

where l_c is the average capillary length (in mum) and v_c is the average bloodstream velocity (in $cm{\cdot}s^{-1}$). These parameters are related to the microvasculature and blood flow properties, and their values are reported in Tab. 4.3. It should be noticed that the diffusion coefficient of MNPs in blood

($D_{m,b}$) is calculated considering blood viscosity, and it is therefore different from the value that the magnetic carriers experiences in the ECM during the attraction to the magnetic scaffold. Given this difference, The Peclet number magnitude is relatively high, since the average velocity of blood in capillaries (v_c) is moderate but the nanoparticles are very small-size object and are subject to high drift in the blood vessels [133]. This causes the velocity of filtration ($L_p(P_e - P_i)$) in Eq. (4.6) to be on the order of $0.5\,\mathrm{mm{\cdot}s^{-1}}$.

For the system geometry in Fig. 4.2, in order to respect symmetry, two Neumann zero-flux boundary conditions were applied to the r- and z-axes. To solve Eq. (4.5), the concentration of MNPs is assumed to be zero at the initial time, so that

$$C_m(r,z,t=0) = 0, \tag{4.10}$$

whilst zero flux boundary condition is considered at the scaffold surface (at the boundary of Ω_1 in Fig. 4.2, so that

$$-\mathbf{n}\cdot\nabla C_m = 0 \tag{4.11}$$

The attraction of the nano-carriers from Tab. 4.2, is assessed for the three scaffolds from Tab. 4.1 under different magnetic field strengths. From this analysis, the most effective MagS is selected.

The *Transport of Dilute Species* interface from Comsol 5.5 is used to solve the mass transport problem (Eq.s (4.5)-(4.11) using the solution of Eq. (4.3)). The concentration is discretized with quadratic elements. The built-in consistent stabilization method working with approximate residual was used. A transient, direct parallel direct solver (PARDISO), with row pre-ordering, in a second-order backward differentiation (BDF) and Newton scheme was used. The maximum number of iteration was set to 100. whilst the initial damping was 0.9 and the Anderson acceleration was used.

4.2.3 Drug Release via RF-Heating

As depicted in Fig. 4.1, after the injection and the following attraction of the magnetic carriers to the scaffold, the static magnetic field is turned off and a time-varying magnetic field is applied [234–236] to heat the magnetic carriers and reach an average macroscopic temperature of 42°C, to destroy the linkers and freeing the biomolecules. The AC magnetic field does not exert significant forces or torques on the MNPs, which retains their final distribution for the RF-heating step. We assume therein that the release temperature does not alter the GFs activity, on the basis of what reported in [235, 236]. Furthermore, the time required to reach 42°C is considered so low that the biological system is not damaged from any thermal effect.

The RF-heating was carefully modeled solving the PBHE (2.28) in the analysis domain ($\Omega_1 - \Omega_3$) of Fig. 4.2. The problem was assumed to be non-linear and fully coupled, as in the multiphysics framework previously developed [117, 118]. A uniform and homogeneous magnetic field distribution is considered as background field. The spatial distribution of the magnetic field is computed

considering the the candidates MagS in Tab. 4.1.

Differently from the interstitial hyperthermia treatment of bone tumors [117, 118, 131], the exposure time is not of tens of minutes, but of the order of few to tens of seconds [234–236], because the threshold temperature of 42°C must be reached locally and in the proximity of the implant. Furthermore, an additional heat source is present. Besides the heat per volume unit dissipated by the magnetic scaffolds ($Q_{sc} = P_m$ from Eq. (2.1)) and the heat dissipated by the induced currents in the tissues (Q_t), the thermal contribution of the power dissipated by the magnetic carriers (Q_m) must be included. The heat dissipated by the concentration of injected MNPs can be estimated as [200]

$$Q_m = SAR \cdot C_m(r,z). \tag{4.12}$$

In Eq. (4.12), the MNPs distribution is recovered from the solution of Eq. (4.5), at the final time, i.e. at the end of the targeting phase. Therefore, $Q_m = Q_m(r,z)$ is a function space. The SAR of the MNPs reported in Tab. 4.2 was retrieved by the initial slope method [200] from the experimental data of [235, 236]. In this framework, the total electromagnetic power per unit volume deposited during the heating is

$$Q_{EM} = P_m + Q_t + Q_m. \tag{4.13}$$

The PBHE for the system shown in Fig. 4.2 is solved assuming open boundary at the outer bone interface (Ω_3)

$$-\mathbf{n} \cdot \nabla T = 0, \tag{4.14}$$

and imposing an initial temperature of 37°C for all tissues, so that

$$T(r,z,t=0) = 0, \tag{4.15}$$

The thermal insulation condition is applied for symmetry along the r- and z-axis.

The electromagnetic problem is solved in the frequency domain by employing the Comsol *AC/DC* module. The magnetic vector potential was discretized by using quadratic finite elements. The electromagnetic problem is bi-directionally coupled to the bioheat transfer problem, which is solved in the time domain using the *Bioheat Transfer* module. The temperature is discretized with quadratic Lagrange elements. A direct MUMPS solver employing BDF scheme and Newton method is used for solving the coupled problem, with a maximum of 500 iterations, a Jacobian update once per time step and no stabilization and acceleration.

4.3 Bone Repair Process: Physiology and Mathematical Modeling

This chapter aimed at modeling and investigating how MagS, after their implantation, could be used as the core of a MDD system for MNPs functionalized with biomolecules. To this aim, it is crucial to include the bone healing process, summarized in Fig. 4.1, in our model [242–246]. Then, this model must be modified to account for new contribution the drug delivery guided by magnetic attraction and triggered by RF-heating.

4.3.1 Physiological Process & Biomathematics Model

In this chapter, the bone healing process (Fig. 4.1) is described by relying on the model of Moreo et al. [244–246]. This model is capable of seizing the essential features of the healing process, and, furthermore, it was already analyzed in the literature in terms of sensitivity, stability, existence of the solution and a priori error estimate [244–246]. Anyway, the set of nine non-linear reaction-diffusion coupled equations proposed for the early stages of bone healing from [244–246] are slightly modified and re-adapted to be used for simulating the effects of the MDD strategy shown in Fig. 4.1. Considering a moderate mechanical stimulation, a continuum-based approach is used to describe the spatio-temporal dynamics of the main biological elements depicted in Fig. 4.1.

In presence of a biomaterial, the bone healing process beings after a surgical or accidental fracture, with blood vessel injury [229, 242, 243]. The bone cavity is immediately filled with blood [243]. Plasma, platelets and proteins invade the injured area. As depicted in Fig. 4.1, firstly proteins (e.g., plasmin, albumin) adsorb onto biomaterial surface (in few μs) [243]. In this regard, proteins (p, in μg·mm^{-2}) adhesion onto the rough biomaterial surface ($p_0 = 0.5\,\mu$g·mm^{-2}) is assumed to be a steady-state process [244–246], so that

$$D_p \nabla^2 p - \gamma_p p = 0 \tag{4.16}$$

where D_p is protein diffusion coefficient and γ_p is the linear decay rate. The value of both D_p and γ_p are chosen to get a characteristic diffusion length of about 0.1 mm, i.e.

$$l_p = \sqrt{\frac{D_p}{\gamma_p}}. \tag{4.17}$$

Subsequently the coagulation process begins with platelets (c, cells·ml^{-1}) activation, migration to the biomaterial and the following release of several GFs, such as VEGF or TGF-β [229]. The platelets density dynamic obeys the following random dispersal motion and taxis

$$\frac{\partial c}{\partial t} = \nabla \cdot [D_c \nabla c - H_c \nabla p] - A_c c \tag{4.18}$$

where H_c is a chemotaxis coefficient and A_c is a linear decay rate (see Tab. 4.4).

As platelets start diffusing and moving down protein chemotactic gradient, they release an angiogenic GFs, whose concentration is $s_1(r,z,t)$ (see Fig. 4.1). This molecule is able to recruit osteo-progenitor cells, exactly as VEGF or TGF-β [227, 229, 235, 236]. Since the proposed magnetic drug delivery strategy, shown in Fig. 4.1, aims to introduce more GFs and boost the cellular response it is fundamental to model the dynamics of the s_1 density. In physiological, normal conditions (i.e., in absence of drug delivery), the mass balance equation for the biomolecule s_1 is [244, 245]

$$\frac{\partial s_1}{\partial t} = \nabla \cdot (D_{s_1} \nabla s_1) + \left(\frac{\alpha_{c1} p}{\beta_{c1} + p} + \frac{\alpha_{c2} s_1}{\beta_{c2} + s_1} b \right) - A_{s_1} s_1 \tag{4.19}$$

where the kinetic terms in parentheses represent GFs secretion by platelets (p) and model their degree of activation. The linear decay rate, A_{s_1}, accounts for the low bio-availability of GFs in vivo.

During the release of the angiogenic growth factor by platelets, the fibrin network assemblies in an ischemic environment [227, 229]. Then hematoma forms, locally necrosis takes place and the inflammatory phase establishes [244]. Around 2-10 days, while MSCs migrate from the host bone following the chemotactic gradient of GFs, the angiogenesis process starts to build new vessels [227]. At about 14 days, the osteoprogenitor cells differentiate in osteoblasts (OBs, b) and initiate to deposit the mineral bone matrix [243]. The main biological actors of bone healing, MSCs, migrate from the host bone towards biomaterial surface along gradients of both the angiogenic, i.e., s_1, and the osteogenic GFs, i.e., s_2. The cell migration direct by chemical stimuli is called chemotaxis [160]. The influence of the GF s_1 is twofold, since it also favors the differentiation of MSCs into the osteoblastic phenotype. In mathematical terms the patterns of osteogenic cells, $m(r,z,t)$ (in cells·ml^{-1}), can be obtained by the following equation [244, 245]

$$\begin{aligned} \frac{\partial m}{\partial t} = {} & \nabla \cdot \left[D_m \nabla m - m(B_{m_1} \nabla s_1 + B_{m_2}) \right] + \\ & \left(\alpha_{m_0} + \frac{\alpha_m s_1}{\beta_m + s_1} + \frac{\alpha_m s_2}{\beta_m + s_2} \right) m \cdot \left(1 - \frac{m}{N} \right) \\ & - \left(\frac{\alpha_{mb} s_1}{\beta_{mb} + s_1} + A_m \right) m \end{aligned} \tag{4.20}$$

where the parameters are listed and explained in Tab. 4.4.

A clarification about the coefficients which describes the chemical stimulus mediated by GFs which can regulate cellular migration is in order. With respect to the model of Moreo et al. [244–246], the taxis coefficients B_{m_1} and B_{m_1} are assumed herein to be not constant, but limited to a maximum velocity value [247, 248], i.e

$$\begin{aligned} B_{m_1} &= \frac{\sigma_1 B_{m_{10}}}{1+\eta_1 s_1} \\ B_{m_2} &= \frac{\sigma_2 B_{m_{20}}}{1+\eta_2 s_2} \end{aligned} \tag{4.21}$$

where σ_1 is equal to 0.05, η_1 was found to be $0.033\,\mathrm{ml{\cdot}ng^{-1}}$, σ_2 and η_2 are 0.01 and $0.050\,\mathrm{ml{\cdot}ng^{-1}}$, respectively. In this way, the chemotaxis coefficients are written in the form of a density-dependent sensitivity model and an upper bound for the chemotaxis velocity exists, thus avoiding solution blow-up and instability issues when the concentration of the chemical agent is elevated [247, 248]. This modification allows maintaining a meaningful and physical representation of cells concentration in the analysis domain.

As regards the osteogenic growth factor s_2 (e.g., the bone morphogenetic protein) the analytical balance regulates its spatio-temporal distribution

$$\frac{\partial s_2}{\partial t} = \nabla \cdot (D_{s_2} \nabla s_2) + \left(\frac{\alpha_{m2} s_2}{\beta_{m2} + s_2} + \frac{\alpha_{b2} s_s}{\beta_{b2} + s_2} b \right) - A_{s_2} s_2. \tag{4.22}$$

The availability of both growth factors causes the MSCs to differentiate into osteoblasts, which then produce the new bone in the fracture gap [243]. The dynamics of osteoblasts (b, in $\mathrm{cells{\cdot}ml^{-1}}$) obeys the following equation

$$\frac{\partial b}{\partial t} = \frac{\alpha_{mb} s_1}{\beta_{mb} + s_1} m - A_b b.labeleq4ob \tag{4.23}$$

After the differentiation, the creation of new and non-mature bone starts with the degradation of the temporary extracellular fibrin assembly produced by the platelets (see Fig. 4.1). Therefore, the fraction of fibrin matrix (v_f) can be investigated by solving the following equation [244–246]

$$\frac{\partial v_f}{\partial t} = -\frac{\alpha_{v_w} s_2}{\beta_{v_w} + s_2} b v_f (1 - v_w). \tag{4.24}$$

Then the periostium can undergo bone formation and intramembraneous ossifications, which determine woven bone production and the callus presence [227, 229, 243]. In mathematical terms

$$\frac{\partial v_w}{\partial t} = \frac{\alpha_{v_w} s_2}{\beta_{v_w} + s_2} b v_f (1 - v_w) - \gamma_b v_w (1 - v_l). \tag{4.25}$$

Finally, bone remodeling process works to form the mature lamellar bone [243], whose spatial and temporal distribution can be computed by solving

$$\frac{\partial v_l}{\partial t} = \gamma_b v_w (1 - v_l). \tag{4.26}$$

In brief, the implant of the MagS initiates a cascade of biological events: protein adsorption (Eq. (4.16)) [227, 229, 243], which determines platelets migration (Eq. (4.18)) [244], leading to the release

of angiogenic (Eq. (4.19)) and osteogenic (Eq. (4.22)) growth factors (i.e., VEGF or TGF-β) [229]. As a result, the stem cells are recruited by the GFs signaling (Eq. (4.20)), then migrate to the scaffold, where they proliferate and differentiate into osteoblast (Eq. (**??**)), which, finally, secrete the bone matrix.

With the model (Eqs. (4.16)-(4.26)), solved on domain Ω_2 in Fig. 4.2) is possible to evaluate the distribution of osteoblasts and then the production of lamellar bone (v_l). The external and additional contribution of the MDD acts directly on Eq. (4.19) and indirectly on osteoblasts.

Zero flux condition applies to all boundaries (host bone, implant surface and symmetry axes in Fig. 4.2 in the manuscript) for p, c, s_1, s_2, m, b, v_f, v_w, v_l.

A time-dependent Dirichlet boundary condition applies for the osteogenic cells at the host bone surface, so that

$$m(r,z,t)|_{\Omega_3} = \begin{cases} m_0 & 0 < t < 14 \\ 0 & t > 14 \end{cases} \tag{4.27}$$

In fact, as derived from physiology, the cell density value is set to $m_0 = 2{\cdot}10^5$ cells·ml^{-1} for the first 14 days. This non-linearity is implemented defining a smoothed step function, continuous in its second derivative, and applying it to host bone boundary. As regards the initial conditions, at $t = 0$ the platelets are assumed to have an initial concentration of $c_0 = 2.5{\cdot}10^8$ cells·ml^{-1}, whereas m and b have a starting concentration of 10^3 cells·ml^{-1}. Regarding the growth factors, both s_1 and s_2 are assumed to be poorly concentrated at the initial time, hence their initial value is set to 1 ng·ml^{-1}.

The bone healing process shown in Fig. 4.1 was simulated for a period of 365 days, with a 1 day step, in presence of the magnetic scaffolds and in absence of external field and drug stimulation. This set the reference situation and acts as a suitable ground truth. The Comsol *Mathematics* interface is used to solve Eqs. (4.16)-(4.26). The protein density are discretized using Lagrange quadratic elements and Eq. (4.16) is solved by using a steady MUMPS solver with Newton method (initial damping factor equal to 1, minimum damping factor equal to 10^{-4}), with 25 maximum iterations. The other variables are discretized with Lagrange quadratic elements, but the other equations are solved with a transient, direct MUMPS solver using the BDF scheme (with maximum order of 5) and using the built-in nonlinear Newton method, with minimal Jacobian update, without stabilization and acceleration.

Given the model complexity, the several physics involved and the large number of model variables, which have a strong mutual interdependence, it is worth to explain the relationship between the aforementioned physical quantities. In Fig. 4.3, the resolution workflow for the bio-mathematics problem is outlined. The protein mass balance is first solved. Then, the spatial distribution of p is employed to evaluate the platelets dynamic, while solving for the growth factors s_1 and s_2, together with the MSCs (m) and the osteoblasts (b). Then, in sequence, v_f is computed, then v_w and, finally v_l.

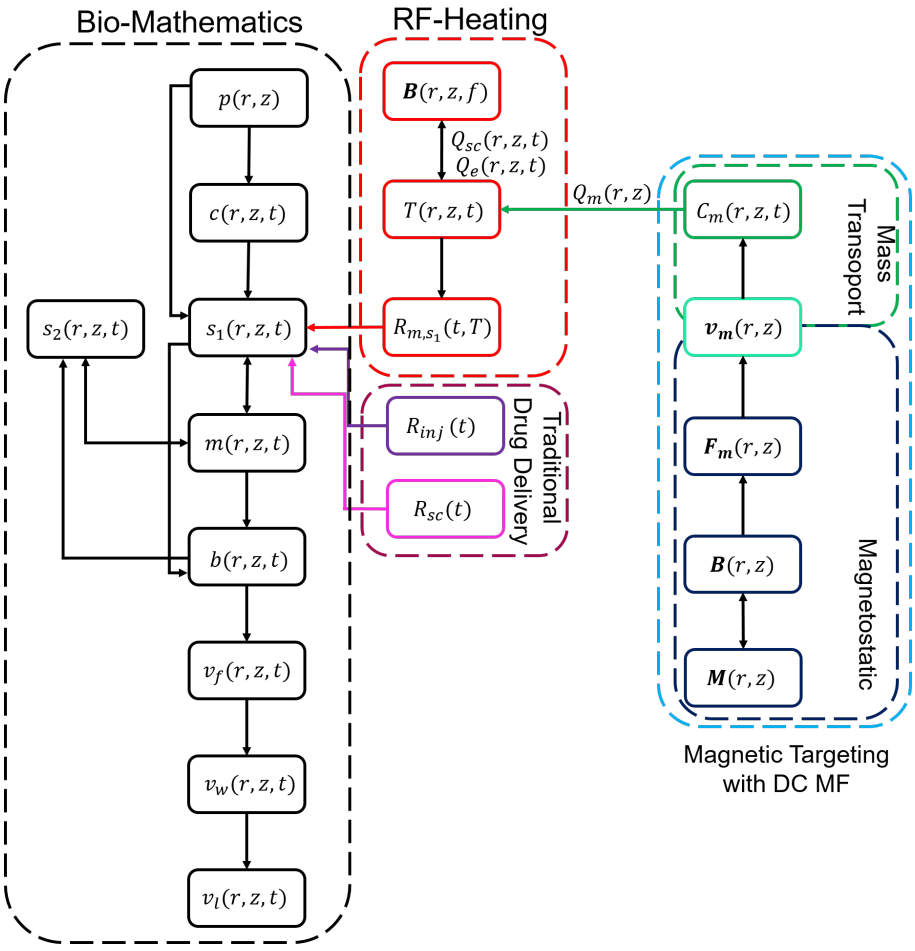

Figure 4.3. Resolution scheme and relationships between the different variables and physics of magnetic drug targeting with magnetic scaffolds for bone tissue engineering. The biomathematics problem of bone repair constitutes the reference frame. Three different drug delivery strategies are compared. The direct injection of growth factor (R_{inj}), the release of biomolecules from loaded scaffolds (R_{sc}) and the magnetic drug delivery (R_{ms1}). The latter approach consist in two steps: i) a magnetic targeting with static fields, which requires the solution of nonlinear magnetostatic and mass transport problems, and ii) a RF heating phase.

4.3.2 Bone Healing Outcomes

Currently available MagS demonstrated the capability to increase MSCs adhesion, proliferation and differentiation thanks to a rough surface microtopography [9, 10, 12, 15]. The bone integration was experimentally observed in absence of any type of drug delivery strategy. However, herein we hypothesize that the bone-healing process can be further enhanced with magnetically targeted drug delivery of MNPs carriers of GFs. Therefore, we consider the physiological osteogenesis in presence of a biomaterial as the reference situation. We aim to evaluate, for the first time, if the

Table 4.4. Parameters for the Bone Healing Simulations for VEGF and TGF-β

Param.	**Value**	Unit
p_0	0.5	μg·mm^{-2}
D_p	0.001	mm^{2}day^{-1}
γ_p	0.01	day^{-1}
D_c	$1.36{\cdot}10^{-2}$	mm^{2}day^{-1}
A_c	0.06	μg·mm^{-2}
H_c	0.33	mm^4(day·μg^{-1})
D_m	1.3	mm^{2}day^{-1}
$B_{m_{10}}$	0.2, 0.66	mm^{2}day^{-1}(ng·ml^{-1})
$B_{m_{20}}$	0.167	mm^{2}day^{-1}(ng·ml^{-1})
α_{m_0}, α_m	0.25	day^{-1}
N	10^6	cells·ml^{-1}
A_m	$2{\cdot}10^{-3}$	day^{-1}
α_{mb}	0.5	day^{-1}
β_{m_0},β_{mb}	10	ng·ml^{-1}
A_b	$6.67{\cdot}10^{-3}$	day^{-1}
D_{s_1}	0.3, 0.85	mm^{2}day^{-1}
D_{s_2}	0.1	mm^{2}day^{-1}
A_{s_1}	10	day^{-1}
α_{c1}	$6.67{\cdot}10^{-5}$	ng·ml^{-1}·day^{-1}(cells/ml)$^{-1}$
α_{c2}	10^{-5}	ng·ml^{-1}·day^{-1}(cells/ml)$^{-1}$
α_{m_2}	$6.67{\cdot}10^{-5}$	ng·ml^{-1}·day^{-1}(cells/ml)$^{-1}$
α_{b2}	$2.5{\cdot}10^{-5}$	ng·ml^{-1}·day^{-1}(cells/ml)$^{-1}$
β_{c1}	0.1	μg·ml^{-1}
β_{c2}, β_{m_2}, β_{b2}	10	ng·ml^{-1}
α_w	10^{-7}	day^{-1}(cells/ml)$^{-1}$
β_w	10	ng·ml^{-1}
γ_b	20	a.u.

combination of MagS and magnetic drug delivery can alter and favor the osteogenesis. To this aim, under physiological conditions, the homogeneity (ξ) of the lamellar bone fraction (v_l) in the fracture gap is considered as biological outcome. This quantity is evaluated as the Fano factor [249] of v_l, i.e. the ratio of the mean value of lamellar bone density ($v_{l,mean}$) to its standard deviation ($v_{l,std}$). In mathematical terms, the homogeneity is computed, for $t = 365$ d, as

$$\xi = \frac{v_{l,mean}}{v_{l,std}}. \tag{4.28}$$

If the mean value of the mature bone fraction is high and its standard deviation is low, the resulting bone is of high quality and the damage can be considered as repaired [243, 244]. Furthermore, Eq. (4.28) as figure of merit to evaluate the quality of bone healing was never considered previously [244–246].

The homogeneity of bone determines the mechanical properties. Hence, the Young modulus (E, in GPa) of new bone is evaluated as a function of lamellar bone [67]

$$\begin{aligned} E(v_l) = {} & 8.83 \cdot 10^5 (1 - v_l)^6 - 2.99 \cdot 10^6 (1 - vl)^5 + 3.99 \cdot 10^6 (1 - v_l)^4 \\ & - 2.64 \cdot 10^6 (1 - v_l)^3 + 9.08 \cdot 10^5 (1 - v_l)^2 - 1.68 \cdot 10^5 (1 - v_l) + 2.37 \cdot 10^4. \end{aligned} \tag{4.29}$$

4.3.3 Effects of Magnetic Drug Delivery

In the case of VEGF or TGF-β release from the MNPs attracted to the scaffold site, MSCs distribution and their differentiation rate into OBs augments due to an increase in s_1 concentration. To model the further availability of s_1 due to the RF-heating release, the following generation term R_{m,s_1} is proposed

$$R_{m,s_1} = k_{rel} \frac{C^0_{GF}}{C^0_{m,inj}} C_m e^{\frac{T - T_{th}}{2\nu^2}} \Pi(t/T_d) \tag{4.30}$$

Eq. (4.30) must be added to the r.h.s. of Eq. (4.19). In Eq. (4.30) the function Π is a rectangular unit window of duration T_d. This function permits to simulate the injection of the MDD system and the GFs release for any given time of the healing process (1, 14, 28, 60 day) shown in Fig. 4.1. T_d is 1 day and C^0_{GF} is the dose of GF linked to the nanoparticle surface in μg·ml^{-1}. The amount of biomolecule tethered to the MNPs is assumed to be a constant for each carrier, e.g., 0.194 μg of VEGF per mg of nanoparticle [236], as reported in Tab. 4.2. The MNPs concentration (C_m) is the solution of Eq. (4.5) at the final time. As explained by Fig. 4.1, the GFs are bound to the MNPs using proteic or aminoacidic linkers which degrade if heated at the threshold temperature $T_{th} = 42$°C for some minutes [235, 236]. The term ν is equal to 0.3°C, to account for the narrow release temperature range observed experimentally in [235, 236].

As summarized by Fig. 4.3, the effects of magnetic drug delivery on the bone healing is accounted by solving the nonlinear magnetostatic problem, then the mass transport equation, and hence the solution to the RF-heating step is computed, so that it is possible to use Eq. (4.30) as new term to solve the biological problem in non-physiological conditions.

4.3.4 Comparison with Traditional Drug Delivery Strategies

The combined use of MagS and MDD is numerically validated against the traditional and established drug delivery methodologies of intravenous injection (IV) and release from a loaded scaffold (ScR), sketched in Fig. 4.4.

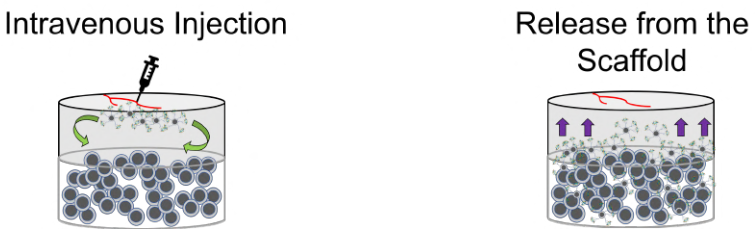

Figure 4.4. Traditional drug delivery approaches: intravenous injection (IV) and release from scaffold (ScR).

The direct injection of VEGF or TGF-β is simulated by solving the bone haling process problem by constraining Eq. (4.19) the following time-dependent Dirichlet boundary condition for s_1 on the boundary between domains Ω_2 and Ω_3

$$R_{inj} = C^0_{GF} \frac{L_p s(1-\theta)(P_e - P_i)}{e^{Pe_{mv}-1}} F_1(t), \tag{4.31}$$

where

$$F_1(t) = \begin{cases} 0 & 0 < t \leq 1 \\ 0.4 & 1 < t \leq 5 \\ 0.5 & 5 < t \leq 10 \\ 0.6 & 10 < t \leq 15 \\ 0.7 & 15 < t \leq 20 \\ 0.8 & 21 < t \leq 28 \\ 0 & t > 28 \end{cases} \tag{4.32}$$

The release profile of the IV case ($F_1(t)$) was derived from the experimental results found in [250,251], and given in Fig. 4.5. It should be noted that the release is quite high after 1 day (i.e. about the 40% of the loaded GF) and then is maximum after 28 days, implying that the release is not sustained and incomplete. The microvascular parameters for the first of Eq. (4.31) are evaluated for the VEGF or the TGF-β.

The proposed MDD strategy was compared to the physiological case and to the IV drug delivery, but also to the GFs release from the scaffold (Fig. 4.5). A drug-loaded implant with similar chemical and physical features was retrieved in the literature [252–254]. The following time-dependent BC for s_1 is imposed on the scaffold boundary (domain Ω_1 in Fig. 4.2) to simulate the concentration profiles derived from the experimental findings from [252–254]

$$R_{sc} = C^0_{GF} e^{-\frac{\sqrt{r^2-z^2}}{k_{sc}}} F_2(t), \tag{4.33}$$

where

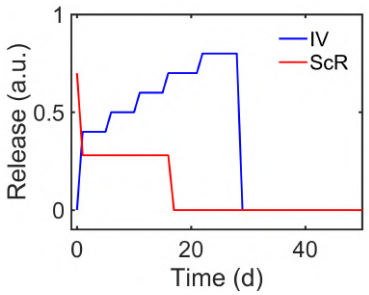

Figure 4.5. Release profiles of intravenous injection (IV) and release from scaffold (ScR) of growth factors (GFs).

$$F_2(t) = \begin{cases} 0.7 & 0 < t \leq 1 \\ 0.28 & 1 < t \leq 16 \\ 0 & 16 < t \leq 365 \end{cases} \tag{4.34}$$

The concentration of GFs released from the scaffold is assumed to exponentially decrease with the distance, being ineffective after distance $k_{sc} = 0.1\,\text{mm}$, and with the cumulative release trend from [252–254], which is shown in Fig. 4.5.

As summarized by Fig. 4.3, Eq. (4.31) and (4.33) has a direct influence on Eq. (4.19). In this framework, the homogeneity of lamellar bone density for the cases of the novel MDD are compared to normal osteogenesis and to the direct injection and the direct release from the scaffold are compared through the bone homogeneity parameter and elastic modulus.

4.4 Findings and Recommendations

The three different type of MagS reported in Tab. 4.1 are tested as potential candidates for the magnetic drug delivery strategy for bone healing shown in Fig. 4.1. The three magnetic scaffolds were analyzed in silico for strengths of the external static magnetic flux density field $\mathbf{B_0}$ ranging from 0.1 T to 1 T. Moreover, the attraction of the magnetic carriers [235, 236] is investigated.

From the analysis of Fig. 4.7.a, the magnetic field distribution in the entire analysis domain ($\Omega_1 - \Omega_3$) in Fig. 4.2) resembles the pattern of a uniformly magnetized sphere [43, 131]. It can be noticed that, the higher the saturation magnetization of the MagS, the higher the maximum amplitude of the magnetic field on the scaffold surface and hence, the magnetic field gradient in the system. By solving Eq. (4.3), the resulting magnetic force magnitude in the fracture gap is shown in Fig. 4.6.a and Fig. 4.7.a. The average intensity of the magnetic force $\mathbf{F_m}$ in the bone and fracture gap is significantly different across the magnetic scaffolds. The higher the magnetization of the scaffold, the stronger the force. Indeed, the ferrofluid impregnated scaffold is the best MagS to be used as attraction platform for MDD. This finding poses an interesting challenge to material science, i.e., the search for a manufacturing method for deriving scaffolds loaded with a high amount

of nanoparticles or synthesizing a magnetic material with high saturation magnetization.

From the physical properties of the MNPs (Tab. 4.2), the nanoparticles carrying the TGF-β are bigger and experience a two orders of magnitude higher magnetic force, i.e., hundreds of pN compared to tens of pN for the MNPs plus VEGF (Fig. 4.6.a).

In the viscous fibrin matrix, the velocity impressed to the magnetic carriers is maximum at a magnetic flux density of 1 T and in the case of impregnated HA, as shown in Fig. 4.6.a and 4.6.b. Hence, for the modeling of MNPs administration and attraction, the applied magnetic field was $\mathbf{B_0} = 1\,\mathrm{T}$.

The solutions of Eq. (4.5) is presented in Fig. 4.7.b, which shows that the MNPs concentration in the bone cavity follows the force distribution of Fig. 4.7.a. Therefore, MagS allows to drive the drug transport by the external magnetic field and distributes it according to a controlled gradient. Indeed, along the equator of the system (r,0), it is possible to notice a small depletion region where the magnetic force is minimum. The results for the MDD system with TGF-β are qualitatively similar and are not shown. The time of attraction is very similar to that experimentally observed in [255, 256], for similar exposure conditions (i.e., $\mathbf{B_0}$ and MNPs size).

According to Fig. 4.1 and Fig. 4.3, after the attraction, the static field is turned off and the RF magnetic field is applied to the system. After calculating C_m it is possible to evaluate the spatio-temporal evolution of Q_m. Therefore, the overall dissipated power P_{EM} can be estimated (see Fig. 4.6.d) and the temperature pattern can be computed using our innovative multiphysics nonlinear approach. From Fig. 4.6.d, it can be noticed that the three MagS considered in this chapter present a different heat dissipation dynamic due to the very different type of MNPs embedded in them and due to the volume fraction of the magnetic phase. Also, we can highlight that the impregnated scaffold has a deposited power which is slightly lower than the other scaffolds. Even though the Impregnated HA scaffolds has a higher content of ferromagnetic MNPs, the MHA and Fe-PCL scaffolds contains superparamagnetic nanoparticles which were synthesized to maximize the hyperthermia effect [28, 43, 150]. This step is crucial, since an accurate planning of the time required to reach the release temperature for the GFs would fasten the treatment, while avoiding tissues overheating. With a homogeneous and radial temperature pattern, as shown in Fig. 4.7.c, the value of T_{th} can be reached within 0.2 mm from the scaffold surface after 2-5 s, depending on the MDD system. This allows to release the growth factor nearby the biomaterial, as presented in Fig. 4.7.c.d, and possibly accelerates the contact osteogenesis.

Having implemented the system of equations for simulating the process in Fig. 4.1, the analysis is devoted to find suitable values of the dose of the GFs and the proper time of delivery. For an initial dose of 40 ng·ml^{-1}, the MDD release of growth factors is simulated for different stages of the healing process. From Fig. 4.8.a, it can be noticed that there is scarce difference (below 1%) between the administration of MDD at day 1 or 14 day, since the highest bone fraction are obtained. On the other hand, feed the GFs after 14 days, results in a lower fraction of newly formed bone. Therefore, relying on the physiology of bone healing process, best time to perform the treatment is within the first 14 days, during the early stage of bone healing (see Fig. 4.7), since the density of

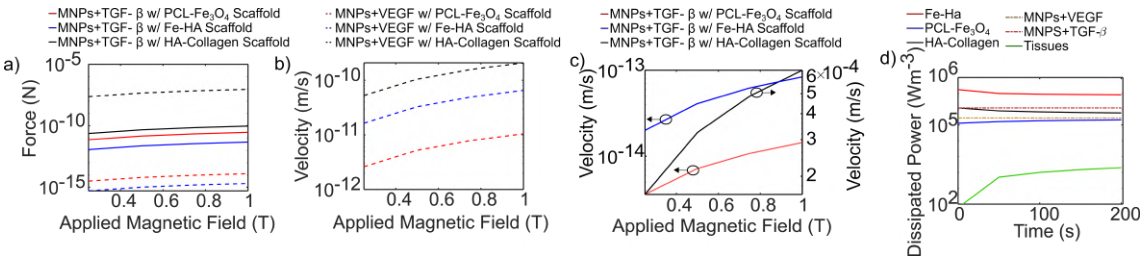

Figure 4.6. a) Force exerted from the MagS in Tab. 4.1 on the two MDD systems. b) Velocity ($\mathrm{m{\cdot}s^{-1}}$) on the MNPs+VEGF. c) Velocity ($\mathrm{m{\cdot}s^{-1}}$) for MNPs+VEGF. d) Dissipated power during the RF-heating step (Q_{sc} for the MagS in Tab. 4.1, Q_m for the MDD under study, and Q_t for biological tissues).

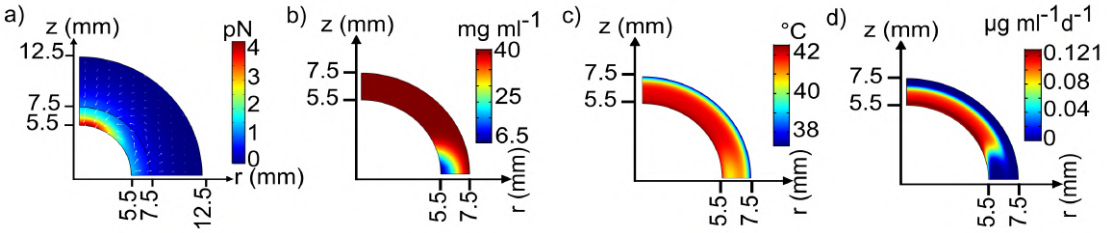

Figure 4.7. 2D distribution of the magnitude of magnetic force ($\mathbf{F_m}$) in the fracture gap and bone. The external magnetic flux density is 0.5 T, the magnetic scaffold is the MHA and the MNPs carrying VEGF are considered. b) Concentration profile (C_m) of MNPs+VEGF in the gap, ($t = 24$ h, $\mathbf{B_0} = 1$ T). c) Temperature distribution ($T(r,z,t)$, in °C) in the gap after 5 s for Impregnated HA, MNPs+VEGF exposed to a 30 mT and 293 kHz magnetic field. d) Pattern of the GF released (R_{m,s_1}) in the gap from the magnetic drug delivery system.

MSCs is still high and the differentiation into osteoblastic phenotype is occurring. Hence, simulating an intravenous injection of MNPs at 13 days, different doses of GFs are tested to evaluate the treatment effectiveness. Concentrations of VEGF and TGF-β from 0.194 $\mu\mathrm{g{\cdot}ml^{-1}}$ to 5 $\mu\mathrm{g{\cdot}ml^{-1}}$ are considered. On average, the higher the dose, the higher the final amount of lamellar bone produced in the cavity, as shown in Fig. 4.8.b. Similar findings holds for the VEGF. The maximum difference with the physiological case is more than 5%. The findings from Fig. 4.8.b allows us to infer that the proposed mathematical model can be useful for computing the dose and time of administration of GFs through magnetic drug delivery.

The distribution of v_l is rather homogeneous when comparing the MagS+MDD case with the normal healing as in Fig. 4.9.a and Fig. 4.9.b. From Fig. 4.9.c., it can be noticed that the intravenous injection allows to reach high value of bone density in the cavity, but there is a thin layer annulus of ∼0.1 mm which present very low value of lamellar bone fraction, in accordance with the experimental findings from [250,251]. This drawback can be attributed to the burst release of the GF [234]. On the other hand, the drug release from the scaffold ensures the apposition of bone layers from the biomaterial surface. However, far from the implant, as shown in Fig. 4.9.d, due to the limited spatial influence of the drug release, the new bone density is lower, resulting in

Figure 4.8. a) Resulting bone fraction for different administration times. b) Time evolution of the lamellar bone fraction in the fracture gap for different doses of TGF-β.

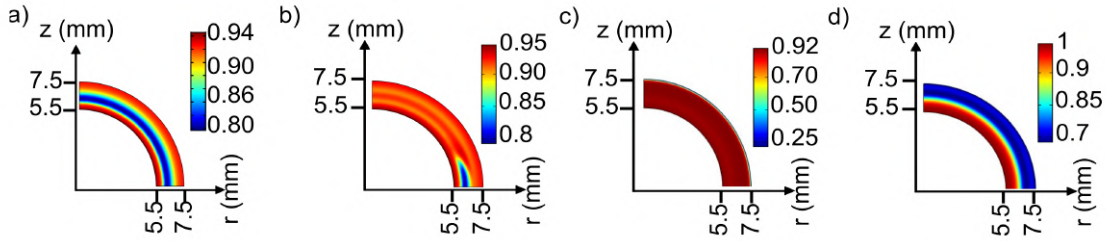

Figure 4.9. a) Pattern of the lamellar bone fraction (vl) at $t = 365$ d in the normal healing case. b) The spatial distribution of v_l at $t = 365$ d following the magnetic drug delivery treatment using TGF-β. c) The spatial distribution of v_l at $t = 365$ d when the growth factors are administered by intravenous injection. d) The spatial distribution of v_l at $t = 365$ d when the growth factors are released from the scaffold surface.

poor mechanical properties (see Tab. VII), as found in [250, 251]. The combined use of magnetic scaffolds and MDD allows to overcome overcoming these limitations.

Results from Tab.4.5 stress that the treatment using MDD and MagS allows the best bone homogeneity and the highest quality of mechanical properties. The MDD with TGF-β is the most effective since tends to $E_{max} = 18$ GPa [257]. In terms of ξ, the direct injection of GFs is comparable to the drug release from the scaffold, but the direct injection ensures better mechanical stability of the newly formed bone.

Table 4.5. Comparison of different methods of drug delivery of TGF-β and VEGF.

	$v_{l,mean}$	$v_{l,std}$	ξ	E (GPa)
Normal healing	0.931	0.0446	20.88	15.95
MagS+TGF-β	0.944	0.0012	787.25	16.78
MagS+VEGF	0.943	0.0058	162.68	16.68
Direct TGF-β injection	0.903	0.162	5.55	13.70
Direct VEGF injection	0.901	0.163	5.550	13.78
TGF-β from scaffold	0.816	0.154	5.301	11.04
VEGF from scaffold	0.835	0.150	5.561	11.45

With the developed numerical model and the in silico experiments we demonstrated that the

combined use of magnetic scaffolds and magnetic drug delivery systems for bone repair can be effective. The feasibility of the methodology should be validated in vitro and in vivo. The proposed model may also help in setup validation experiments, under controlled condition. Furthermore, the multiphysics non-linear framework could be used to plan this innovative treatment modality with great advantages for regenerative medicine and post-operative management of bone cancers, even after the control of local recurrence by interstitial hyperthermia. Our mathematical framework could be used as tool for investigating new type of magnetic carriers and magnetic scaffolds to enhance this therapeutic process, since, from an electromagnetic engineering perspective, it could help in bridging the gap between nanotechnology and biomedicine.

Chapter 5

Diagnostics and Monitoring

5.1 Introduction

MagS are multifunctional platforms suitable for TE, DD and HT. These magneto-responsive therapeutic materials can act also as diagnostic and monitoring tools, as shown in Fig. 1.1. Given the presence of the MNPs, MRI was investigated as diagnostic tool to probe the state of the biomaterial degradation and tissue growth [73–75]. The re-growth of the tissues occurs at expenses of the biomaterials, but also the MNPs are degraded by cells and the iron content of MagS decays $\sim\propto e^{-t/\tau_{deg}}$, being τ_{deg} the characteristic degradation time ($\simeq$14-30 days), modifying both the typical MRI parameters of spin-lattice (T_1) and transverse (T_2) relaxation times [74]. Recently, magnetic HA MagS were tested as theranostic tool for the in vivo regeneration [75]. The T_2 values decreases as the MNPs content in the biomaterial increases, and large contrast with body tissues can be achieved ($\sim \pm 20$ ms). Iron bioresorbable stents were tested in 1 T-3 T systems to evaluate the safety by estimating the displacement forces and torques, as well as the RF-heating [76]. Artifacts and heating can be controlled [76]. Despite these promising findings, due to their recent nature, the use of MRI as non-invasive thermometric method to monitor the temperature during the HT of bone tumors was not proposed. However, MRI is currently considered the key technology to increase the quality of HT, as epitomized by an intense recent research activity in the field of MW radiative hyperthermia [258–260]. Even though some pre-clinical studies are available, the problem of data processing comes with the cost and discomfort of MRI [73–76, 258–260]. In this framework, alternative, innovative technologies, such as MPI [83] or MWI can be used to setup real-time, cost-effective monitoring approaches of TE, DD and HT with MagS. Microwave as a diagnostic and sensing tool are appealing and interesting, since they use safe, non-ionizing radiations, while requiring low-cost components, and working in the frequency range of several wide-spread apparatuses, but also offering the unique opportunity to highlight additional details about the part of interest of the human body [261, 262]. Anyway, to date, the possibility of exploiting MagS as part of a MWI system has never been investigated. MNPs, in ferrofluid, were proposed as contrast agents

to enhance the MWI detection of breast tumors [77–82]. Feasibility studies, dedicated forward and inverse modeling, but also sensitivity analysis, as well as design of suitable systems, must be carried out to deal with magnetic materials and MWI [77–82]. Given the methods and findings from [77–82] it would be possible to setup and develop preliminary study for investigating the feasibility of using MWI as tool for monitoring the MagS during TE, DD or HT applications. We consider pivotal the HT application, as first. Since the investigation of MWI as thermometric system for hyperthermia, performed with antennas [263] or MNPs [264], is an ongoing field of science [265–267], and given that the problem is complex, we propose a preliminary feasibility analysis.

5.2 Related Works

Monitoring the temperature distribution inside tissue treated with hyperthermia is the pivotal aspect of this innovative thermal therapy [84, 88]. Active MWI has been proposed as a promising non-invasive approach for monitoring the tissue temperature, during hyperthermia [267] and ablation [268]. The inverse problem and reconstruction algorithms presents similar features. As first, the definition of a reference configuration and contrast must be provided [265–267]. Most of the work assume the beginning of the treatment as the reference configuration, so that the contrast in dielectric properties is due to the variation with temperature. However, the solution of a MWI problem is not trivial, since the inverse problem is an ill-posed one [261, 262]. In this framework, several approaches can be proposed. For a qualitative imaging, the delay-and-sum (DAS) algorithm can be used [265, 267]. The DAS approach is fast and allows to setup empirical threshold to detect event or anomalous distribution. To perform quantitative imaging, and extract the permittivity and conductivity maps, the distorted born iterative method [266], the contrast source inversion [268] or solution in L-p Banach space can be used [261]. However, for MWI with magnetic materials, such as MNPs or MagS, the inverse problem requires a different definition. As outlined in [77–82], so that the scattered field recovered at the measurement points can be related to an impinging magnetic field and to a magnetic contrast. In the case of HT with MagS, the magnetic and dielectric contrast can vary during the therapy. This further complicate the MWI problem. A possible solution, which is now gathering relevant attention by the EM community, is to use machine learning (ML) to solve the reconstruction problem [262]. In this framework, there is need of recovering all the primary data about the geometry, the material properties and possible operative conditions due to the HT scenario.

The usual methodology for setting up a MWI study is to investigate the problem in a simplified geometry and propagation scenario, in order to determine if and which type of matching medium would be require to avoid significant reflections of the impinging MW signal, as well as to determine a suitable range of operative frequencies [268, 269]. These information are fundamental for the design of antennas, but also for the setup of validation experiments and the manufacturing of tissue phantoms [218]. In this chapter, we will follow an approach similar to that of [268, 269], so that the essential information about the physiology, the treatment physics and the material properties

are recovered and used to preliminary study the feasibility of using MW as noninvasive tool for monitoring the hyperthermia treatment.

5.3 Feasibility Study Using a Simplified Forward Problem

5.3.1 Geometry

Bone tumors can affect several body sites, mainly limbs, such as legs and arms [97, 98, 100]. In this framework, we envisaged herein, an imaging system, composed of transmitting (TX) and receiving (RX) antennas deployed around a cylindrical structure, which extend indefinitely along the z-direction, as shown in Fig. 5.1.a. However, working directly on cylindrical geometry can complicate the analysis, thus hampering the fundamental understanding of the role of material properties and of the HT dynamics on the propagation. Therefore, we further simplify the anatomical problem by relying on the 2D surface phantom model proposed in [118] (see Fig. 2.7.b) and investigate a planar case. We neglect the presence of blood vessels and focus on the white straight line depicted in Fig. 5.1.a. Therefore, the geometry can be simplified and assumed to be a planar, multilayered structure composed of $N = 8$ layers, as presented in Fig. 5.1.b. The layers of biological tissues are skin, fat, muscle, bone, a generic bone tumor (e.g., FS and OS) and the fracture gap. Two semi-infinite media are considered, i.e., a matching medium, having an unknown relative permittivity $\epsilon_m \in [\epsilon_0, 80]$, and the MagS. The matching medium is assumed to be lossless, given that this contribution is negligible [261, 269]. The thicknesses and physical sizes of the tissue layers are derived from [118] and reported in Tab. 5.1.

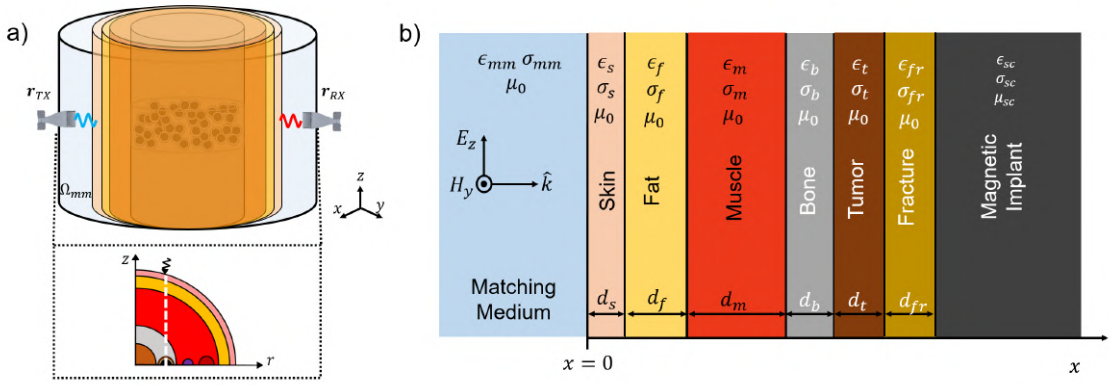

Figure 5.1. a) Envisioned system and schematic description of the simplified imaging problem. b) Mono-dimensional layered model for a transverse magnetic (TM), linearly polarized plane wave impinging on a multilayer structure composed of skin, fat, muscle, tumor and fracture tissue and a MagS, assumed as semi-infinite medium.

Table 5.1. Parameters of the simplified geometry for the propagation problem.

	Thickness (mm)	**Var. Name**
Skin	1.5	d_s
Fat	10	d_f
Muscle	45	d_m
Bone	2	d_b
Tumor	0.5	d_t
Fracture gap	0.3	d_{fr}

5.3.2 Monodimensional Propagation Model for Multi-Layered Lossy Structures

The system is assumed to be homogeneous and indefinite in the xy-plane. A planar, linearly polarized, time-harmonic transverse-magnetic (TM) wave is impinging on the system shown in Fig. 5.1.b, traveling along the x-direction. The media are characterized by a complex permittivity ϵ_i, an electrical conductivity σ_i (S/m) and permeability μ_i, for $i = 1,2,\ldots,N$. All tissues are assumed to be non-magnetic, so that $\mu_i = \mu_0$, for $i = 1,2,\ldots,N-1$. A dedicated discussion on material properties and contrast will follow.

The system shown in Fig. 5.1.b is analyzed by using the wave-amplitude transmission matrix (WATM) method [268–271]. By knowing the amplitude of the propagating and reflected electric field, along the x-axis, $E_{x+}^{(1)}$ at the first layer, the multilayered structure can be fully described by

$$\begin{bmatrix} E_{x+}^{(1)} \\ E_{x-}^{(1)} \end{bmatrix} = [M_1][T_1][M_2][T_2]...[T_{N-1}][M_{N-1}] \begin{bmatrix} E_{x+}^{(N)} \\ 0 \end{bmatrix} \tag{5.1}$$

The matrix M_i account for the EM wave in the i-th medium as a function of the MW signal in the $i+1$-th medium, so that

$$M_i = \frac{Z_i - Z_{i+1}}{Z_i + Z_{i+1}} \begin{bmatrix} 1 & \frac{2Z_i}{Z_i+Z_{i+1}} \\ \frac{2Z_i}{Z_i+Z_{i+1}} & 1 \end{bmatrix} \tag{5.2}$$

where the wave impedance of the i-th medium (Z_i) is

$$Z_i = \sqrt{\frac{\mu_i}{\epsilon_i}} \tag{5.3}$$

The propagation in the i-th layer is described by the transmission matrix T_i, defined as

$$T_i = \begin{bmatrix} e^{k_i d_i} & 0 \\ 0 & e^{-k_i d_i} \end{bmatrix} \tag{5.4}$$

being the wavenumber k_i defined as

$$k_i = \sqrt{\mu_i \epsilon_i}. \tag{5.5}$$

By relying on the fact that the electric field is continuous at the interface between the i-th and the $i+1$-th layers, and considering that the field amplitude can be computed considering the forward and backward propagating waves, it is possible to write the following system

$$\begin{bmatrix} E_{x+}^{(1)} \\ E_{x-}^{(1)} \end{bmatrix} = \begin{bmatrix} \zeta & \xi \\ \gamma & \delta \end{bmatrix} \begin{bmatrix} E_{x+}^{(N)} \\ 0 \end{bmatrix} \tag{5.6}$$

From Eq. (5.6), the total reflection (ρ_t) and transmission τ_t can be found as

$$\rho_t = \frac{\gamma}{\zeta} \tag{5.7}$$

and

$$\tau_t = \frac{1}{\zeta}. \tag{5.8}$$

Therefore, the reflection (R) and transmission (T) can be found as

$$R = |\rho_t|^2 \tag{5.9}$$

The generic reflection response $\Gamma_i = \frac{E_{i-}}{E_{i+}}$ must satisfy the recursion [270]

$$\Gamma_i = \frac{\frac{Z_i - Z_{i+1}}{Z_i + Z_{i+1}} + \Gamma_{i+1} e^{-2k_i d_i}}{1 + \frac{Z_i - Z_{i+1}}{Z_i + Z_{i+1}} \Gamma_{i+1} e^{-2k_i d_i}}. \tag{5.10}$$

With Eq. (5.10) is possible to evaluate the reflection of the i-th layer.

The WATM method have been implemented in Matlab 2021a (The MathWorks Inc., Boston USA). The reflection and transmission is studied for $f \in [0.1,10]$ GHz in order to find properties of the matching medium EM which ensure an effective signal transmission, while determining the operative bandwidth to use MWI as tool for monitoring the MagS biomedical applications.

Once the matching medium properties and the working frequencies are selected, in order to study if MWI can be used to monitor the HT of bone tumors with MagS, we followed the approach summarized in Fig. 5.2. In particular, we solved the PBHE with our nonlinear, multiphysics model for extracting the thermal distributions in the MagS and biological tissues. Then, we evaluated the average temperature in the media shown in Fig. 5.1.b. We used the simulated results (i.e., Fig. 2.8.b, 3.10.c and 3.10.d) to compute, for each time step of the simulated HT, the variation of the scaffolds and tissue properties (according to Eq. (2.29)). In this way, we solved the propagation problem for each time step and evaluated if substantial differences in the propagation exists. In mathematical terms, we computed a $\Gamma(t,T)$ and investigated the transmission difference with respect to the initial time $t = 0$ and uniform temperature distribution ($T = T_b \ \forall x$), which is

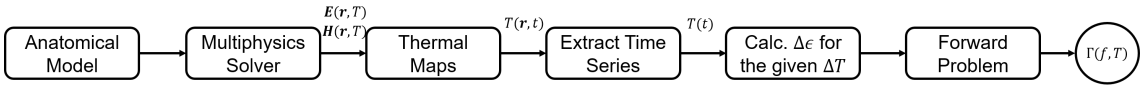

Figure 5.2. Proposed approach for study, in silico, the feasibility of using microwave imaging for monitoring the hyperthermia treatment of bone tumors using magnetic scaffolds.

assumed as reference configuration for the imaging problem, i.e.

$$\Delta[1-|\Gamma|^2] = [1-|\Gamma(t=0,T_b)|^2] - [1-|\Gamma(t,T)|^2]. \tag{5.11}$$

5.3.3 Materials Properties

The properties of the skin, fat and muscle tissues, shown in Fig. 5.1, at $T = T_b$ =37°C, are taken from [151], and given in Fig. 5.3. The properties of the fracture gap are assumed to be equal to the effective properties of blood and tissue, in a volume-weighted homogenization scheme, as demonstrated by [272]. The fracture gap is assumed to be in the inflamed state [117, 118] and its EM properties are reported in Fig. 5.3.

As regards the bone tumor, the EM properties in the kHz range reported in [117, 118] cannot be used for analyzing the MW problem. In the literature there is lack of ex vivo or in vivo characterization of the dielectric permittivity of bone tumors [273–275]. Anyway, the data reported in [273], even if measured for mouse tumor, offers different staging and are limited to 10 GHz. The data have been digitized [134] and fitted, using the Matlab fitting tool, to the following expressions

$$\begin{aligned} \epsilon_t(f,T_b) &= c_1 + \frac{c_2}{1+\frac{f^{c_4}}{c_3}} \\ \sigma_t(f,T_b) &= c_5 + \frac{c_6}{1+\frac{f^{c_7}}{c_8}}. \end{aligned} \tag{5.12}$$

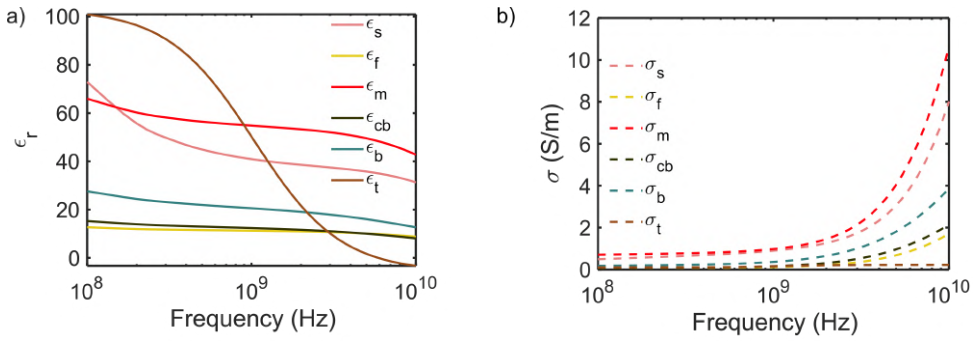

Figure 5.3. a) Relative dielectric permittivity ϵ_r of the tissues for the layered phantom. b) Electrical conductivity σ (S/m) of the tissues for the layered phantom.

The variation of the dielectric properties of biological tissues is assumed to be linear [117,118,138]. On the other hand, is more complicated to find data for the characterization of MagS at MW. It

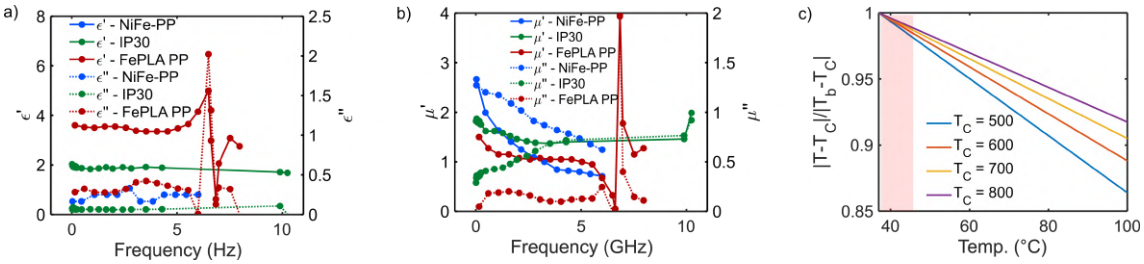

Figure 5.4. a) Complex dielectric permittivity, in both the real (ϵ') and imaginary (ϵ'') of the magneto-dielectric scaffolds. b) Complex magnetic permeability, in both the real (μ') and imaginary (μ'') of the magneto-dielectric scaffolds. c) Coefficient for the variation of the magnetic properties as a function of temperature. The dependence from the Curie temperature of the materials is highlighted.

is true that a complete characterization of similar composite MW-absorbing materials can be found, and, in principle, some of them could be used to our purpose. However, the biocompatibility, and hence the feasibility of using these materials as MagS must be considered. Therefore, we selected three different composite ferromagnetic biomaterials characterized at MW. In particular, among the magneto-dielectrics selected in this chapter, the NiFe-PE (Ni_81Fe_19 poly-ethylene), with a 40% loading of μm-sized spherical inclusions, was considered [276]. The 30% Fe-PLA, manufactured with a two-step mixture process, from [277] was selected. Finally, the Fe-PLA from Proto-Pasta, recently characterized by a dedicated broadband method [215], which have been tested for HT in this thesis work (see Sect. 3.2), was also considered. The comparison of the properties of the three magneto-dielectrics is given in Fig. 5.4.

The definition of the variation of the properties of magneto-dielectrics reported in Fig. 5.4 is more complicated. A characterization of these materials as a function of the temperature have not been carried out yet. However, we assume in this chapter that the dielectric properties of the scaffolds remains almost constant and to not vary during the treatment. On the other hand, the magnetic properties are assumed to be variable during the RF HT. We hypothesize that the temperature increase in the scaffold is far from the Curie-Weiss temperature of the material, so that

$$T_C \gg T \tag{5.13}$$

Therefore, the material retains its natural ferromagnetism and the magnetic phase does not change [24]. This is a reasonable assumption since magnetite, iron, nickel and their alloys presents T_C of several hundreds of °C. Indeed, for μm-sized iron $T_C = 700$°C, whilst for NiFe permalloy particles $T_C \simeq 500$°C [24]. In this framework, relying on the classical mean-field theory of ferromagnets, the magnetization of the material is assumed to decreases as temperature increases ($M_{sc} \propto \frac{1}{T}$) [24], whilst the magnetic susceptibility, and hence the permeability ($\mu = 1 + \chi$), follows the following relationship [24]

$$\mu(T) \simeq 1 + \frac{C_{cw}}{|T - T_C|}. \tag{5.14}$$

where C_{cw} is the material specific Curie constant, which can be found in [24]. Under the assumption of Eq. (5.13), we can linearize Eq. (5.14) after finding the coefficient of variation by taking the ratio of $\mu(T)$ and $\mu(T_b)$, i.e.

$$\frac{\mu(T)}{\mu(T_b)} = \frac{1 + \frac{C_{cw}}{|T-T_C|}}{1 + \frac{C_{cw}}{|T_b-T_C|}} = \frac{|T - T_C| + C_{cw}|T - T_C|}{|T_b - T_C| + C_{cw}|T_b - T_C|} = \frac{|T - T_C|}{T_b - T_C}, \tag{5.15}$$

to get

$$\mu(T) \simeq \frac{|T - T_C|}{|T_b - T_C|}\mu(T_b). \tag{5.16}$$

The coefficient, for different values of T_C is shown in Fig. 5.4.c. It can be noticed that, in the range of temperature typical of hyperthermia (41-45°C), the variation of the MagS properties is relatively narrow (∼2.5%). However, as shown in Fig. 2.10.d and Fig. 2.12.a, the scaffold temperature can reach higher temperatures. Therefore, the complex magnetic permittivity can reduce of about 5% of the initial value.

5.4 Findings and Recommendations

In order to evaluate the feasibility of using MWI as tool for monitoring the HT of bone tumors using MagS, we performed a simplified analysis based on a monodimensional propagation model for the geometry shown in Fig. 5.1.b. We investigated the transmission coefficient over the frequency range 0.1-10 GHz by varying the dielectric properties of the matching medium. Furthermore, we considered three different magneto-dielectric candidates as MagS. For the initial time $t = 0$, and a homogeneous temperature distribution in tissues ($T = T_b$), the results are shown in Fig. 5.5. Given the contrast between the biological tissues (Fig. 5.3) and the MW response of the MagS (Fig. 5.4), the transmission coefficient are not identical for all of the investigated cases. In particular, for the NiFe-PE scaffold, from Fig. 5.5.a, high level of transmission are achieved if a matching medium with $\epsilon_{mm} \in [20,80]$ is used, for $f \in [2,5]$ GHz. Different conclusions can be sought for the two iron-filled PLA scaffolds. The dispersion of IP30 and PP magneto-dielectrics are not identical, as can be verified from Fig. 5.4.a and 5.4.b. Therefore, slight differences in the transmission maps can be observed in Fig. 5.5.b and 5.5.c. For these materials, a region where the transmission coefficient is around 0.8 can be found around 2.45 GHz for IP30 and the PP scaffolds and $\epsilon_{mm} \simeq 20$. Other maxima in the transmission can be achieved for $\epsilon_{mm} > 40$ and $f > 4$ GHz. The maxima are reported in Tab. 5.2. Given these findings, the ISM frequencies of 434 and 915 MHz, 2.45 and 5.8 GHz could be tested. From our results, we can choose $\epsilon_{mm} \simeq 40$ for all the scaffolds.

The propagation for the proposed simplified model (Fig. 5.1.b) could be used to study if

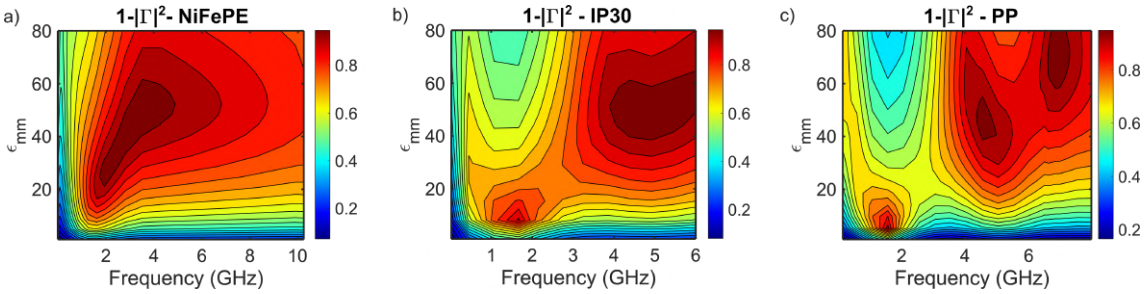

Figure 5.5. a) Transmission coefficient as a function of frequency (f) and the properties of the matching medium (ϵ_{mm}) for the NiFe-PE scaffold. b) Transmission coefficient as a function of frequency (f) and the properties of the matching medium (ϵ_{mm}) for the IP30 Fe-PLA. c) Transmission coefficient as a function of frequency (f) and the properties of the matching medium (ϵ_{mm}) for the Proto-Pasta MagS. The transmission is evaluated a the matching medium-skin interface.

Table 5.2. Comparison of different methods of drug delivery of TGF-β and VEGF.

Material	ϵ_{mm}	f (GHz)
IP30	58.455	5.2
NiFe-PE	10	4.6
PP	66.833	7.25

differences in the transmitted/reflected MW signal during HT arise. By setting $\epsilon_{mm} \simeq 40$, we evaluated the transmission coefficient during a simulated HT. The findings are reported in Fig. 5.6.a-5.6.c. We can notice that few frequency spots offer a significant variation in the transmission during the treatment time. The IP30 and PP MagS exhibit a similar response.

Given that any MWI inverse problem would be carried out in a differential scenario, we investigated if significant differences in the transmission coefficient during the thermal therapy of bone tumors with MagS arise. The evaluation of the figure of merit defined by Eq. (5.11) is shown in 5.6.d-5.6.f. For the three magneto-dielectric scaffolds large variations (at least ∼20-30 dB) occurs in some non-ISM bands, such as around 4-5 GHz. However, the permalloy material, exhibit significant changes in the MWI signal levels at lower frequencies ($f < 2$ GHz). The two PLA-based implant show similar features, but the differences in the magnitude is large, since the PP material has a wider dynamic range. With these information, we can investigate better what is occurring at specific frequencies during the treatment time, and, also, try to correlate our simplified propagation analysis with the HT simulations.

In Fig. 5.7, we report the relative changes in the transmission coefficient, at the first interfaces, over the treatment time, with superimposed the average tumor temperature derived from the simulations. At the lowest frequency of 434 MHz (Fig. 5.7.a), as the average tumor temperature increases, the transmission coefficient increases of about 15 dB for the IP30 and PP scaffold, and of more than 30 dB for the NiFePe material. As the external RF field is turned off and the biological system cools down, the transmission coefficient almost recovers its initial value, with an almost

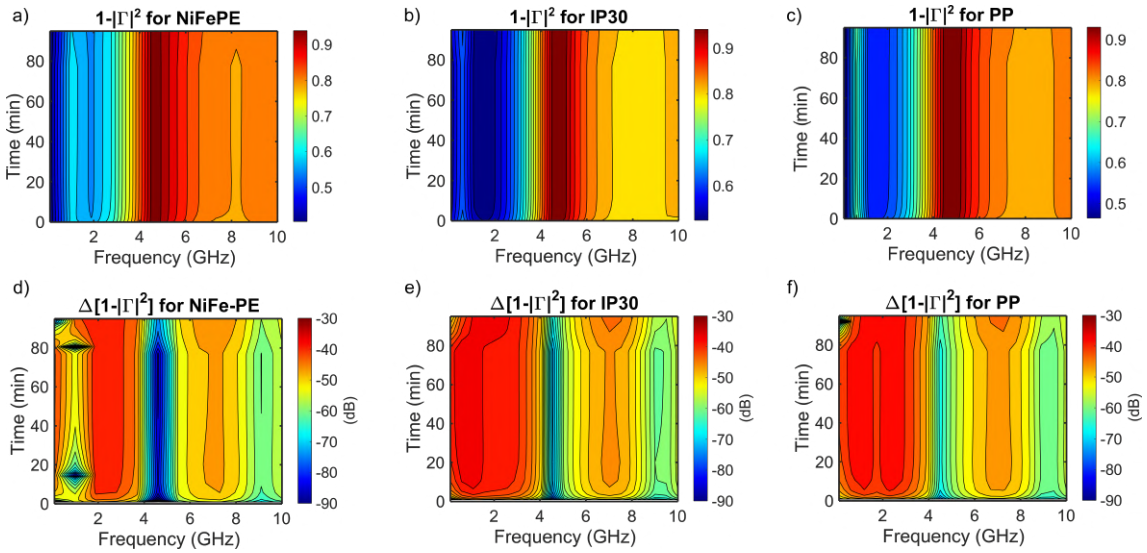

Figure 5.6. Transmission coefficient at the matching medium-skin interface, for $\epsilon_{mm} = 40$, as a function of treatment time and frequency, for the a) NiFe-PE magneto dielectric implant, b) IP30 magnetic scaffold and c) PP magnetic PLA. Difference, in dB, between the transmission coefficient evaluated at the initial time $t = 0$ and during the treatment for the a) NiFe-PE magneto dielectric implant, b) IP30 magnetic scaffold and c) PP magnetic PLA.

negligible lag (∼1 min). In Fig. 5.7.a, we highlighted the therapeutic range of HT (41-45°C). Given the variations, we can hypothesize that an empirical threshold can be established to identify the changes in the target temperature. On the other hand, at 915 MHz differences in the materials appears. It is remarkable that for the case of a NiFe-PE scaffold, abrupt changes (> 25 dB) at the peak temperature occurs (5.7.b). On the other hand, the curves for the IP30 and PP materials exhibit a ∼10 dB decrease as the HT is terminated. As the working frequency increases and $f = 2.45$ GHz, the dynamic range of the difference in the transmission coefficient reduces, as can be noticed in Fig. 5.7.c. The differences between the three MagS candidates is narrower and at the initial time ($t = 0$) the conditions are almost identical. As the MagS and the tumor are heated, a ∼7-10 dB increase can be noticed (Fig. 5.7.c). At $t = 80$ min, the PP scaffold exhibit a reduction in the differential transmission coefficient, whilst in the case of IP30 magneto-dielectric implant the figure of merit increases (±2 dB). The NiFe-PE retains an intermediate behavior. For the highest ISM frequency of $f = 5.8$ GHz, similar considerations holds and the differences between the materials is lower, as shown in Fig. 5.7.c. The differences in the findings in Fig. 5.7.a-b from that given in Fig. 5.7.c-d can be due to the increased frequency and, then, to the reduced penetration depth, which results in a lower mark of the EM properties change due to the MagS heating.

We investigated the possibility of using microwave as a tool for monitoring the HT of bone tumors using MagS. We developed a simplified monodimensional propagation model for a layered planar geometry (5.1.b). We identified suitable matching medium properties and the possible working frequencies. By simulating the HT with our nonlinear and multiphysics model, we assumed

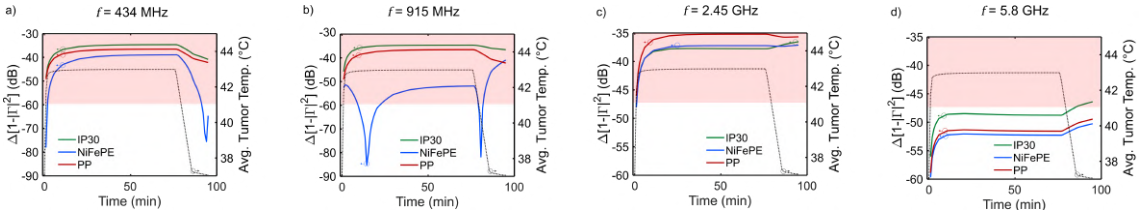

Figure 5.7. Difference in the transmission coefficient evaluated at the first time and during the simulated hyperthermia treatment a) as a function of treatment time (in dB), and b) as a function of tumor temperature (in dB).

temperature/time-dependent EM properties and evaluated in silico the dynamic response of the MW signal transmission during the HT with three different ferromagnetic scaffolds. We have found that a lossless matching medium with $\epsilon_{mm} = 40$ ensure suitable transmission for all the tested magneto-dielectric implants. In this framework, we analyzed the transmission coefficients as a function of the treatment time and over frequencies. The changes in the transmission from the initial time were evaluated for the major ISM bands of 434, 915 MHz and 2.45, 5.8 GHz. Our study identified the levels of signal changes, highlighting that these variation could be ascribed and correlated to the variation of the MagS or tumor temperature.

Given the promising results for our simplified case, the proposed analysis would be extended to a 2D or 3D cylindrical geometry to assess if similar variations in the propagation occurs. Then, with all the information of the forward propagation problem, the design of a simplified system could be performed and numerically tested, as first. By relying on the works on MNPs and MWI [77–82], an inverse problem could be setup. In particular, considering differential scattering data matrix ($\Delta\underline{S}$) for p and q antennas, it is possible to define the scattering element $\Delta s_{p,q}$ as [77–82]

$$\Delta s_{p,q} = \int_{\Omega_{mm}} \mathbf{G}^{EM}(\mathbf{r_p},\mathbf{r}) \cdot \Delta\chi(\mathbf{r})\mathbf{H}_q(\mathbf{r}) \tag{5.17}$$

where the electric-magnetic Greens' function for the problem in hand (Fig. 5.1.a) is $\mathbf{G}^{EM}$, and accounts for the $\mathbf{E}$ field radiated by a magnetic elementary source, located in the position $\mathbf{r}$, and measured at the location $\mathbf{r}_p$. The magnetic contrast in the systems is $\Delta\chi(\mathbf{r})$, whilst $\mathbf{H}_q$ is the magnetic field induced in the tissues at site $\mathbf{r}_q$ [77–82]. The solution of Eq. (5.17) can provide relevant information about the MagS properties and their evolution during the HT of bone tumors. However, the information about the dielectric contrast, which is also helpful for deriving information about the dynamics of tumor temperature, calls for suitable setting of the scattering problem [77–82]. Anyway, the non-linear, ill-posed problem (5.17) can be solved relying on qualitative [267], quantitative [261] or machine learning-based [262] methods. With these tools, the planning of experiments and validation tests could be devised and performed, thus paving the route for innovative and effective modalities in the hyperthermia treatment of tumors using MagS.

Chapter 6

Conclusions

In this thesis we investigated the modeling, design and characterization of magnetic scaffolds for biomedical applications at radiofrequency. To this aim, in Chap. 1, we critically reviewed the state of the art about magnetic implants to be used for tissue engineering, drug delivery and hyperthermia of bone tumors. We identified that an engineering point of view is missing to drive quantitatively the design of these materials or properly use them for the aforementioned applications.

Given that a relevant and appealing application of MagS is their potential use as thermoseed for bone cancer treatment, in Chap. 2 we propose a nonlinear, multiphysics model to investigate and plan the hyperthermia treatment with these innovative multifunctional biomaterials.

Having studied how to link the MagS properties with an effective therapeutic outcome, in Chap. 3 we designed, manufactured, characterized and model two sets of MagS. In Sect. 3.1 we investigated experimentally and in silico how the loading pattern of the magnetic nanoparticles in the biomaterial could affect and impact the HT. Our findings highlight that the inhomogeneous loading calls for a more in-depth analysis.
In Sect. 3.2 we designed biomimetic ferromagnetic scaffolds with both hyperthermic and regenerative potential. Furthermore, we investigated how to reliably estimate the SAR of MagS by performing extensive experiments and supporting them with multiphysics simulations. A novel protocol is proposed.

Since MagS can also be the core element of innovative drug delivery system remotely controlled by static or dynamic magnetic field, in Chap. 4, we dealt with the modeling of an innovative MDD strategy for bone repair. To this end, a multiphysics model was developed to describe the static attraction of magnetic carriers, the RF-heating triggering of growth factor release and, also, the biological effects. We found that MagS can drive an effective and faster bone regeneration. The numerical framework could be used to setup experiments for validation and test.

Finally, in Chap. 5, we studied the feasibility of using microwave to monitor the hyperthermia treatment of bone tumors with MagS. In particular, we developed a simplified propagation model and coupled it to the HT models in order to identify matching medium properties and working

frequencies suitable to ensure significant transmission, for three different ferromagnetic scaffold, and studied the dynamic variation of the MW signal during the thermal therapy. Our preliminary findings are promising and allow to setup more refined analysis.

6.1 Contributions Summary

The research under this thesis resulted in the following contributions:

- In Chap. 1, as novel, extensive and critical analysis of the state-of-the-art about magnetic scaffolds was performed and the lack of quantitative rationales for designing and using these multifunctional biomaterials for tissue engineering, drug delivery and hyperthermia was found.

- MagS can be a powerful tool for treating bone tumors with interstitial hyperthermia, and therefore, in Chap. 2, we challenged the modeling of this innovative therapy and its treatment planning. In particular:

  The complex magnetic susceptibility of MagS was better understood, by proposing a Cole-Cole model which was validated against literature data.

  An analytical, closed-form solution to the bio-heat transfer problem related to the HT of bone tumors with MagS in a spherical geometry was found, so that the intrinsic material and extrinsic field parameters can be related to the temperature increase in the bone tumor.

  Given that during the HT the physical properties of MagS and biological tissues varies with the system temperature, we proposed a nonlinear, multiphysics model to solve a coupled electromagneto-thermal set of equations and investigate the HT in silico on 2D geometries.

  Our numerical experiments highlighted that magnetic field inhomogeneities and a non-uniform loading of the magnetic nanoparticles in the biomaterial can lead to the selection of different treatment parameters or the misleading estimation of the therapeutic outcome.

- In Chap. 3, we made us of the gained knowledge about MagS to design, characterize and test two different kind of MagS.

  In Sect. 3.1, we developed a drop-casting procedure to control the loading pattern of MNPs in MagS.

  We used different morphological and physical characterization methods to retrieve MagS intrinsic properties, which were used to investigate numerically how the MNPs distribution impacts the HT outcome, finding that homogeneous loading and annular patterns can be effective for treating bone cancers with interstitial RF heating.

  In Sect. 3.2, we designed biomimetic scaffolds based on TPMS, with regenerative potential, then 3D printed them with a commercial ferromagnetic PLA filament, and tested their hyperthermic potential both experimentally and in silico.

To deal with the reliable estimation of the SAR of MagS, several experimental setups and thermometric methods were adopted, leading to the proposal of a protocol for averaging the measured temperatures and quantifying the hyperthermic potential in a robust way.

- In Chap. 4, we developed a multiphysics model to evaluate, for the first time, the use of MagS as core element of an innovative magnetic drug delivery system.
- The feasibility of using microwave as noninvasive, nondestructive tool to remotely monitor the hyperthermia treatment of bone tumors using magnetic scaffolds was investigated, for the first time, in Chapter 5.

6.2 Take-Home Messages

- Superparamagnetic scaffolds with high saturation magnetization are appealing for tissue engineering, drug delivery and hyperthermia applications.
- Ferromagnetic scaffolds can be used for HT and to active devices for a microwave-based monitoring of the thermal therapy.
- Simplified modeling of the HT of bone tumors with MagS can lead to overestimation of the extrinsic treatment parameter. Therefore, magnetic field inhomogeneities and materials non-linearities must be included in the design of MagS and in the treatment planning.
- Ferromagnetic scaffolds with TPMS architecture can be effective for performing hyperthermia treatment ($300 < f < 450\,\text{kHz}$).
- The SAR of MagS vary in the biomaterial volume, due to the loading pattern and temperature sampling, thus calling for a precise thermometric method for performing a calorimetric measurement of the hyperthermic potential.
- The uncertainty and variability in the SAR measurements can be reduced by following our protocol of averaging the temperature curves recovered at different scaffold locations.
- MagS can be used as core element of magnetic drug delivery strategy.
- Magnetic nano-carriers of growth factors could be attracted to high saturation MagS under the action of moderate-to-high static magnetic field.
- The spatial distribution of the MNPs can be controlled by the shape and magnetization of MagS.
- The RF-heating for triggering the release of the GFs has to be carefully controlled in terms of exposure parameters.

- Compared to traditional drug delivery strategy, the MDD with MagS results in a more homogeneous new bone formation.
- The use of MWI for monitoring the HT of bone tumors performed with MagS could be feasible.
- The average temperature variations of the EM properties of biological tissues and MagS during the HT results in significant changes in the MW signal transmission, thus allowing to correlate the outcome of the thermal therapy with the signal propagation.

6.3 Future Research Directions

This thesis focused on the modeling, design and characterization of magnetic scaffolds for biomedical applications. Despite the contributions are several and significant, there still are interesting and relevant challenges that demands for investigation:

- **Biocompatibility.** Given that the ultimate application of magnetic scaffolds is their implantation to be used as thermoseeds for bone tumors, as core elements for magnetically targeted drug delivery and as active device for microwave monitoring strategies, it is mandatory, for the multifunctional systems manufactured in this thesis, to experimentally determine their in vitro and in vivo the biocompatibility [8–10, 12, 13, 15].
- **Micromagnetic Modeling.** We have highlighted that in the literature about MagS there is lack of works which dealt with the modeling and with the fundamental understanding of the magnetic response, as well as the treatment planning. In this regards, micromagnetic simulations have never been applied to magnetic bioceramic or polymer loaded with MNPs. Recently, it was demonstrated that optimal size of permalloy nanodisk and the AC field parameters to achieve therapeutic SAR could be find multi-scale simulations, relying on micromagnetics and electromagneto-thermal models [278]. This same approach could be adapted and extended to the design of MagS.
- **Microwave Theranostics.** The use of MW as a tool for monitoring the HT is feasible, as highlighted in Chap. 5, but the extension to 2D and 3D, the development of inverse problem, the design of suitable systems, as well as experimental tests has to be performed. Furthermore, the use of MWI as alternative tool for assessing the implant integration in the post-HT phase could be studied with the developed framework.
- **Magnetic Particle Imaging.** MPI is an new, noninvasive and tomographic imaging technique which make use of static and dynamic magnetic fields to exploit SPM MNPs as tracers, as the only source of signals in tissues [83]. The use of MPI as diagnostic means to monitor MFH is currently under study [279]. In this framework, MagS could be monitored

during HT and during tissue repair with commercial MPI scans to track temperature changes or assess the biomaterial degradation.

- **NIR Photo-Thermal Therapy of Bone Tumors.** Recently, the treatment of bone diseases and bone tissue regeneration through NIR light-responsive scaffolds was reviewed [280]. In this field, the utmost relevant challenge is to design and manufacture a light-responsive scaffold capable of minimal invasiveness and high selectivity. Carbon-based nanomaterials, metals, metal oxides and sulfides, MXenes or organic nanostructures have been incorporated in biomaterials [280]. However, there is room for studying different nano-systems, biomaterials, manufacturing approaches or modeling. In this framework, recently, we investigated how to engineer the depletion layer in Sn:In_2O_3/In_2O_3 core-shell nanocrystals to achieve controlled energetic band profiles, electronic and optical properties [281]. Future work can deal with the engineered design of metal oxide nanocrystals, to be embedded in biomimetic TPMS scaffolds, with properties tuned and optimized to perform an effective photothermal treatment of bone cancers.

Bibliography

[1] H. Qu, H. Fu, Z. Han, and Y. Sun, "Biomaterials for bone tissue engineering scaffolds: a review," *RSC advances*, vol. 9, no. 45, pp. 26 252–26 262, 2019.

[2] G. L. Koons, M. Diba, and A. G. Mikos, "Materials design for bone-tissue engineering," *Nature Reviews Materials*, vol. 5, no. 8, pp. 584–603, 2020.

[3] S. Amukarimi, S. Ramakrishna, and M. Mozafari, "Smart biomaterials-a proposed definition and overview of the field," *Current Opinion in Biomedical Engineering*, p. 100311, 2021.

[4] J. Liao, R. Han, Y. Wu, and Z. Qian, "Review of a new bone tumor therapy strategy based on bifunctional biomaterials," *Bone Research*, vol. 9, no. 1, pp. 1–13, 2021.

[5] F. Khan and M. Tanaka, "Designing smart biomaterials for tissue engineering," *International journal of molecular sciences*, vol. 19, no. 1, p. 17, 2018.

[6] M. B. Lodi and A. Fanti, "Multiphysics modeling of magnetic scaffolds for biomedical applications," in *2021 IEEE 11th International Conference Nanomaterials: Applications & Properties (NAP)*. IEEE, 2021, pp. 1–4.

[7] D. Bahadur and J. Giri, "Biomaterials and magnetism," *Sadhana*, vol. 28, no. 3, pp. 639–656, 2003.

[8] A. Baeza, D. Arcos, and M. Vallet-Regí, "Thermoseeds for interstitial magnetic hyperthermia: from bioceramics to nanoparticles," *Journal of Physics: Condensed Matter*, vol. 25, no. 48, p. 484003, Nov. 2013. [Online]. Available: https://doi.org/10.1088/0953-8984/25/48/484003

[9] Y. Li, G. Huang, X. Zhang, B. Li, Y. Chen, T. Lu, T. J. Lu, and F. Xu, "Magnetic hydrogels and their potential biomedical applications," *Advanced Functional Materials*, vol. 23, no. 6, pp. 660–672, 2013.

[10] H.-Y. Xu and N. Gu, "Magnetic responsive scaffolds and magnetic fields in bone repair and regeneration," *Frontiers of Materials Science*, vol. 8, no. 1, pp. 20–31, 2014.

[11] A. A. Adedoyin and A. K. Ekenseair, "Biomedical applications of magneto-responsive scaffolds," *Nano Research*, vol. 11, no. 10, pp. 5049–5064, 2018.

[12] B. Smolková, M. Uzhytchak, A. Lynnyk, Š. Kubinová, A. Dejneka, and O. Lunov, "A critical review on selected external physical cues and modulation of cell behavior: Magnetic nanoparticles, non-thermal plasma and lasers," *Journal of functional biomaterials*, vol. 10, no. 1, p. 2, 2019.

[13] M. Miola, Y. Pakzad, S. Banijamali, S. Kargozar, C. Vitale-Brovarone, A. Yazdanpanah, O. Bretcanu, A. Ramedani, E. Vernè, and M. Mozafari, "Glass-ceramics for cancer treatment: so close, or yet so far?" *Acta biomaterialia*, vol. 83, pp. 55–70, 2019.

[14] J. Peng, J. Zhao, Y. Long, Y. Xie, J. Nie, and L. Chen, "Magnetic materials in promoting bone regeneration," *Frontiers in Materials*, vol. 6, p. 268, 2019.

[15] S. S. Danewalia and K. Singh, "Bioactive glasses and glass–ceramics for hyperthermia treatment of cancer: State-of-art, challenges and future perspectives," *Materials Today Bio*, p. 100100, 2021.

[16] O. Sedighi, A. Alaghmandfard, M. Montazerian, and F. Baino, "A critical review of bioceramics for magnetic hyperthermia," *Journal of the American Ceramic Society*, 2021.

[17] P. I. Soares, J. Romao, R. Matos, J. C. Silva, and J. P. Borges, "Design and engineering of magneto-responsive devices for cancer theranostics: Nano to macro perspective," *Progress in Materials Science*, vol. 116, p. 100742, 2021.

[18] M. Angelakeris, "Magnetic nanoparticles: A multifunctional vehicle for modern theranostics," *Biochimica et Biophysica Acta (BBA)-General Subjects*, vol. 1861, no. 6, pp. 1642–1651, 2017.

[19] S. Laurent, D. Forge, M. Port, A. Roch, C. Robic, L. Vander Elst, and R. N. Muller, "Magnetic iron oxide nanoparticles: synthesis, stabilization, vectorization, physicochemical characterizations, and biological applications," *Chemical reviews*, vol. 108, no. 6, pp. 2064–2110, 2008.

[20] A. Akbarzadeh, M. Samiei, and S. Davaran, "Magnetic nanoparticles: preparation, physical properties, and applications in biomedicine," *Nanoscale research letters*, vol. 7, no. 1, pp. 1–13, 2012.

[21] Q. A. Pankhurst, J. Connolly, S. K. Jones, and J. Dobson, "Applications of magnetic nanoparticles in biomedicine," *Journal of physics D: Applied physics*, vol. 36, no. 13, p. R167, 2003.

[22] A. K. Gupta and M. Gupta, "Synthesis and surface engineering of iron oxide nanoparticles for biomedical applications," *biomaterials*, vol. 26, no. 18, pp. 3995–4021, 2005.

[23] Q. Pankhurst, N. Thanh, S. Jones, and J. Dobson, "Progress in applications of magnetic nanoparticles in biomedicine," *Journal of Physics D: Applied Physics*, vol. 42, no. 22, p. 224001, 2009.

[24] R. Skomski, *Simple models of magnetism*. Oxford University Press on Demand, 2008.

[25] K. Ohura, M. Ikenaga, T. Nakamura, T. Yamamuro, Y. Ebisawa, T. Kokubo, Y. Kotoura, and M. Oka, "A heat-generating bioactive glass–ceramic for hyperthermia," *Journal of Applied Biomaterials*, vol. 2, no. 3, pp. 153–159, 1991.

[26] P. Ji, Y. Wang, M. Zhang, B. Li, and G. Zhang, "P2o5-fe2o3-cao-sio2 ferromagnetic glass-ceramics for hyperthermia," *International Journal of Applied Ceramic Technology*, vol. 15, no. 5, pp. 1261–1267, 2018.

[27] S. Dong, Y. Chen, L. Yu, K. Lin, and X. Wang, "Magnetic hyperthermia–synergistic h2o2 self-sufficient catalytic suppression of osteosarcoma with enhanced bone-regeneration bioactivity

by 3d-printing composite scaffolds," *Advanced Functional Materials*, vol. 30, no. 4, p. 1907071, 2020.

[28] A. Tampieri, M. Iafisco, M. Sandri, S. Panseri, C. Cunha, S. Sprio, E. Savini, M. Uhlarz, and T. Herrmannsdorfer, "Magnetic bioinspired hybrid nanostructured collagen–hydroxyapatite scaffolds supporting cell proliferation and tuning regenerative process," *ACS applied materials & interfaces*, vol. 6, no. 18, pp. 15 697–15 707, 2014.

[29] ——, "Magnetic bioinspired hybrid nanostructured collagen–hydroxyapatite scaffolds supporting cell proliferation and tuning regenerative process," *ACS applied materials & interfaces*, vol. 6, no. 18, pp. 15 697–15 707, 2014.

[30] M. Kamitakahara, N. Ohtoshi, M. Kawashita, and K. Ioku, "Spherical porous hydroxyapatite granules containing composites of magnetic and hydroxyapatite nanoparticles for the hyperthermia treatment of bone tumor," *Journal of Materials Science: Materials in Medicine*, vol. 27, no. 5, p. 93, 2016.

[31] F. D. Cojocaru, V. Balan, M. I. Popa, A. Lobiuc, A. Antoniac, I. V. Antoniac, and L. Verestiuc, "Biopolymers–calcium phosphates composites with inclusions of magnetic nanoparticles for bone tissue engineering," *International journal of biological macromolecules*, vol. 125, pp. 612–620, 2019.

[32] Y. Zhao, T. Fan, J. Chen, J. Su, X. Zhi, P. Pan, L. Zou, and Q. Zhang, "Magnetic bioinspired micro/nanostructured composite scaffold for bone regeneration," *Colloids and Surfaces B: Biointerfaces*, vol. 174, pp. 70–79, 2019.

[33] A. Farzin, M. Fathi, and R. Emadi, "Multifunctional magnetic nanostructured hardystonite scaffold for hyperthermia, drug delivery and tissue engineering applications," *Materials Science and Engineering: C*, vol. 70, pp. 21–31, Jan. 2017. [Online]. Available: https://doi.org/10.1016/j.msec.2016.08.060

[34] S. Sahmani, A. Khandan, S. Saber-Samandari, and M. Aghdam, "Vibrations of beam-type implants made of 3d printed bredigite-magnetite bio-nanocomposite scaffolds under axial compression: Application, communication and simulation," *Ceramics International*, vol. 44, no. 10, pp. 11 282–11 291, Jul. 2018. [Online]. Available: https://doi.org/10.1016/j.ceramint.2018.03.173

[35] M. Fernandes, D. Correia, A. da Costa, S. Ribeiro, M. Casal, S. Lanceros-Méndez, and R. Machado, "Multifunctional magnetically responsive biocomposites based on genetically engineered silk-elastin-like protein," *Composites Part B: Engineering*, vol. 153, pp. 413–419, 2018.

[36] F. Ghorbani, A. Zamanian, A. Shams, A. Shamoosi, and A. Aidun, "Fabrication and characterisation of super-paramagnetic responsive plga–gelatine–magnetite scaffolds with the unidirectional porous structure: a physicochemical, mechanical, and in vitro evaluation," *IET nanobiotechnology*, vol. 13, no. 8, pp. 860–867, 2019.

[37] D. J. Indrani, B. S. Purwasasmita, A. A. Wisnu, and J. Simanjuntak, "Preparation and characterization of magnetic carbonate apatite/chitosan/alginate composite scaffold," in

Materials Science Forum, vol. 827. Trans Tech Publ, 2015, pp. 75–80.

[38] Y. Sapir-Lekhovitser, M. Y. Rotenberg, J. Jopp, G. Friedman, B. Polyak, and S. Cohen, "Magnetically actuated tissue engineered scaffold: insights into mechanism of physical stimulation," *Nanoscale*, vol. 8, no. 6, pp. 3386–3399, 2016.

[39] S. Aliramaji, A. Zamanian, and M. Mozafari, "Super-paramagnetic responsive silk fibroin/chitosan/magnetite scaffolds with tunable pore structures for bone tissue engineering applications," *Materials Science and Engineering: C*, vol. 70, pp. 736–744, 2017.

[40] R. K. Singh, K. D. Patel, J. H. Lee, E.-J. Lee, J.-H. Kim, T.-H. Kim, and H.-W. Kim, "Potential of magnetic nanofiber scaffolds with mechanical and biological properties applicable for bone regeneration," *PloS one*, vol. 9, no. 4, p. e91584, 2014.

[41] N. H. A. Ngadiman, A. Idris, M. Irfan, D. Kurniawan, N. M. Yusof, and R. Nasiri, "γ-fe2o3 nanoparticles filled polyvinyl alcohol as potential biomaterial for tissue engineering scaffold," *Journal of the mechanical behavior of biomedical materials*, vol. 49, pp. 90–104, 2015.

[42] E. Moradian, S. M. Rabiee, N. Haghighipour, and H. Salimi-Kenari, "Fabrication and physicochemical characterization of a novel magnetic nanocomposite scaffold: Electromagnetic field effect on biological properties," *Materials Science and Engineering: C*, vol. 116, p. 111222, 2020.

[43] N. Bock, A. Riminucci, C. Dionigi, A. Russo, A. Tampieri, E. Landi, V. A. Goranov, M. Marcacci, and V. Dediu, "A novel route in bone tissue engineering: magnetic biomimetic scaffolds," *Acta Biomaterialia*, vol. 6, no. 3, pp. 786–796, 2010.

[44] A. Riminucci, C. Dionigi, C. Pernechele, G. de Pasquale, T. de Caro, G. M. Ingo, F. Mezzadri, N. Bock, M. Solzi, G. Padeletti, M. Sandri, A. Tampieri, and V. A. Dediu, "Magnetic and morphological properties of ferrofluid-impregnated hydroxyapatite/collagen scaffolds," *Science of Advanced Materials*, vol. 6, no. 12, pp. 2679–2687, Dec. 2014. [Online]. Available: https://doi.org/10.1166/sam.2014.1986

[45] C. Chen, J. Wu, S. Wang, and H. Shao, "Effect of fe3o4 concentration on 3d gel-printed fe3o4/casio3 composite scaffolds for bone engineering," *Ceramics International*, 2021.

[46] F. Xu, C.-a. M. Wu, V. Rengarajan, T. D. Finley, H. O. Keles, Y. Sung, B. Li, U. A. Gurkan, and U. Demirci, "Three-dimensional magnetic assembly of microscale hydrogels," *Advanced materials*, vol. 23, no. 37, pp. 4254–4260, 2011.

[47] C. Dang, N. Bhattarai, D. Edmondson, A. Cooper, and M. Zhang, "Aligning poly (l-lactic acid) nanofibers with magnetic fe3o4 nanoparticles using modified electrospinning methods," *J. Undergrad. Res. Bioeng*, vol. 5, pp. 29–32, 2009.

[48] M. Miola, A. Bellare, F. Laviano, R. Gerbaldo, and E. Verne, "Bioactive superparamagnetic nanoparticles for multifunctional composite bone cements," *Ceramics International*, vol. 45, no. 12, pp. 14 533–14 545, 2019.

[49] J. Zhang, S. Zhao, M. Zhu, Y. Zhu, Y. Zhang, Z. Liu, and C. Zhang, "3d-printed magnetic fe 3 o 4/mbg/pcl composite scaffolds with multifunctionality of bone regeneration, local anticancer drug delivery and hyperthermia," *Journal of Materials Chemistry B*, vol. 2, no. 43,

pp. 7583–7595, 2014.

[50] P. R. Stauffer, T. C. Cetas, and R. C. Jones, "Magnetic induction heating of ferromagnetic implants for inducing localized hyperthermia in deep-seated tumors," *IEEE Transactions on Biomedical Engineering*, vol. BME-31, no. 2, pp. 235–251, Feb. 1984. [Online]. Available: https://doi.org/10.1109/tbme.1984.325334

[51] F. Pelaez, N. Manuchehrabadi, P. Roy, H. Natesan, Y. Wang, E. Racila, H. Fong, K. Zeng, A. M. Silbaugh, J. C. Bischof *et al.*, "Biomaterial scaffolds for non-invasive focal hyperthermia as a potential tool to ablate metastatic cancer cells," *Biomaterials*, vol. 166, pp. 27–37, 2018.

[52] A. M. Osintsev, I. L. Vasilchenko, D. B. Rodrigues, P. R. Stauffer, V. I. Braginsky, V. V. Rynk, E. S. Gromov, A. Y. Prosekov, A. D. Kaprin, and A. A. Kostin, "Characterization of ferromagnetic composite implants for tumor bed hyperthermia," *IEEE Transactions on Magnetics*, vol. 57, no. 9, pp. 1–8, 2021.

[53] M. T. Lopez-Lopez, G. Scionti, A. C. Oliveira, J. D. Duran, A. Campos, M. Alaminos, and I. A. Rodriguez, "Generation and characterization of novel magnetic field-responsive biomaterials," *PLoS One*, vol. 10, no. 7, p. e0133878, 2015.

[54] H.-M. Yun, S.-J. Ahn, K.-R. Park, M.-J. Kim, J.-J. Kim, G.-Z. Jin, H.-W. Kim, and E.-C. Kim, "Magnetic nanocomposite scaffolds combined with static magnetic field in the stimulation of osteoblastic differentiation and bone formation," *Biomaterials*, vol. 85, pp. 88–98, 2016.

[55] P. S. Castro, M. Bertotti, A. F. Naves, L. H. Catalani, D. R. Cornejo, G. D. Bloisi, and D. F. Petri, "Hybrid magnetic scaffolds: The role of scaffolds charge on the cell proliferation and ca2+ ions permeation," *Colloids and Surfaces B: Biointerfaces*, vol. 156, pp. 388–396, 2017.

[56] U. D'Amora, T. Russo, A. Gloria, V. Rivieccio, V. D'Antò, G. Negri, L. Ambrosio, and R. De Santis, "3d additive-manufactured nanocomposite magnetic scaffolds: Effect of the application mode of a time-dependent magnetic field on hmscs behavior," *Bioactive materials*, vol. 2, no. 3, pp. 138–145, 2017.

[57] V. Goranov, T. Shelyakova, R. De Santis, Y. Haranava, A. Makhaniok, A. Gloria, A. Tampieri, A. Russo, E. Kon, M. Marcacci *et al.*, "3d patterning of cells in magnetic scaffolds for tissue engineering," *Scientific reports*, vol. 10, no. 1, pp. 1–8, 2020.

[58] R. De Santis, I. Papallo, I. Onofrio, V. Peluso, V. Gallicchio, A. Rega, V. D'Antò, G. Improta, M. Catauro, A. Gloria *et al.*, "Analyzing the role of magnetic features in additive manufactured scaffolds for enhanced bone tissue regeneration," in *Macromolecular Symposia*, vol. 396, no. 1. Wiley Online Library, 2021, p. 2000314.

[59] A. Markaki and A. Justin, "A magneto-active scaffold for stimulation of bone growth," *Materials Science and Technology*, vol. 30, no. 13, pp. 1590–1598, 2014.

[60] H. Zhang, J. Xia, X. Pang, M. Zhao, B. Wang, L. Yang, H. Wan, J. Wu, and S. Fu, "Magnetic nanoparticle-loaded electrospun polymeric nanofibers for tissue engineering," *Material Science Engineering: C*, vol. 73, pp. 537–543, Apr. 2017. [Online]. Available: https://doi.org/10.1016/j.msec.2016.12.116

[61] Z. Liu, S. Zhu, L. Liu, J. Ge, L. Huang, Z. Sun, W. Zeng, J. Huang, and Z. Luo, "A

magnetically responsive nanocomposite scaffold combined with schwann cells promotes sciatic nerve regeneration upon exposure to magnetic field," *International journal of nanomedicine*, vol. 12, p. 7815, 2017.

[62] S. Panseri, C. Cunha, T. D'Alessandro, M. Sandri, A. Russo, G. Giavaresi, M. Marcacci, C. T. Hung, and A. Tampieri, "Magnetic hydroxyapatite bone substitutes to enhance tissue regeneration: evaluation in vitro using osteoblast-like cells and in vivo in a bone defect," *PloS one*, vol. 7, no. 6, p. e38710, 2012.

[63] R. Koohkan, T. Hooshmand, D. Mohebbi-Kalhori, M. Tahriri, and M. T. Marefati, "Synthesis, characterization, and in vitro biological evaluation of copper-containing magnetic bioactive glasses for hyperthermia in bone defect treatment," *ACS Biomaterials Science & Engineering*, vol. 4, no. 5, pp. 1797–1811, 2018.

[64] J. He, H. Hu, X. Zeng, F. Lan, F. Wu, and Y. Wu, "A magnetic hydroxyapatite composite scaffold-based magnetic therapy for bone repair: an experimental study in canis lupus familiaris," *Regenerative Biomaterials*, vol. 4, no. 2, pp. 97–103, 2017.

[65] J. Meng, B. Xiao, Y. Zhang, J. Liu, H. Xue, J. Lei, H. Kong, Y. Huang, Z. Jin, N. Gu *et al.*, "Super-paramagnetic responsive nanofibrous scaffolds under static magnetic field enhance osteogenesis for bone repair in vivo," *Scientific reports*, vol. 3, no. 1, pp. 1–7, 2013.

[66] A. Matsumine, K. Takegami, K. Asanuma, T. Matsubara, T. Nakamura, A. Uchida, and A. Sudo, "A novel hyperthermia treatment for bone metastases using magnetic materials," *International Journal of Clinical Oncology*, vol. 16, no. 2, pp. 101–108, Mar. 2011. [Online]. Available: https://doi.org/10.1007/s10147-011-0217-3

[67] C. Qu, Q.-H. Qin, and Y. Kang, "A hypothetical mechanism of bone remodeling and modeling under electromagnetic loads," *Biomaterials*, vol. 27, no. 21, pp. 4050–4057, 2006.

[68] A. Bagde, A. Kuthe, S. Quazi, V. Gupta, S. Jaiswal, S. Jyothilal, N. Lande, and S. Nagdeve, "State of the art technology for bone tissue engineering and drug delivery," *Irbm*, vol. 40, no. 3, pp. 133–144, 2019.

[69] S. Kondaveeti, A. T. S. Semeano, D. R. Cornejo, H. Ulrich, and D. F. S. Petri, "Magnetic hydrogels for levodopa release and cell stimulation triggered by external magnetic field," *Colloids and Surfaces B: Biointerfaces*, vol. 167, pp. 415–424, 2018.

[70] M. Paulides, H. D. Trefna, S. Curto, and D. Rodrigues, "Recent technological advancements in radiofrequency-andmicrowave-mediated hyperthermia for enhancing drug delivery," *Advanced drug delivery reviews*, vol. 163, pp. 3–18, 2020.

[71] G. Calori, E. Mazza, M. Colombo, and C. Ripamonti, "The use of bone-graft substitutes in large bone defects: any specific needs?" *Injury*, vol. 42, pp. S56–S63, 2011.

[72] S. K. Samal, V. Goranov, M. Dash, A. Russo, T. Shelyakova, P. Graziosi, L. Lungaro, A. Riminucci, M. Uhlarz, M. Bañobre-López *et al.*, "Multilayered magnetic gelatin membrane scaffolds," *ACS applied materials & interfaces*, vol. 7, no. 41, pp. 23 098–23 109, 2015.

[73] S. Bettini, V. Bonfrate, Z. Syrgiannis, A. Sannino, L. Salvatore, M. Madaghiele, L. Valli, and G. Giancane, "Biocompatible collagen paramagnetic scaffold for controlled drug release,"

Biomacromolecules, vol. 16, no. 9, pp. 2599–2608, 2015.

[74] M. Filippi, B. Dasen, J. Guerrero, F. Garello, G. Isu, G. Born, M. Ehrbar, I. Martin, and A. Scherberich, "Magnetic nanocomposite hydrogels and static magnetic field stimulate the osteoblastic and vasculogenic profile of adipose-derived cells," *Biomaterials*, vol. 223, p. 119468, 2019.

[75] K. M. Sajesh, A. Ashokan, G. S. Gowd, T. B. Sivanarayanan, A. Unni, S. V. Nair, and M. Koyakutty, "Magnetic 3d scaffold: a theranostic tool for tissue regeneration and non-invasive imaging in vivo," *Nanomedicine: Nanotechnology, Biology and Medicine*, vol. 18, pp. 179–188, 2019.

[76] D. Bian, L. Qin, W. Lin, D. Shen, H. Qi, X. Shi, G. Zhang, H. Liu, H. Yang, J. Wang *et al.*, "Magnetic resonance (mr) safety and compatibility of a novel iron bioresorbable scaffold," *Bioactive materials*, vol. 5, no. 2, pp. 260–274, 2020.

[77] G. Bellizzi, O. M. Bucci, and I. Catapano, "Microwave cancer imaging exploiting magnetic nanoparticles as contrast agent," *IEEE Transactions on Biomedical Engineering*, vol. 58, no. 9, pp. 2528–2536, 2011.

[78] R. Scapaticci, G. Bellizzi, I. Catapano, L. Crocco, and O. M. Bucci, "An effective procedure for mnp-enhanced breast cancer microwave imaging," *IEEE Transactions on Biomedical Engineering*, vol. 61, no. 4, pp. 1071–1079, 2013.

[79] O. M. Bucci, L. Crocco, and R. Scapaticci, "On the optimal measurement configuration for magnetic nanoparticles-enhanced breast cancer microwave imaging," *IEEE Transactions on Biomedical Engineering*, vol. 62, no. 2, pp. 407–414, 2014.

[80] O. M. Bucci, G. Bellizzi, A. Borgia, S. Costanzo, L. Crocco, G. Di Massa, and R. Scapaticci, "Experimental framework for magnetic nanoparticles enhanced breast cancer microwave imaging," *IEEE Access*, vol. 5, pp. 16 332–16 340, 2017.

[81] O. M. Bucci, G. Bellizzi, S. Costanzo, L. Crocco, G. Di Massa, and R. Scapaticci, "Assessing detection limits in magnetic nanoparticle enhanced microwave imaging," *IEEE Access*, vol. 6, pp. 43 192–43 202, 2018.

[82] ——, "Experimental characterization of spurious signals in magnetic nanoparticles enhanced microwave imaging of cancer," *Sensors*, vol. 21, no. 8, p. 2820, 2021.

[83] J. Weizenecker, B. Gleich, J. Rahmer, H. Dahnke, and J. Borgert, "Three-dimensional real-time in vivo magnetic particle imaging," *Physics in Medicine & Biology*, vol. 54, no. 5, p. L1, 2009.

[84] M. M. Paulides, P. R. Stauffer, E. Neufeld, P. F. Maccarini, A. Kyriakou, R. A. Canters, C. J. Diederich, J. F. Bakker, and G. C. Van Rhoon, "Simulation techniques in hyperthermia treatment planning," *International Journal of Hyperthermia*, vol. 29, no. 4, pp. 346–357, 2013.

[85] N. R. Datta, H. P. Kok, H. Crezee, U. S. Gaipl, and S. Bodis, "Integrating loco-regional hyperthermia into the current oncology practice: Swot and tows analyses," *Frontiers in oncology*, vol. 10, p. 819, 2020.

[86] S.-Y. Lee, G. Fiorentini, A. M. Szasz, G. Szigeti, A. Szasz, and C. A. Minnaar, "Quo vadis

oncological hyperthermia (2020)?" *Frontiers in Oncology*, vol. 10, 2020.

[87] C. Meazza, S. Bastoni, and P. Scanagatta, "What is the best clinical approach to recurrent/refractory osteosarcoma?" *Expert review of anticancer therapy*, vol. 20, no. 5, pp. 415–428, 2020.

[88] H. Dobšíček Trefná, M. Schmidt, G. Van Rhoon, H. Kok, S. Gordeyev, U. Lamprecht, D. Marder, J. Nadobny, P. Ghadjar, S. Abdel-Rahman *et al.*, "Quality assurance guidelines for interstitial hyperthermia," *International Journal of Hyperthermia*, vol. 36, no. 1, pp. 276–293, 2019.

[89] H. P. Kok, E. N. Cressman, W. Ceelen, C. L. Brace, R. Ivkov, H. Grüll, G. Ter Haar, P. Wust, and J. Crezee, "Heating technology for malignant tumors: A review," *International Journal of Hyperthermia*, vol. 37, no. 1, pp. 711–741, 2020.

[90] L. Zhu, M. B. Altman, A. Laszlo, W. Straube, I. Zoberi, D. E. Hallahan, and H. Chen, "Ultrasound hyperthermia technology for radiosensitization," *Ultrasound in medicine & biology*, vol. 45, no. 5, pp. 1025–1043, 2019.

[91] H. D. Trefná and A. Ström, "Hydrogels as a water bolus during hyperthermia treatment," *Physics in Medicine & Biology*, vol. 64, no. 11, p. 115025, 2019.

[92] G. G. Bellizzi, T. Drizdal, G. C. van Rhoon, L. Crocco, T. Isernia, and M. M. Paulides, "The potential of constrained sar focusing for hyperthermia treatment planning: Analysis for the head & neck region," *Physics in Medicine & Biology*, vol. 64, no. 1, p. 015013, 2018.

[93] B. Mues, B. Bauer, A. A. Roeth, J. Ortega, E. M. Buhl, P. Radon, F. Wiekhorst, T. Gries, T. Schmitz-Rode, and I. Slabu, "Nanomagnetic actuation of hybrid stents for hyperthermia treatment of hollow organ tumors," *Nanomaterials*, vol. 11, no. 3, p. 618, 2021.

[94] M. B. B. Lodi, G. Muntoni, A. Ruggeri, A. Fanti, G. Montisci, and G. Mazzarella, "Towards the robust and effective design of hyperthermic devices: Case study of abdominal rhabdomyosarcoma with 3d perfusion," *IEEE Journal of Electromagnetics, RF and Microwaves in Medicine and Biology*, vol. 5, no. 3, pp. 197–205, 2020.

[95] A. Luetke, P. A. Meyers, I. Lewis, and H. Juergens, "Osteosarcoma treatment–where do we stand? a state of the art review," *Cancer treatment reviews*, vol. 40, no. 4, pp. 523–532, 2014.

[96] Y. Yang, L. Han, Z. He, X. Li, S. Yang, J. Yang, Y. Zhang, D. Li, Y. Yang, and Z. Yang, "Advances in limb salvage treatment of osteosarcoma," *Journal of bone oncology*, vol. 10, pp. 36–40, 2018.

[97] E. Santini-Araujo, R. Kali, F. Bertoni, and P. YK, *Tumors and Tumor-Like Lesions of Bone*. Springer-Verlag London, 2015.

[98] F. Schajowicz, *Histological typing of bone tumours*. Springer Science & Business Media, 2012.

[99] C. Fletcher, "Pathology and genetics of tumors of soft tissue and bone," *World Health Organization Classification of Tumors*, vol. 4, pp. 35–46, 2002.

[100] T. D. Peabody and S. Attar, *Orthopaedic Oncology*. Springer, 2016.

[101] I. Karmaniolou, A. Makris, K. Lamprou, and C. Staikou, "Perioperative management of

patients with bone and soft tissue tu-mors: a narrative review," *Acta Anæsthesiologica Belgica*, vol. 68, no. 1, pp. 1–12, 2017.

[102] V. Carina, V. Costa, M. Sartori, D. Bellavia, A. De Luca, L. Raimondi, M. Fini, and G. Giavaresi, "Adjuvant biophysical therapies in osteosarcoma," *Cancers*, vol. 11, no. 3, p. 348, 2019.

[103] Q.-Y. Fan, B.-A. Ma, X.-C. Qiu, Y.-L. Li, J. Ye, and Y. Zhou, "Preliminary report on treatment of bone tumors with microwave-induced hyperthermia," *Bioelectromagnetics: Journal of the Bioelectromagnetics Society, The Society for Physical Regulation in Biology and Medicine, The European Bioelectromagnetics Association*, vol. 17, no. 3, pp. 218–222, 1996.

[104] Q.-Y. Fan, B.-A. Ma, Y. Zhou, M.-H. Zhang, and X.-B. Hao, "Bone tumors of the extremities or pelvis treated by microwave-induced hyperthermia." *Clinical Orthopaedics and Related Research (1976-2007)*, vol. 406, no. 1, pp. 165–175, 2003.

[105] Q.-Y. Fan, Y. Zhou, M. Zhang, B. Ma, T. Yang, H. Long, Z. Yu, and Z. Li, "Microwave ablation of malignant extremity bone tumors," *Springerplus*, vol. 5, no. 1, pp. 1–6, 2016.

[106] K. Han, P. Dang, N. Bian, X. Chen, T. Yang, Q. Fan, Y. Zhou, T. Zhao, and P. Wang, "Is limb salvage with microwave-induced hyperthermia better than amputation for osteosarcoma of the distal tibia?" *Clinical Orthopaedics and Related Research®*, vol. 475, no. 6, pp. 1668–1677, 2017.

[107] W. Andrä, C. d'Ambly, R. Hergt, I. Hilger, and W. Kaiser, "Temperature distribution as function of time around a small spherical heat source of local magnetic hyperthermia," *Journal of Magnetism and Magnetic Materials*, vol. 194, no. 1-3, pp. 197–203, 1999.

[108] H. Bagaria and D. Johnson, "Analytical and numerical solution to a concentric sphere model and optimization for magnetic fluid hyperthermia treatment," *International Journal of Hyperthermia*, vol. 21, pp. 57–75, 2005.

[109] M. A. Giordano, G. Gutierrez, and C. Rinaldi, "Fundamental solutions to the bioheat equation and their application to magnetic fluid hyperthermia," *International Journal of Hyperthermia*, vol. 26, no. 5, pp. 475–484, 2010.

[110] S. C. Hill, D. A. Christensen, and C. H. Durney, "Power deposition patterns in magnetically-induced hyperthermia: a two-dimensional low-frequency numerical analysis," *International Journal of Radiation Oncology • Biology • Physics*, vol. 9, no. 6, pp. 893–904, 1983.

[111] E. Kurgan and P. Gas, "Treatment of tumors located in the human thigh using rf hyperthermia," *Electrical Review*, vol. 87, no. 12b, pp. 103–106, 2011.

[112] R. Martínez-Valdez, C. Trujillo-Romero, L. Castellanos, J. Gutiérrez-Martínez, A. Vera-Hernández, A. Ramos, and L. Leija, "Feasibility of the microwave and ultrasound ablation as alternatives to treat bone tumors," in *2017 Global Medical Engineering Physics Exchanges/Pan American Health Care Exchanges (GMEPE/PAHCE)*. IEEE, 2017, pp. 1–6.

[113] F. Lujan, B. Pinilla, J. Gutiérrez-Martínez, A. Vera-Hernández, L. Leija, and C. Trujillo-Romero, "Theoretical model of mw antennas to treat bone tumors: One slot and one slot choked antennas," in *2017 14th International Conference on Electrical Engineering, Computing*

Science and Automatic Control (CCE). IEEE, 2017, pp. 1–6.

[114] H. Arkin, L. Xu, and K. Holmes, "Recent developments in modeling heat transfer in blood perfused tissues," *IEEE Transactions on Biomedical Engineering*, vol. 41, no. 2, pp. 97–107, 1994.

[115] Z. Z. He, X. Xue, J. Xiao, and J. Liu, "Anatomical model-based finite element analysis of the combined cryosurgical and hyperthermic ablation for knee bone tumor," *Computer methods and programs in biomedicine*, vol. 112, no. 3, pp. 356–366, 2013.

[116] G. Bellizzi and O. M. Bucci, "On the optimal choice of the exposure conditions and the nanoparticle features in magnetic nanoparticle hyperthermia," *International Journal of Hyperthermia*, vol. 26, no. 4, pp. 389–403, 2010.

[117] A. Fanti, M. B. Lodi, G. Vacca, and G. Mazzarella, "Numerical investigation of bone tumor hyperthermia treatment using magnetic scaffolds," *IEEE Journal of Electromagnetics, RF and Microwaves in Medicine and Biology*, vol. 2, no. 4, pp. 294–301, 2018.

[118] M. B. Lodi, A. Fanti, A. Vargiu, M. Bozzi, and G. Mazzarella, "A multiphysics model for bone repair using magnetic scaffolds for targeted drug delivery," *IEEE Journal on Multiscale and Multiphysics Computational Techniques*, vol. 6, pp. 201–213, 2021.

[119] R. E. Rosensweig, "Heating magnetic fluid with alternating magnetic field," *Journal of magnetism and magnetic materials*, vol. 252, pp. 370–374, 2002.

[120] E. Myrovali, K. Papadopoulos, I. Iglesias, M. Spasova, M. Farle, U. Wiedwald, and M. Angelakeris, "Long-range ordering effects in magnetic nanoparticles," *ACS Applied Materials & Interfaces*, vol. 13, no. 18, pp. 21 602–21 612, 2021.

[121] A. F. Abu-Bakr and A. Y. Zubarev, "On the theory of magnetic hyperthermia: clusterization of nanoparticles," *Philosophical Transactions of the Royal Society A*, vol. 378, no. 2171, p. 20190251, 2020.

[122] R. K. Singh, M. Srivastava, N. K. Prasad, P. H. Shetty, and S. Kannan, "Hyperthermia effect and antibacterial efficacy of fe3co2 co-substitutions in ca3(po4)2 for bone cancer and defect therapy," *Journal of Biomedical Materials Research Part B: Applied Biomaterials*, vol. 106, no. 3, pp. 1317–1328, Jun. 2017. [Online]. Available: https://doi.org/10.1002/jbm.b.33921

[123] R. Hergt, R. Hiergeist, M. Zeisberger, G. Glockl, W. Weitschies, L. P. Ramirez, I. Hilger, Kaiser, and WA, "Enhancement of ac-losses of magnetic nanoparticles for heating applications," *Journal of Magnetism and Magnetic Materials*, vol. 280, no. 2-3, pp. 358–368, 2004.

[124] S. Van Berkum, J. T. Dee, A. P. Philipse, and B. H. Erné, "Frequency-dependent magnetic susceptibility of magnetite and cobalt ferrite nanoparticles embedded in paa hydrogel," *International Journal of Molecular Sciences*, vol. 14, no. 5, pp. 10 162–10 177, 2013.

[125] G. T. Landi, F. R. Arantes, D. R. Cornejo, A. F. Bakuzis, I. Andreu, and E. Natividad, "Ac susceptibility as a tool to probe the dipolar interaction in magnetic nanoparticles," *Journal of Magnetism and Magnetic Materials*, vol. 421, pp. 138–151, 2017.

[126] M. B. Lodi and A. Fanti, "Biomedical applications of biomaterials functionalized with magnetic nanoparticles," in *Smart Nanosystems for Biomedicine, Optoelectronics and Catalysis*.

IntechOpen, Nov. 2020. [Online]. Available: https://doi.org/10.5772/intechopen.89199

[127] A. Gloria, T. Russo, U. d'Amora, S. Zeppetelli, T. d'Alessandro, M. Sandri, M. Bañobre-López, Y. Piñeiro-Redondo, M. Uhlarz, A. Tampieri *et al.*, "Magnetic poly (ε-caprolactone)/iron-doped hydroxyapatite nanocomposite substrates for advanced bone tissue engineering," *Journal of the Royal society interface*, vol. 10, no. 80, p. 20120833, 2013.

[128] A. L. Elrefai, T. Sasayama, T. Yoshida, and K. Enpuku, "Magnetic core-size distribution of magnetic nanoparticles estimated from magnetization, ac susceptibility, and relaxation measurements," *IEEE Transactions on Magnetics*, vol. 53, no. 11, pp. 1–5, 2017.

[129] M. E. Villamin and Y. Kitamoto, "Influence of ph on dynamic magnetic susceptibility of iron-oxide nanoparticles in a chitosan hydrogel matrix," *IEEE Transactions on Magnetics*, vol. 55, no. 2, pp. 1–4, 2018.

[130] K. S. Cole and R. H. Cole, "Dispersion and absorption in dielectrics i. alternating current characteristics," *The Journal of chemical physics*, vol. 9, no. 4, pp. 341–351, 1941.

[131] A. Fanti, M. B. Lodi, and G. Mazzarella, "Enhancement of cell migration rate toward a superparamagnetic scaffold using lf magnetic fields," *IEEE Transactions on Magnetics*, vol. 52, no. 10, pp. 1–8, 2016.

[132] A. Rinkevich and D. Perov, "Cole-cole formula for dependence of dynamic magnetic susceptibility of rare-earth titanates on magnetic field," *Journal of Magnetism and Magnetic Materials*, vol. 530, p. 167917, 2021.

[133] A. D. Grief and G. Richardson, "Mathematical modelling of magnetically targeted drug delivery," *Journal of magnetism and magnetic materials*, vol. 293, no. 1, pp. 455–463, 2005.

[134] A. Rohatgi, "Webplotdigitizer: Version 4.5," 2021. [Online]. Available: https://automeris.io/WebPlotDigitizer

[135] A. G. Kolhatkar, A. C. Jamison, D. Litvinov, R. C. Willson, and T. R. Lee, "Tuning the magnetic properties of nanoparticles," *International journal of molecular sciences*, vol. 14, no. 8, pp. 15 977–16 009, 2013.

[136] J. Mosayebi, M. Kiyasatfar, and S. Laurent, "Synthesis, functionalization, and design of magnetic nanoparticles for theranostic applications," *Advanced Healthcare Materials*, vol. 6, no. 23, p. 1700306, 2017.

[137] M. B. Lodi, "Theoretical considerations for the design of magnetic scaffolds for bone tumor hyperthermia," in *2021 XXXIVth General Assembly and Scientific Symposium of the International Union of Radio Science (URSI GASS)*. IEEE, 2021, pp. 1–4.

[138] C. Rossmann and D. Haemmerich, "Review of temperature dependence of thermal properties, dielectric properties, and perfusion of biological tissues at hyperthermic and ablation temperatures," *Critical Reviews™ in Biomedical Engineering*, vol. 42, no. 6, 2014.

[139] M. Ikenaga, K. Ohura, T. Yamamuro, Y. Kotoura, M. Oka, and T. Kokubo, "Localized hyperthermic treatment of experimental bone tumors with ferromagnetic ceramics," *Journal of orthopaedic research*, vol. 11, no. 6, pp. 849–855, 1993.

[140] T. Albrektsson and C. Johansson, "Osteoinduction, osteoconduction and osseointegration,"

European spine journal, vol. 10, no. 2, pp. S96–S101, 2001.

[141] M. Montagu and J. C. Brožek, "A handbook of anthropometry." 1960.

[142] V. R. Preedy, *Handbook of anthropometry: physical measures of human form in health and disease*. Springer Science & Business Media, 2012.

[143] Y. Tomiyama, K. Yoshinaga, S. Fujii, N. Ochi, M. Inoue, M. Nishida, K. Aziki, T. Horie, C. Katoh, and N. Tamaki, "Accurate quantitative measurements of brachial artery cross-sectional vascular area and vascular volume elastic modulus using automated oscillometric measurements: comparison with brachial artery ultrasound," *Hypertension Research*, vol. 38, no. 7, p. 478, 2015.

[144] K. D. Paulsen, J. W. Strohbehn, and D. R. Lynch, "Theoretical electric field distributions produced by three types of regional hyperthermia devices in a three-dimensional homogeneous model of man," *IEEE transactions on biomedical engineering*, vol. 35, no. 1, pp. 36–45, 1988.

[145] V. Labinac, N. Erceg, and D. Kotnik-Karuza, "Magnetic field of a cylindrical coil," *American journal of physics*, vol. 74, no. 7, pp. 621–627, 2006.

[146] P. S. Ruggera and G. Kantor, "Development of a family of rf helical coil applicators which produce transversely uniform axially distributed heating in cylindrical fat-muscle phantoms," *IEEE transactions on biomedical engineering*, no. 1, pp. 98–106, 1984.

[147] D. C. Ellinger, F. Chute, and F. Vermeulen, "Evaluation of a semi-cylindrical solenoid as an applicator for radio-frequency hyperthermia," *IEEE transactions on biomedical engineering*, vol. 36, no. 10, pp. 987–994, 1989.

[148] M. Hiraoka, S. Jo, Y. Dodo, K. Ono, M. Takahashi, H. Nishida, and M. Abe, "Clinical results of radiofrequency hyperthermia combined with radiation in the treatment of radioresistant cancers," *Cancer*, vol. 54, no. 12, pp. 2898–2904, 1984.

[149] J. Li, H. Yao, Y. Lei, W. Huang, and Z. Wang, "Numerical simulation of magnetic fluid hyperthermia based on multiphysics coupling and recommendation on preferable treatment conditions," *Current Applied Physics*, vol. 19, no. 9, pp. 1031–1039, 2019.

[150] M. Bañobre-López, Y. Piñeiro-Redondo, M. Sandri, A. Tampieri, R. De Santis, V. A. Dediu, and J. Rivas, "Hyperthermia induced in magnetic scaffolds for bone tissue engineering," *IEEE Transactions on Magnetics*, vol. 50, no. 11, pp. 1–7, 2014.

[151] P. Hasgall, F. Di Gennaro, C. Baumgartner, E. Neufeld, M. Gosselin, D. Payne, A. Klingenböck, and N. Kuster, "It'is database for thermal and electromagnetic parameters of biological tissues," *Version 3.0*, 2015.

[152] M. Van der Gaag, M. De Bruijne, T. Samaras, J. Van Der Zee, and G. Van Rhoon, "Development of a guideline for the water bolus temperature in superficial hyperthermia," *International journal of hyperthermia*, vol. 22, no. 8, pp. 637–656, 2006.

[153] B. Prasad, J. K. Kim, and S. Kim, "Role of simulations in the treatment planning of radiofrequency hyperthermia therapy in clinics," *Journal of Oncology*, vol. 2019, 2019.

[154] R. K. Jain and K. Ward-Hartley, "Tumor blood flow-characterization, modifications, and role in hyperthermia," *IEEE Transactions on sonics and ultrasonics*, vol. 31, no. 5, pp. 504–525,

1984.

[155] F. Fanari, L. Mariani, and F. Desogus, "Heat transfer modeling in bone tumour hyperthermia induced by hydroxyapatite magnetic thermo-seeds," *The Open Chemical Engineering Journal*, vol. 14, no. 1, 2020.

[156] B. Hildebrandt, P. Wust, O. Ahlers, A. Dieing, G. Sreenivasa, T. Kerner, R. Felix, and H. Riess, "The cellular and molecular basis of hyperthermia," *Critical reviews in oncology/hematology*, vol. 43, no. 1, pp. 33–56, 2002.

[157] T. Samaras, A. Christ, A. Klingenbock, and N. Kuster, "Worst case temperature rise in a one-dimensional tissue model exposed to radiofrequency radiation," *IEEE Transactions on Biomedical Engineering*, vol. 54, no. 3, pp. 492–496, 2007.

[158] M. Ferreira and J. Yanagihara, "A heat transfer model of the human upper limbs," *International Communications in Heat and Mass Transfer*, vol. 39, no. 2, pp. 196–203, 2012.

[159] R. B. Bird, "Transport phenomena," *Applied Mechanics Reviews*, vol. 55, no. 1, pp. R1–R4, 2002.

[160] R. L. Fournier, *Basic transport phenomena in biomedical engineering*. CRC press, 2017.

[161] J. Dickson and S. Calderwood, "Temperature range and selective sensitivity of tumors to hyperthermia: a critical review," *Annals of the New York Academy of Sciences*, vol. 335, no. 1, pp. 180–205, 1980.

[162] S. A. Sapareto, "Thermal isoeffect dose: addressing the problem of thermotolerance," *International journal of hyperthermia*, vol. 3, no. 4, pp. 297–305, 1987.

[163] A. Fanti, M. Spanu, M. B. Lodi, F. Desogus, and G. Mazzarella, "Nonlinear analysis of soil microwave heating: Application to agricultural soils disinfection," *IEEE Journal on Multiscale and Multiphysics Computational Techniques*, vol. 2, pp. 105–114, 2017.

[164] M. B. Lodi, "Challenging the modeling of magnetic hyperthermia of secondary bone tumors using magnetic prosthetic implants," in *2020 XXXIIIrd General Assembly and Scientific Symposium of the International Union of Radio Science*. IEEE, pp. 1–4.

[165] M. B. Lodi, N. Curreli, S. Zappia, L. Pilia, M. F. Casula, S. Fiorito, I. Catapano, F. Desogus, T. Pellegrino, I. Kriegel, and et al., "Influence of magnetic scaffold loading patterns on their hyperthermic potential against bone tumors," Aug 2021. [Online]. Available: https://www.techrxiv.org/articles/preprint/Influence_of_Magnetic_Scaffold_Loading_Patterns_on_their_Hyperthermic_Potential_against_Bone_Tumors/15098061/1

[166] M. B. Lodi, A. Makridis, N. M. Carboni, K. Kazeli, N. Curreli, T. Samaras, M. Angelakeris, G. Mazzarella, and A. Fanti, "Design and characterization of magnetic scaffolds for bone tumor hyperthermia," *IEEE Access*, vol. 10, pp. 19 768–19 779, 2022.

[167] M. B. Lodi, A. Markidis, K. Kazeli, A. Fanti, T. Samara, M. Angelakeris, and G. Mazzarella, "A universal protocol for evaluating the specific absorption rate of magnetic scaffolds," *UnderPreparation*, 2022.

[168] K. Lai, W. Jiang, J. Z. Tang, Y. Wu, B. He, G. Wang, and Z. Gu, "Superparamagnetic nano-composite scaffolds for promoting bone cell proliferation and defect reparation without

a magnetic field," *RSC advances*, vol. 2, no. 33, pp. 13 007–13 017, 2012.

[169] S. El-Dek, M. A. Ali, S. M. El-Zanaty, and S. E. Ahmed, "Comparative investigations on ferrite nanocomposites for magnetic hyperthermia applications," *Acta Biomaterialia*, vol. 458, pp. 147–155, Jul. 2018. [Online]. Available: https://doi.org/10.1016/j.jmmm.2018.02.052

[170] X. Zeng, X. Zeng, Hu, Xie, Lan, Wu, Jiang, and Z. Gu, "Magnetic responsive hydroxyapatite composite scaffolds construction for bone defect reparation," *International Journal of Nanomedicine*, p. 3365, Jul. 2012. [Online]. Available: https://doi.org/10.2147/ijn.s32264

[171] Y. Amemiya, A. Arakaki, S. S. Staniland, T. Tanaka, and T. Matsunaga, "Controlled formation of magnetite crystal by partial oxidation of ferrous hydroxide in the presence of recombinant magnetotactic bacterial protein mms6," *Biomaterials*, vol. 28, no. 35, pp. 5381–5389, Dec. 2007. [Online]. Available: https://doi.org/10.1016/j.biomaterials.2007.07.051

[172] J.-J. Kim, R. K. Singh, S.-J. Seo, T.-H. Kim, J.-H. Kim, E.-J. Lee, and H.-W. Kim, "Magnetic scaffolds of polycaprolactone with functionalized magnetite nanoparticles: physicochemical, mechanical, and biological properties effective for bone regeneration," *Rsc Advances*, vol. 4, no. 33, pp. 17 325–17 336, 2014.

[173] H. Hu, W. Jiang, F. Lan, X. Zeng, S. Ma, Y. Wu, and Z. Gu, "Synergic effect of magnetic nanoparticles on the electrospun aligned superparamagnetic nanofibers as a potential tissue engineering scaffold," *Rsc Advances*, vol. 3, no. 3, pp. 879–886, 2013.

[174] M. L. Mather, S. P. Morgan, L. J. White, H. Tai, W. Kockenberger, S. M. Howdle, K. M. Shakesheff, and J. A. Crowe, "Image-based characterization of foamed polymeric tissue scaffolds," *Biomedical Materials*, vol. 3, no. 1, p. 015011, Mar. 2008. [Online]. Available: https://doi.org/10.1088/1748-6041/3/1/015011

[175] I. Busboom, T. T. Nguyen, S. Christmann, V. K. S. Feige, H. Haehnel, and B. Tibken, "Terahertz imaging of 3d print infill structures," in *2021 15th European Conference on Antennas and Propagation (EuCAP)*. IEEE, Mar. 2021. [Online]. Available: https://doi.org/10.23919/eucap51087.2021.9411331

[176] R. Fukusawa, "Terahertz imaging: Widespread industrial application in non-destructive inspection and chemical analysis," *IEEE Transactions on Terahertz Science and Technology*, vol. 5, no. 6, p. 015011, Nov. 2015. [Online]. Available: https://doi.org/10.1088/1748-6041/3/1/015011

[177] A. A. Mahmoud and A. H. Salama, "Norfloxacin-loaded collagen/chitosan scaffolds for skin reconstruction: Preparation, evaluation and in-vivo wound healing assessment," *European Journal of Pharmaceutical Sciences*, vol. 83, pp. 155–165, Feb. 2016. [Online]. Available: https://doi.org/10.1016/j.ejps.2015.12.026

[178] J. Takayanagi, H. Jinno, S. Ichino, K. Suizu, M. Yamashita, T. Ouchi, S. Kasai, H. Ohtake, H. Uchida, N. Nishizawa, and K. Kawase, "High-resolution time-of-flight terahertz tomography using a femtosecond fiber laser," *Optics Express*, vol. 17, no. 9, p. 7533, Apr. 2009. [Online]. Available: https://doi.org/10.1364/oe.17.007533

[179] I. Catapano and F. Soldovieri, "THz imaging and spectroscopy: First experiments and

preliminary results," in *2015 8th International Workshop on Advanced Ground Penetrating Radar (IWAGPR)*. IEEE, Jul. 2015. [Online]. Available: https://doi.org/10.1109/iwagpr.2015.7292702

[180] ——, "A data processing chain for terahertz imaging and its use in artwork diagnostics," *Journal of Infrared, Millimeter, and Terahertz Waves*, vol. 38, no. 4, pp. 518–530, Nov. 2016. [Online]. Available: https://doi.org/10.1007/s10762-016-0340-3

[181] U. Holzwarth and N. Gibson, "The scherrer equation versus the'debye-scherrer equation'," *Nature nanotechnology*, vol. 6, no. 9, pp. 534–534, 2011.

[182] C. Shuai, Y. Cheng, W. Yang, P. Feng, Y. Yang, C. He, F. Qi, and S. Peng, "Magnetically actuated bone scaffold: Microstructure, cell response and osteogenesis," *Composites Part B: Engineering*, vol. 192, p. 107986, 2020.

[183] R. Canters, P. Wust, J. Bakker, and G. Van Rhoon, "A literature survey on indicators for characterisation and optimisation of sar distributions in deep hyperthermia, a plea for standardisation," *International Journal of Hyperthermia*, vol. 25, no. 7, pp. 593–608, 2009.

[184] G. Augustin, S. Davila, K. Mihoci, T. Udiljak, D. S. Vedrina, and A. Antabak, "Thermal osteonecrosis and bone drilling parameters revisited," *Archives of orthopaedic and trauma surgery*, vol. 128, no. 1, pp. 71–77, 2008.

[185] E. B. Dolan, T. J. Vaughan, G. L. Niebur, C. Casey, D. Tallon, and L. M. McNamara, "How bone tissue and cells experience elevated temperatures during orthopaedic cutting: an experimental and computational investigation," *Journal of biomechanical engineering*, vol. 136, no. 2, p. 021019, 2014.

[186] K. Ikuta, H. Urakawa, E. Kozawa, S. Hamada, T. Ota, R. Kato, H. Honda, T. Kobayashi, N. Ishiguro, and Y. Nishida, "In vivo heat-stimulus-triggered osteogenesis," *International Journal of Hyperthermia*, vol. 31, no. 1, pp. 58–66, 2015.

[187] T. Ota, Y. Nishida, K. Ikuta, R. Kato, E. Kozawa, S. Hamada, T. Sakai, and N. Ishiguro, "Heat-stimuli-enhanced osteogenesis using clinically available biomaterials," *PLoS One*, vol. 12, no. 7, p. e0181404, 2017.

[188] M. Ghini, N. Curreli, A. Camellini, M. Wang, A. Asaithambi, and I. Kriegel, "Photodoping of metal oxide nanocrystals for multi-charge accumulation and light-driven energy storage," *Nanoscale*, 2021.

[189] K. Simeonidis, C. Martinez-Boubeta, D. Serantes, S. Ruta, O. Chubykalo-Fesenko, R. Chantrell, J. Oró-Solé, L. Balcells, A. Kamzin, R. Nazipov *et al.*, "Controlling magnetization reversal and hyperthermia efficiency in core–shell iron–iron oxide magnetic nanoparticles by tuning the interphase coupling," *ACS applied nano materials*, vol. 3, no. 5, pp. 4465–4476, 2020.

[190] A. Makridis, S. Curto, G. Van Rhoon, T. Samaras, and M. Angelakeris, "A standardisation protocol for accurate evaluation of specific loss power in magnetic hyperthermia," *Journal of Physics D: Applied Physics*, vol. 52, no. 25, p. 255001, 2019.

[191] I. Rubia-Rodríguez, A. Santana-Otero, S. Spassov, E. Tombácz, C. Johansson, P. De La Presa,

F. J. Teran, M. del Puerto Morales, S. Veintemillas-Verdaguer, N. T. Thanh *et al.*, "Whither magnetic hyperthermia? a tentative roadmap," *Materials*, vol. 14, no. 4, p. 706, 2021.

[192] M. M. Fernandes, D. M. Correia, C. Ribeiro, N. Castro, V. Correia, and S. Lanceros-Mendez, "Bioinspired three-dimensional magnetoactive scaffolds for bone tissue engineering," *ACS applied materials & interfaces*, vol. 11, no. 48, pp. 45 265–45 275, 2019.

[193] J. Shi, J. Yang, L. Zhu, L. Li, Z. Li, and X. Wang, "A porous scaffold design method for bone tissue engineering using triply periodic minimal surfaces," *IEEE Access*, vol. 6, pp. 1015–1022, 2017.

[194] A. Syahrom, M. R. A. Kadir, J. Abdullah, and A. Öchsner, "Permeability studies of artificial and natural cancellous bone structures," *Medical engineering & physics*, vol. 35, no. 6, pp. 792–799, 2013.

[195] A. Boccaccio, A. E. Uva, M. Fiorentino, G. Mori, and G. Monno, "Geometry design optimization of functionally graded scaffolds for bone tissue engineering: A mechanobiological approach," *PloS one*, vol. 11, no. 1, p. e0146935, 2016.

[196] V. J. Challis, A. P. Roberts, J. F. Grotowski, L.-C. Zhang, and T. B. Sercombe, "Prototypes for bone implant scaffolds designed via topology optimization and manufactured by solid freeform fabrication," *Advanced Engineering Materials*, vol. 12, no. 11, pp. 1106–1110, 2010.

[197] H. A. Almeida and P. J. Bartolo, "Design of tissue engineering scaffolds based on hyperbolic surfaces: Structural numerical evaluation," *Medical engineering & physics*, vol. 36, no. 8, pp. 1033–1040, 2014.

[198] K. Yu, B. Liang, Y. Zheng, A. Exner, M. Kolios, T. Xu, D. Guo, X. Cai, Z. Wang, H. Ran *et al.*, "Pmma-fe3o4 for internal mechanical support and magnetic thermal ablation of bone tumors," *Theranostics*, vol. 9, no. 14, p. 4192, 2019.

[199] D. Tompkins, B. Partington, R. Steeves, S. Bartholow, and B. Paliwal, "Effect of implant variables on temperatures achieved during ferromagnetic hyperthermia," *International journal of hyperthermia*, vol. 8, no. 2, pp. 241–251, 1992.

[200] A. Cervadoro, C. Giverso, R. Pande, S. Sarangi, L. Preziosi, J. Wosik, A. Brazdeikis, and P. Decuzzi, "Design maps for the hyperthermic treatment of tumors with superparamagnetic nanoparticles," *PloS one*, vol. 8, no. 2, p. e57332, 2013.

[201] S. A. Shah, M. Hashmi, S. Alam, and A. Shamim, "Magnetic and bioactivity evaluation of ferrimagnetic znfe2o4 containing glass ceramics for the hyperthermia treatment of cancer," *Journal of magnetism and magnetic materials*, vol. 322, no. 3, pp. 375–381, 2010.

[202] Y. Jiang, J. Ou, Z. Zhang, and Q.-H. Qin, "Preparation of magnetic and bioactive calcium zinc iron silicon oxide composite for hyperthermia treatment of bone cancer and repair of bone defects," *Journal of Materials Science: Materials in Medicine*, vol. 22, no. 3, pp. 721–729, 2011.

[203] F. Wang, Y. Yang, Y. Ling, J. Liu, X. Cai, X. Zhou, X. Tang, B. Liang, Y. Chen, H. Chen *et al.*, "Injectable and thermally contractible hydroxypropyl methyl cellulose/fe3o4 for magnetic hyperthermia ablation of tumors," *Biomaterials*, vol. 128, pp. 84–93, 2017.

[204] K. Zhang, G. Li, Z. Pei, S. Zhao, A. Jing, and G. Liang, "Injectable graphite-modified fe3o4/calcium phosphate bone cement with enhanced heating ability for hyperthermia," *Materials Technology*, vol. 35, no. 13-14, pp. 863–871, 2020.

[205] P. J. Gandy, D. Cvijović, A. L. Mackay, and J. Klinowski, "Exact computation of the triply periodic d (diamond') minimal surface," *Chemical physics letters*, vol. 314, no. 5-6, pp. 543–551, 1999.

[206] P. J. Gandy and J. Klinowski, "Exact computation of the triply periodic schwarz p minimal surface," *Chemical Physics Letters*, vol. 322, no. 6, pp. 579–586, 2000.

[207] ——, "Exact computation of the triply periodic g (gyroid') minimal surface," *Chemical Physics Letters*, vol. 321, no. 5-6, pp. 363–371, 2000.

[208] D.-J. Yoo, "Computer-aided porous scaffold design for tissue engineering using triply periodic minimal surfaces," *International Journal of Precision Engineering and Manufacturing*, vol. 12, no. 1, pp. 61–71, 2011.

[209] R. Goldman, "Curvature formulas for implicit curves and surfaces," *Computer Aided Geometric Design*, vol. 22, no. 7, pp. 632–658, 2005.

[210] J. Dinis, T. Morais, P. Amorim, R. Ruben, H. Almeida, P. Inforçati, P. Bártolo, and J. Silva, "Open source software for the automatic design of scaffold structures for tissue engineering applications," *Procedia Technology*, vol. 16, pp. 1542–1547, 2014.

[211] M. B. Lodi, "Tpms scaffold," Retrieved November 5, 2021. [Online]. Available: https://www.mathworks.com/matlabcentral/fileexchange/99379-tpms-scaffold

[212] Sveni, "stlwrite - write ascii or binary stl files," Retrieved May 19, 2021. [Online]. Available: https://www.mathworks.com/matlabcentral/fileexchange/20922-stlwrite-write-ascii-or-binary-stl-files

[213] J. Laureto, J. Tomasi, J. A. King, and J. M. Pearce, "Thermal properties of 3-d printed polylactic acid-metal composites," *Progress in Additive Manufacturing*, vol. 2, no. 1, pp. 57–71, 2017.

[214] L. M. Bollig, M. V. Patton, G. S. Mowry, and B. B. Nelson-Cheeseman, "Effects of 3-d printed structural characteristics on magnetic properties," *IEEE Transactions on Magnetics*, vol. 53, no. 11, pp. 1–6, 2017.

[215] J. Sorocki, I. Piekarz, and M. Bozzi, "Broadband permittivity and permeability extraction of 3-d-printed magneto-dielectric substrates," *IEEE Microwave and Wireless Components Letters*, vol. 31, no. 10, pp. 1174–1177, 2021.

[216] O. Zmeskal, L. Marackova, T. Lapcikova, P. Mencik, and R. Prikryl, "Thermal properties of samples prepared from polylactic acid by 3d printing," in *AIP Conference Proceedings*, vol. 2305, no. 1. AIP Publishing LLC, 2020, p. 020022.

[217] A. International, *ASTM E1269-11(2018), Standard Test Method for Determining Specific Heat Capacity by Differential Scanning Calorimetry*, West Conshohocken, PA, 2018. [Online]. Available: www.astm.org

[218] S. Di Meo, J. Bonello, M. B. Lodi, I. Farhat, L. Farrugia, A. Fanti, M. Pasian, F. Desogus,

and C. V. Sammut, "On the dielectric/thermal characterization and calibration of solutions and materials for biomedical applications," in *2020 14th European Conference on Antennas and Propagation (EuCAP)*. IEEE, 2020, pp. 1–4.

[219] J. Wells, D. Ortega, U. Steinhoff, S. Dutz, E. Garaio, O. Sandre, E. Natividad, M. M. Cruz, F. Brero, P. Southern *et al.*, "Challenges and recommendations for magnetic hyperthermia characterization measurements," *International Journal of Hyperthermia*, vol. 38, no. 1, pp. 447–460, 2021.

[220] I. Andreu and E. Natividad, "Accuracy of available methods for quantifying the heat power generation of nanoparticles for magnetic hyperthermia," *International Journal of Hyperthermia*, vol. 29, no. 8, pp. 739–751, 2013.

[221] H. Kato, K. Yoshimura, M. Kuroda, A. Yoshida, K. Hanamoto, S. Kawasaki, K. Shibuya, Y. Yamamoto, M. Tsunoda, M. Takemoto *et al.*, "Development of a phantom compatible for mri and hyperthermia using carrageenan gel—relationship between dielectric properties and nacl concentration," *International journal of hyperthermia*, vol. 20, no. 5, pp. 529–538, 2004.

[222] R. A. Jaime, R. L. Basto, B. Lamien, H. R. Orlande, S. Eibner, and O. Fudym, "Fabrication methods of phantoms simulating optical and thermal properties," *Procedia Engineering*, vol. 59, pp. 30–36, 2013.

[223] C. Dichtl, P. Sippel, and S. Krohns, "Dielectric properties of 3d printed polylactic acid," *Advances in Materials Science and Engineering*, vol. 2017, 2017.

[224] E. Natividad, M. Castro, and A. Mediano, "Adiabatic vs. non-adiabatic determination of specific absorption rate of ferrofluids," *Journal of Magnetism and Magnetic Materials*, vol. 321, no. 10, pp. 1497–1500, 2009.

[225] S. K. Kandala, A. Sharma, S. Mirpour, E. Liapi, R. Ivkov, and A. Attaluri, "Validation of a coupled electromagnetic and thermal model for estimating temperatures during magnetic nanoparticle hyperthermia," *International Journal of Hyperthermia*, vol. 38, no. 1, pp. 611–622, 2021.

[226] T. Ghassemi, A. Shahroodi, M. H. Ebrahimzadeh, A. Mousavian, J. Movaffagh, and A. Moradi, "Current concepts in scaffolding for bone tissue engineering," *Archives of bone and joint surgery*, vol. 6, no. 2, p. 90, 2018.

[227] R. A. Perez, S.-J. Seo, J.-E. Won, E.-J. Lee, J.-H. Jang, J. C. Knowles, and H.-W. Kim, "Therapeutically relevant aspects in bone repair and regeneration," *Materials Today*, vol. 18, no. 10, pp. 573–589, 2015.

[228] A. Marino, C. Filippeschi, V. Mattoli, B. Mazzolai, and G. Ciofani, "Biomimicry at the nanoscale: current research and perspectives of two-photon polymerization," *Nanoscale*, vol. 7, no. 7, pp. 2841–2850, 2015.

[229] R. A. Carano and E. H. Filvaroff, "Angiogenesis and bone repair," *Drug discovery today*, vol. 8, no. 21, pp. 980–989, 2003.

[230] W. Zhou, J. Um, Y. Zhang, A. P. Nelson, Z. Nemati, J. Modiano, B. Stadler, and R. Franklin, "Development of a biolabeling system using ferromagnetic nanowires," *IEEE Journal of*

Electromagnetics, RF and Microwaves in Medicine and Biology, vol. 3, no. 2, pp. 134–142, 2018.

[231] G. Barrera, M. Coïsson, F. Celegato, E. S. Olivetti, L. Martino, I. Miletto, and P. Tiberto, "Magnetic and thermal characterization of core-shell fe-oxide@ sio 2 nanoparticles for hyperthermia applications," *IEEE Journal of Electromagnetics, RF and Microwaves in Medicine and Biology*, vol. 2, no. 4, pp. 257–261, 2018.

[232] B. Liang, D. Zuo, K. Yu, X. Cai, B. Qiao, R. Deng, J. Yang, L. Chu, Z. Deng, Y. Zheng *et al.*, "Multifunctional bone cement for synergistic magnetic hyperthermia ablation and chemotherapy of osteosarcoma," *Materials Science and Engineering: C*, vol. 108, p. 110460, 2020.

[233] S. Erokhin and D. Berkov, "Magnetic targeted drug delivery to the human eye retina: an optimization methodology," *IEEE Journal of Electromagnetics, RF and Microwaves in Medicine and Biology*, vol. 3, no. 1, pp. 3–8, 2018.

[234] O. L. Lanier, A. G. Monsalve, P. S. McFetridge, and J. Dobson, "Magnetically triggered release of biologics," *International Materials Reviews*, vol. 64, no. 2, pp. 63–90, 2019.

[235] A. Monsalve, A. C. Bohórquez, C. Rinaldi, and J. Dobson, "Remotely triggered activation of tgf-with magnetic nanoparticles," *IEEE Magnetics Letters*, vol. 6, pp. 1–4, 2015.

[236] S. Meikle, Y. Piñeiro, M. B. López, J. Rivas, and M. Santin, "Surface functionalization superparamagnetic nanoparticles conjugated with thermoresponsive poly (epsilon-lysine) dendrons tethered with carboxybetaine for the mild hyperthermia-controlled delivery of vegf," *Acta biomaterialia*, vol. 40, pp. 235–242, 2016.

[237] M. B. Lodi, A. Fanti, A. Vargiu, M. Bozzi, and G. Mazzarella, "Mathematical modeling of magnetic scaffolds for targeted drug delivery and bone repair," Sep 2021. [Online]. Available: https://www.techrxiv.org/articles/preprint/Mathematical_Modeling_Of_Magnetic_Scaffolds_For_Targeted_Drug_Delivery_And_Bone_Repair/16545669/1

[238] S. Behrens, "Preparation of functional magnetic nanocomposites and hybrid materials: recent progress and future directions," *Nanoscale*, vol. 3, no. 3, pp. 877–892, 2011.

[239] S. J. Kuhn, D. E. Hallahan, and T. D. Giorgio, "Characterization of superparamagnetic nanoparticle interactions with extracellular matrix in an in vitro system," *Annals of biomedical engineering*, vol. 34, no. 1, pp. 51–58, 2006.

[240] K. Rege and I. L. Medintz, *Methods in Bioengineering: Nanoscale Bioengineering and Nanomedicine*. Artech House, 2009.

[241] J. M. Stukel, J. J. Heys, and M. R. Caplan, "Optimizing delivery of multivalent targeting constructs for detection of secondary tumors," *Annals of biomedical engineering*, vol. 36, no. 7, pp. 1291–1304, 2008.

[242] A. Phillips, "Overview of the fracture healing cascade," *Injury*, vol. 36, no. 3, pp. S5–S7, 2005.

[243] J. E. Davies, "Bone bonding at natural and biomaterial surfaces," *Biomaterials*, vol. 28, no. 34, pp. 5058–5067, 2007.

[244] P. Moreo, J. M. García-Aznar, and M. Doblaré, "Bone ingrowth on the surface of endosseous

implants. part 1: Mathematical model," *Journal of theoretical biology*, vol. 260, no. 1, pp. 1–12, 2009.

[245] ——, "Bone ingrowth on the surface of endosseous implants. part 2: Theoretical and numerical analysis," *Journal of theoretical biology*, vol. 260, no. 1, pp. 13–26, 2009.

[246] J. Baldonedo, J. R. Fernández, and A. Segade, "Numerical analysis of an osseointegration model," *Mathematics*, vol. 8, no. 1, p. 87, 2020.

[247] T. Hillen and K. J. Painter, "A user's guide to pde models for chemotaxis," *Journal of mathematical biology*, vol. 58, no. 1, pp. 183–217, 2009.

[248] A. Colombi, M. Scianna, and L. Preziosi, "A measure-theoretic model for collective cell migration and aggregation," *Mathematical Modelling of Natural Phenomena*, vol. 10, no. 1, pp. 4–35, 2015.

[249] U. Fano, "Ionization yield of radiations. ii. the fluctuations of the number of ions," *Physical Review*, vol. 72, no. 1, p. 26, 1947.

[250] R. R. Chen, E. A. Silva, W. W. Yuen, and D. J. Mooney, "Spatio–temporal vegf and pdgf delivery patterns blood vessel formation and maturation," *Pharmaceutical research*, vol. 24, no. 2, pp. 258–264, 2007.

[251] Y.-I. Chung, S.-K. Kim, Y.-K. Lee, S.-J. Park, K.-O. Cho, S. H. Yuk, G. Tae, and Y. H. Kim, "Efficient revascularization by vegf administration via heparin-functionalized nanoparticle–fibrin complex," *Journal of Controlled Release*, vol. 143, no. 3, pp. 282–289, 2010.

[252] A. Lode, C. Wolf-Brandstetter, A. Reinstorf, A. Bernhardt, U. König, W. Pompe, and M. Gelinsky, "Calcium phosphate bone cements, functionalized with vegf: release kinetics and biological activity," *Journal of Biomedical Materials Research Part A: An Official Journal of The Society for Biomaterials, The Japanese Society for Biomaterials, and The Australian Society for Biomaterials and the Korean Society for Biomaterials*, vol. 81, no. 2, pp. 474–483, 2007.

[253] M. B. Keogh, F. J. O'Brien, and J. S. Daly, "A novel collagen scaffold supports human osteogenesis—applications for bone tissue engineering," *Cell and tissue research*, vol. 340, no. 1, pp. 169–177, 2010.

[254] E. Wernike, M.-O. Montjovent, Y. Liu, D. Wismeijer, E. B. Hunziker, K.-A. Siebenrock, W. Hofstetter, F. M. Klenke *et al.*, "Vegf incorporated into calcium phosphate ceramics promotes vascularisation and bone formation in vivo," *Eur Cell Mater*, vol. 19, no. 3, 2010.

[255] D. L. Holligan, G. T. Gilies, and J. P. Dailey, "Magnetic guidance of ferrofluidic nanoparticles in an in vitro model of intraocular retinal repair," *Nanotechnology*, vol. 14, no. 6, p. 661, 2003.

[256] J. Wang, Y. Chen, B. Chen, J. Ding, G. Xia, C. Gao, J. Cheng, N. Jin, Y. Zhou, X. Li, M. Tang, and X. M. Wang, "Pharmacokinetic parameters and tissue distribution of magnetic fe3o4 nanoparticles in mice," *International Journal of Nanomedicine*, vol. 5, pp. 861–866, 2010.

[257] H. H. Bayraktar, E. F. Morgan, G. L. Niebur, G. E. Morris, E. K. Wong, and T. M. Keaveny, "Comparison of the elastic and yield properties of human femoral trabecular and cortical bone

tissue," *journal of Biomechanics*, vol. 37, no. 1, pp. 27–35, 2004.

[258] K. Sumser, G. G. Bellizzi, R. Forner, T. Drizdal, J. A. H. Tamames, G. C. Van Rhoon, and M. M. Paulides, "Dual-function mr-guided hyperthermia: an innovative integrated approach and experimental demonstration of proof of principle," *IEEE Transactions on Biomedical Engineering*, vol. 68, no. 2, pp. 712–717, 2020.

[259] F. Adibzadeh, K. Sumser, S. Curto, D. T. Yeo, A. A. Shishegar, and M. M. Paulides, "Systematic review of pre-clinical and clinical devices for magnetic resonance-guided radiofrequency hyperthermia," *International Journal of Hyperthermia*, vol. 37, no. 1, pp. 15–27, 2020.

[260] T. V. Feddersen, J. A. Hernandez-Tamames, M. Franckena, G. C. van Rhoon, and M. M. Paulides, "Clinical performance and future potential of magnetic resonance thermometry in hyperthermia," *Cancers*, vol. 13, no. 1, p. 31, 2021.

[261] C. Dachena, A. Fedeli, A. Fanti, M. B. Lodi, M. Pastorino, and A. Randazzo, "Microwave imaging for the diagnosis of cervical diseases: A feasibility analysis," *IEEE Journal of Electromagnetics, RF and Microwaves in Medicine and Biology*, 2020.

[262] C. Dachena, A. Fedeli, A. Fanti, M. B. Lodi, G. Fumera, A. Randazzo, and M. Pastorino, "Microwave imaging of the neck by means of artificial neural networks for tumor detection," *IEEE Open Journal of Antennas and Propagation*, 2021.

[263] O. Fiser, M. Helbig, J. Sachs, S. Ley, I. Merunka, and J. Vrba, "Microwave non-invasive temperature monitoring using uwb radar for cancer treatment by hyperthermia," *Progress In Electromagnetics Research*, vol. 162, pp. 1–14, 2018.

[264] W. Maamoun, M. I. Badawi, A. A. Aly, and Y. Khedr, "Nanoparticles in enhancing microwave imaging and microwave hyperthermia effect for liver cancer treatment," *Reviews on Advanced Materials Science*, vol. 60, no. 1, pp. 223–236, 2021.

[265] G. Chen, J. Stang, M. Haynes, E. Leuthardt, and M. Moghaddam, "Real-time three-dimensional microwave monitoring of interstitial thermal therapy," *IEEE Transactions on Biomedical Engineering*, vol. 65, no. 3, pp. 528–538, 2017.

[266] M. G. Aram, L. Beilina, and H. D. Trefna, "Microwave thermometry with potential application in non-invasive monitoring of hyperthermia," *Journal of Inverse and Ill-posed Problems*, vol. 28, no. 5, pp. 739–750, 2020.

[267] A. Prokhorova, S. Ley, A. Y. Ruiz, R. Scapaticci, L. Crocco, and M. Helbig, "Preliminary investigations of microwave imaging algorithms for tissue temperature estimation during hyperthermia treatment," in *2021 International Conference on Electromagnetics in Advanced Applications (ICEAA)*. IEEE, 2021, pp. 079–084.

[268] M. Wang, L. Crocco, and M. Cavagnaro, "On the design of a microwave imaging system to monitor thermal ablation of liver tumors," *IEEE Journal of Electromagnetics, RF and Microwaves in Medicine and Biology*, vol. 5, no. 3, pp. 231–237, 2021.

[269] R. Scapaticci, L. Di Donato, I. Catapano, and L. Crocco, "A feasibility study on microwave imaging for brain stroke monitoring," *Progress In Electromagnetics Research B*, vol. 40, pp. 305–324, 2012.

[270] S. J. Orfanidis. Rutgers University New Brunswick, NJ, 2002.

[271] N. Curreli, A. Fanti, G. Mazzarella, and I. Kriegel, "Linear and nonlinear optical propagation in 2d materials," *arXiv preprint arXiv:2103.13884*, 2021.

[272] S. Symeonidis, W. G. Whittow, M. Zecca, and C. Panagamuwa, "Bone fracture monitoring using implanted antennas in the radius, tibia and phalange heterogeneous bone phantoms," *Biomedical Physics & Engineering Express*, vol. 4, no. 4, p. 045006, 2018.

[273] A. Swarup, S. Stuchly, and A. Surowiec, "Dielectric properties of mouse mca1 fibrosarcoma at different stages of development," *Bioelectromagnetics*, vol. 12, no. 1, pp. 1–8, 1991.

[274] E. Odelstad, S. Raman, A. Rydberg, and R. Augustine, "Experimental procedure for determination of the dielectric properties of biological samples in the 2-50 ghz range," *IEEE journal of translational engineering in health and medicine*, vol. 2, pp. 1–8, 2014.

[275] Z. Macit, C. Aydinalp, T. Yilmaz, A. B. O. Sert, and F. N. Kok, "Microwave dielectric properties of osteosarcoma cell line (saos-2) suspensions," in *2019 23rd International Conference on Applied Electromagnetics and Communications (ICECOM)*. IEEE, 2019, pp. 1–4.

[276] Y. Arbaoui, P. Agaciak, A. Chevalier, V. Laur, A. Maalouf, J. Ville, P. Roquefort, T. Aubry, and P. Queffelec, "3d printed ferromagnetic composites for microwave applications," *Journal of Materials Science*, vol. 52, no. 9, pp. 4988–4996, 2017.

[277] X.-N. Guan, X.-N. Xu, R. Kuniyoshi, H.-H. Zhou, and Y.-F. Zhu, "Electromagnetic and mechanical properties of carbonyl iron powders-pla composites fabricated by fused deposition modeling," *Materials Research Express*, vol. 5, no. 11, p. 115303, 2018.

[278] A. Manzin, R. Ferrero, and M. Vicentini, "From micromagnetic to in silico modeling of magnetic nanodisks for hyperthermia applications," *Advanced Theory and Simulations*, vol. 4, no. 5, p. 2100013, 2021.

[279] N. Panagiotopoulos, R. L. Duschka, M. Ahlborg, G. Bringout, C. Debbeler, M. Graeser, C. Kaethner, K. Lüdtke-Buzug, H. Medimagh, J. Stelzner *et al.*, "Magnetic particle imaging: current developments and future directions," *International journal of nanomedicine*, vol. 10, p. 3097, 2015.

[280] Z. Wan, P. Zhang, L. Lv, and Y. Zhou, "Nir light-assisted phototherapies for bone-related diseases and bone tissue regeneration: A systematic review," *Theranostics*, vol. 10, no. 25, p. 11837, 2020.

[281] M. Ghini, N. Curreli, M. B. Lodi, N. Petrini, M. Wang, M. Prato, A. Fanti, L. Manna, and I. Kriegel, "Control of electronic band profiles through depletion layer engineering in core–shell nanocrystals," *Nature Communications*, vol. 13, no. 1, pp. 1–9, 2022.